INVESTIGATIONS ON FLEXURAL RESPONSE OF FRC BEAMS REINFORCED WITH BASALT FIBER REINFORCED POLYMER REBARS

Submitted in partial fulfilment of the requirements
for the award of the degree of

DOCTOR OF PHILOSOPHY

in

CIVIL ENGINEERING

by

BHANAVATH SAGAR
(Roll No. 717006)

Research Supervisor

Dr. M.V.N. SIVAKUMAR

DEPARTMENT OF CIVIL ENGINEERING
NATIONAL INSTITUTE OF TECHNOLOGY WARANGAL
TELANGANA STATE, INDIA – 506004

December-2023

NATIONAL INSTITUTE OF TECHNOLOGY WARANGAL

CERTIFICATE

This is to certify that the thesis entitled **"INVESTIGATIONS ON FLEXURAL RESPONSE OF FRC BEAMS REINFORCED WITH BASALT FIBER REINFORCED POLYMER REBARS"** being submitted by **Mr. BHANAVATH SAGAR** for the award of the degree of **DOCTOR OF PHILOSOPHY** in the Department of Civil Engineering, National Institute of Technology, Warangal, is a record of bonfire research work carried out by him under my supervision and it has not been submitted elsewhere for the award of any degree.

Dr. M.V.N. SIVAKUMAR

Thesis Supervisor
Associate Professor
Department of Civil Engineering
NIT Warangal (T.S), India

NATIONAL INSTITUTE OF TECHNOLOGY WARANGAL

Dissertation Approval

This dissertation entitled **"Investigations on Flexural Response of FRC Beams Reinforced with Basalt Fiber Reinforced Polymer Rebars"** by **Mr. Bhagavanth Sagar** is approved for the degree of **Doctor of Philosophy.**

Examiners

_____

_____

_____

Supervisor(s)

_____

_____

_____

Chairman

_____

Date: _____

Place: _____

NATIONAL INSTITUTE OF TECHNOLOGY WARANGAL

DECLARATION

This is to certify that the work presented in the thesis entitled **"Investigations on Flexural Response of FRC Beams Reinforced with Basalt Fiber Reinforced Polymer Rebars"** is a bonafide work done by me under the supervision of Dr. M.V.N. Sivakumar and was not submitted elsewhere for the award of any degree.

I declare that this written submission represented my ideas in my own words and where others' ideas or words have been included, I have adequately cited and referenced the original sources. I also declare that I have adhered to all principles of academic honesty and integrity and have not misrepresented or fabricated or falsified any idea / data / fact / source in my submission. I understand that any violation of the above will be a cause for disciplinary action by the Institute and can also evoke penal action from the sources which have thus not been properly cited or from whom proper permission has not been taken when needed.

_____

(BHANAVATH SAGAR)

(Roll No: **717006**)

Date: _____

Dedicated to

My

Beloved Parents

ACKNOWLEDGEMENTS

With great pleasure and proud privilege, I manifest my heartfelt thanks to my research supervisor, **Dr. MV.N. Sivakumar**, Associate Professor, Department of Civil Engineering, for his invaluable suggestions, sagacious guidance, scholarly advice, and comprehensive critical remarks in bringing out this research work with artistry. I am grateful to him for giving me the opportunity to work under his guidance.

I am deeply grateful to Prof. D. Ramaseshu, Chairman, Doctoral Scrutiny Committee, Department of Civil Engineering, for his immense support in bringing out this research work.

I would like to extend my sincere gratitude to the members of the Doctoral Scrutiny Committee, Prof. T.D. Gunneswara Rao, Professor and Head in the Department of Civil Engineering, Dr. T.P. Tezeswi, Associate Professor in the Department of Civil Engineering, Dr. Bonta Srinivasa Rao, Associate Professor in the Department of Metallurgical and Material Engineering, for their insightful comments and suggestions throughout my research work.

I am grateful to Mr. M. Sudhakar, Associate Professor, Department of Civil Engineering, for his support and resources in carrying out my research work.

I would like to thank Dr. B. Umesh, Assistant Professor, Department of Civil Engineering, for his help and motivation during the period of my research work.

I am thankful to Prof. C.B. Kameshwar Rao, Prof. G. Rajesh Kumar, Prof. P. Rathish Kumar, Dr. S. Venkateswara Rao, Dr. D. Ravi Prasad, Dr. K. Gopikrishna, Dr. S. Anitha Priyadharshani, and Dr. B. Kavitha, the faculty members of Structure Division, NITW, for giving me constant encouragement during my research work.

I would like to thank my senior research scholars, Dr. Oggu Praveen, Dr. B. Raja Rajeswari, and Dr. M. Venu, for their motivation and scholarly advice during my research work.

I express my gratitude to my friends, Dr. K. Satish Kumar, Dr. Jithender, Mrs. K. Srilatha, Dr. G. Venkata Rao, Dr. B. Sumanth Kumar, Mr. Sathish Polu, Mr. V. Guru Prathap Reddy, Mr. CH. Rajesh, Mr. Y. Subba Rao, and Mr. PVRK Reddy, who have always encouraged and supported me during my tough times. I would like to thank all my co-research scholars who helped me directly and indirectly with my research work.

I would like to thank the technical assistant, Mr. A. Laxman, for helping out with material procurement and laboratory work. I would like to thank Mr. M. Naresh and Mr. Ahmad, the

laboratory assistants from the concrete and material testing laboratory, for the smooth functioning of the experiments.

I would like to thank Sri Md. Hussain and the administrative staff for the help done during the research period.

I would like to thank M. Tech students Kshiteeja Shinde, Muhammad Saood, Ankur Paul, and Pawan Kumar for their direct or indirect help in doing the laboratory work.

I take immense pleasure in showing my heartfelt love to my parents, B. Lalu and B. Parvathi, and to my brother and his wife, B. Nagarjuna and B. Bhavani, for their patience in bearing me during this research period because of who and what I am today.

Last but not least, I heartfully thank D. Sruthilaya, who is close to my heart, for her consistent support and encouragement she gave me in my low and high times during this research to reach my goal.

Finally, I acknowledge the help given by all the individuals, either directly or indirectly, in support of my research work.

Bhanavath Sagar
Roll No: 717006

ABSTRACT

Investigations on the flexural response of fiber reinforced concrete (FRC) beams reinforced with basalt fiber reinforced polymer (BFRP) rebars are presented. The development of durability related issues in traditional steel reinforced concrete (RC) structures due to embedded steel reinforcement corrosion is the biggest problem that is causing the shortening of service life of the steel RC structures. Reinforcing the concrete structures using non-metallic and non-corrosive fiber reinforced polymer (FRP) rebars will ensure that the structure remains corrosion-free. BFRP rebar is a newly developed FRP rebar that is emerging as a green construction material, and it has become one of the best alternatives to existing FRP rebars. All FRP rebars have a lower Young's modulus and higher tensile strength than steel reinforcing bars. As a result, FRP reinforced plain concrete beams become less ductile, experience more deflections, and produce more cracks at higher flexural strengths. The flexural behaviour of steel or FRP RC beams not only depends on the area and type of reinforcement provided but also on the properties of the concrete used. The application of BFRP rebars in FRC can increase its performance as a longitudinal reinforcement, as the drawbacks associated with plain concrete (PC) beams reinforced with BFRP rebars can be decreased by increasing the strength and tensile properties of concrete with the addition of fibers. In this study, an attempt was made to develop an eco-friendly reinforcing system (BFRP rebars + basalt fibers and/or polyvinyl alcohol (PVA) fibers) to investigate the flexural response of BFRP reinforced basalt fiber reinforced concrete (BFRC) and PVA fiber reinforced concrete (PVAFRC) beams. Therefore, the present study was aimed to investigate the flexural response of PC, BFRC and PVAFRC beams reinforced with BFRP rebars. This investigation was carried out using two concrete grades: normal strength concrete (NSC) of M30 grade and high strength concrete (HSC) of M70 grade.

The use of pozzolanic materials in concrete manufacturing provides economical, technological, and environmental benefits. In this study, alccofine-1203 and fly ash were used as supplementary cementitious materials (SCMs) to partially replace cement in the development of HSC. 4%, 6%, 8%, 10%, 12% and 14% alccofine-1203 with 20% fly ash combination were used to partially replace cement to find the optimum percentage of alccofine-1203 to be used in the development of HSC. For this, a total of seven binder proportions were prepared and evaluated for mechanical properties, microstructural characteristics and compressive stress-strain behavior. From the obtained results, it was found that the use of alccofine-1203 in combination with fly ash was beneficial in the development of HSC. Among all, the

replacement of cement with 10% alccofine-1203 with a 20% fly ash combination attributed superior microstructural characteristics for binder mixes and showed highest mechanical properties and compressive stress-strain behaviour for the concrete.

In this study, to improve the flexural performance of BFRP RC beams, BFRC was developed using basalt fibers and PVAFRC was developed using PVA fibers. To determine the optimum percentage of basalt fibers and PVA fibers to use for manufacturing BFRC and PVAFRC, additions of 0.1%, 0.2%, 0.3%, 0.4%, and 0.5% (of the volume of concrete) basalt fibers and PVA fibers were made to the developed NSC and HSC. Consequently, a total of 20 mixes (10 BFRC mixes and 10 PVAFRC mixes) were developed and evaluated for fresh and hardened properties. The workability, compressive strength, flexural strength, split tensile strength, load-deflection behaviour, and uniaxial compressive stress-strain behaviour of BFRCs and PVAFRCs were studied experimentally. Young's modulus, and energy absorption capacity, peak-stress, and strain at peak-stress of BFRCs and PVAFRCs have also been studied analytically. Scanning electron microscopy analysis was performed to examine microstructural characteristics of BFRCs and PVAFRCs. The results indicated that the addition of basalt or PVA fibers reduced the workability of concrete mixes. The maximum compressive strength, flexural strength, split tensile strength and better load-deflection and stress-strain behaviour were obtained with the addition of 0.3% of basalt fibers in two strengths of BFRCs and 0.3% PVA fibers in two strengths of PVAFRCs. The modified constitutive analytical model and relationships between properties of compressive stress-strain curves of BFRCs and PVAFCs such as peak-stress, strain at peak stress and material parameter (β_n) with modified reinforcing index values of fibbers were proposed for analytical modelling of stress-strain curves of BFRCs and PVAFRCs of two strengths, and a good agreement with experimental results was observed. Additionally, in the literature, the proposed constitutive analytical model and relationships between the material parameter and reinforcing index for analytical modelling of FRC's stress-strain curves failed to accurately predict the experimental stress-strain curves of BFRCs and PVAFRCs.

To test the flexural response of BFRP RC (PC, BFRC, and PVAFRC) beams, 16 single-reinforced concrete beams with a pure bending region were cast and tested experimentally. Twelve beams were longitudinally reinforced with BFRP rebars in the tension region and four beams were fully reinforced with steel reinforcing bars. Two grades of concrete- NSC and HSC; two types of FRC- BFRC and PVAFRC; and two types of RC sections- under-reinforced and over-reinforced were parameters considered in the investigation. All the beams were tested for

load-deflection behaviour, moment-curvature relationships, ductility, cracking pattern and failure mode evaluation. The optimum percentage of basalt fibbers and PVA fibers (0.3%) was taken to prepare BFRC and PVAFRC. The obtained results showed that the load-deflection and moment-curvature response of BFRP-reinforced PC, BFRC, and PVAFRC beams exhibited two phases which bounded the cracking point, whereas steel-reinforced PC beams exhibited three phases which bound the cracking and yielding points. Although BFRP rebar is a brittle material with no clear yielding point, BFRP RC beams exhibited more deformation and curvature prior to failure during testing. The amount of deflection, curvature, stiffness and ductility that were exhibited by BFRP-reinforced PC beams were partially countered by reinforcing PC with basalt fibers and PVA fibers. However, due to the higher bond strength and better strain softening behaviour, PVA fibers improved flexural behaviour of BFRP RC beam better than the basalt fibers.

ABAQUS based non-linear finite element numerical modelling was conducted to validate the experimental results of BFRP-reinforced PC, BFRC, and PVAFRC beams. The investigation parameters considered in experimental evaluation were the same as those considered in numerical modelling. All the numerically modelled beams were evaluated for load-deflection behaviour, moment-curvature response, ductility and damage pattern. The results showed that the numerical modelled beams behaved similar to the experimentally tested beams. The percentage of error between experimental and numerical results was found within 10%. This shows good agreement between them. The numerically modelled beams accurately illustrated concrete damage in compression and tension, as well as a cracking pattern in tension, in a manner similar to that of the experimental cracking and the damage patterns of concrete in compression and tension.

CONTENTS

LIST OF TABLES

LIST OF FIGURES

ABBREVIATIONS

PC	Plain Concrete
RC	Reinforced Concrete
FRP	Fiber Reinforced Polymer
BFRP	Basalt Fiber Reinforced Polymer
BF	Basalt fiber
PVA	Polyvinyl Alcohol
FRC	Fiber Reinforced Concrete
BFRC	Basalt Fiber Reinforced Concrete
PVAFRC	PVA Fiber Reinforced Concrete
NSC	Normal Strength Concrete
HSC	High Strength Concrete
SCMs	Supplementary Cementitious Materials
EAC	Energy Absorption Capacity
FEM	Finite Element Method
OPC	Ordinary Portland Cement
SEM	Scanning Electron Microscopy
EDS	Energy Dispersive Spectroscopy
DAC	Data Acquisition System
LVDTs	Linearly Varying Displacement Transducers
IST	Initial Setting Time
FST	Final Setting Time
C-S-H	Calcium-Silicates-Hydrated
MRI	Modified Reinforcing Index
RI	Reinforcing Index
RMSE	Root Mean Square Error
AFV	Absolute Fraction of Variance
UR	Under-reinforced
OR	Over-reinforced
CDP	Concrete Damaged Plasticity

NOTATIONS

ρ	Reinforcement ratio
$E_f A_f$	Axial stiffness
ρ_f	BFRP reinforcement ratio
ρ_{fb}	Balanced BFRP reinforcement ratio
A_f	Area of BFRP rebars
A_s	Area of steel reinforcing bars
β_n	Material parameter
f_c	Stresses on stress-strain curve
ε_c	Strains on stress-strain curve
f'_{cf}	Cylindrical compressive strength of FRC
ε_{of}	Strain at cylindrical compressive strength of FRC
f_{cp}	Cylindrical compressive strength of PC
ε_{cp}	Strain at cylindrical compressive strength of PC
l_f	Length of the fiber
d_f	Diameter of the fiber
v_f	Volume fraction of fibers
w_f	Weight fraction of fibers
k_i	Anchoring factor of PVA fiber
k_a	Adhesion coefficient of PVA fiber
σ_p	Tensile strength of PVA fiber
b_i	Anchoring factor of basalt fiber
b_j	Adhesion coefficient of basalt fiber
σ_b	Tensile strength of basalt fiber
α	Tension stiffening parameter of fiber
P_{FCL}	First cracking load of RC beam
δ_{FCL}	Deflection at first cracking load of RC beams
P_{UL}	Ultimate load of RC beams
δ_{UL}	Deflection at ultimate load of RC beams

M	Moment of beams
φ	Curvature of beam
M_{FCL}	Cracking moment of RC beam
φ_{FCL}	Curvature at cracking of RC Beams
M_{UL}	Ultimate moment of RC beams
φ_{UL}	Curvature at ultimate of RC beam
ε	Flow potential eccentricity
ψ	Dilation angle
μ	Viscosity parameter
σ_{b0}	Biaxial compressive yield stress
σ_{c0}	Uniaxial compressive yield stress
P'_{FCL}	Percentage of error experimental and numerical curvature first crack load of RC beams
δ'_{FCL}	Percentage of error experimental and numerical curvature deflection at first crack load of RC beams
P'_{UL}	Percentage of error experimental and numerical curvature ultimate load of RC beams
δ'_{UL}	Percentage of error experimental and numerical curvature deflection at ultimate load of RC beams
M'_{FC}	Percentage of error experimental and numerical curvature first crack moment of RC beams
φ'_{FCM}	Percentage of error experimental and numerical curvature at first crack moment of RC beams
M'_{UM}	Percentage of error between experimental and numerical ultimate moment of RC beams
φ'_{UM}	Percentage of error between experimental and numerical curvature at ultimate moment of RC beams
μ_E	Ductility indices of RC beams
μ'_E	Percentage of error between experimental and numerical ductility indices of RC beams

Chapter 1
Introduction

1.1 General

The corrosion of embedded steel reinforcement in reinforced concrete (RC) structures, due to various harsh environmental conditions, deteriorates the strength and service life of the structures. The use of fiber-reinforced polymer (FRP) rebars as an alternative to steel reinforcing bars to reinforce concrete structural members can eliminate corrosion problems, resulting in structures with higher strength and longer service life. The FRP RC beams are less ductile and produce more deflections compared to the steel RC beams due to the low modulus of elasticity of FRP rebars. Reinforcing plain concrete (PC) using small, discrete fibers can improve the ductility and flexural toughness characteristics of concrete. Therefore, reinforcing FRP rebars in fiber-reinforced concrete (FRC) can be an alternative way to improve the ductility and flexural behavior of FRP RC beams. The use of silica fume in the development of high-strength concrete (HSC) is expensive due to the high cost of silica fume. As an alternative to silica fume, alccofine-1203 can be used as a supplementary cementitious material (SCM) for partial replacement of cement in the development of HSC. The aim of this research is to study the flexural behavior of basalt fiber-reinforced polymer (BFRP) rebars reinforced normal strength and high-strength basalt fiber-reinforced concrete (BFRC) and polyvinyl alcohol fiber-reinforced concrete (PVAFRC) beams.

1.2 Corrosion of Steel Reinforcement in RC Structures

In the construction of RC structures, long-term durability is a major concern and is considered a superior priority in design [1-3]. Conventional steel reinforcement does not have corrosion resistance. Hence, steel reinforcement and steel RC members are highly prone to corrosion in aggressive, acidic, alkaline, and marine environmental conditions [4,5]. This corrosion problem not only leads to the deterioration of the physical strength of steel reinforcement but also lowers the bond strength between concrete and steel reinforcement in RC structural members [5,6]. The service life of steel RC structures decreases with durability-related issues of steel reinforcement [7-9]. The progression and detachment of concrete caused by the corrosion of embedded steel reinforcement in RC structural members are shown in Figure 1.1. The stages in the progression of the embedded steel reinforcement deterioration level over the service life of RC structural member are graphically represented in Figure 1.2. Some examples of strength degradation in RC structures because of the steel reinforcement corrosion other than buildings

are bridges, underwater structures, and water retaining structures [5], de-icing salts used to melt ice on concrete pavements and in parking garages in cold regions [10-12], concrete structure in marine settings, industrial and domestic wastewater treatment plants, chemical treatment plants and structures subjected to high temperatures [13,14]. The RC members damaged by corrosion of the embedded steel reinforcing bars are shown in Figure 1.3.

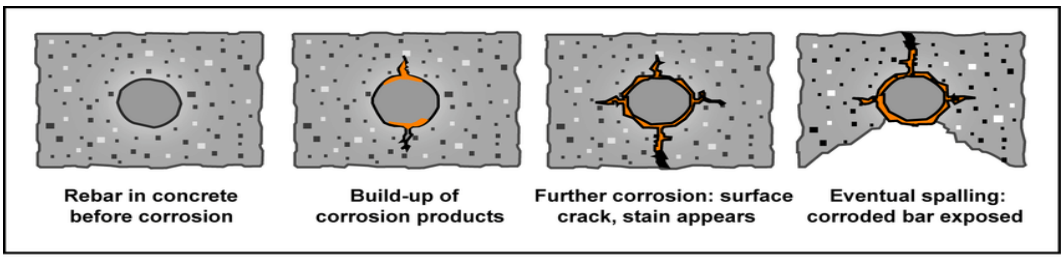

Figure 1.1 Concrete cracking and spalling due to progression of embedded steel reinforcement corrosion [15]

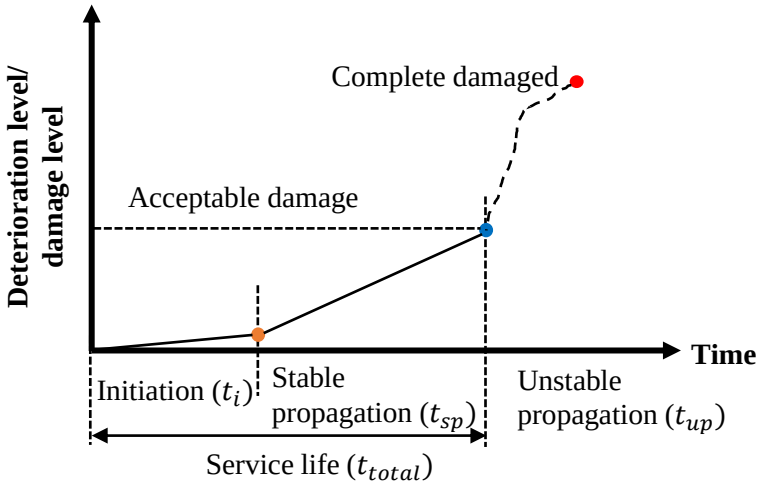

Figure 1.2 Stages of deterioration of steel reinforcement due to corrosion [16]

Figure 1.3 Damaged RC members due to corrosion of embedded steel reinforcement.

1.3 Alternate Methods Used to Control the Rate of Steel Reinforcement Corrosion

Under normal circumstances, corrosion in steel RC structures is controlled through periodic repairs involving retrofitting and rehabilitation, both of which are very expensive [17,18]. To mitigate the steel reinforcement corrosion in RC strcutures, several solutions have been suggested by various authors, such as the addition of SCMs to decrease the permeability of concrete, the use of stainless and epoxy-coated steel reinforcing bars, and galvanizing the steel reinforcing bars [19], etc. However, none of these have provided long-term, sustainable corrosion resistance solutions [20,21].

1.4 Basalt Fiber Reinforced Polymer Rebars

The deterioration of RC structures due to embedded steel reinforcement corrosion is evaded by replacing conventional steel reinforcing bars with sustainable, eco-friendly, non-metallic, and non-corrosive reinforcing bars such as fiber reinforced polymer (FRP) rebars [5]. Over the last thirty years, many studies have been carried out to see the feasibility of replacing the steel reinforcing bars with FRP rebars such as aramid, glass, and carbon as internal reinforcement for RC structures. The investigators emerged with good results and concluded that FRP rebars could be used as an ideal alternative to steel reinforcement in manufacturing of RC members, with certain limitations. The introduction of FRP reinforcement will ensure that RC structure remains corrosion-free, and this is an inexpensive way of combating corrosion [22,23]. FRP rebars have a lot of potential as longitudinal reinforcement such as in bridge deck slabs, floor slabs, stems, wing walls, abutments, and footings, where steel reinforcement is susceptible to corrosion [24]. All the FRP rebars are composite materials and their manufacturing follows the principles of sustainable development [14]. The use of FRP reinforcing bars in the construction of RC structures significantly increases the economic viability as well as durability of the construction [5,22,23]. The service life of FRP RC members is more than the service life of steel RC members [23,25]. Aramid-, carbon-, and glass-FRP rebars have been extensively investigated as reinforcing members in RC structures. The use of AFRP, CFRP, and GFRP as the main reinforcement in RC structures is permitted by contemporary design codes and guidelines including ACI 440.1R, CSA S806, and CSA S6. These standards also include design recommendations for using these rebars [22]. As FRP rebars are already recognized worldwide as being effective in strengthening RC structures both externally and internally [24,26], continuous and extensive effort has been made in the technology of FRP manufacturing to develop a new FRP reinforcing bar called basalt fiber reinforced polymer (BFRP) rebar [9]. The desirable mechanical properties of basalt fibers, combined with cost-effective

manufacturing, have led to the development of BFRP rebars for use as internal and external reinforcing members in concrete structures.

1.5 Manufacturing of BFRP Rebars

BFRP rebars are manufactured with high tensile strength basalt fibers embedded in polymer resins such as vinyl ester or epoxy. Basalt fibers are made from a single-origin material called basalt rock. Hence, they are referred to as inorganic, eco-friendly, non-toxic, with high stability, and insulating property materials [25,27,28]. Basalt rocks are available all over the world and are formed on the earth's surface by solidified lava sent by volcanic eruption. The crushed basalt rocks melt between 1400° and 1700°C and extrude through a small nozzle to obtain basalt fiber filaments ranging in diameter from 10 to 20 micrometers [9,14].

1.6 Properties of BFRP Rebars Over Steel Reinforcing Bars

BFRP's outstanding properties have attracted the attention of the construction industry, making it a replacement for other conventional FRP as well as steel reinforcing bars. The density of BFRP rebars is nearly three times lower than that of steel reinforcing bars. Therefore, the weight of structural members made of concrete and reinforced with BFRP rebars is lower than that of the same members made of concrete and reinforced with steel reinforcing bars. BFRP rebars have superior properties and are like lightweight, have high tensile strength, are ease to manufacture, show high and low temperature resistance, have good freeze-thaw performance, show resistance to corrosion in aggressive environments like marine, acid, alkaline, and chemical, show resistance to thermal and UV light, non-magnetic, are non-metallic, have low water absorption, are environmental-friendly, and coefficient of thermal expansion is the same as that of the concrete thermal coefficient of expansion [14,29-31].

1.7 Advantage of BFRP Rebar Over Other FRP Rebars

The development of BFRP rebars has become one of the best alternatives to existing FRP rebars [32]. According to Zhishen et al. 2012 [25], BFRP rebars were developed to improve the reliability and safety of the structural system over aramid-, carbon-, and glass-FRP rebars. The durability investigations on conventional FRP RC members revealed that the alkaline environment within concrete affects the performance of aramid-, carbon-, and glass-FRP rebars, causing them to break down, whereas BFRP rebars do not deteriorate in alkaline environment [33].

1.8 Drawbacks and limitations of FRP rebars

Along with excellent advantageous properties, FRP rebars also have a few drawbacks that limit their use as reinforcing material in concrete structural members, they are [34]

- Low modulus of elasticity
- Construction limitation

1.9 Behaviour of BFRP-reinforced concrete beams

The biggest advantage of BFRP rebars is their tensile strength carrying capacity which is higher than steel reinforcing bars. Concrete beam reinforced with BFRP rebars have higher flexural strength than steel RC beam. On the other hand, BFRP rebars also have some disadvantages over steel reinforcing bars. Young's modulus of BFRP rebars is nearly three times lower than that of steel reinforcing bars. Due to this, BFRP RC beams exhibit low ductility and high deformation with long and wider cracks in bending and shear regions compared to steel RC beams. The stress-strain behavior of BFRP rebar is liner. As a result, BFRP RC beams experience sudden brittle failure at the ultimate stage.

1.10 Fiber reinforced concrete

The reinforcing of PC with discrete fibers has long been known to decrease its brittleness and increase its mechanical properties. Concrete incorporated with discrete fibers is called fiber reinforced concrete (FRC) [35]. Compared with PC of the same mix, FRC may have an increase or decrease in compressive strength (CS) depending on the type and quantity of fibers used. When an appropriate quantity of fibers is used in concrete, it controls the opening of cracks and their subsequent development and extension, and improves tensile strength, deformation capability, load-bearing capacity after cracking, toughness, ductile behavior, and other engineering properties of concrete [36-38]. FRC is considered a structural material due to its residual tensile strength during the post-cracking stage and improved strain energy absorption capacity (EAC) due to the fiber bridging action over the crack surface [39]. So far, researchers have developed FRC using a wide variety of fibers such as steel, cellulose, asbestos, aramid, polypropylene, glass, PVA, carbon, wood, and basalt. In this study, based on the research gap as well as due to their excellent mechanical properties, basalt fibers and PVA fibers are selected to investigate the flexural behaviour BFRP-reinforced BFRC and PVAFRC beams.

1.11 Basalt Fiber

Basalt fibers have gained significant popularity as a potential material for reinforcing concrete in a variety of applications in the field of civil engineering construction due to their exceptional mechanical properties and eco-friendly manufacturing process. Basalt fiber is an inorganic material, and it has excellent mechanical properties such as non-conductivity, a good modulus of elasticity, heat resistance, good interfacial shear strength, higher tensile strength, and an eco-friendly manufacturing process. Basalt fiber exhibits excellent chemical stability in harsh environmental conditions and strong corrosion resistance [40,41]. The basalt fibers in concrete have a good dispersion rate and develop high bonding strength with concrete. The use of basalt fiber in concrete exhibits an obvious crack resistance and increases the concrete energy absorption by its toughening effect. All these properties contribute to basalt fibers being a very popular and suitable alternative to steel, glass, aramid, and carbon fibers in the manufacturing of FRC.

1.12 Polyvinyl Alcohol Fibers

PVA fibers are high-performance fibers used to reinforce concrete as well as mortar. Their incorporation into the concrete or mortar develops several advantages for them [42]. PVA fibers have excellent properties like a high aspect ratio, superior crack-arresting properties, a high modulus of elasticity, higher tensile and molecular bond strength, high resistance to UV, chemicals, alkali, fatigue, and abrasion, and good affinity with water and good chemical compatibility with cement, and no health hazards. All these properties make PVA fibers well-suited for different applications. PVA fibers have an excellent post-crack hardening zone, resulting in a concrete ductile failure mode [43]. The incorporation of PVA fibers in concrete increases its mechanical properties and bending strength because they are usually stiffer than concrete and offer a strong interfacial bond with the cementitious matrix [44]. PVA fibers' high tensile strength assists in extending the initial crack load and resisting pull-out stresses by developing a strong interfacial bond with the cementitious matrix [45].

1.13 Alccofine-1203

The use of SCMs like fly ash, rice husk ash, silica fume, ground granulated blast furnace slag (GGBS), and metakaolin, etc., is indeed a revolutionary step in the field of civil engineering. Due to the pozzolanic properties of SCMs, the combination of SCMs with cement can produce different strengths and durable concrete. Thus, using SCMs as an alternative or partial replacement to cement can reduce the use of cement in concrete manufacturing. This reduction

not only lowers carbon dioxide emissions from cement production plants but also helps minimize the excavation of raw materials used in cement manufacture. This also provides a solution for safe disposal of industrial waste. Globally, the application of SCMs incorporated concretes is increasing widely due to its eco-friendly nature, good performance, and energy-conserving capacity [46]. So far, SCMs have been playing a major role in the development of sustainable concrete and will continue to do so in the future.

The increase in demand for SCMs has led to the development of a new micro-mineral SCM called alccofine-1203 by Ambuja Cements Pvt Ltd, one of India's major cement manufacturing plants. Alccofine-1203 is a low calcium silicate-based micro fine material which consist of high amount of glass content with high reactivity. It is a highly processed material obtained from GGBS. Alccofine-1203 particles are ultra-fine with fineness 12,000 cm^2/gm and unique chemistry obtained through controlled granulation process [47]. The exceptional chemical properties of alccofine-1203 allows to replace silica fume in the manufacturing of HSC and high-performance concrete (HPC). The presence of lime (CaO) and silica (SiO_2) content in alccofine-1203 makes its performance superior to all other admixtures [48]. In the development of HSC and HPC, alccofine-1203 can be used in two ways: as a replacement to binder material and as an additive material [49]. Particles of alccofine-1203 material are very finer than cement, GGBS, silica fume, rice husk ash, fly ash, etc. The excellent particle packing effect of alccofine-1203 results in improved rheology, resulting in good flowability [50] and the voids present between the cement particles can be minimized by particles of alccofine-1203. Due to unique chemistry and ultrafine particles, its incorporation in the development of concrete results in formation of dense cement matrix core structure of concrete. Because of all the advantageous properties, in recent years, the use of alccofine-1203 has been increasing in the development of various types of concrete. Therefore, in this study, alccofine-1203 was used to partially replace cement for the development of HSC for evaluating flexural behavior of BFRP-reinforced HSC beams.

1.14 Numerical Modelling

For evaluating flexural behaviour of BFRP rebars RC beams, conducting tests in laboratory requires various parameters to be considered viz: specimen geometry, shear span to depth ratio, percentage of reinforcement, type of RC section (under-reinforced or over-reinforced) and other material parameters. To reduce these many numbers of physical prototypes and experiments, numerical modelling comes in handy as it can optimize components in their design phase and develop better products at a faster rate. Numerical modelling further benefits by reducing issues

related to inadequacy of lab resources. Numerical simulation mathematically represents a physical or any other behavior based on compatible hypotheses and simplifying assumptions. One of the numerical simulation methods is finite element method (FEM), which estimates a certain behavior of the investigated component under a given load by computing relevant quantities of a structure (like stresses, strains, deflections, etc.,).

1.15 Thesis Organization

The complete thesis is organised as follows:

1. **Chapter I** of the thesis introduces the need for this study by discussing the following points: corrosion of steel reinforcement in RC structures, alternate reinforcing materials to steel reinforcement for reinforcing concrete members, FRP types and advantageous and disadvantageous of BFRP rebar, behaviour of FRC and advantages of basalt fibers and PVA fibers, use of alccofine-1203 in the development of HSC, and numerical modelling.
2. **Chapter II** reviews literature on flexural behavior of BFRP RC beams, mechanical properties of BFRC, PVAFRC, and alccofine-1203 based various concrete. A summary of the literature review is also presented at the end.
3. **Chapter III** describes the scope and objectives of the research.
4. **Chapter IV** describes the mechanical and microstructural studies and compressive stress-strain behaviour carried out on various mixes of HSC developed using alccofine-1203 and fly ash as partial replacements for cement. The optimal dosage of alccofine-1203 was identified based on mechanical properties and stress-strain behaviour for the development of HSC of M70 grade.
5. **Chapter V** describes the experimental, analytical, and micro-structural studies carried out on PVAFRC and BFRC of NSC of M30 grade and HSC of M70 grade. Based on mechanical properties and stress-strain behavior of PVAFRC mixes and BFRC mixes, the ideal percentage of PVA fibers and basalt fibers was determined.
6. **Chapter VI** describes the experimental flexural behavior of BFRP-reinforced PC, BFRC, and PVAFRC beams of M30 and M70 grades. The load-deflection behavior, moment-curvature relationships, ductility, crack pattern, and failure mode of beams were evaluated.
7. **Chapter VII** describes the ABAQUS based numerical simulation of experimentally tested BFRP-reinforced PC, BFRC, and PVAFRC beams of both M30 and M70 grades. The obtained numerical results were used to validate experimental results.

8. **Chapter VIII** presents the conclusions of the research, contribution from the research work and the scope of the research for further investigations and publications related to the research work.

1.16 Concluding Remarks

The present chapter dealt with five important points:

- The influence of embedded steel reinforcement corrosion on the strength and service life of RC structures.
- BFRP rebars as an alternate reinforcing material for combating corrosion of steel reinforcement in RC structures.
- Advantages of BFRP rebars over steel and other FRP rebars and its draw backs and limitation as reinforcing material.
- Advantages of addition of basalt fibers and PVA fibers in improving the mechanical and engineering properties of concrete, and
- Efficiency of alccofine-1203 as a SCM for the development of HSC.

In-detailed literature on flexural behaviour of BFRP RC beams, mechanical and engineering properties of BFRC and PVAFRC and alccofine-1203 incorporated various types of concrete were studied to identify research gaps and scope for the present study. Detailed literature review is presented in Chapter 2.

Chapter 2
Literature Review

2.1 General

Based on the topics of interest presented in Chapter 1, a detailed literature survey was conducted and is presented in this chapter.

2.2 Literature Review on BFRP-Reinforced Concrete Beams

2.2.1 Flexural behaviour of BFRP-Reinforced Concrete Beams

In early stages of research on flexural behaviour of BFRP RC beams, Huo et al. 2012 [51] reported that due to BFRP rebar's brittleness and lower Young's modulus, at the last stage of testing of beams, the development of longitudinal strains in rebars led to higher deformations of the beams before they collapse. From this observation, the author concluded that BFRP RC beams possessed enough ductility performance as a flexural member. As BFRP rebars have lower elastic modulus, the authors recommended using BFRP rebars as prestressing tendons to avoid excessive deflections of the flexural members. Similar to Huo et al. 2012 [51], Urbanski et al. 2013 [23] also determined that because BFRP rebar has a lower Young's modulus and ductility, BFRP RC beams have greater deformations, deflections, and larger cracks width at higher loads than steel RC beams. Urbanski et al. 2013 [23] reported that under the tensile test, BFRP rebar exhibited linear stress-strain behaviour in contrast to non-linear stress-strain behaviour of steel reinforcing bar. The authors mentioned that the linear stress-strain behaviour of BFRP rebars significantly influences the behaviour of BFRP RC beams.

Tomlinson and Fam 2014 [11] tested BFRP RC beams under four-point bending to evaluate the effect of flexural reinforcement ratio ranging from 0.28 to 1.60. The authors reported that, for a given reinforcement ratio (ρ), BFRP RC beams with either BFRP or steel shear reinforcement exhibited greater flexural strength than steel RC beams. The beams with BFRP stirrups and without stirrups failed in shear whereas, beams with steel stirrup beams failed in flexure.

Lapko and Urbański 2015 [5] and Inman et al. 2017 [52] reported that beams reinforced with smaller cross-section stiffness of BFRP rebars exhibited higher deflections and crack width compared to beams reinforced with the same cross-sectional stiffness of steel reinforcing bars.

Fan and Zhang 2016 [33] investigated the BFRP inorganic polymer concrete (IPC) beams in flexure and compared them with conventional steel RC beams. From the test results, the authors reported that BFRP-reinforced IPC beams did not show any yielding stage and exhibited higher

deflections compared to steel-reinforced IPC beams. The development of crack and crack patterns were similar in both BFRP-reinforced IPC beams and steel-reinforced IPC beams, but larger crack widths were revealed by BFRP-reinforced IPC beams.

Elgabbas, Vincent, et al. 2016 [9] evaluated the behaviour of helically wrapped sand-coated BFRP RC beams. The authors evaluated the effect of reinforcement ratio (ρ) on cracking, beam stiffness, and reinforcement strains. From the experimental test results, it was observed that BFRP RC beams exhibited bi-linear behaviour for deflection and strain until the beams collapsed. At the same load level, beams with a higher reinforcement ratio were stiffer and developed less strain than beams with a lower reinforcement ratio. The beams with a lower reinforcement ratio suffered bar rupture failure and exhibited higher deflections.

Elgabbas, Ahmed, et al. 2016 [53] studied the influence of flexural reinforcement axial stiffness $(E_f A_f)$ on the flexure and serviceability performance of ribbed BFRP RC beams. From the experimental test results, the authors reported that BFRP RC beams attained higher deflections before they failed due to concrete crushing. The authors concluded that BFRP RC beams achieve better-cracking behaviour by using smaller diameter BFRP rebars due to higher bond strength. The deflections of the beams decreased and increased the moment-carrying capacity and ultimate load-carrying capacity of the beams with increase of $E_f A_f$ ratio.

Ovitigala et al. 2016 [54] investigated the effect of BFRP reinforcement ratio to balanced BFRP reinforcement ratio (ρ_f/ρ_{fb}) on ultimate load carrying capacity and serviceability performance of BFRP RC beams. The authors reported that the ultimate flexural capacity of the beams directly related to ρ_f/ρ_{fb} ratio. The rate of change in deflection and moment capacity of the beam decreased with an increase in ρ_f/ρ_{fb}. The authors observed that when ρ_f/ρ_{fb} ratio was less than 7, there was a significant influence on reducing the deflections of the beam more than the increase in moment carrying capacity. In contrast, beams reinforced with ρ_f/ρ_{fb} ratio more than 7 exhibited a better increase in moment capacity than decrease in the ultimate deflections of beams.

Duic et al. 2018 [55] discussed the effectiveness of BFRP rebars in BFRP RC beams. The authors reported that BFRP RC beams with lower reinforcement ratio showed higher flexural and shear cracks than steel RC beams, while higher reinforcement ratio BFRP-reinforced beams exhibited fewer flexure and shear cracks with slightly steeper crack angles. According to CSA-S6-19 [56], BFRP RC beams had acceptable deformability. The cracking moments of BFRP

RC beams were less than that of steel RC beams. The authors suggested designing a BFRP RC beam to fail under flexural tension or compression until pre-manufactured BFRP stirrups were available to use as stirrup reinforcement.

Yuan et al. 2013 [13] used engineered cementitious composites (ECC) to overcome the disadvantages associated with BFRP RC beams. The authors tested a total of six beams to evaluate the flexural behaviour of BFRP rebars in ECC or ECC/concrete composite beams. The compressive strains of BFRP-reinforced ECC beams were higher than that of pure BFRP RC beams. The authors also highlighted that providing an ECC layer in the tension zone of FRP reinforced beams results in rupture failure of the rebar at the ultimate stage.

Younes et al. 2017 [57] tested pre-stressed BFRP rebar-reinforced RC beams to evaluate fatigue behaviour. From the test results, the authors concluded that beams reinforced with BFRP rebars pre-stressed to 40% of its ultimate strength had higher fatigue resistance strength than those of beams reinforced with 0% and 20% pre-stressed BFRP rebars. Younes et al. 2017 reported that there was a significant effect of pre-stressing on the initial cracking load and the deflection response of pre-stressed BFRP RC beams compared to non-pre-stressed BFRP RC beams. The authors noticed the effect of pre-stressing from the initial cracking load and the deflection response of pre-stressed BFRP RC beams compared to non-pre-stressed BFRP RC beams. The ultimate load-carrying capacity of pre-stressed and non pre-stressed beams appears to be the same. Under monotonic loading, pre-stressed BFRP RC beams failed in concrete crushing fallowed by BFRP rebar rupture, while non-pre-stressed BFRP RC beams failed by rebar rupture followed by concrete crushing in the compression zone. Under fatigue loading, pre-stressed BFRP RC beams failed by concrete crushing in the compression zone at higher load range and failed by rebar rupture at lower load range, while non-pre-stressed BFRP RC beams failed by rebar rupture.

Gopinath et al. 2016 [26] investigated the flexural performance of RC beams externally strengthened with BFRP rebars. The authors used near-surface mounted (NSM) technique for external strengthening of RC beams at the bottom of the tension zone. In the study, the parameters looked at were the size of the groove, the size of the BFRP rebar, and the number of BFRP rebars. The authors reported that flexural strength and effective pre-yield stiffness of the beams increased with an increase in NSM reinforcement percentage, but higher percentage of NSM reinforcement significantly reduces deflections of the strengthened beams. From this study, the author found that by using this technique, it is possible to double the load-carrying

capacity of RC beams without loss of beam ductility. Some of the strengthened beams failed in a combination of shear and flexural, and some of the strengthened beams failed in pure flexural. There was no bond failure observed between BFRP rebars and RC beams.

Abed and Rahman 2019 [58] reported that the incorporation of synthetic fibers and basalt fibers increased the ultimate moment carrying capacity and curvature ductility of BFRP RC beams. The flexural capacity of BFRP RC beams increased with an increase of BFRP reinforcement ratio, and this increment was supported by ACI 440.1R-15 [22]. According to the authors, the introduction of basalt fibers effectively restricted the crack openings and crack propagations due to bridging action, which kept the crack width below the allowable limit 0.7 at serviceability condition. From the test results, the authors perceived that basalt fibers controlled the cracking of concrete better than synthetic fiber.

In order to increase the flexural response of FRP RC beams, researchers investigated two different types of hybrid reinforcement systems. The first is the replacement of FRP rebars with hybrid FRP rebars, and the second is a hybrid reinforcement system developed by combination of FRP and steel reinforcement [6,30,59,60]. Hybrid FRP rebar is a composite rebar developed by warping steel reinforcement with a thick FRP composite sheet. Hybrid FRP rebars consist of steel as the inner core and FRP warped sheet as the outer core. Researchers, Harris and Somboonsong et al. 1998 [61], Saikia et al. 2005 [20], and Ju et al. 2017 [62] have reported the flexural response of hybrid FRP rebars RC beams, but literature for hybrid BFRP rebar RC beams is lacking. The investigations by Ge et al. 2015 [30], Gopinath et al. 2017 [63], and Akiel et al. 2018 [64] have reported the structural behaviour of RC beams with hybrid (BFRP and steel) reinforcement.

Ge et al. 2015 [30] studied the influence of the ratio of area of BFRP rebar to the area of steel rebar (A_f/A_s) on the flexure performance of RC beam with hybrid BFRP reinforcement. The resulst of the study showed that the increase in A_f/A_s ratio led to a reduction in the stiffness factor of hybrid BFRP RC beams. The deflections, crack width, and crack spacing of RC beams with hybrid (BFRP and steel) reinforcement was between that of steel RC beams and BFRP RC beams. The authors mentioned that the theory used to calculate the average crack spacing of steel RC beams was suitable to calculate the crack spacing of RC beams with hybrid reinforcement, and the theoretical calculations were in accordance with experimental values.

Gopinath et al. 2017 [63] concluded that the RC beam with hybrid reinforcement (BFRP and steel) was more flexible and had a lower ultimate moment resistance than pure BFRP RC

beams. On the other hand, the ultimate deflections of RC beams with hybrid reinforcement were higher than those of RC beams with steel reinforcement. The authors reported that RC beam with hybrid reinforcement could be designed using a serviceability limit rather than the ultimate limit to avoid sudden and brittle failure. The authors concluded that RC beam with hybrid reinforcement had shown fewer and wider cracks than beams reinforced with pure BFRP rebars.

Akiel et al. 2018 [64] found that two-span continuous RC beams with hybrid (BFRP and steel) reinforcement showed lower deflections, smaller crack widths, and significant deformation before failure compared to RC beams with pure BFRP rebars. The use of steel reinforcing bars along with BFRP rebars limited crack growth before yielding of the steel bars and decreased the difference in flexural rigidity between sagging and hogging regions. The moment redistribution ratios were lower in continuous RC beams with hybrid reinforcement than in pure BFRP RC continuous beams. From the test results, the authors reported that under-reinforced concrete beams with hybrid reinforcement exhibited post-peak stage until steel reinforcing bar rupture took place after the rupturing of BFRP rebars. In contrast, at ultimate load, RC beams with pure BFRP rebars failed suddenly by BFRP rebar rupture.

As reviewed above, the hybrid reinforcement (FRP and steel) approach has proven effective to improve the structural performance of RC beams. However, the steel reinforcement's tendency to corrosion is a major problem in the proposed hybrid reinforcement system [6,60]. In this regard, to improve the structural and serviceability performance of pure BFRP RC beams, H. Zhu et al. 2018 [6] experimentally investigated the effect of steel fiber reinforced HSC layer thickness and BFRP reinforcement ratio on the flexural performance of BFRP RC beams. The authors reported that at a higher BFRP reinforcement ratio, BFRP RC beams showed improved flexural capacity with post-cracking stiffness and ductility and minimal crack widths. According to authors, the addition of steel fiber in the tension zone of BFRP RC beams led to the reduction of large deflections, crack widths, and improved the ductility of pure BFRP RC beams. The authors observed that the flexural capacity of fiber reinforced high strength concrete (FRHSC) beams partially reinforced with BFRP rebars was not highly significant by the thickness of FRHSC layer and steel volume fraction. The authors concluded that 0.57 times the total depth of beam was the optimum thickness to provide FRHSC layer in BFRP RC beams.

2.2.2 Shear behaviour of BFRP-Reinforced Concrete Beams

The ultimate shear strength (V_{ult}) of RC is measured by the sum of the shear strength contribution from concrete (V_c) and the transverse reinforcement (V_s). The assessment of the

shear strength of BFRP rebars is essential for their safe and reliable applications in structures as a shear resistant member. Therefore, a brief review of the shear strength of BFRP rebars and the shear performance of BFRP RC beams are presented.

To assess the direct shear strength of BFRP rebars, Wang et al. 2014 [27] conducted a double shear test and reported on the parameters influencing the shear strength of BFRP rebars. Based on the test results, the authors concluded that BFRP rebars exhibited shear strength comparable to that of steel reinforcing bars. They observed that the shear strength of BFRP rebars is primarily contributed by their internal fibers, with the contribution from resin type being negligible. The authors achieved highly accurate predictions of the shear strength of BFRP rebars by considering shear contribution separately for fiber type and resin type. In order to comprehend the development of shear strength from the overall contributions of resin and fibers, Wang et al. presented a graphical representation model depicting the shear stress-to-shear deformation ratio. Additionally, an equation was proposed to calculate the shear strength contribution of fibers in FRP rebar, as well as the overall shear strength of FRP rebar.

Tomlinson and Fam 2015 [11] experimentally assessed the shear capacity of BFRP RC beams with and without BFRP transverse reinforcement. The research parameters of the study included various flexural reinforcement ratios to balanced reinforcement ratios (ρ_f/ρ_{fb}) and several shear spans to depth ratios (a/d). The authors reported that the ultimate flexural capacity and the load at which a major diagonal crack occurred increased as the BFRP flexural reinforcement ratio increased. The failure of all BFRP-reinforced beams, with and without BFRP stirrups, occurred in shear due to the rupture of stirrups. According to the test results, the authors reported that shear reinforcement did not exhibit any influence on the load–deflection response within service loads.

In another study, Issa et al. 2016 [24] assessed the shear strength of BFRP rebars in flexural BFRP RC beams and reported that beams without stirrups failed in shear tension mode, becoming increasingly brittle as the ρ_f/ρ_{fb} ratio increased. For BFRP RC beams with BFRP stirrups, the failure mode shifted from shear tension to shear compression due to the presence of BFRP stirrups. Additionally, some beams with stirrups failed in diagonal tension failure mode. From the test results, the authors noted a marginal influence of BFRP stirrups on the shear capacity of the beam. The shear capacity of beams, both with and without BFRP stirrups, increased as the ρ_f/ρ_{fb} ratio increased under the same a/d ratio, while shear strength decreased with an increase in the a/d ratio. The predicted shear strength of beams with BFRP

stirrups, based on available design guidelines, exhibited good comparative results with the shear characteristics of beams reinforced with FRP stirrups.

The size effect on the nominal shear strength capacity of BFRP RC slender beams without shear reinforcement was investigated experimentally and numerically by Korol et al. 2017 [14]. The authors examined four identical beams in two directions. To reproduce the experimental results, a 2-D finite element method based on a coupled elastic–plastic-damage formulation was employed, and the authors reported a satisfactory agreement between numerical and experimental results. Korol et al. also observed a considerable reduction in the nominal shear strength of BFRP RC beams with an increased beam size. Shear tension failure was observed due to the development of a critical diagonal crack between the middle point of the shear span and the loading point, demonstrating a fragile failure in BFRP RC beams as the size of the beams increased.

Farid Abed et al. 2019 [65] conducted experimental and finite element investigations on the shear performance of BFRP-RC short beams, comparing the test results with steel-RC short beams. The authors concluded that the parameters influencing the shear behavior of the steel-RC beams are the same factors governing the performance of the BFRP-RC beams. Despite BFRP-RC beams having lower stiffness than steel-RC beams due to the lower Young's modulus of BFRP rebars, the study suggests that BFRP rebars can be used as full-scale reinforcement for short deep concrete beams. Short deep beams were found to exhibit less significant deformation compared to the slender and long BFRP-RC beams.

The shear response of hybrid fiber-reinforced geopolymer concrete (GPC) beams, longitudinally reinforced with BFRP rebars and without transverse reinforcement, was investigated by Tran et al. 2020 [66]. The authors employed macro-steel fibers, macro-synthetic polypropylene fibers, micro-polyvinyl alcohol fibers, micro-carbon fibers, and a hybridization of these fibers. From the test results, the authors reported that the addition of 0.5% steel fibers demonstrated the highest improvement in post-cracking stiffness, cracking behavior, and shear capacity (increasing by 56%). Subsequently, the addition of 0.5% polypropylene fibers enhanced the shear strength of GPC beams by 33%. The hybridization of polyvinyl alcohol fibers and steel fibers exhibited great synergy, improving the shear and cracking behavior of GPC more effectively than the hybridization of polypropylene fibers and carbon fibers. Based on the findings, the authors stated that the combination of polypropylene fiber, BFRP rebars, and GPC can be a feasible solution for the development of sustainable and durable structures.

Abed et al. 2021 [67] conducted an experimental investigation to examine the enhancement in shear capacity and cracking response of short concrete beams reinforced with BFRP rebars and incorporating basalt microfibers. The study explored different a/d ratios, concrete compressive strengths, longitudinal reinforcement ratios (ρ), basalt fibers, and synthetic fibers. The authors concluded that the presence of basalt microfibers and synthetic fibers significantly enhances the stiffness, toughness, and ultimate shear strength of the tested beams. The load-carrying capacity of the short beams increased more with basalt microfibers than synthetic fibers compared to the PC beams. The addition of basalt microfibers increased shear strength by 42.1%, attributed to their effective bridging of microcracks and stress transfer, delaying overall failure. BFRP rebars reinforced in basalt microfibers RC experienced 16.8% and 27.9% higher strain values compared to BFRP rebars reinforced in synthetic FRC beams and PC beams due to the greater tensile strength and modulus of elasticity of basalt microfibers. The development of strain in BFRP rebars decreased with a decrease in the a/d ratio and an increase in ρ. The shear strength of beams increased up to certain increment levels of ρ; beyond that, there is no contribution from ρ for additional improvement in shear strength.

Ahmed El Refai et al. 2022 [68] conducted a comprehensive study on the shear performance of basalt fiber-reinforced concrete (BFRC) beams reinforced with BFRP rebars. Fourteen BFRP-reinforced BFRC beams, tested without stirrups under four-point loading, explored various parameters, including fiber volume fraction (0.75% and 1.5%), BFRP rebar longitudinal reinforcement ratios (0.31, 0.48, 0.69, 1.05, and 1.52%), and a/d ratios of 3.3 and 2.5 for slender and short beams. Authors reported that adding 0.75% basalt macrofibers (BMF) improved shear capacity by 46% for slender beams and 43% for short beams, compared to 81% and 82% with 1.5% of BMF. The impact of BMF on shear strength decreased with higher reinforcement ratios. All beams failed in shear, showing a primary diagonal crack. BFRC beams exhibited more flexural cracks at failure than those cast with PC, and BMF delayed shear crack formation, limiting widening due to fiber bridging. Beams with BFRC mixes showed flatter diagonal cracks at failure, highlighting improved shear resistance through the addition of BMF to the concrete mixes.

2.3 Literature Review on Polyvinyl Alcohol Fiber Reinforced Concrete

Hamoush et al. 2010 [69] conducted experimental and theoretical investigations to evaluate the stress-strain and load-deflection behaviour of PVA micro-fiber reinforced concrete. Based on test results, the authors concluded that the addition of PVA fibers does not have any influence on the compressive strength of concrete. Instead, it enhances the ductile property of the

concrete, increases toughness, and prevents the sudden brittle failure of the concrete. It was also concluded that the deflection of PVA micro-FRC beams has ductile behaviour and has a post-peak failure point. PVA fiber is a very suitable fiber to be used as reinforcement in concrete materials, though the very strong fiber–matrix bond resulting from high chemical bonding causes the micro-fibers to rupture instead of being pulled out. Larger ductility may be achieved by fiber pull-out rather than rupture.

Bangi and Horiguchi 2012 [70] found that the inclusion of PVA fibers in concrete reduces the fresh properties of concrete by reducing the workability of mix. In this study authors used 16 and 40 micrometre diameters of PVA fibers of same length, 6 mm. The authors noticed that as the diameter of the fibers increased, the slump decreased from 209 mm to 49 mm.

Hu et al. 2013 [71] examined the fresh and hardened properties of concrete prepared with PVA fibers. From fresh concrete results, the addition of PVA fibers reduced the slump of the concrete mixture; and from experimental results on hardened concrete, split tensile strength improved with increasing fiber content while compressive strength decreased with an increasing percentage of PVA fiber content. Beyond the addition of an optimal percentage of fiber content, the Young's modulus of concrete was reduced, but the dose of PVA fiber enhanced the tensile strain.

The effect of PVA fibers on the dynamic and material properties of FRC was investigated by Noushini, Samali, et al. 2013 [43]. The author reported that the addition of PVA fibers in a low volume fraction of less than 0.5% significantly improved the static mechanical properties of the FRC, whereas no such improvement was noticed in the case of dynamic characteristics.

Noushini, Samali, et al. 2013 [72] evaluated the effect of addition of 6 mm and 12 mm length of PVA fibbers of three volume fractions (0.25%, 0.5% and 1%) on workability and compressive strength of concrete. The authors concluded that workability of concrete decreased with increasing volume fraction of fibers, where longer length fibers exhibited lower workability compared to short length fibers and higher compressive strength was observed at 0.25% fiber addition compared to other volume fractions of fibers.

Nuruddin et al. 2014 [73] reported that adding PVA fibers led to higher stiffness in concrete and also increased the flexural toughness of concrete by improving the deflection hardening behaviour.

Yew et al. 2014 [74] studied the effect of addition of 0%, 0.125%, 0.25%, 0.375%, and 0.5% PVA fibers on mechanical properties of light weight concrete prepared using oil palm shell.

The authors reported the decrease in workability of concrete mixes with an increase in the percentage of PVA fibers additions. Due to improved fiber matrix interfacial bond strength, the increase in addition of PVA fiber content improved ductility by increasing strain at peak-stress of the PVA fiber reinforced light weight oil palm shell concrete while also improving its compressive strength. Furthermore, the flexural strength and split tensile strength of the concrete increased by 30% and 32%, respectively, and the highest improvement in modulus of elasticity of PVA fiber reinforced light weight oil palm shell concrete was noted.

Noushini et al. 2015 [75] studied the fresh and compressive strength properties of PVAFRC. The authors considered four different proportions of PVA fiber content based on volume of concrete, i.e., 0.125%, 0.25%, 0.375%, and 0.5% and carried out the investigation. The slump values of fresh concrete decreased with PVA fiber additions, while the compressive strength of concrete increased. The optimum fiber volume fraction was found to be 0.25% with 12% improvement noted in compressive strength of concrete at 28-days ageing compared to control mix. The authors also concluded that improvement in the compressive strength of concrete was better with the addition of shorter fibers compared to the improvement achieved by the addition of longer-length fibers.

Nuruddin et al. 2015 [76] reported that the addition of PVA fibers did not show a significant influence on compressive strength but enhanced the ductility and toughness properties of concrete and also reported improvement in post-peak behaviour of PVAFRC.

Devi et al. 2017 [77] found that the addition of PVA fibers of 0.3% by volume of concrete showed the highest improvement in flexural, split tensile and compressive strength and load-deflection behaviour of PVAFRC. Compared to the control mix, compressive strength of PVA fibers mixed concrete increased by 48.5%, flexural strength increased by 21.4%, split tensile strength increased by 50.4%, and ultimate load in the load-deflection behaviour increased by 68%. The ductility index of the PVAFRC with 0.3% fiber content was improved by 25% compared to the control mix and addition of other fiber percentages.

Xu et al. 2017 [78] investigated the mechanical properties and flexural toughness of PVAFRC. From the results of the investigation, the authors reported that the compressive strength, flexural strength, and split tensile strength of PVAFRC with 2% fiber content increased by 70%, 270%, and 220%, respectively, compared to PC mix. The authors observed a significant improvement in the toughening effect of PVAFRC with the addition of 12 mm PVA fibers compared to 8 mm PVA fibers. From the scanning electron microscopy (SEM) analysis, the authors observed

the continuous geopolymer gel network structure formation in the matrix that results in an improvement of the strong interfacial transition zone between PVA fiber and the matrix.

Pakravan et al. 2018 [79] evaluated the flexural behaviour of ECC prepared using PVA fiber at 1.2%, 1.5%, 1.6% and 2% volume of composite. The authors found from the test results that the increase in fiber content increased flexural strength, toughness, and flexural modulus. The authors also reported a linear increment in the ratio of the load at the post-cracking stage to first-cracking stage. The flexural ductility, better deflection hardening behaviour, EAC, and flexural toughness significantly improved with the addition of PVA fiber content of 1.2% to 1.6%, whereas the addition of 2% fiber content decreased due to the low workability of the mix. From SEM observations, the authors noticed good bond affinity between the matrix and PVA fiber, and the formation of a strong bond was evident from the results of the pull-out test.

C. Zhu et al. 2018 [80] compared the microstructural and mechanical properties of gypsum-based composites reinforced with PVA fibers to those of gypsum-based composites reinforced with polypropylene fibers. In this investigation, the authors considered fibers of length 6 mm and 12 mm with volume fractions of 0, 0.3%, 0.6%, 0.9%, and 1.2%. The authors reported that the workability of concrete remarkably decreased with increasing length and volume percentage of fibers of both types. The authors also noted that compared to polypropylene fibers, PVA fibers significantly increased the flexural strength and flexural toughness, and the negative effect on the compressive strength of gypsum-based composites was low. From the SEM images, it was observed that the interfacial transition zone between PVA fiber and dihydrate crystals was extremely compact and had a negligible gap compared to polypropylene fibers.

Loh et al. 2019 [81] carried out an investigation on the fiber reinforced cementitious composite (FRCC) developed using 1.0%, 1.5%, and 2.0% of PVA fibers and basalt fibers contents. Based on the test results, the authors reported that the inclusion of PVA fibers and basalt fibers reduced the workability of composites with an increasing percentage of both types of fiber. Particularly when compared to PVA fibers, the reduction in workability of BFRC was severe with basalt fibers. The PVA and basalt fibers had little effect on the compressive strength of the composite, but both types of fiber significantly improved the flexural and split tensile strengths when compared to control mix. PVA fiber improved FRCC's flexural performance more than basalt fiber, and 1.5% was found to be the optimal amount to add. PVAFRCC specimens showed a more ductile failure mode compared to BFRCC specimens.

R. Zhang et al. 2019 [82] reported that the incorporation of PVA fibers significantly improved flexural toughness, flexural strength, and split tensile strength and slightly decreased the compressive strength of PVA fiber-reinforced ultra-high strength concrete (UHSC).

Hong et al. 2020 [83] examined the bonding and microstructural behaviour of FRC. The authors carried out the investigation using three types of fibers, such as PVA fiber, glass fiber, and basalt fibers. From the interfacial tensile bond tests, the author found that PVA fiber had developed greater bond strength with the concrete, followed by basalt fiber, and then glass fiber. Furthermore, the authors also studied the splitting tensile strength of three types of FRCs. From these results, the authors noticed that PVAFRC has the highest splitting tensile strength, followed by BFRC, and then glass-FRC.

Mosavinejad et al. 2020 [84] investigated the electrical and microstructural analysis of Ultra-High Performance Concrete (UHPC) containing PVA fibers. For the development of UHPC, the authors used 0%, 0.3%, 0.6%, 0.9%, and 1.2% PVA fiber content as well as 15 to 40% silica fume as a partial replacement for cement. The authors observed from the test results that with the addition of PVA fibers of all different percentages, the flexural strength of concrete increased linearly. A maximum of 30% increment was led to the UHPC up on addition of 1.2% of PVA fibers compared to control mix. All PVAFRC mixes show higher electrical resistivity and a decrease in chloride diffusion and penetration than that of steel-FRC. SEM and energy dispersive spectroscopy (EDS) examinations revealed that increasing the silica fume replacement ratio results in a homogeneous cement paste with a Ca/Si ratio close to one, implying a stronger matrix.

Souza et al. 2021 [85] studied the behaviour of PVAFRC under cyclic loading. From quasi-static test results, the authors concluded that the ductility and toughness characteristics of PVAFRC improved greatly compared to PC. The cycling results showed that PVA fibers contributed to maintaining stiffness by lowering material damage, which in turn reduced crack width and propagation. The PVA specimen had lower damage during the cycles, which translated into a smaller crack mouth opening displacement (CMOD) variation when compared to polypropylene FRC.

P. Zhang et al. 2021 [86] reported the effects of PVAFRC fiber content on the mechanical and fracture properties of geopolymer concrete (GPC). For this investigation, the authors considered 0%, 0.2%, 0.4%, 0.6%, 0.8%, and 1.0% of PVA fiber of 12 mm in length and 40 μm in diameter. Among all the additions, the highest compressive strength and modulus of elasticity were

obtained at an addition of 0.2% of fiber content. From the load-deflection behaviour, it was reported that on adding 0.8% of fiber content, the PVAFRC mix had the highest flexural strength, initial crack load, initial fracture toughness, and fracture energy compared to other percentages of PVA fiber additions as well as the control mix.

Prashanth Naik et al. 2021 [87] carried out an investigation to improve the flexural performance of Hybrid (GFRP rebars and steel rebars) fiber-reinforced polymer (HFRP) concrete beams using the addition of 0.25% and 0.5% of PVA fiber content. For this investigation, the authors considered one pure FRP reinforced beam, one HFRP concrete beam, and one HFRP concrete beam with PVA fibers. From the test results, the authors concluded that the addition of PVA fibers to the HFRP concrete beams significantly improved their load carrying capacity, deflection behaviour, flexural strength, and ductility behaviour. The addition of 0.25% of PVA fibers showed the highest improvement in flexural strength by 200% and 31.1% and ductility by 112.2% and 55.12% as compared to pure FRP beam and HFRP concrete beam without PVA fibers.

Xiao et al. 2022 [88] improved the mechanical properties of recycled ceramic coarse aggregate pervious concrete (RCCAPC) with the inclusion of PVA fibers. In this investigation, the authors used different volume percentages of PVA fibers (0%, 0.1%, 0.15%, 0.2%, 0.25%, 0.3%, and 0.35%). Based on the results, it was reported that the RCCAPC reinforced with PVA fibers showed plastic deformation in the bending test and cube compressive strength test. At 0.25% and 0.3%, the highest compressive and bending strengths were reported. The increase in flexural strength of PVA fiber reinforced RCCAPC was more significant than compressive strength. The toughening effect of PVA fibers is clearly evident from the stress-strain and stress deflection curves. From the test results, the optimum volume percentage of PVA fibers was obtained as 0.3%.

2.4 Literature Review on Basalt Fiber Reinforced Concrete

Zych and Krasodomski 2012 [89] investigated the mechanical properties of cement mortar using basalt fibers of 5 mm and 12 mm in length and densities of 0.4 kg/m^3, 1 kg/m^3, and 2 kg/m^3. From the test results, the authors reported that the compressive strength of the cement mortar decreased with the addition of basalt fibers compared to cement mortar without fibers. Basalt fibers of 12 mm in length improved the flexural strength of cement mortar better than 5 mm in length basalt fibers. The reduction in compressive strength of cement mortar was greater with the addition of 12 mm in length of basalt fibers compared to the addition of 5 mm in length of basalt fibers. In addition, the authors reported that, due to low adhesion between basalt fibers

and mortar, cement mortars with basalt fibers show no discernible improvement in post-peak behaviour after peak load.

F. Chen 2013 [90] evaluated the mechanical properties of BFRC manufactured with 1.2 kg/m^3 of basalt fibers with a length of 24 mm and diameter of 17 μm. According to the authors, compared to PC, BFRC showed a 4.29% improvement in compressive strength and a 19.27% improvement in flexural strength. This proves that basalt fibers are more advantageous for improving the tensile strength of concrete than compressive strength. It was also concluded that as BFRC ages, the load transfer mechanism and bridging action of basalt fibers become more significant, improving the ductility of concrete before it totally fractures.

Borhan 2013 [91] determined the thermal and mechanical properties of BFRC. In this investigation, the authors used 0%, 0.1%, 0.2%, 0.3%, 0.4%, and 0.5% volume fraction of basalt fibers with a length of 25.4 mm and a diameter of 13 μm. From the test results, it was reported that the workability of concrete decreased with an increase in fiber content. The compressive strength, modulus of elasticity, and splitting tensile strength increased on adding 0.3% of basalt fibers and decreased with the addition of 0.5%. It was also observed that the thermal conductivity of BFRC specimen decreased with an increase in the addition of basalt fibers.

Shafiq et al. 2014 [92] evaluated the effect of the addition of 0.25%, 0.5%, 0.75%, 1%, 2%, and 3% basalt fibers on the workability, and compressive and tensile strengths and compressive stress-strain behaviour of basalt fiber reinforced fly ash HSC. The authors reported from the results of the study that fresh properties of concrete decreased linearly with an increase in fiber content. The compressive strength of the concrete decreased with the addition of all percentages of basalt fibers, and this decrement was more severe with the addition of higher fiber content (1%, 2%, and 3%). The split and flexural tensile strength of BFRC increased linearly and the area under compressive stress-strain curve improved with the addition of all percentage of basalt fibers, which showed clear improvement in toughness and ductility characteristics of concrete.

Ayub et al. 2014 [93] studied compressive and split tensile strengths of BFRC on a cylindrical specimens of size 100 × 200 mm. The authors used 1%, 2%, and 3% basalt fiber by volume of the concrete mix. The authors found that at 2% addition of basalt fibers, the BFRC mix showed greater enhancement in compressive strength, and at 3% addition, the compressive strength of concrete decreased compared to the control mix. The stain at ultimate compressive strength and splitting tensile strength increased with increasing fiber content, and this increment was

significantly greater than the control mix. This resulted in an improvement in the ductile behaviour of the BFRC compared to PC.

Kizilkanat et al. 2015 [94] evaluated the fracture behaviour and mechanical properties of BFRCs developed using 0%, 0.25%, 0.5%, 0.75%, and 1% (by the volume of concrete) basalt fibers. The authors noticed 5.1% improvement in compressive strength with the addition of 0.5% fiber content. Basalt fibers did not show any influence on the modulus of elasticity of BFRC; however, due to the low modulus of elasticity of basalt fibers, the modulus of elasticity of BFRC slightly decreased with the increase in fiber content. The fracture energy, flexural strength, and split tensile strength of BFRC increased with the addition of all percentages of fiber content, and at 1% addition of basalt fibers, 50%, 34%, and 40% of increments in fracture energy, flexural strength, and split tensile strength were reported by the authors.

Iyer et al. 2015 [40] carried out the investigation to evaluate the effect of the addition of different lengths (12 mm, 36 mm, and 50 mm) and volume percentages (0%, 0.15%, 0.31%, and 0.46%) of basalt filament fibers on workability, compressive strength, and modulus of rupture of BFRCs. The workability of concrete decreased as fiber length and fiber quantity increased. The lowest slump was obtained for BFRC with 0.46% basalt fibers among all other percentages. The balling effect of basalt fiber was evident in all the mixes for the addition of 0.46% of basalt fibers, and this problem becomes severe as the length of the basalt fibers increased from 12 mm to 50 mm. The highest improvement in compressive strength was noticed for 12 mm long basalt fibers of 0.15% and the highest improvement in modulus of rupture was noticed for 36 mm long basalt fibers of 0.31%.

Branston et al. 2016 [41] evaluated the mechanical behavior of BFRC through by flexural and impact testing. The author used both basalt bundled fibers and basalt minibars to develop BFRC. It was reported that the addition of basalt fibers increased the first-crack strength of concrete subjected to flexural loading but was not significantly influential when subjected to impact loading. Basalt fibers in concrete failed by fiber rapture on account of poor post-cracking response of BFRC specimens.

Ayub et al. 2016 [95] investigated the compressive stress-strain behaviour of high-strength fiber reinforced concrete (HSFRC) mix types that had compressive strengths of 70 to 85 MPa and contained basalt fibers in volume fractions of 1 to 3%. The authors concluded that none of the percentage additions of basalt fibers showed substantial improvement in the compressive strength of concrete (a maximum of 4% improvement was observed), but the strains at

maximum compressive strength and toughness ratio of HSFRC improved by 12.24% and 47.15% compared to the same properties of PC.

Arslan 2016 [96] determined the fracture behavior, mechanical properties, and microstructural characterization of high-strength BFRC. The author also determined the fracture energy of BFRC using a three-point bending test on a notched beam. According to the authors, the workability of the concrete mixes decreased with the addition of 1, 2 and 3 kg/m^3 volume of both 12 mm and 24 mm long basalt fibers. The mix consisting of the highest volume of fibers as well as long-length fibers showed greater reduction in slump. From the hardened properties of BFRCs, it was noticed that the mix with basalt fibers of 24 mm length and 2 kg/m^3 volume showed the highest split tensile and flexural strength and fracture energy with respect to the control mix. SEM images revealed a strong coating of cement paste around the basalt fiber, indicating the existence of a strong bond between basalt fibers and the cement matrix.

Jalasutram et al. 2017 [97] investigated the mechanical properties of BFRCs prepared using basalt fibers of 12.7 mm in length and volume fractions of 0%, 0.5%, 1.0%, 1.5%, and 2%. From the test results, the authors concluded that the compressive strength of concrete decreased with addition of all percentages of fibers. Compared to the control mix, a maximum of 3% and a 12% decrease were noted for cube and cylindrical specimens, which had of 2% fiber content. However, due to the addition of basalt fibers, the brittle failure mode of compressive test specimens turned into a ductile compression failure mode. The increase in fiber dose in concrete improved the flexural and splitting strengths of BFRC specimens. A maximum of 75%, 60%, and 14% improvement in flexural strength, flexural toughness, and split tensile strength, respectively, was observed.

H. Zhang et al. 2017 [98] studied the effects of fiber content, concrete grade, and strain rates on the properties of BFRC mixes made with 12 mm long basalt fibers at volume percentages of 0%, 0.05%, 0.1%, 0.15%, 0.2%, and 0.25%. The authors confirmed that the toughening effect of basalt fibers decreased the brittleness of concrete. The optimum percentage of basalt fibers differs according to the strength grade of concrete. An adequate volume of fibers can improve the toughness of concrete effectively. The higher the concrete strength grade, the higher the toughening effect of basalt fibers due to the development of higher bond strength compared to the development of bond strength with concrete of low strength grade. It was also stated that basalt fibers can reduce the micropore structure of concrete at the plastic shrinkage and hardening phase of the concrete through reinforcing effect.

The experimental study conducted by Y. R. Zhao et al. 2017 [99] provided a new approach to understand the effect of the basalt fibers and the freeze-thaw cycles on the impact resistance performance of concrete. The authors considered 0, 1 kg/m^3, 1.5 kg/m^3, 2 kg/m^3, and 2.5 kg/m^3 volumes of basalt fibers with lengths of 18 mm and diameters of 15 μm for this study. The test results of the study proved that as basalt fiber content increased, the impact time for the development of initial crack and ultimate failure of the concrete increased. This is because basalt fibers added to concrete created a three-dimensional system that could increase the transmission range of the impact stress waves and thereby improve the elastic deformation performance of the concrete, i.e., it increases the concrete's initial cracking capability to impact resistance.

The effect of 0.1%, 0.3%, and 0.5% (to concrete volume) basalt fibers of 3 mm, 6 mm, 12 mm and 24 mm length on the mechanical properties of self-compacting concrete (SCC) was investigated by Algin and Ozen 2018 [100]. The basalt fibers increased the strength properties of SCC but decreased the fresh properties. The flexural and split tensile strengths increased to a maximum extent on addition of 0.5% of basalt fibers of 24 mm length and maximum compressive strength was obtained at 0.1% basalt fibers of 12 mm and 24 mm length.

J. Zhang et al. 2018 [101] examined the compressive strength and flexural strength and microstructural properties of SCMs based HPC with 0%, 0.1%, 0.2%, and 0.3% volume percentages of basalt fibers. The test results of the study indicate that HPC with 0.1% basalt fibers showed the highest improvement in compressive and flexural strength of concrete. Therefore, the authors concluded that 0.1% of basalt fiber content could be an optimum amount to achieve better mechanical properties to HPC. Microstructural observation showed that the addition of SCMs improved the core structure of concrete and formed the dense matrix around the fibers that led to the development of a strong bond between fiber and cement matrix, which resulted in improved compressive and flexural strength for HPC with 0.1% basalt fibers.

According to D. Wang et al. 2019 [102], the addition of basalt fibers is more effective in improving the flexural and split tensile strengths than the compressive strength of concrete. In this study, the authors attempted to evaluate the effects of the addition of 0.1%, 0.15%, and 0.2% volume percentages of basalt fibers of 12 mm length on the mechanical properties of concrete. Based on the results of the study, the authors reported that when compared to the control mix, among all other percentage additions of basalt fibers, the addition of 0.2% showed the highest improvement of 7.21%, 15.30%, and 38.3% of compressive, flexural, and split tensile strength, respectively.

X. Sun et al. 2019 [103] carried out multiscale numerical simulations and evaluated the experimental mechanical properties of BFRCs. In this investigation, 6 mm and 12 mm long basalt fibers of 0%, 1 %, 2%, 3%, 4%, and 5% by volume of concrete were taken to prepare the BFRCs. The test results showed that the mechanical properties of concrete increased first and then decreased. The compressive and splitting tensile test results show that concrete with 6 mm fiber performed significantly better in terms of improving strength than concrete with 12 mm fiber. The bending strength of concrete improved with the addition of all percentages of basalt fibers for 6 mm and 12 mm length. The mechanical properties of concrete mostly improved through basalt fiber at a length of 6 mm and volume of 2%.

The effect of alkali-resistant basalt fibers on mechanical properties of concrete was investigated by M. Li et al. 2020 [104]. Experimental results show that compressive, split, and flexural strengths increased the highest with the addition of 0.1% alkali-resistant basalt fibers compared to 0.05%, 0.2%, and 0.3% additions. From SEM image observations it was reported that adding alkali resistant basalt fibers to concrete enhanced the pore size distribution of concrete and bonding between fibers and the concrete matrix also improved.

Zhou et al. 2020 [105] experimentally evaluated the effect of 0%, 0.1%, 0.2%, 0.3%, 0.4%, 0.5% and 0.6% basalt fibers (by volume of concrete) additions on the mechanical properties of concrete. The toughness and fracture resistance of concrete greatly increased with the addition of basalt fibers. The compressive strength of concrete is enhanced by basalt fibers to a lesser extent than tensile and flexural strengths. From the test results, the authors noticed that the improvement in mechanical properties was greatest with the addition of 0.3% and 0.4% fibers.

Ramesh and Eswari 2021 [106] studied the fresh and hardened properties of BFRCs prepared using 0%, 0.5%, 1%, 1.5%, and 2% of basalt fibers. The authors determined that the workability of concrete decreased gradually with respect to increase in the addition of basalt fiber percentages. The test results showed that there was a slight improvement in the compressive strength of concrete up to an addition of 1.5% and a decrease in increment for a 2% addition of basalt fibers. The tensile strength and flexural strength of concrete increased with the addition of all percentages of fibers. Among all, at 1.5% addition of basalt fibers, the compressive strength, flexural strength, and split tensile strength of concrete improved by 4.45%, 57%, and 22.58%, respectively. The authors also observed change in failure mode of compressive specimens from brittle compression to ductile compression failure.

Y. Wang et al. 2021 [107] investigated the effects of basalt fibers of 3 mm, 6 mm, 12 mm, and 18 mm in length on the mechanical properties of GPC. The authors concluded that the compressive and split tensile strength, peak load, fracture energy absorption, and fracture toughness were highest with the addition of 6 mm length basalt fibers than basalt fibers of other lengths.

Haido et al. 2021 [108] stated that the compressive strength of SCC mixtures decreased with the incorporation of 0.25%, 0.5%, and 1.0% of basalt fibers of 24 mm in length, and flexural strength increased with the addition of basalt fibers of all additions. The authors of the study reported that decrease in workability was the reason for decrease in compressive strength. Similarly, the split tensile strength of SCC increased with the addition of 0.25% of basalt fibers and thereafter the strength decreased.

The influence of basalt fiber on the fresh and fracture behaviour of SCC was examined by Gültekin et al. 2022 [109]. In this study, the authors used three different lengths of basalt fibers (6 mm, 12 mm, and 24 mm) in two different densities (2 kg/m^3 and 4 kg/m^3). From the test results obtained, the authors reported that basalt fiber showed a negative effect on the workability of SCC; that is, the values obtained from different workability measuring methods decreased with the addition of both types and the volume content of basalt fibers. The compressive strength of SCC mixes decreased regardless of the length and content of the basalt fibers but significantly improved the flexural strength in the range of 12.5% to 43.5% compared to the control mix.

2.5 Literature Review on Alccofine-1203 Based Concrete

The efficiency of alccofine-1203 in the development of SCC was investigated by some researchers. Pawar and Saoji 2013 [110] attributed self-compatibility characteristics to concrete by the addition of 0%, 5%, 10% and 15% volume percentages of alccofine-1203 while keeping cement, fly ash, and coarse and fine aggregates proportions constant. The test results of alccofine-1203 based SCC were compared with normal SCC. It was found that incorporating alccofine-1203 improved the fresh and hardened properties of SCC significantly compared to normal SCC. From the test results, it was determined that SCC with 10% alccofine-1203 exhibited superior workability and compressive strength than SCC with 0%, 5%, and 15% of alccofine-1203.

Kavitha and Felix Kala 2016 [111] examined the effect of 5%, 10%, 15% and 20% alccofine-1203 replacement levels with a combination of 30% GGBS on workability properties and

compressive, flexural and split tensile strengths of SCC. It was reported that the replacement of cement using alccofine-1203 with a combination of GGBS improved the workability and strength properties of SCC. The workability properties of SCC improved due to high fineness and glassy surface characteristics with low calcium silicate chemical composition of alccofine-1203. Based on the test results authors concluded that the highest compressive and split tensile strengths to SCC are attained by replacing cement with 10% alccofine-1203 and 30% GGBS than other replacement levels of alccofine-1203.

Kavyateja et al. 2020 [112] investigated the mechanical properties of SCC, developed by partial replacement of cement using 25% fly ash with 0%, 5% 10% and 15% alccofine-1203 combinations. From the test results, the authors observed that at 3, 7, 28, and 90 days, the specimens of SCC mix having 65% cement, 25% fly ash and 10% alccofine-1203 showed the highest compressive and split tensile strengths and modulus of rupture than the specimens of other mixes. Based on this, it was concluded that 25% fly ash and 10% alccofine-1203 is an optimum percentage to partially replace cement to achieve SCC with superior strength properties.

A. A. Khating et al. 2018 [113] studied the effect of the addition of steel fibers on the workability and compressive, flexural, and split tensile strength properties of alccofine-1203 and fly ash-based steel fiber reinforced SCC. From the test results authors reported that fresh properties of steel fiber reinforced SCC that incorporating ultra-fine particles of alccofine-1203 imparted good flowability and good self-compacting characteristics to steel fiber-reinforced SCC and also satisfied the EFNARC specifications given for the development of SCC. The mix with 15% alccofine-1203 exhibited the highest compressive, flexural and split tensile strength than other mixes.

Sanjeev Kumar et al. 2019 [114] investigated the possibility of enhancing the strength properties of lightweight aggregate concrete using alccofine-1203. The authors of this study attempted to increase the reduced strength of lightweight concrete by partially replacing coarse aggregates with coconut shells by partially replacing cement with alccofine-1203. From the test results, the authors noticed that partial replacement of coarse aggregates with coconut shells reduced the compressive strength of concrete from 44.8 MPa to 35.49 MPa, and by replacing cement with 8% alccofine-1203, the compressive strength of lightweight concrete increased to 42.41 MPa.

Balamuralikrishnan and Saravanan 2021 [115] studies the effect of alccofine-1203 on the compressive strength of cement mortar. 0%, 5%, 10%, 15% and 20% of cement was replaced with alccofine-1203. The authors determined that by replacing 10% cement with alccofine-1203, the mortar specimen showed highest compressive strength of 53.12 MPa, whereas the specimen with 100% cement attained only 44.74 MPa.

Soni et al. 2013 [50] conducted an experimental investigation to optimise the percentage of fly ash and alccofine-1203 to partially replace the cement for HPC development. It was observed that replacing cement with 16% fly ash and 8% alccofine-1203 led to the development of HPC with better properties. The authors compared the test results of alccofine-1203 based HPC with silica fume based HPC. It was found that the alccofine-1203 based HPC mixes had higher compressive and flexural strengths than silica fume-based mixes.

Based on compressive and flexural strength results, Suthar et al. 2013 [116] reported that the replacement of cement with 8% alccofine-1203 and 20% fly ash led to higher compressive and flexural strengths compared to the same percentages of cement replacement with silica fume and fly ash. This is because the particle packing of binder mass has increased with the incorporation of ultra-fine particles of alccofine-1203, which led to the gain of high strength to concrete in the early stages of curing.

Gupta et al. 2015 [48] stated that the presence of lime (CaO) enhances and provides the secondary hydrated C-S-H gel products that result in gaining high strengths at early ages of curing and also result in low heat generation in the hydration process.

Gautham and Ramadoss 2020 [117] mentioned that alccofine-1203 can be considered as SCM in the development of UHSC. The mechanical properties of UHSC improved with the presence of alccofine-1203 compared to silica fume based UHSC. At 28 days test, alccofine-1203 and GGBS based UHSC yielded compressive strength of 136.67 MPa, flexural strength of 31.88 MPa, and split tensile strength of 15.20 MPa whereas silica fume and GGBS based UHSC yielded compressive strength of 119.31 MPa, flexural strength of 27.82 MPa and split tensile strength of 13.26 MPa.

According to Upadhyay and Jamnu 2014 [118], the highest compressive strength of HPC was attained at replacement of cement with 10% of alccofine-1203 and 30% of fly ash. The self-compatibility characteristics such as passing and filling ability and segregation resistance of concrete increased with the addition of alccofine-1203. Since, the cost of alccofine-1203 was

lower than that of ordinary Portland cement (OPC), it is economical to use alccofine-1203 in the development of HSC and HPC.

Soni et al. 2013 [50] reported that the incorporation of ultra-fine particles of alccofine-1203 minimises the voids present between cement particles and improves the rheology and flow ability of concrete. The combination of cement hydration and the alccofine-1203 pozzolanic reaction results in the formation of a dense core matrix structure.

Boobalan et al. 2021 [119] carried out the literature survey on alccofine-1203 based HPC, and reported that incorporation of alccofine-1203 caused concrete to attain high strength at an early stage and improved the workability, strength and durability characteristics of concrete. The presence of CaO in alccofine-1203 leads to the formation of additional C-S-H gel that leads higher strength to concrete at an early age. As alccofine-1203 is low calcium silicate-based material, its incorporation in concrete development enhances the pH value to protect it against corrosion and improves durability characteristics.

Magdum and Karjinni 2016 [120] investigated the compressive and flexural strength of hybrid fiber reinforced HSC. The highest compressive and flexural strengths were obtained by adding 1.5% of hybrid fibers (80% steel fibers and 20% polypropylene fiber) and by partial replacement of cement with 7.5% of alccofine-1203.

The effect of alccofine-1203 on the rapid strength gain property of HSC was evaluated by Srinivas et al. 2021 [121]. From the control mix, 0%, 5%, 10% and 15% of cement were replaced with alccofine-1203. The developed mixes are tested for mechanical properties at 1, 2, 7 and 28 days. All the alccofine-1203 based mixes were had superior quick setting property than concrete without alccofine-1203. From the results of the study, the authors noticed that with the incorporation of alccofine-1203, there was a great increase in compressive, flexural and split tensile strengths at early age curing. At 10% alccofine-1203, the highest compressive, flexural and split tensile strengths were obtained in all stages of curing.

Sharma et al. 2016 [122] carried out an investigation to optimise the percentage of alccofine-1203 in the development of HSC by replacing cement with 0%, 5%, 10%, 15% and 20% alccofine-1203- 1203. At 15% replacement level, the mix obtained the highest compressive, flexural and split tensile strengths. Based on these results, the authors proposed that the replacement of cement with 15% alccofine-1203 could be an optimum dosage for the development of HSC.

Saurav and Gupta 2014 [123] compared the cube and cylindrical compressive strength results of alccofine-1203 based HSC. In this investigation, cement was replaced with 0%, 3%, 5%, 7%, 10%, 13%, 15% and 18% alccofine-1203. It was found that the replacement of cement with alccofine-1203 effectively increased the compressive strength of concrete up to 10%, and slightly increased for 13% and decreased for 15% and 18% replacements. The highest cube and cylindrical compressive strength were obtained at 13% replacement. The cylindrical specimens showed lower compressive strengths than the cube specimens.

From the study conducted on HSC, Rajesh et al. 2015 [124] reported that replacement of cement with 10% alccofine-1203 led to the development of the highest compressive and flexural strengths at 7 and 28 days than the replacement of cement with 0%, 5%, 15% and 20% alccofine-1203.

A.N. Reddy and Meena 2017 [125] stated that replacement of cement with alccofine-1203 in combination with fly ash resulted in the development of eco-friendly concrete having better and superior properties than only cement-based concrete. The authors concluded that replacement of cement with 15% fly ash and 10% alccofine-1203 showed higher compressive, flexural, and split tensile strength. In another investigation, A.N. Reddy and Meena 2017 [126] studied the change in behaviour of fresh properties of concrete developed by partial replacement of cement with alccofine-1203 in combination with GGBS. It was reported that the replacement of cement with alccofine-1203 and GGBS decreased the setting time of concrete and showed better workability than the control mix.

Jindal, Praveen, et al. 2017 [49] developed geopolymer concrete (GPC) by partial replacement of low calcium fly ash with 0%, 5% and 10% alccofine-1203. The developed mixes were cured in ambient and heat curing conditions for 3-, 7- and 28-day. From the test results, the authors concluded that the compressive, flexural and split tensile strengths of GPC cured in both curing conditions were increased with the incorporation of alccofine-1203. The heat-cured GPC attained higher strengths than that of the ambient cured GPC because alccofine-1203 enhanced the geopolymerization process significantly under high temperature curing conditions than normal ambient temperature curing conditions. However, the ambient cured GPC attained the required compressive strength for purpose of general construction.

From the compressive strength results of oven-cured GPC, Jindal, Singhal, et al. 2017 [127] concluded that the specimens of mix replacing 10% fly ash with alccofine-1203 showed higher resistance to compressive loads than specimens of mixes replaced with 0% and 5%. To

strengthen this, the authors also studied the microstructural characteristics using SEM analysis on GPC with and without alccofine-1203. From SEM analysis of GPC, the authors reported that during the polymerization process, amorphous materials are converted into crystalline materials, and this transformation is even greater in the case of alccofine-1203 incorporated GPC, so does the GPC with 10% alccofine-1203 has exhibited higher compressive strength than normal GPC. It was suggested that the GPC manufactured by incorporating alccofine-1203 is suitable for general constructions and for pre-cast plain and RC members due to its early strength gaining property.

Srinivasreddy and Balamurugan 2019 [128] reported the setting time, consistency and compressive strength behaviour of ternary blended GPC manufactured using fly ash, GGBS and alccofine-1203, and replaced 100% fine aggregate with msand. The authors observed that compared to the control mix, by partial replacement of fly ash with alccofine-1203, the compressive strength of GPC increased significantly at 7 and 28 days but partial replacement of GGBS with alccofine-1203 significantly decreased the compressive strength of GPC at 7 and 28 days compared to fly ash–based GPC. Based on results obtained from this study, the authors concluded that manufacturing concrete using fly ash, GGBS and alccofine-1203 leads to 100% replacement of OPC and effective utilisation of industrial waste products as beneficial materials.

Parveen et al. 2018 [129] studied the mechanical and microstructural properties of fly ash and alccofine-1203 based GPC cured in ambient conditions. The microstructural and phase composition properties of GPC were examined using SEM and XRD analysis. It was found that the compressive, flexural, and split tensile strengths of GPC were obtained similar to conventional concrete. The GPC exhibited better microstructural and strength properties because the incorporated alccofine-1203 enhanced the polymerization process of GPC, which resulted in fewer micro-cracks and pores and the formation of denser matrix which attributed higher strength to concrete.

2.6 Summary on Literature Review

From the detailed literature review presented above on BFRP RC beams, BFRC, PVAFRC, and various types of alccofine-1203 based concretes, the following are the main gist of the study:

- BFRP rebars had higher tensile strength and a lower Young's modulus compared to steel reinforcing bars. Due to this, BFRP RC beams showed higher flexural strength and higher deflections, deformations, and wider cracks compared to steel RC beams.

- The BFRP rebars do not have standard design code, guidelines, and specifications. Since BFRP rebars comply with ACI and CSA requirements, the design of BFRP RC members can be done by the design codes and guidelines of existing conventional FRP RC members.
- BFRP RC beams do not harden by deformation after the cracking begins. The yield stage of BFRP RC beams was negligible compared to steel RC beams, and investigations revealed that BFRP RC beams failed in a fragile failure mode.
- The design code of FRP ACI-318-2019(22) [130] allows to design over-reinforced FRP sections to avoid or minimize failures due to larger deflections and wider cracks. But with special consideration and care, BFRP RC beams can be designed as under-reinforced sections but not balanced.
- Providing more area of BFRP reinforcement in tension zone decreases the deflections and increases the moment carrying capacity and ultimate load carrying capacity of the beams.
- The pre-stressing of the BFRP rebar is an effective technique to use all its strength in RC beams.
- The strength of BFRP rebars was completely used in ECC beams compared to concrete beams.
- The structural performance, serviceability and ductility of BFRP RC beams increased with the hybrid (BFRP and steel) reinforcement system and this reduced the disadvantages associated with pure BFRP-reinforced concrete beams.
- The addition of steel FRC layer in the tension zone of the beams led to reduction of large deflections, crack widths, and improved the ductility of pure BFRP RC beams.
- The corrosion problem related to steel reinforcing bars, and steel fibers is still a critical problem in the hybrid reinforcement system and steel FRC layer.
- The ductility characteristics of FRP RC beams depend to a large extent on the properties of concrete due to the lack of ductility of BFRP rebars. The FRC beams with BFRP rebars showed better flexural performance and ductility characteristics than pure BFRP RC beams with normal concrete.
- Deflections and crack width of BFRP RC beams can be controlled by the addition of discrete fibers.

- The addition of basalt fiber to concrete had a greater influence on the pre-cracking stage of concrete: it increased first cracking strength, pre-hardening zone, and pre-peak behavior.
- Inclusion of basalt fibers has negative effect on the workability of fresh concrete mix, whereas it improves the flexural strength, toughness, ductility, and fracture energy of concrete composites.
- The addition of PVA fibers to concrete partially increased its compressive strength, offered resistance to shear forces under uniaxial stress, and improved the first crack strength of the concrete as the fibers were effectively involved in bridging the cracks.
- PVA fiber reinforced samples largely improved the post-cracking extension and fracture energy.
- The addition of PVA fibers to concrete improved its deflection hardening behavior, imparted higher stiffness to the concrete, and showed higher flexural strength than the concrete without PVA fibers.
- The presence of a good amount of calcium (CaO) and silica (SiO_2) in alccofine-1203 made its performance superior to other SCMs, which resulted in denser matrix and fewer micro cracks, pores, and achieved higher strength for concrete in early hardening stages.
- The combination of 8% to 15% of alccofine-1203 with other SCMs for partial or full replacement of cement led to the development of eco-friendly concrete having good workability and superior mechanical properties.
- The optimal percentage of alccofine-1203 to be used for partial replacement of cement in HSC development is unclear. Therefore, it needs to be identified.

Based on a detailed literature survey on the flexural behavior of BFRP RC beams, as well as the behavior of BFRC and PVAFRC, and on alccofine-1203-based various types of concrete, it is identified that there is an ample need to explore the flexural response of BFRP-reinforced BFRC and PVAFRC beams in two different concrete strengths. The next chapter will present the objectives of the research work along with the scope of the investigation.

Chapter 3
Scope and Objectives of the Research

3.1 General

For the present research work, a gap was identified through a detailed literature survey and was aimed to study the flexural behaviour of BFRP-reinforced BFRC and PVAFRC beams.

3.2 Research Gap

With high tensile strength, toughness, and ductility, and sufficient durability, FRC has become a new viable material widely used in various buildings, pavements, large industrial floors, and tracks. Therefore, the application of BFRP rebars in FRC can increase its potential as longitudinal reinforcement, as the disadvantages associated with PC beams reinforced with BFRP rebars can be reduced by increasing the strength and tensile properties of concrete with the addition of fibers. From a sustainable point of view, as BFRP rebar is an eco-friendly and non-corrosive material, to develop FRC for the present investigation, eco-friendly and non-corrosive fibers such as basalt and PVA fibers were selected. These fibers were chosen based on their physical properties and the strength they bring to concrete upon their addition. The influence of BFRC and PVAFRC of M30 and M70 grades on load-deflection behavior, moment-curvature relationships, ductility behavior, crack pattern, and failure mode of the BFRP-reinforced BFRC and PVAFRC beams, and the validation of these results with the results of ABAQUS-based finite element numerical model analysis, have not been found in the literature. This was identified as a major research gap.

3.3 Scope and Objectives of the Research Work

3.3.1 Objectives of the Research

- To develop HSC using alccofine-1203 as partial replacement to cement.
- To identify the ideal percentage of PVA fibers and basalt fibers based on the mechanical and compressive stress-strain behavior of concrete, and to develop and propose a constitutive model for the analytical modelling of compressive stress-strain curves of PVAFRC and BFRC.
- To evaluate the flexural behaviour of BFRC and PVAFRC beams reinforced with BFRP rebars experimentally.
- To perform Abaqus based finite element modelling (FEM) analysis on BFRC and PVAFRC beams reinforced with BFRP rebars for validating experimental results.

3.3.2 Scope of the Research Work as Follows

- To determine the mechanical and microstructural properties, and the compressive stress-strain behavior of alccofine-1203-based concrete developed by the partial replacement of cement with various percentages of alccofine-1203, in order to identify the optimal dosage for use in the development of HSC.
- To determine the mechanical and microstructural properties and the compressive stress-strain behavior of different BFRC and PVAFRC mixes developed by the addition of various percentages of basalt fibers and PVA fibers, in order to identify optimal dosage of fibers to reinforcing plain concrete for investigating the flexural behavior of BFRP-reinforced BFRC and PVAFRC beams. Additionally, a modified constitutive analytical model can be proposed for the analytical modelling of compressive stress-strain curves of BFRCs and PVAFRCs of M30 and M70 grades.
- To experimentally investigate the flexural behavior of BFRC and PVAFRC beams reinforced with BFRP rebars.
- Numerical modelling of the flexural behavior of BFRC and PVAFRC beams reinforced with BFRP rebars using FEM-based software, ABAQUS.

3.4 Research Methodology

Based on the stated objectives and the scope of the work, a comprehensive research methodology was developed by dividing the research into four phases.

Phase-1: The different binder mix proportions were developed by partial replacement of cement with various volume percentages of alccofine-1203. All the developed binder mixes investigated for consistency, initial and final setting times, and microstructural properties. Then, the concrete mixes are evaluated for workability, mechanical properties, and compressive stress-strain behavior. Based on the test results, the optimum percentage of alccofine-1203 for the development of HSC was determined.

Parameter considered in Phase-1: i) various volume percentages of alccofine-1203 - 0%, 4%, 6%, 8%, 10%, 12%, and 14%.

Phase-2: The mix design for the normal strength concrete (NSC) of M30 grade was developed by partial replacement of cement with class-F fly ash. The workability, mechanical properties and compressive stress-strain behavior of the NSC were evaluated. Then, various volume percentages of basalt fibers and PVA fibers were used to develop different BFRC and PVAFRC mixes of M30 and M70 grades. Then, the developed mixes were evaluated for workability,

mechanical and micro-structural properties, and uniaxial compressive stress-strain behavior. Based on the test results, the ideal volume percentage of basalt fibers and PVA fibers that yielded the highest strength and stress-strain properties was considered for the development of BFRC and PVAFRC for evaluating the flexural behavior of BFRP-reinforced BFRC and PVAFRC beams. In addition to this, a modified constitutive analytical model was proposed for analytical modeling of compressive stress-strain curves of BFRCs and PVAFRCs of both M30 and M70 grades.

Parameter considered in Phase-2: i) volume percentages of basalt fibers – 0%, 0.1%, 0.2%, 0.3%, 0.4%, and 0.5%, ii) various volume percentages of PVA fibers – 0%, 0.1%, 0.2%, 0.3%, 0.4%, and 0.5%, and iii) two grades of concrete – M30 and M70.

Phase-3: The ideal percentage of basalt fibers and PVA fibers was taken from the results of phase-2 work for the development of BFRC and PVAFRC. Then, BFRP-reinforced PC, BFRC and PVAFRC beams were evaluated for flexural behavior experimentally. In addition to this, steel-reinforced PC beams were also cast and tested.

Parameter considered in Phase-3: i) concrete type: PC, BFRC and PVAFRC, ii) two grades of concrete: M30 and M70, and iii) type of RC section: under-reinforced and over-reinforced.

Phase-4: The numerical simulation of experimentally evaluated BFRP-reinforced PC, BFRC, and PVAFRC beams, and steel-reinforced PC beams, was done using finite element modelling software, ABAQUS. The numerical simulation results were used to validate experimental results.

Parameter considered in Phase-4: same as considered in Phase-3 work.

A schematic diagram of the research methodology followed along with the variables considered at each phase of the research is shown in Table 3.1.

Table 3.1 Research methodology followed for the research work

Work phases	Variables	Parameters investigated	Out put
Phase-1: Studies on alccofine-1203 based concrete mixes for the development of HSC.	❖ **Various volume percentages of alccofine-1203 –** 0%, 4%, 6%, 8%, 10%, 12%, and 14%.	**Experimental:** Workability, mechanical properties, compressive stress-strain behavior and micro-structural properties. **Analytical:** Young's modulus, EAC.	❖ Strength properties and compressive stress-strain behavior of alccofine-1203 incorporated concrete mixes ❖ The optimum percentage of alccofine-1203 for the development of HSC.
Phase-2: **Part-A:** Experimental, microstructural, and analytical studies on PVAFRCs. **Part B:** Experimental, microstructural, and analytical studies on BFRCs.	❖ **Volume percentages of PVA fibers** – 0%, 0.1%, 0.2%, 0.3%, 0.4%, and 0.5%. ❖ **Volume percentages of basalt fibers** – 0%, 0.1%, 0.2%, 0.3%, 0.4%, and 0.5% ❖ **Grades of concrete** – M30 and M70.	**Experimental:** Workability, mechanical properties, compressive stress-strain behavior, and micro-structural properties. **Analytical:** Young's modulus, EAC and analytical modelling of stress-strain curves.	❖ Strength properties and compressive stress-strain behavior of PVAFRC and BFRC mixes. ❖ The optimum percentage of basalt fiber and PVA fibers for the development of BFRC and PVAFRC of M30 and M70 grades.
Phase-3: Experimental investigation on flexural behaviour of BFRP-reinforced PC, BFRC and PVAFRC beams and steel-reinforced PC beams.	❖ **Concrete type:** Plain concrete, BFRC and PVAFRC of M30 and M70 grades. ❖ **Section type:** Under-reinforced and over-reinforced.	**Experimental:** midpoint load-deflection behavior, strain in concrete, strain in rebars and moment curvature response, cracking pattern, and failure behavior.	❖ Load-deflection curves ❖ Moment-curvature relationships, ❖ Ductility indices, ❖ Crack pattern and failure mode.
Phase-4: Numerical modelling of flexural behaviour of BFRP-reinforced PC, BFRC and PVAFRC beams and steel-reinforced PC beams using Abaqus software.	❖ **Concrete type:** Plain concrete, BFRC and PVAFRC of M30 and M70 grades. ❖ **Section type:** Under-reinforced and over-reinforced.	**Numerical:** midpoint load-deflection behavior, strain in concrete, strain in rebars and moment curvature response, cracking and damage response.	❖ Load-deflection curves ❖ Moment-curvature relationships, ❖ Ductility indices, ❖ Damage profiles.

Chapter 4

Experimental and Microstructural Investigations on Alccofine-1203 Based HSC

4.1 General

Based on the objectives framed in Chapter 3, the experimental work was planned accordingly to evaluate mechanical and microstructural properties and compressive stress-strain behaviour of alccofine-1203 based concrete mixes. The present chapter explains the results of experimental and analytical investigations carried out on different alccofine-1203 based concrete mixes developed using partial replacement of cement with various volume percentages of alccofine-1203. From the test results presented, the ideal volume percentage of alccofine-1203 for partial replacement of cement for the development of HSC of M70 grade was determined. The experimental programme includes evaluation of the effect of alccofine-1203 on standard consistency and setting times of the binder mixes and microstructural properties of hardened binder mixes, and mechanical properties and compressive stress-strain behaviour of concrete mixes. The effect of alccofine-1203 on Young's modulus and energy absorption capacity (EAC) of concrete mixes was evaluated analytically from compressive stress-strain curves. The present phase (Phase-I) of the research work was carried out based on the strength criteria considering the parameters as various volume percentages of alccofine-1203. The details of materials used, mix proportions, preparation of mixes and cast of specimens, test methods and discussion on obtained results is presented in the following sections.

4.2 Materials-Physical Properties

The following are the materials used for present phase of the research work according to Indian Bureau of Standards.

4.2.1 Cement

Ordinary Portland cement of 53 grade with specific surface area of 3300 cm^2/gm and specific gravity of 3.12 was used in accordance with IS 12269-2013 [131]. The chemical composition of cement used in this research is shown in Table 4.1. The SEM image of the cement is shown in Figure 4.1 and the figure shows that the cement particles are irregular in shape with sharp edges. The particle size distribution of cement is shown in Figure 4.2.

4.2.2 Fly Ash

Fly ash used in this study is classified as alumina silicate fly ash, popularly known as class-F fly ash in accordance with IS 3812 (Part-I) - 2013 [132]. The chemical composition of fly ash used in this study is presented in Table 4.1. The specific surface area of fly ash is 3600 cm^2/gm with a specific gravity of 2.26. The SEM image of fly ash is shown in Figure 4.3 and the figure shows that the Gray coloured fly ash particles were spherical in shape with glassy nature. The particle size distribution of fly ash is shown in Figure 4.2.

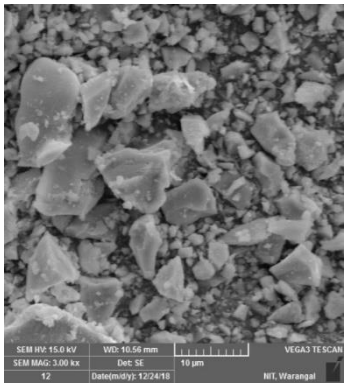

Figure 4.1 SEM image of cement

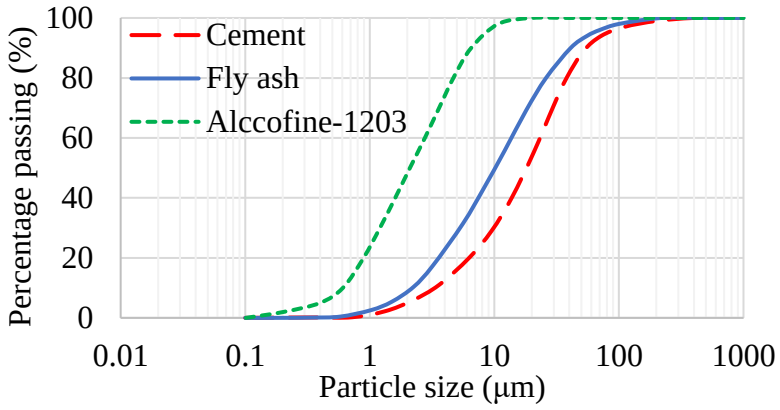

Figure 4.2 Particle size distribution of binder materials

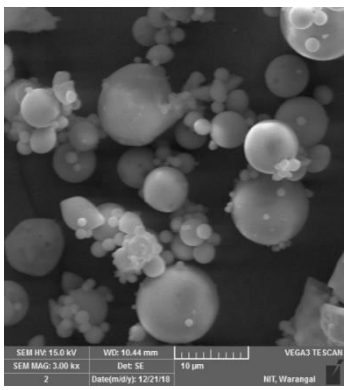

Figure 4.3 SEM image of fly ash

4.2.3 Alccofine-1203

Alccofine-1203 used for the development of HSC complies with IS 456-2000 [133] and IS 12089-1987 [134]. Alccofine-1203 used in this study is shown in Figure 4.4, and its chemical composition of is presented in Table 4.1. The SEM image of alccofine-1203 is shown in Figure 4.5 and the figure shows that alccofine-1203 particles are irregular in shape with sharp edges. The specific surface area of alccofine-1203 is 12000 cm^2/gm and specific gravity is 2.7. The partial size distribution of alccofine-1203 is shown in Figure 4.2. The size of alccofine-1203 particles range from 1 to 75 μm with a major fraction in the range of 20-50 μm.

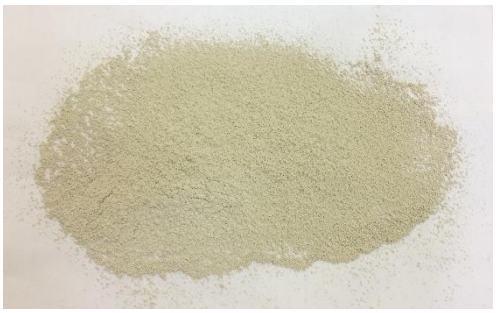

Figure 4.4 Alccofine-1203

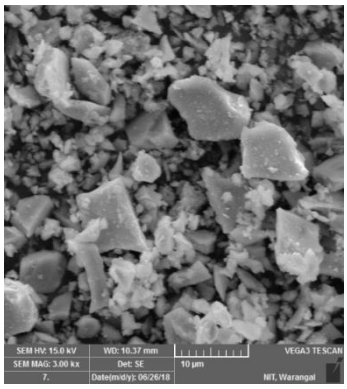

Figure 4.5 SEM image of alccofine-1203

Table 4.1 Chemical compositions of cement, fly ash, and alccofine-1203

Composition	CaO	Al_2O_3	Fe_2O_3	MgO	SiO_2	Na_2O	K_2O	SO_3	MnO	LOI
Cement	63.68	4.72	3.38	1.46	22.53	0.37	0.71	1.32	0.05	0.75
Fly ash	2.35	28.15	4.22	1.02	61.55	0.21	1.75	0.25	-	0.3
Alccofine-1203	29.46	24.57	0.92	5.23	37.53	0.032	0.61	0.18	-	0.58

4.2.4 Aggregates

Natural river sand used as fine aggregate (Zone-II), and crushed granite of maximum size of 16 mm used as coarse aggregates in accordance with IS 383-2016 [135]. The specific gravity,

water absorption, fineness modulus of fine and coarse aggregates is 2.65, 0.78%, 2.63 and 2.7, 0.8%, 6.8 respectively. The particle size distribution of fine aggregates and coarse aggregate are shown in Figure 4.6.

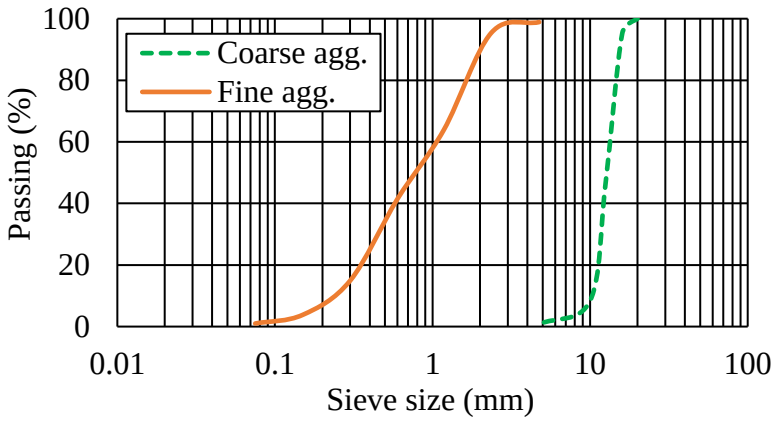

Figure 4.6 Particle size distribution of aggregates

4.2.5 Water

Potable water free of any chemicals and organic matter was used in the manufacture of concrete in accordance with IS 456-2000 [133].

4.2.6 Superplasticizer

Polycarboxylic ether based high-performance superplasticizer (SP), namely, Masterglenium SKY-8233 was used to enhance the workability of concrete in accordance with IS 9103-1999 [136]. The properties of Masterglenium SKY-8233 are shown in Table 4.2.

Table 4.2 Properties of Masterglenium SKY-8233 superplasticizer

Parameters	**Specifications (As per IS 1903)**	**Results**
Physical state	Reddish brown free flowing liquid	Reddish brown free flowing liquid
Chemical name of active ingredient	Polycarboxylate polymer	Polycarboxylate polymer
Relative density at 25°C	1.08 ± 0.02	1.080
pH	≥ 6	7.05
Chloride ion content (%)	< 0.2	0.014
Dry material content (%)	$34 \pm (5\%)$	34.64

4.3 Mix Proportions and Mixes

The mix design for the present phase of the research work was developed based on the concrete mix proportion guidelines given in IS 10262-2019 [137]. The mix proportion and constituent material quantities are shown in Table 4.3. A total of 7 different percentages of alccofine-1203,

0, 4%, 6%, 8%, 10%, 12%, and 14%, was used to replace the cement from the control mix. Thus, a total of 7 mixes were prepared with water to binder ratio of 0.26. As alccofine-1203 is rich in calcium oxide and aluminium oxide, the combination of alccofine-1203 with cement alone in the manufacturing of HSC may lead to undesirable behaviour. On the hand, the use of higher amount of cement in the manufacturing of HSC may also lead to undesirable behaviour such as formation of large number of micro-cracks in the binder matrix, increase in brittleness and cracking due to drying shrinkage. To reduce these undesirable effects and to improve the performance of the concrete such as workability, consolidation, and cohesiveness, a 20% of class-F fly ash was used to replace the cement in all the concrete mixes. The changes in binder mix proportion with respect to alccofine-1203 replacement levels are presented in Table 4.4. In Table 4.4, out of 7 mixes, M-C is the control mix with 80% cement, 20% fly ash, and 0% alccofine-1203, and for the remaining 6 mixes with respect to the partial replacement of cement with various percentages of alccofine-1203, each mix is designated as shown in Table 4.4. In the given mix designation, M stands for Mix, AF stands for alccofine-1203 and number with % stands for percentage replacement of cement with alccofine-1203. The percentage of superplasticizer dosage given in Table 4.3 is to the total weight of the total binder (600 kg/m^3) of each mix.

Table 4.3 Mix proportion and constituent material quantities

Mix proportion	**Constitutive material (kg/m^3)**			**Water (kg/m^3)**	**w/b ratio**	**SP (%)**
B:FA:CA	**Binder (B)**	**Fine agg. (FA)**	**Coarse agg. (CA)**			
1:1.22:1.58	600	732	948	156	0.26	0.725

Table 4.4 Variation in binder mix proportion with respect to alccofine-1203 percentages

Mix Designation	**Cement (C) kg/m^3**	**Fly ash (FA) kg/m^3**	**Alccofine-1203 (AF) kg/m^3**	**Binder Proportion (C%:FA%:AF%)**
M-C	480	120	-	80%:20%:0%
M-4%AF	456	120	24	76%:20%:4%
M-6%AF	444	120	36	74%:20%:6%
M-8%AF	432	120	48	72%:20%:8%
M-10%AF	420	120	60	70%:20%:10%
M-12%AF	408	120	72	68%:20%:12%
M-14%AF	396	120	84	66%:20%:14%

4.4 Mixing, Cast and Curing of Concrete Specimens

The mixing of concrete was done according to the guidelines given in IS 456-2000 [133]. Surface-dry conditioned coarse and fine aggregates were dry mixed in a concrete mixer for 1 minute. Then, the binder materials were mixed separately until they obtained a uniform color, and they were then transferred to the concrete mixer, where they continued to mix for an additional 1 minute. Half of the measured water was added to the dry mixer and mixed for 30 seconds. The remaining water was then added, and superplasticizer was added and transferred to the wet mixture, mixed for another 60 seconds to obtain good consistency, and achieve the desired workability for the mixture. Fresh concrete was filled into oiled iron moulds and compacted with the help of a vibrating table. Cast specimens, as seen in Figure 4.7, were demoulded after 24 hours and cured in water at 27 ± 2 °C until the test age.

Figure 4.7 Cast specimens of alccofine-1203 based concrete mixes

4.5 Test Specimens and Methods

4.5.1 Tests on Binder

The standard consistency of the binder paste was identified according to IS 4031 (Part 4)-1998 [138], and the setting times (initial setting time and final setting time) of the binder paste were determined according to IS 4031 (Part 5)-1998 [136]. Both tests were performed using the Vicat apparatus [139]. The standard consistency and setting times of all binder mixes were determined following the procedures used for determining the standard consistency and setting time of cement. In accordance with the guidelines provided in IS 4031 (Part 4)-1998 [138] and IS 4031 (Part 5)-1998 [140], 400 gm of cement was taken first, and then, according to the binder mix proportion percentages presented in Table 4.4, partial replacement of cement was done with Alccofine-1203 and fly ash. The initial and final setting times of binders were determined by gauging the binders with 0.85 times the water required to give a paste of standard consistency.

4.5.2 Tests on Concrete

4.5.2.1 Workability

Slump cone test was performed to find out the workability of the alccofine-1203 based concrete mixes according to IS 1199 (Part 2)-2018 [141]. The measuring slump value of concrete mix is shown in Figure 4.8.

Figure 4.8 Slump cone test on alccofine-1203 based concrete mix

4.5.2.2 Compressive strength

Cube specimens of size 100 × 100 × 100 mm were used for evaluating the compressive strength of concrete in accordance with IS 516-1959 [142]. The test was conducted using a compressive testing machine of capacity 2000kN. The load was applied constantly until the failure of the specimen. Then ultimate load on specimens was noted, and the compressive strength was calculated using equation 4.1. Three identical specimens were tested for each mix. The compressive strength was recorded by taking the average of three specimens with a variation not more than ±15% of the average.

$$CS = \frac{P}{bd} \qquad \text{Eq. (4.1)}$$

where, CS - Compressive strength

P - Maximum Load applied on to the specimen (Newton)

b - width of the specimen (mm)

d - depth of the specimen (mm)

4.5.2.3 Flexural strength

A Tinius Olsen testing machine with a capacity of 2000 kN was used to test the flexural strength of concrete specimens. A four-point bending test method was carried out on specimens of size 500×100×100 mm according to IS 516-1959 [142]. The load was applied constantly until the

complete failure of the specimen in two halves. Then, the ultimate load on specimens was noted, and the flexural strength was calculated using equation 4.2. Three identical specimens were tested for each mix, and their average was recorded as the flexural strength.

$$FS = \frac{Pl}{bd^2} \quad \text{Eq. (4.2.)}$$

where, FS - Flexural strength

P - Maximum Load applied on to the specimen (Newton)

l - length of the span on which the specimen was supported (mm)

b - width of the specimen (mm)

d - depth of the specimen at the point of failure (mm)

4.5.2.4 Split tensile strength

A compressive testing machine of capacity 2000 kN was used to test split tensile strengths of concrete. Cylindrical specimen of size 200 mm ×100 mm (heigh × diameter) was used for evaluating the split tensile strength of concrete in accordance with IS 5816-1999 [143]. Compressive load was applied axially on the line which is diametrically opposite. The load was applied constantly until the failure of the specimen. Then ultimate load on specimens was noted, and the split tensile strength was calculated using equation 4.3. Three identical specimens were tested for each mix and their average was recorded as the split tensile strength.

$$STS = \frac{2P}{\pi dl} \quad \text{Eq. (4.3.)}$$

where, STS- Split tensile strength

P - Maximum Load applied on to the specimen (Newton)

d - Diameter of the specimen (mm)

l - Height of the specimen (mm)

The compressive, flexural and split tensile strength tests conducted on alccofine-1203 based concrete mixes are shown in Figure 4.9.

4.5.2.5 Compressive stress-strain behavior

In accordance with ASTM C469 [144], uniaxial compression stress-strain behavior of concrete was evaluated on specimens of size 200×100 mm using a 2000 kN capacity compression testing machine. Under the load, the axial deformations developed in the specimens with respect to applied load was noted from the data acquisition system (DAC) by means of connected linearly varying displacement transducers (LVDTs) and load cell, as shown in Figure 4.10.

(a) (b) (c)

Figure 4.9 Test on alccofine-1203 based concrete mixes: (a) compressive strength, (b) split tensile strength, (c) flexural strength

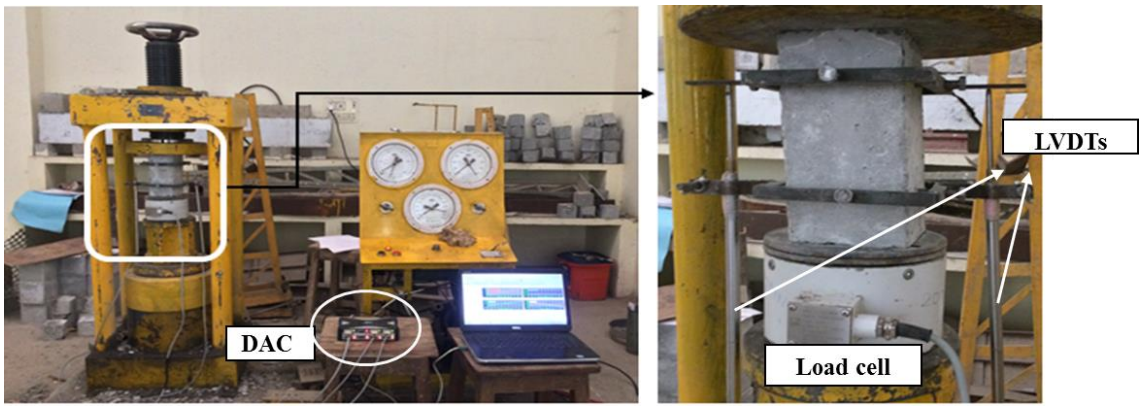

Figure 4.10 Test setup for concrete stress-strain behaviour under uniaxial compression

4.6 Results and Discussion

4.6.1 Effect of Alccofine-1203 on Binder

4.6.1.1 Standard consistency

The effect of alccofine-1203 incorporation on the standard consistency of the binder mixes was investigated and the test results are presented in Table 4.5. Standard consistency was reported as percentage of total binder weight. Before testing the binder for standard consistency, ordinary Portland cement was tested alone for standard consistency and it was found to be 29% of its weight whereas, standard consistency for the control mix binder was decreased to 26%. This was attributed to incorporation of fly ash. The spherical shape of fly ash particles reduces the development of internal frictional forces between binder particles during mixing and allows water to move freely between the binder particles to lubricate them easily. This made the Vicat's plunger movement easier at low water content [37]. On the other hand, incorporation of alccofine-1203 had very limited effect on standard consistency. There was no change in standard consistency for 4% and 6% replacement levels. But in case of 8%, 10%, 12% and 14%, a slight increase was noticed. It can be said that the standard consistency of alccofine-1203

based mixes may increase due to an increase in the percentage of fine alccofine-1203 particles in each binder mix. The increased fine particles of alccofine-1203 may require a little more water to get the standard consistency as more internal forces are likely to be develop during the mixing of the binder paste and also may be due to the irregular shape of alccofine-1203 particles. However, the standard consistency of all the developed binder mix proportions was found to be lower than the standard consistency of ordinary Portland cement.

Table 4.5 Standard consistency of the alccofine-1203 based concrete binder mixes

Mix designation	Standard consistency
M-C	26%
M-4%AF	26%
M-6%AF	26%
M-8%AF	26.5%
M-10%AF	27%
M-12%AF	27%
M-14%AF	27.5%

4.6.1.2 Initial setting time and final setting time

The effect of alccofine incorporation on initial setting time (IST) and final setting time (FST) of the binder mixes was investigated and the test results are graphically represented in Figure 4.11. The IST and FST of control mix binder was found to be higher compared to alccofine-1203 based binder mixes. The control mix binder had higher IST and FST because of 20% cement replacement with fly ash. In case of alccofine-1203 based binder mixes, with increasing percentage of alccofine-1203 from 4% to 14%, gradual decrease in IST and FST were observed at an average rate of 7.27% for an IST and 6.27% for FST compared to control mix binder. An increase in percentage of cement replacement with alccofine-1203, increases the percentage of calcium oxide and alumina oxide in the binder mixes, that attributed to the loss of plasticity of the paste at early stages by accelerating the hydration process of binder mixes. This led to the decrease in IST and FST of alccofine-1203 based mixes.

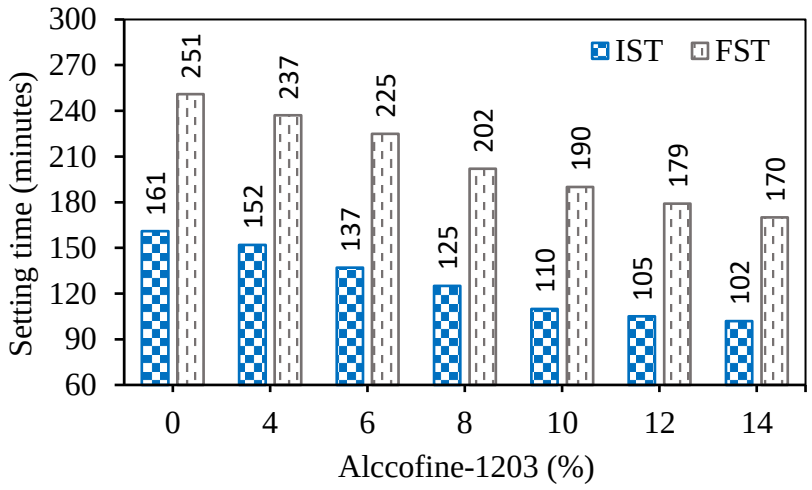

Figure 4.11 Influence of alccofine-1203 on IST and FST of binder of concrete mixes

4.6.2 Effect of Alccofine-1203 on Workability of Concrete Mixes

The measured slump values of alccofine-1203 based concrete mixes are graphically presented in Figure 4.12. According to the suggested range of workability of concrete in IS 456-2000 [133], a higher degree of workability was obtained for control mix and alccofine-1203 based concrete mixes. The replacement of cement with alccofine-1203 increased the workability of alccofine-1203 based concrete mixes compared to control mix. All the alccofine-1203 incorporated concrete mixes had higher slump values than control mix. The control mix exhibited a slump value of 120 mm. This can be attributed to replacing 20% of cement with fly ash. The glassy surface spherical shaped fly ash particles provide a lubricant effect that led to achieve a high degree of workability for the control mix without segregation [37,145,146]. Compared to control mix, at constant superplasticizer, water-binder ratio, and aggregate weights, the slump values of alccofine-1203 incorporated concrete mixes increased linearly with increasing percentage of alccofine-1203 incorporation from 4% to 12% [125]. The use of various percentages of alccofine-1203 along with 20% fly ash increases the specific surface area of particles of binder mixes due to the particle packing effect of alccofine-1203. Compared to cement, and fly ash particles, alccofine-1203 particles are highly fine with glassy surface characteristics up on partial replacement of cement with alccofine-1203, the specific surface area of binder mixes increases. Due to this the plasticity of fresh alccofine-1203 concrete mixes increases and allow the movement of constituent materials in the mix smoothly [50]. This attributed to achieve higher slump values for alccofine-1203 based concrete mixes without segregation and bleeding. The replacement of cement with 14% alccofine-1203 increased the cohesion of the concrete and exhibited a lower slump value than the mix with 12% alccofine-1203. It was also noticed that as the percentage of alccofine-1203 increased, cohesiveness

increased, and the setting time of concrete decreased. This attributed because of accelerated hydration process due to presence of more CaO in the alccofine-1203 based concrete mixes.

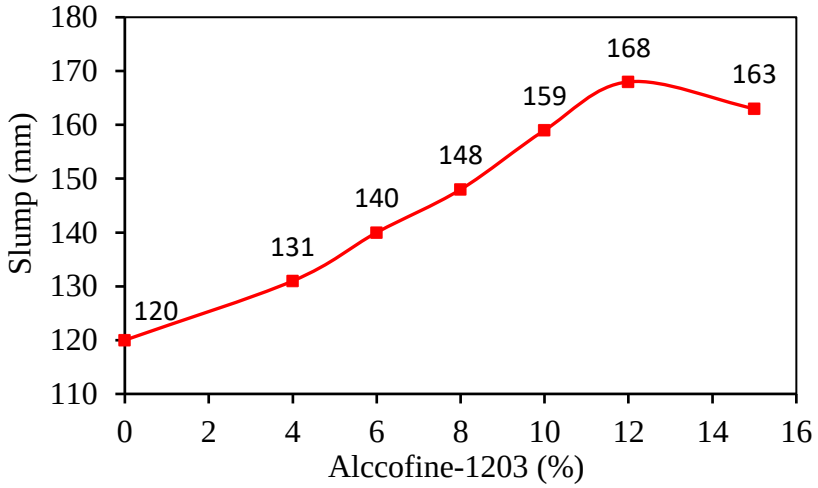

Figure 4.12 Influence of alccofine-1203 on workability of concrete

4.6.3 Strength Properties of Alccofine-1203 Based Concrete Mixes

4.6.3.1 Compressive strength

The compressive strength of alccofine-1203 incorporated concrete mixes was evaluated at 28-days curing age and the test results are presented in Table 4.6. The control mix exhibited a compressive strength of 68.33 MPa upon replacing 20% of cement with fly ash. The reaction between the silica in fly ash and Portlandite at later stages of the curing of concrete led to the formation of more calcium-silicates-hydrated (C-S-H) gel to impart higher strength to concrete [147]. It was observed from the test results that all the alccofine-1203 based concrete mixes exhibited higher compressive strength compared to the control mix. The replacement of cement with alccofine-1203 was beneficial up to 10%, and further, for 12% and 14% replacement levels, a fall in strength was observed compared to the mix with 10% alccofine-1203 [148]. The percentage increase in the compressive strength of alccofine-1203 based concrete mixes with respect to control mix is presented in Table 4.7. The reason for the increase in the compressive strength of concrete mixes with increasing alccofine-1203 percentages may be due to the formation of an additional C-S-H gel network in the cementitious matrix as a result of the hydration of cement along with pozzolanic reactions of both fly ash and alccofine-1203. Ultra-fine particles of alccofine-1203 have a unique chemical composition, so its inclusion led to the formation of a dense matrix structure in concrete [129]. As alccofine-1203 comprise nearly 30% of CaO, the pozzolanic reaction of alccofine-1203 develops aluminates and silicates of calcium as Portlandite. The resulting Portlandites then react with silica in fly ash to provide an

additional C-S-H gel to achieve high strength in concrete [149]. The reduction in compressive strength for concrete mixes with 12% and 14% alccofine-1203 was observed. This may be attributed to the unsoundness of binder mixes caused by an increase in unreacted calcium oxide (CaO), alumina oxide (Al_2O3), and magnesium oxide (MgO), which upon the hydration process resulted in excessive expansion and micro-cracks in the concrete and showed lower resistance against compression load [37]. From the test results, it was evident that the replacement of cement with alccofine-1203 in combination with fly ash does not have a negative influence on achieving higher strength in concrete. Particularly, though 34% of cement was replaced with 14% of alccofine-1203 and 20% of fly ash, an HSC of compressive strength 72.27 MPa was achieved at the 28 days curing period. The failure of specimens tested for compressive strength evaluation is shown in Figure 4.13. The failure mode of specimens is explained in Chapter 5.

4.6.3.2 Flexural strength

The flexural strength results of alccofine-1203 incorporated concrete mixes evaluated at 28-days curing age are presented in Table 4.6. From the test results, it was observed that the flexural strength of concrete specimens follows a similar pattern as the compressive strength. The percentage increase in the flexural strength of alccofine-1203 concrete mixes in comparison to the control mix is presented in Table 4.7. Alccofine-1203 based concrete mixes exhibited higher flexural strengths than the control mix and the highest improvement was achieved with the mix with 10% alccofine-1203. The increase in flexural strength to alccofine-1203 incorporated concrete mixes may be attributed to the development of a strong bond (interfacial transition zone) between aggregates and paste because of the combination of the hydration process of cement and pozzolanic reactions of both alccofine-1203 and fly ash [150]. As expected, mixes with 12 and 14% alccofine-1203 exhibited lower flexural strength than the mix with 10% alccofine-1203 [124]. This behavior can be attributed to the development of macro and nano cracks inside the binder paste which is due to the presence of free lime and magnesia in the binder. The failure of flexural specimens occurred by opening a single crack in the loading span along the depth of the specimens. The specimens which failed under flexural strength test are shown in Figure 4.13. The failure mode of the flexural specimens is explained in Chapter 5.

4.6.3.3 Split tensile strength

The effect of incorporation of alccofine-1203 on the split tensile strength of concrete mixes was evaluated at 28-days curing age, and test results are tabulated in Table 4.6. The split tensile strength of concrete mixes was found to be similar to the compressive strength and flexural strength results. All the alccofine-1203 concrete mixes exhibited higher split tensile strength

compared to the control mix. The increase in the percentage of split tensile strength of alccofine-1203 based concrete mixes in comparison to control mix is presented in Table 4.7. The mix with 10% alccofine-1203 exhibited higher split tensile strength, and up to10% replacement of cement with alccofine-1203 showed a gradual increase in split tensile strength but for 12% and 14% replacement levels, decrease in strength was noticed compared to the mix with 10% alccofine-1203 [125]. All the test specimens cracked at the middle before attaining ultimate load and split into two parts immediately after attaining the ultimate load. The specimens that are failed under split tensile strength test are shown in Figure 4.13, and the failure mode of the specimens is explained in Chapter 5.

Table 4.6 Strength properties of alccofine-1203 based concrete mixes

Mix designation	Compressive Strength (MPa)	Flexural Strength (MPa)	Split Tensile Strength (MPa)
M-C	68.33	5.27	5.01
M-4%AF	69.47	5.61	5.18
M-6%AF	74.13	5.70	5.31
M-8%AF	76.20	5.85	5.47
M-10%AF	80.33	6.22	5.81
M-12%AF	77.35	6.02	5.49
M-14%AF	72.27	5.65	5.13

Table 4.7 Percentage increase in strength properties of alccofine-1203 based concrete mixes compared to control mix

Mix designation	Compressive Strength	Flexural Strength	Split Tensile Strength
M-C	-	-	-
M-4%AF	1.67	6.45	3.39
M-6%AF	8.49	8.16	6.00
M-8%AF	11.52	11.01	9.18
M-10%AF	17.56	18.03	15.97
M-12%AF	13.20	14.23	9.58
M-14%AF	5.77	7.21	2.40

(a) Compressive strength (b) Flexural strength (c) Split tensile strength

Figure 4.13 Failure pattern of alccofine-1203 incorporated concrete specimens

4.6.3.4 Uniaxial compressive stress-strain behavior

The compressive stress-strain curves of alccofine-1203 incorporated concrete mixes are drawn for the data collected from the DAC system. As shown in Figure 4.10, two LVDTs were connected to the test specimen by means of steel frames to record the longitudinal deformation under the compression load. The load applied to the specimen was recorded in the DAC system by means of a connected load cell of 200 MN capacity. From the DAC, the longitudinal deformations developed in concrete specimens with respect to the applied load were used to calculate the strains and stress to draw the compressive stress-strain curves. For each specimen, the average of two LVDT's longitudinal deformations were considered to measure the strains. The data obtained for each specimen was considered to plot the stress-strain curve for each mixture and is shown in Figure 4.14. The load on specimen increased at a higher rate in the initial stages up to 75% of its ultimate load and up to the ultimate load, the rate of increase in load was slow. The test on specimen continued until load dropped by 60-65% of the ultimate load. During the test it was observed that the vertical cracks distributed around the specimens were noticed on the specimen with increase in the load. The cracks propagated from the bottom phase to the top phase of the specimen with further increase of load. The initial cracks on the specimens appeared at around 80-85% of the ultimate load. Crack propagation and crack width increased after the ultimate load. The rate of decrease of load after the peak (in descending portion of stress-strain curve) was faster due to rapid crack growth. This led to the failure of the specimen once it reached its maximum failure strain.

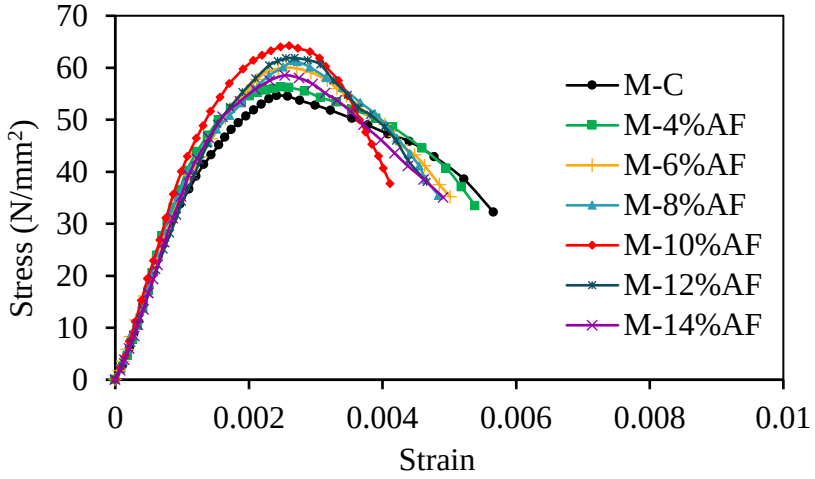

Figure 4.14 Compressive stress-strain behavior of alccofine-1203 based concrete mixes

4.6.3.5 Young's modulus

Young's modulus is one of the key parameters for assessing the properties of concrete material and plays a significant role in the analysis and design of concrete structure. Young's modulus is a useful indicator of the concrete ability to experience elastic deformation in a concrete structure. Young's modulus of concrete increases by decreasing water-cement ratio and increase in maximum nominal size of aggregate to a certain limit; therefore, HSC has a higher Young's modulus than NSC [151].

Due to the enhancement in compressive strength of concrete by addition of alccofine-1203, the change in Young's modulus of concrete mixes has been analyzed and it was determined according to ASTM C469 standards [144]. From the experimental compressive stress-strain curves, Young's modulus was determined as secant modulus, that is ratio of stress to strain at stress equal to 40% of compressive strength of concrete. The calculated experimental Young's modulus values of alccofine-1203 based concrete mixes graphically represented in Figure 4.15. Compared to control mix, alccofine-1203 based mixes have higher Young's modulus except the mix with 12% replacement. The percentage increase in Young's modulus with respect to control mix was 2.91%, 3.23%, 8.66%, 11.09%, and 0.45% for replacements of 4%, 6%, 8%, 10% and 14% respectively. The Young's modulus values may increase due to the strong interfacial transition zone between aggregates and cement paste and the presence of unreacted fly ash particles which may act as fine aggregate [152].

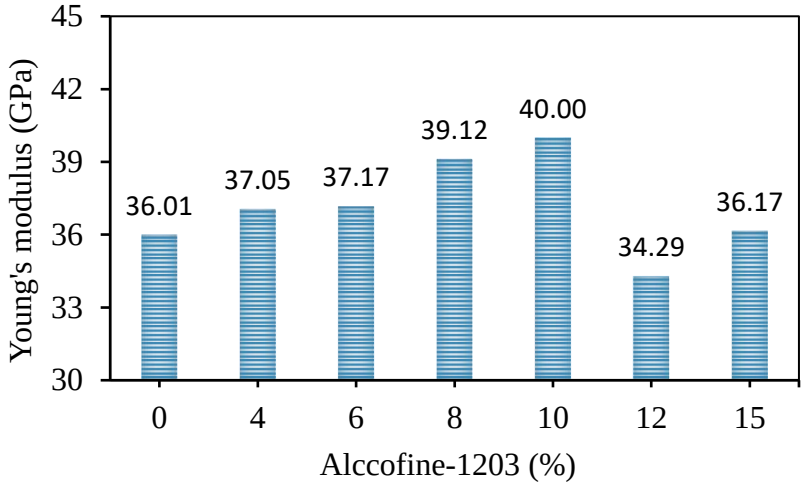

Figure 4.15 Young's modulus of alccofine-1203 based concrete mixes

4.6.3.6 Energy absorption capacity

From Figure 4.14, it can be observed that as alccofine-1203 replacement levels increased from 4% to 10%, the compressive strength and compressive strains increased. A large linear portion

of stress-strain curves achieved as alccofine-1203 replacement levels increased. This indicates the increase in brittleness of concrete. To understand this behaviour, EAC of the all the mixes were analysed. Generally, EAC of concrete specimens was measured as the area under the load-deflection curve. The same method was adopted in this study to evaluate the EAC of concrete from the stress-strain curves of specimens of alccofine-1203 based concrete mixes. The determined EAC is graphically presented in Figure 4.16. The obtained result shows that alccofine-1203 based concrete mixes had lower EAC than the control mix. The replacement of cement with 4% to 14% of alccofine-1203 increased its compressive strength, but it also increased its brittleness. Due to this, the deflection behavior of concrete specimens after attaining ultimate load was decreased. Eventually, this behavior led to a decrease in the area under the stress-strain curves. The percentage of decrease in EAC with respect to 4%, 6%, 8%, 10%, 12% and 14% replacement of cement with alccofine-1203 was approximately 1.61%, 5.45%, 7.72%, 17.70%, 11.35% and 10.28%, respectively. It can be seen that at a 10% replacement, the specimens showed lowest EAC than that of control mix and other alccofine-1203 based mixes. This was due to brittleness of the concrete mix, the specimens developed lowest area under the stress-strain curve.

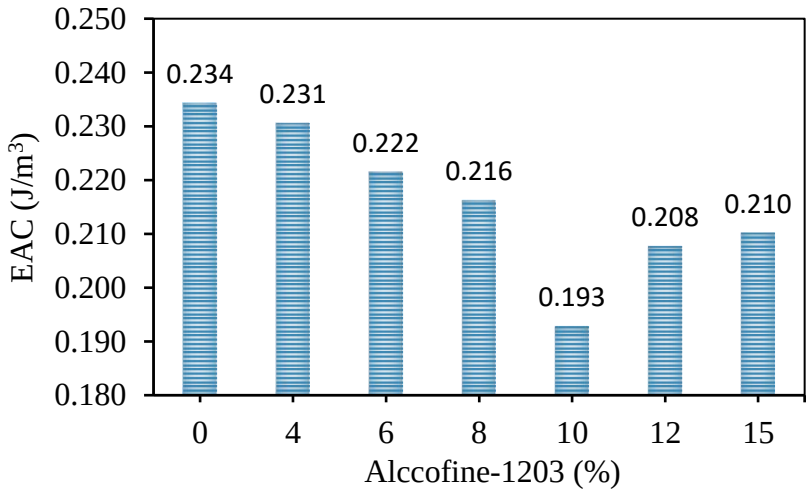

Figure 4.16 Energy absorption capacity of alccofine-1203 based concrete mixes

4.6.4 Microstructural Analysis

The effect of alccofine-1203 incorporation on the behaviour of binder mixes was investigated at the microstructure level using SEM and energy dispersive spectroscopy (EDS). The secondary electron imaging method was adopted for SEM analysis. After finding the standard consistency of each binder mix, the prepared pastes were then filled in 50 mm size cube moulds and compacted well with the help of a trowel. A total of seven cubes were prepared and cured

in water until the test age of 28 days. After the curing period, specimens were taken out of the water and air-dried to get the surface-dry condition. Then, the cubes were broken into approximately small samples and oven-dried for 2 h at 110 °C to remove any excess moisture present. The samples thus prepared were used for SEM and EDS analysis.

4.6.4.1 SEM observation

From the oven-dried samples, a suitable one was selected for each mix for the SEM and EDS analysis. The SEM image of all the mix binders is shown in Figure 4.17a-g. SEM images showed micro-cracks, nonreactive fly ash particles, and voids in all mix binders. From the SEM images, calcium hydroxide was found as one of the major compounds with a crystalline structure in all the mix binders. Calcium hydroxide may have formed in all mix binders because of the hydrolysis processes of calcium and silicates present in the binder constituents after a few hours of hydration process. As observed from the SEM images, the solid phase of the binders consists of calcium hydroxide mainly in the form of Portlandite at the early stages of the hydration process. Portlandite is present in hexagonal crystal shape in the form of columns and plates, as seen in Figure 4.17a-g. It was observed from SEM images that Portlandite structures were numerous in the case of alccofine-1203 based binder mix. This could've occurred due to the pozzolanic reaction of alccofine-1203 with tricalcium silicates and dicalcium silicates in cement. In case of alccofine-1203 based binder mixes, the formation of stratlingites was observed. The Portlandite and stratlingite crystals are upon reaction with silica in fly ash turned into a honeycomb structure called C-S-H gel at the lateral stages of the hydration process to impart maximum strength to concrete [153]. For this reason, all alccofine-1203 based mixes may have higher strength compared to the strength of control mix. The stratlingite structure formed in alccofine-1203 concrete mix binders had aluminium as primary composition, and this may have resulted due to the availability of higher amount of alumina in alccofine-1203. Stratlingite is also known as hydrated Gehlenite. It is identified as one of the mineral compositions in alccofine-1203. Due to the maturation of the hydration process and pozzolanic reaction of all binder mixes, alccofine-1203 based mix binders had massive C-S-H gel characteristics that led achieve higher strength compared to control mix [154]. It was observed from SEM images that binder mix with 12% and 14% alccofine-1203 had more micro-cracks. On loading, these microcracks in the specimens propagated into major cracks and offered lower resistance to the applied load, may be because of which, a reduction in strengths was observed.

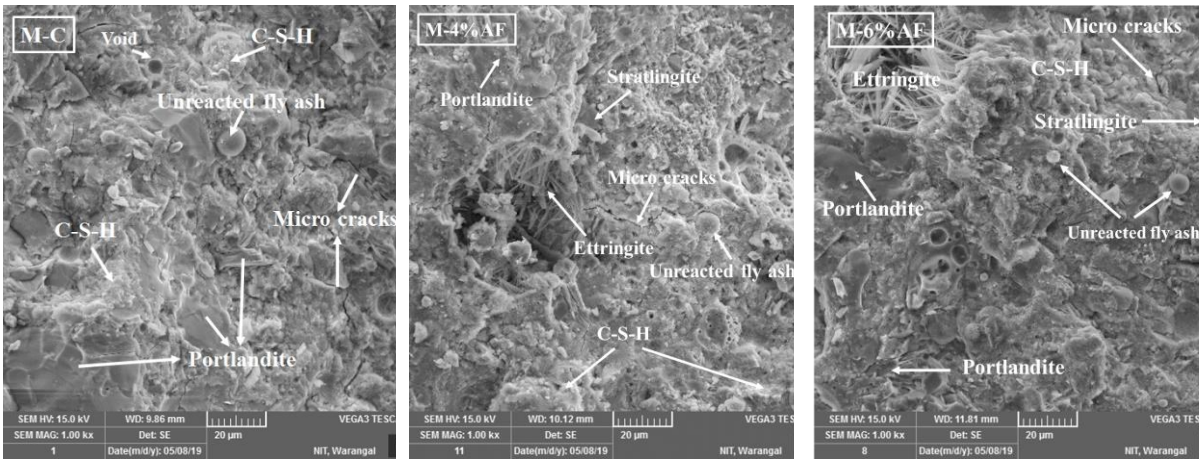

(a) Control mix (b) Alccofine-1203 (4%) (c) Alccofine-1203 (6%)

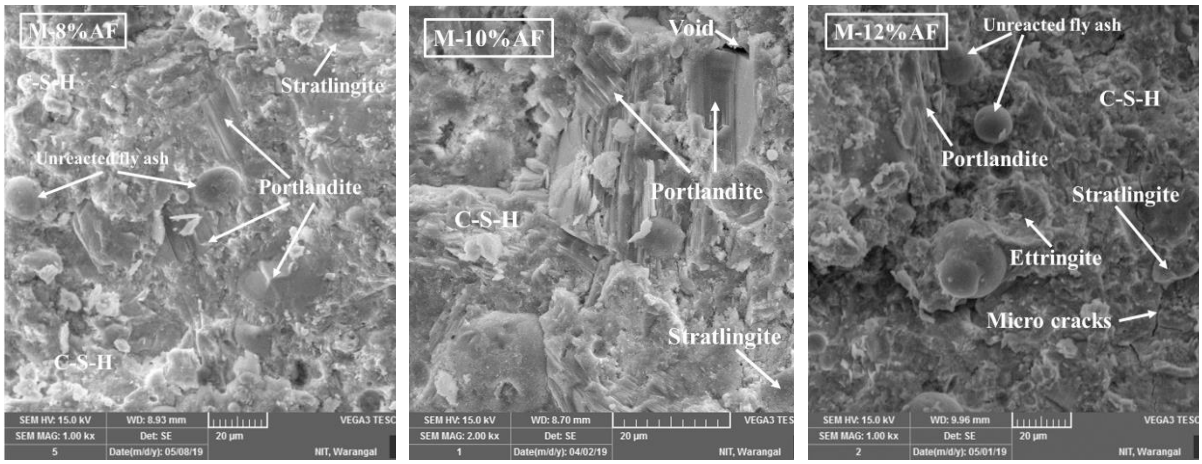

(d) Alccofine-1203 (8%) (e) Alccofine-1203 (10%) (f) Alccofine-1203 (12%)

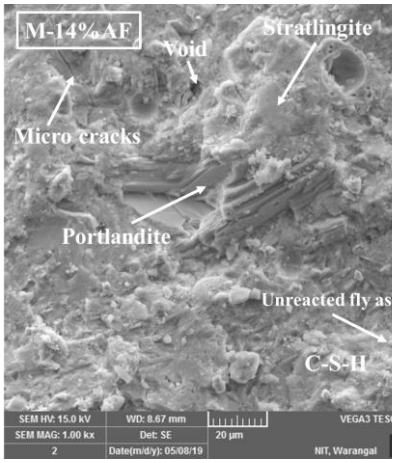

(g) Alccofine-1203 (14%)

Figure 4.17 SEM images of alccofine-1203 incorporated concrete binder mixes

4.6.4.2 Energy dispersive spectroscopy analysis

The EDS analysis for each binder mix is shown in Figure 4.18a-g. The quantification of the atomic percentage of elements present in each binder is tabulated in Table 4.8. To quantify C-S-H gel formation in each mix binder, the atomic Ca/Si ratio was performed using atomic

percentages of Ca and Si obtained from the EDS analysis. Based on the results of the atomic Ca/Si ratio, the control mix had a Ca/Si ratio of 2.87, whereas alccofine-1203 based binder mixes had atomic Ca/Si ratios of 2.56, 2.32, 1.77, 1.26, 2.23, and 2.37 with respect to 4%, 6%, 8%, 10%, 12%, and 14% alccofine-1203 replacement levels. Compared to all other mixes, mix M-10%AF had a low atomic Ca/Si ratio of 1.26 and exhibited a high compressive strength of 80.33 MPa, whereas the control mix had a high atomic Ca/Si ratio of 2.87 and showed a low compressive strength of 68.33 MPa. Based on these results, it can be concluded that the lower the atomic Ca/Si ratio, the better the C-S-H gel formation; therefore, the higher the compressive strength of concrete. Similarly, the higher the atomic Ca/Si ratio, the lower the C-S-H gel formation, thereby lowering the compressive strength of concrete. This analysis was done according to the classification given by researchers [150].

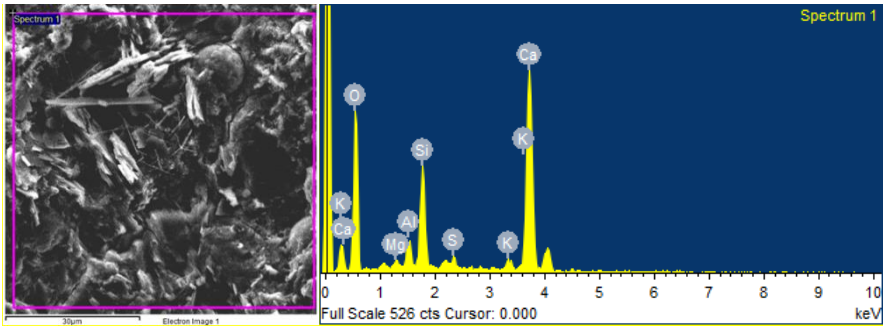

(a) Control mix

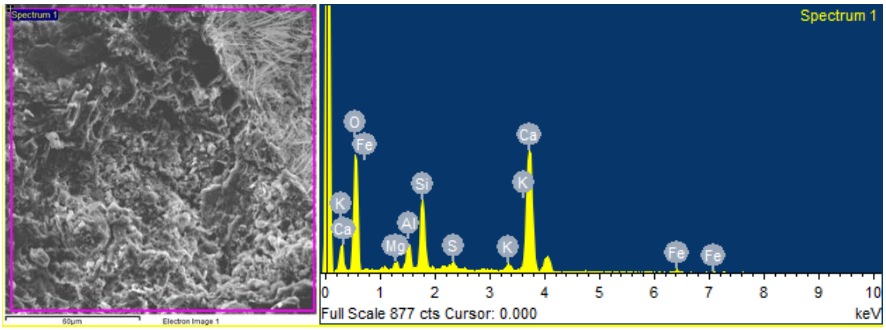

(b) Alccofine-1203 (4%)

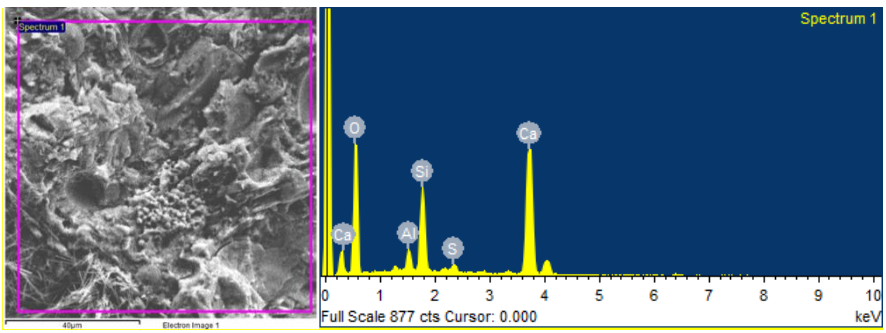

(c) Alccofine-1203 (6%)

Figure continues...

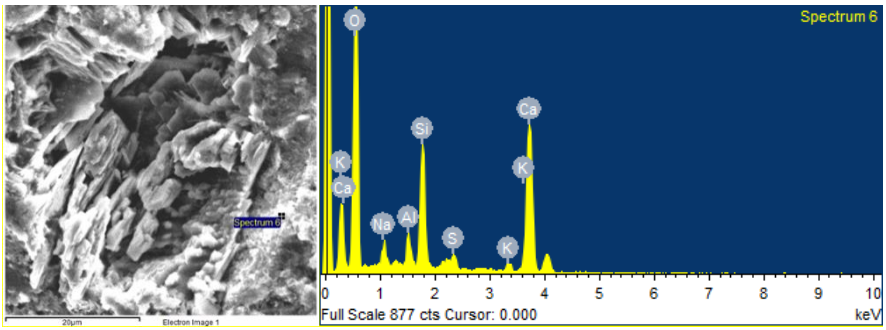

(d) Alccofine-1203 (8%)

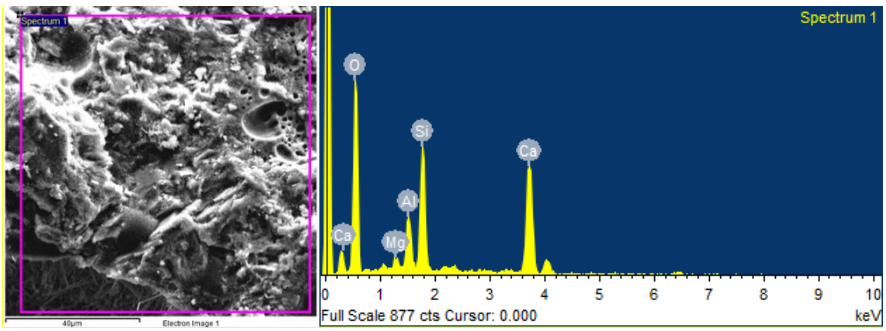

(e) Alccofine-1203 (10%)

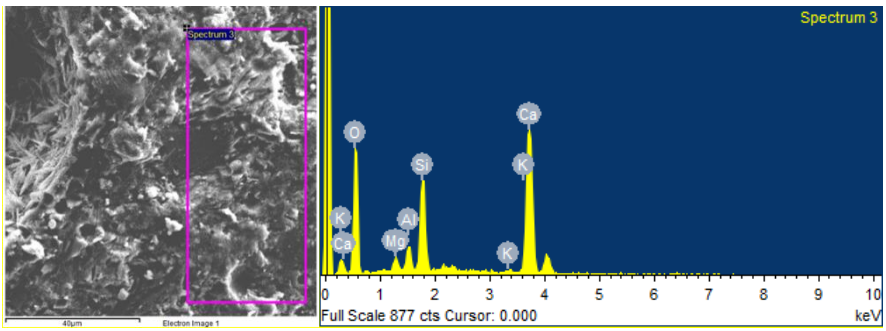

(f) Alccofine-1203 (12%)

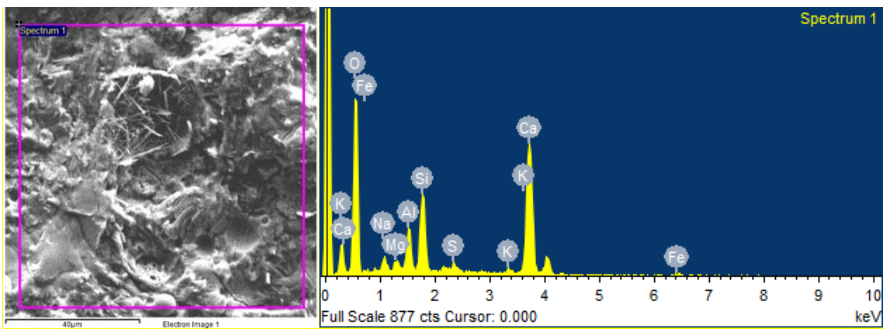

(g) Alccofine-1203 (14%)

Figure 4.18 EDS analysis of alccofine-1203 incorporated concrete binder mixes

Table 4.8 Atomic percentage of elements present in alccofine-1203 incorporated concrete binder mixes

Elements	Atomic % of elements according to mixes						
	M-C	M-4%AF	M-6%AF	M-8%AF	M-10%AF	M-12%AF	M-14%AF
O	74.29	74.93	76.84	81.39	77.07	73.77	76.43
Na	-	-	-	1.60	-	-	1.28
Mg	0.54	0.62	-	-	0.80	0.85	0.72
Al	1.59	1.97	1.56	1.16	3.30	1.76	2.62
Si	5.78	5.76	6.32	5.33	8.30	7.21	5.22
S	0.53	0.55	0.59	0.58	-	-	0.35
K	0.69	0.67	-	0.46	-	0.30	0.46
Ca	16.59	14.79	14.70	9.47	10.53	16.11	12.40
Fe	-	0.71	-	-	-	-	0.52

4.7 Conclusions

The viability of developing HSC by partial replacement of cement with various percentages of alccofine-1203 in combination with 20% fly ash was studied in this chapter. First, the effect of alccofine-1203 on the standard consistency and setting times (IST and FST) of binder mixes was investigated. Following that, the effect of alccofine-1203 on workability, compressive strength, flexural strength, split tensile strength, and compressive stress-strain behavior was investigated. SEM and EDS analysis were performed to evaluate the effect of alccofine-1203 incorporation on the internal microstructural behavior of binder mixes and to correlate the strength characteristics of concrete mixes. Based on the results presented, the conclusions drawn from the present chapter are:

- The use of alccofine-1203 with a combination of fly ash in the development of HSC was found to be advantageous.
- The standard consistency of the control mix binder was slightly increased by the partial replacement of 8%, 10%, 12%, and 14% of cement with alccofine-1203. This could be due to the increased surface area of binder particles of control mix as the percentage of alccofine-1203 increases.
- The IST and FST of the binder mixes decreased as the percentage of cement replaced with alccofine-1203 increased. This may be due to the increase of calcium and alumina in binder mass as a result of alccofine-1203 percentage increment in binder mixes.

- ❖ At constant superplasticizer dosage, water-binder ratio and aggregate weight, partial replacement of cement with alccofine-1203 increased the workability of concrete mixes.
- ❖ The 10% replacement of cement with alccofine-1203 yielded highest strength properties for HSC compared to other replacement levels. The beneficial effect of alccofine-1203 began to weaken after 10% incorporation.
- ❖ The peak-stress and strain at peak-stress of the alccofine-1203 based mixes were increased with increase in percentage of cement replacement with alccofine-1203. Compared to control mix, the highest peak-stress and strain at peak-stress were obtained to a mix with 10% alccofine-1203. As a result of this the mix had highest Young's modulus than the other mixes.
- ❖ The increase in compressive strength of concrete decreased its EAC due to decrease in area under the stress-strain curve. The mix with 10% alccofine-1203 showed lower EAC due to highest peak-stress and strain at peak-stress and lowest failure strain than the other mixes.
- ❖ The increase in percentage of alccofine-1203 incorporation increased formation of C-S-H gel; the mix with 10% alccofine-1203 showed dance core structure.
- ❖ The Ca/Si ratio decreased with increase in percentage of replacement of cement with alccofine-1203. The mix with 10% alccofine-1203 had lowest Ca/Si ratio, that signifying the development of high strength to concrete.
- ❖ The results of the investigation provide ample scope for developing HSC by replacement of cement with 10% alccofine-1203 and 20% fly ash combination that leads to the development of sustainable construction materials. With this, the cost of producing HSC will be reduced.

Chapter 5

Experimental, Microstructural, and Analytical Studies on PVAFRC and BFRC

5.1 General

This chapter presents the results of experimental and analytical studies carried out on PVA fiber reinforced concrete (PVAFRC) and basalt fiber reinforced concrete (BFRC) of M30 and M70 grade. The aim of the present phase of the research work is to find the optimum percentage of PVA fibers and basalt fiber based on the strength properties and compressive stress-strain behaviour of various PVAFRC and BFRC mixes. The present chapter is divided into two parts, Part A and Part B. Part A presents the study on PVAFRCs, and Part B presents the study on BFRCs. The experimental evaluation of the study includes workability, compressive strength, flexural strength, split tensile strength, and load-deflection, and compressive stress-strain curve behavior. The analytical evaluation of the study includes Young's modulus, EAC, peak-stress, and strain at peak-stress. In addition to this, a modified constitutive analytical model and relationships developed for properties of stress-strain curves such as peak-stress, strain at peak-stress and material parameter with modified reinforcing index (MRI) values of fibers are presented for analytical modelling of compressive stress-strain curves of PVAFRCs and BFRCs. Furthermore, to study the microstructural characteristics and to correlate the strength properties of PVAFRC and BFRC mixes, SEM analysis was performed. The research work presented in the present phase (Phase-II) was carried out based on the strength criteria, considering the parameters as various volume percentages of PVA fibers and basalt fibers and two grades of concrete, i.e., M30 and M70. The optimum percentage of alccofine-1203 obtained from the Phase-I of the research work was used to develop HSC of M70 grade in the present Phase. The details of constituent materials used, physical properties and percentages of PVA fibers and basalt fibers used, mix proportions, preparation of mixes and cast of specimens, test methods and discussion of obtained results are presented in the following sections with respect to PVAFRCs (Part A) and BFRCs (Part B).

5.2 Part A: Study on PVA Fiber Reinforced Concretes (PVAFRCs)

5.2.1 Materials Used for the Development of PVAFRCs

The constituent materials used for the development of PVAFRCs are in accordance with the Bureau of Indian standards. The constituent materials used for the development of HSC in Phase-I of the research work were the same used for the development of PVAFRCs of M30 and

M70 grades. Ordinary Portland cement (OPC) of 53 grade, class-F fly ash, and alccofine-1203 were used as binder materials. Natural river sand confirming to Zone-II was used as fine aggregates, and crushed granite of maximum size 16 mm was used as coarse aggregates. Masterglenium SKY-8233, a polycarboxylic ether based high-performance superplasticizer was used to enhance the workability of concrete. The filament type kuralon (REC15) PVA fibers of length 12 mm and diameter of 40 μm, shown in Figure 5.1, are used for the development of PVAFRCs. The properties of PVA fibers are presented on Table 5.1.

Figure 5.1 PVA fibers

Table 5.1 Properties of PVA fiber

Properties	**Details**
Diameter	0.04 mm
Density	1290 kg/m^3
Tensile strength	1600 N/mm^2
Length	12 mm
Aspect ratio	300
Specific gravity	1.26
Fiber type	Filament
Elongation (%)	7

5.2.2 Mix Proportions and Mixes of PVAFRCs

The present investigation on PVAFRCs includes development of NSC of M30 grade and HSC of M70 grade. The optimum percentage of alccofine-1203 to replace cement with a 20% fly ash combination was adopted from Phase-I of the research work to develop HSC. The mix proportion for NSC developed according to concrete mix proportioning guidelines given in IS 10262-2019 [137]. In this study, plain concrete (PC) with a cube compressive strength of 38.57 MPa was considered as NSC of M30 grade and PC with a cube compressive strength of 80.33MPa was considered as HSC of M70 grade. The mix proportion of NSC and HSC are

given in Table 5.2. Based on the compressive strength of PC, two mix proportions are named PVAFRC30, and PVAFRC70, where 30 and 70 stands for the grade of concrete. PVA fibers were added to each grade at 0%, 0.1%, 0.2%, 0.3%, 0.4% and 0.5% of the total volume of concrete. Therefore, a total of 10 PVAFRC mixes and 2 PC mixes were developed to evaluate the engineering properties and stress–strain behaviour of concretes. The constituent material quantities, mix proportions and mix designations of all the developed mixes are shown in Table 5.2. In the given mix designation, first term stands for strength of the concrete and second term stands for volume percentage of fibers added. For example, in N-0.1PVA, N stands for NSC and 0.1PVA stands for addition of 0.1% PVA fibers, and similarly, in H-0.1PVA, H stands for HSC and 0.1PVA stands for addition of 0.1% PVA fibers. In both PVAFRC30 and PVAFRC70, mixes with 0% PVA fibers was considered control mix or PC mix. In the mix design of PVAFRC30, 25% of cement replaced with class-F fly ash. In the mix design of PVAFRC70, 30% of cement replaced with 10% alccofine-1203 and 20% class-F fly ash. The percentage of superplasticizer dosage given in Table 5.2 is to the total weight of the total binder (600 kg/m^3 for HSC and 450 kg/m^3 for NSC) of each mix.

Table 5.2 Mix proportions, mix designations and constituent materials quantities for PVAFRCs

Grade of concrete	**Mix designation**	**PVA fiber (%)**	**Mix proportion**	**Constituent material (kg/m^3)**					**w/b ratio**	**SP**
				Binder material			**FA**	**CA**		
				OPC	**Fly ash**	**AF-1203**				
PVA FRC30 (Normal strength PVAFRC)	N-0PVA	0	1:1.81:2.57	315	105	-	760	1080	0.4	0.25%
	N-0.1PVA	0.1								
	N-0.2PVA	0.2								
	N-0.3PVA	0.3								
	N-0.4PVA	0.4								
	N-0.5PVA	0.5								
PVA FRC70 (High strength PVAFRC)	H-0PVA	0	1:1.22:1.58	420	120	60	730	950	0.26	0.725%
	H-0.1PVA	0.1								
	H-0.2PVA	0.2								
	H-0.3PVA	0.3								
	H-0.4PVA	0.4								
	H-0.5PVA	0.5								

w/b-water to binder ratio, SP-Superplasticizer, AF-1203-Alccofine-1203, FA-Fine aggregates, CA-Coarse aggregate

5.2.3 Mixing, Cast, and Curing of PVAFRC Specimens

The guidelines given in IS 456-2000 [133] were followed for concrete mixing. Before mixing concrete, aggregates were prepared for the saturated dry surface condition. Initially, binder materials, fine aggregates, and coarse aggregates were mixed in a 100 kg pan mixer for 60 seconds. Half of the measured water was added to the dry mix and mixed for 30 seconds. In the remaining water, a fixed quantity of superplasticizer was mixed thoroughly and then transferred to the wet mix and allowed to be mixed for another 60 seconds. Then, the pre-weighed PVA fibers were added to the wet concrete mix, as shown in Figure 5.2, and allowed the fibers to mix uniformly into the concrete. The mixing time of fibers into the concrete increased as the weight of PVA fibers increased. The vibrating table was used to ensure good compaction of concrete in the iron moulds. All test specimens were demoulded after the cast of 24 hours and kept in water for curing for 28 days and then tested.

Figure 5.2 PVA fibers mixing into wet concrete

5.2.4 Test Specimens and Methods for PVAFRCs

5.2.4.1 Workability

According to IS 1199 (Part 2)-2018 [141], the slump cone test was performed to measure the workability of the PVAFRC mixes, as shown in Figure 5.3(a).

5.2.4.2 Compressive strength

Cube specimens of size 100×100×100 mm were used for evaluating the compressive strength of PVAFRCs in accordance with IS 516-1959 [142]. The test was conducted using a compressive testing machine of capacity 2000 kN. During the test, a constant load was applied until failure of the specimens occurs. Then ultimate load on specimens was noted, and the compressive strength was calculated using equation 4.1 given in Phase-I of the research work.

Three identical specimens were tested for each mix. The compressive strength was recorded by taking average of three specimens with a variation of not more than ±15% of the average. Testing of cube specimen for compressive strength is shown in Figure 5.3(b).

5.2.4.3 Flexural strength and load-deflation behavior

The flexural strength and load–deflection behaviour of PVAFRCs was evaluated by a four point bending test method on the specimens of size 500×100×100 mm in accordance with IS 516-1959 [142]. The test was conducted using a universal testing machine of capacity 200 kN. The deflections developed in the flexural specimens with respect to applied load were noted from the DAC system using an LVDT and a load cell, shown in Figure 5.3(c). A constant load was applied until failure of the specimens occurs. Then ultimate load on specimens was noted, and the flexural strength was calculated as per equation 4.2 given in Phase-I of the research work. Three identical specimens were tested for each mix and their average was taken as the flexural strength.

5.2.4.4 Split tensile strength

The split tensile strength of PVAFRCs was evaluated on cylindrical specimens of size 200×100 mm (height × width) according to IS 5816-1999 [143]. A compressive testing machine of capacity 2000 kN was used for split tensile strength testing. Load was applied constantly until the specimen lost resistance against the applied load. Then, the ultimate load on specimens was noted, and the split tensile strength was calculated as per equation 4.3 given in Phase-I of the research work. Three identical specimens were tested for each mix, and their average was taken as the split tensile strength. Testing of cylindrical specimen for split tensile strength is shown in Figure 5.3(d).

5.2.4.5 Compressive stress-strain behavior

The compressive stress-strain behavior of PVAFRCs under uniaxial compression was evaluated on 200 × 100 mm (height × diameter) size specimens in accordance with ASTM C469 [144]. Under the load, the axial deformations developed in the cylindrical specimens with respect to applied load were noted from the DAC system using LVDTs and a load cell, as shown in Figure 5.3(e).

(a) Slump

(b) Compressive strength

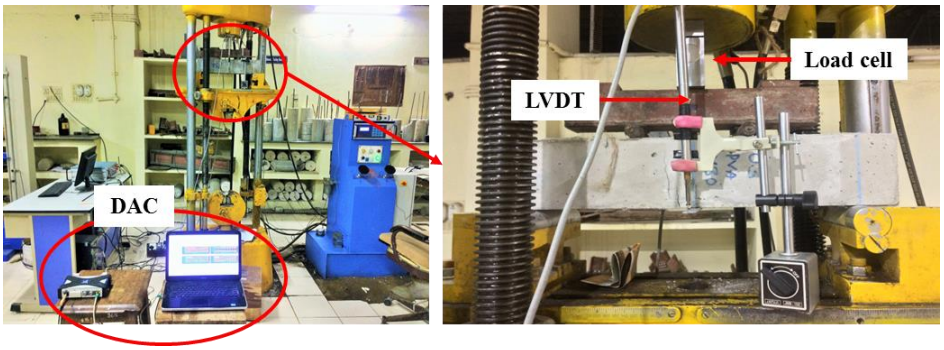

(c) Flexural strength and load-deflection behaviour

(d) Split tensile strength

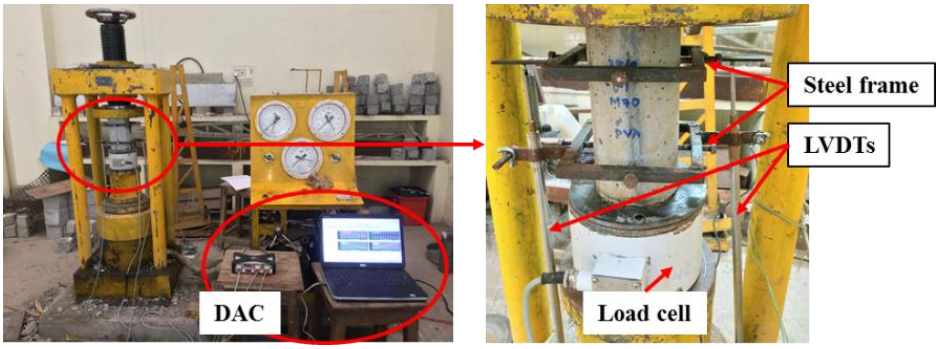

(e) Compressive stress-strain behaviour

Figure 5.3 Tests on PVAFRC mixes

5.2.5 Results and Discussions of PVAFRCs

5.2.5.1 Workability

The slump cone test results of PVAFRC30 and PVAFRC70 mixes are shown in Figure 5.4. It is well known that the use of fibers intrinsically influences the workability and flowability of concrete [155]. At a given water-to-binder ratio and superplasticizer dosage, compared to the control mix, the increase in the percentage of PVA fiber additions decreased the slump value of all the mixes of PVAFRC30 and PVAFRC70 [72]. The addition of 0.1% of PVA fibers mixed into concrete homogeneously, and no balling effect was observed in N-0.1PVA and H-0.1PVA mixes. In the case of PVAFRC70, the addition of 0.2% of PVA fibers took some time to mix properly into the concrete to obtain a uniform consistency. Further, the mixing time of fibers into concrete slightly increased with the addition of 0.3% PVA fibers, and a decrease in water content was observed during mixing compared to the previous mix due to the water absorption property of PVA fibers. Furthermore, the addition of 0.4% fibers led to the development of balling effect, and it took extra time to mix into concrete, and a further decrease in water content was observed compared to the previous mix. This effect was severe on the further addition of 0.5% PVA fibers. Similar to PVAFRC70 mixes, in the case of PVAFRC30 mixes also, the addition of 0.2% of PVA fibers took some time to mix properly into the concrete and decreased workability of concrete. The development of a minor balling effect was observed for 0.3% PVA fibers addition due to fibers absorbing water from the mix during concrete mixing. This effect increased when 0.4% of PVA fibers was added and severe on further addition of 0.5% PVA fibers. The balling effect of PVA fibers was dominant in the case of mixes N-0.4PVA, N-0.5PVA, H-0.4PVA, and H-0.5PVA. This led to difficulty in mixing and resulted in the lowest slump values. Regardless of the grade of PVAFRCs, the decrease in workability of concrete with increasing percentage of PVA fibers additions was attributed to void increment in mixes caused by PVA fiber intrusion and hydrophilia of PVA fibers leading to absorption of water from the mix resulting from the large surface area of PVA fibers [156]. This led to the formation of a fiber network-like structure in the mixes, which prevented the mix from segregating and flowing. In literature, Noushini et al. 2014 [157] and Yew et al. 2014 [74] reported the decrease in workability of concrete with increasing PVA fiber content. However, the balling effect of PVA fiber can be reduced by increasing the percentage of superplasticizer dosage.

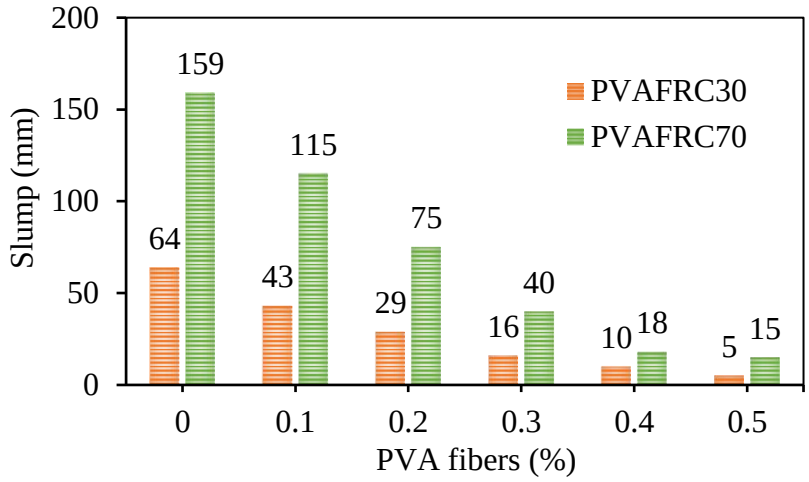

Figure 5.4 Workability of PVAFRCs mixes

5.2.5.2 Compressive strength

The cube compressive strength results of two strengths of PVAFRCs (PVAFRC30 and PVAFRC70) mixes are presented in Table 5.3. The effect of increasing the PVA fiber content on the compressive strengths of PVAFRC30 and PVAFRC70 mixes is graphically shown in Figure 5.5. The test results show that the compressive strength of concrete increased with the addition of 0.1%, 0.2%, and 0.3% PVA fibers and decreased when the addition rate of PVA fibers increased to 0.4% and 0.5%. The change in compressive strength of PVAFRC mixes with respect to the addition of PVA fibers percentages is presented in Table 5.4. These results indicate that the addition of fibers beyond a certain limit is not beneficial to the compressive strength of concrete [43,158]. In PVAFRC30, compared to the control mix N-0PVA, the compressive strength of N-0.1PVA, N-0.2PVA, and N-0.3PVA increased by 2.18%, 5.34%, and 7.63%, with respect to 0.1%, 0.2%, and 0.3% PVA fiber additions. In PVAFRC70, compared to control mix H-0PVA, the compressive strength of H-0.1PVA, H-0.2PVA, and H-0.3PVA increased by 1.51%, 3.11%, and 4.79%, with respect to 0.1%, 0.2%, and 0.3% PVA fibers additions. The addition of PVA fiber content above 0.3% resulted in lower compressive strength than that of control mixes in both PVAFRC30 and PVAFRC70. Previously, Amin et al. [43] also reported that the addition of 0.25% volume fraction of 12 mm length PVA fibers showed up to a 7.5% increment in compressive strength compared to the control mix. From the test results of the present study, it can be observed that the PVAFRC mixes with a low volume fraction of PVA fibers have higher compressive strength than the mix without any fibers. This is because the incorporated short PVA fibers may act as tiny reinforcements against the shear forces generated in a specimen under the uniaxial compression loads and can hold the shear planes together by a confining effect [159]. The decrease in compressive strength of PVAFRC

mixes with 0.4% and 0.5% fibers is because of the addition of a higher volume fraction of PVA fibers can make the consolidation of concrete more difficult, leading to an increase in entrapped air [160]. Since the strength of a material is mainly influenced by its microstructural features such as porosity and pore size distribution [161], the addition of a higher volume fraction of PVA fibers may lead to improper dispersion of fibers, which probably act as imperfections [159], and increase the possibility of pore concentration in the matrix [43] and also the formation of a weak fiber–matrix interphase, thereby resulting in lower compressive strength under compressive loads.

Failure mode of compressive strength specimens

During testing, small cracks appeared on the surface of the PC specimens just before reaching the ultimate load. The load on the specimens dropped quickly after they attained the ultimate load because of faster crack propagation and crack widening. The PC specimens crushed with a faint noise immediately after attaining the ultimate load (especially H-0PVA specimens), and the surrounding concrete spalled due to the cyclo-hoop effect, and the shape of the concrete block appeared to be pyramidal [105], (refer Figure 5.6(a)). In the case of specimens with PVA fibers, initial cracks formed on the surface of the PVAFRC specimens before the maximum load was obtained. Once the specimens reach the ultimate load, these cracks were widened and propagated further with a gradual decrease of load. The failure of these specimens is not as quick as that of PC specimens. However, the specimens were cracked, and no spalling of concrete occurred for mixes with 0.2%, 0.3%, and 0.4% PVA fibers but minimal spalling of concrete occurred for mixes with PVA fiber content of 0.1% and 0.5%, but the cross-sectional area of the specimens was not crushed as that of the specimens of PC in PVAFRC30 as well as PVAFRC70 (refer Figure 5.6(b)).

Table 5.3 Strength properties of PVAFRCs mixes

Mix designation	**PVAFRC30**			**PVAFRC70**		
	CS (MPa)	**FS (MPa)**	**STS (MPa)**	**CS (MPa)**	**FS (MPa)**	**STS (MPa)**
0PVA	38.57	4.27	4.09	80.33	6.22	5.81
0.1PVA	39.41	5.08	4.27	81.55	7.34	6.13
0.2PVA	40.63	5.93	4.71	82.83	8.63	6.53
0.3PVA	41.52	6.70	5.54	84.18	9.71	6.84
0.4PVA	38.75	6.38	5.16	79.43	9.08	6.40
0.5PVA	33.50	5.14	4.77	75.06	8.31	5.93

CS: Compressive strength; FS: Flexural strength; STS: Split tensile strength

Table 5.4 Percentage increase or decrease in strength properties of PVAFRC mixes compared to control mix

Mix designation	PVAFRC30			PVAFRC70		
	CS	FS	STS	CS	FS	STS
0PVA	-	-	-	-	-	-
0.1PVA	2.18	18.85	4.28	1.51	18.14	5.48
0.2PVA	5.34	38.81	15.18	3.11	38.84	12.33
0.3PVA	7.63	56.81	35.41	4.79	56.14	17.81
0.4PVA	0.45	49.34	26.07	-1.13	46.12	10.14
0.5PVA	-13.15	20.26	16.73	-6.56	33.61	2.07

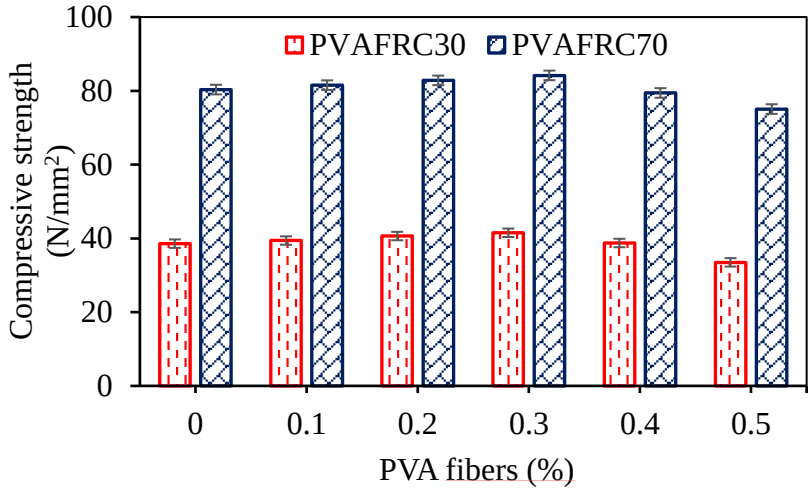

Figure 5.5 Compressive strength of PVAFRCs

(a) Plain concrete (b) PVAFRC

Figure 5.6 Failure of compressive strength specimens of PVAFRCs

5.2.5.3 Flexural strength and load-deflection behavior

The flexural strength results of PVAFRC30 and PVAFRC70 mixes are presented in Table 5.3. The effect of increasing percentage of PVA fiber content on the flexural strengths of PVAFRCs mixes is graphically represented in Figure 5.7. Unlike the compressive strength, the addition of PVA fibers of 0.1% to 0.5% significantly increased the flexural strength of PVAFRC30 and PVAFRC70 mixes. The percentage increase in flexural strength of PVAFRC mixes with respect to percentage of PVA fibers additions is presented in Table 5.4. The specimens of mixes with 0.3% PVA fiber content showed highest flexural strength in two grades of PVAFRCs. With an

increase in PVA fibers content from 0 to 0.3%, the flexural strength of N-0.3PVA specimens increased by 56.81% and the flexural strength of H-03PVA specimens increased by 56.14%, respectively. However, in two strengths of PVAFRCs, the flexural strength of the mixes with 0.4% and 0.5% fiber content was greater than that of the control mixes. Early in literature, Noushini, Vessalas, et al. (2013) [162] also observed that compared to the control mix, the addition of 0.25% volume fraction of 12 mm length PVA fibers showed a 19.64% increment in flexural strength than the addition of 0.5% volume fraction of PVA fibers. The mid-span deflection behaviour of two grades of PVAFRCs is also evaluated, and the corresponding load–deflection curves are presented in Figure 5.8. In two strengths of PVAFRCs, the concrete specimens with PVA fibers exhibited a linear load-deflection behaviour up to ultimate load like PC specimens. Similar observations have been previously reported by researchers [82]. The specimens with 0.3% fiber content exhibited the highest deflection with respect to ultimate load in both PVAFRC30 and PVAFRC70. In PVAFRC30, compared to control mix N-0PVA, by increasing percentage of PVA fibers from 0 to 0.3%, the mid-span ultimate deflection of N-0.3PVA was increased by 147.20%. In PVAFRC70, compared to control mix H-0PVA, the increasing the percentage of PVA fibers from 0-0.3%, increased the mid-span ultimate deflection of H-0.3PVA by 119.76%. The specimens of mixes with 0.4% and 0.5% fiber content showed lower deflections than those of mixes with 0.3% fiber content. However, in two grades of PVAFRCs, the deflections at ultimate load of specimens of mixes with 0.4% and 0.5% fiber content were higher than those of respective control mixes. The increase in flexural strength of PVAFRC specimens was because of the greater crack bridging phenomena offered by the small (12 mm) length of PVA fibers. Incorporation of small-length PVA fibers not only shows resistance to propagation of micro-cracks but also increases the stiffness of concrete [162].

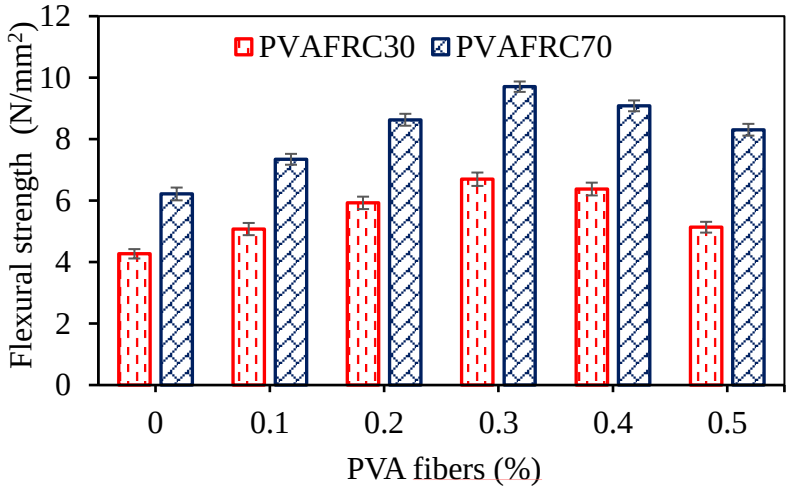

Figure 5.7 Flexural strength of PVAFRCs

Failure mode of flexural strength specimens

The PC specimens failed in two halves at ultimate load, as shown in Figure 5.9(a). The failure of these specimens was obviously brittle in nature because the rupture failure of these specimens occurred at the ultimate load extremely suddenly and quickly, and there was no early crack formation prior to failure. In case of PVAFRC specimens, a single crack developed in the loading span before the specimen reached its ultimate load and this led to the complete failure of specimens in two halves at ultimate load. Primarily, crack developed in the tension interface region because of tensile strains formed by the flexural load that led to the fiber pull-out or breakage in the tension zone of the specimen, leading thereby to an extension of micro-cracks in the concrete mix. Under flexural loading, the initial crack appeared in the tension zone of specimens at a level of 85–90% of peak-stress and further extended to concrete matrix with higher stresses, leading to failure of the specimen at the ultimate load as shown in Figure 5.9(b).

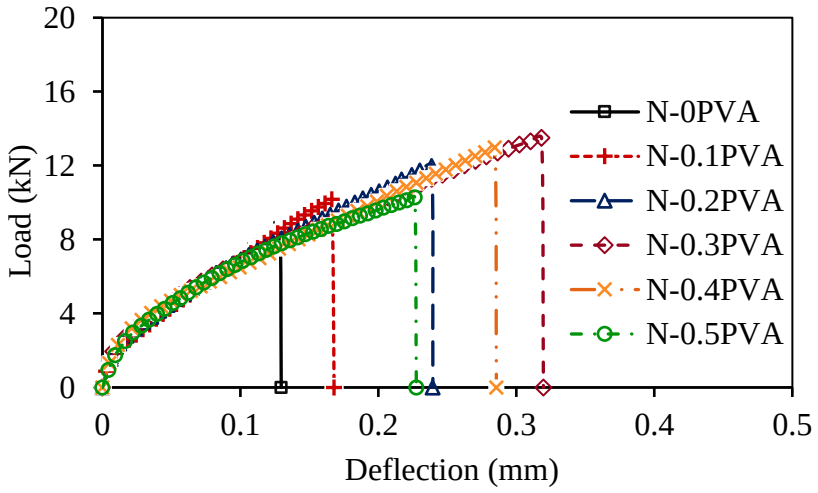

(a) PVAFRC30

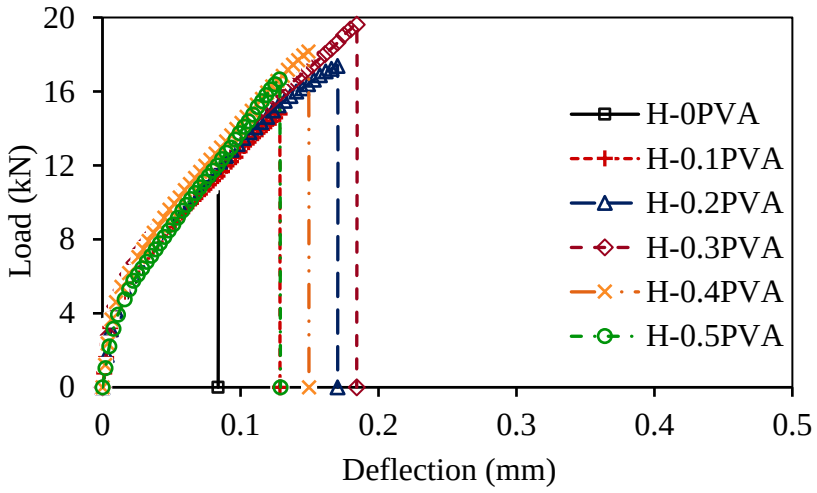

(b) PVAFRC70

Figure 5.8 Flexural load-deflection behaviour of PVAFRCs

(a) Plain concrete

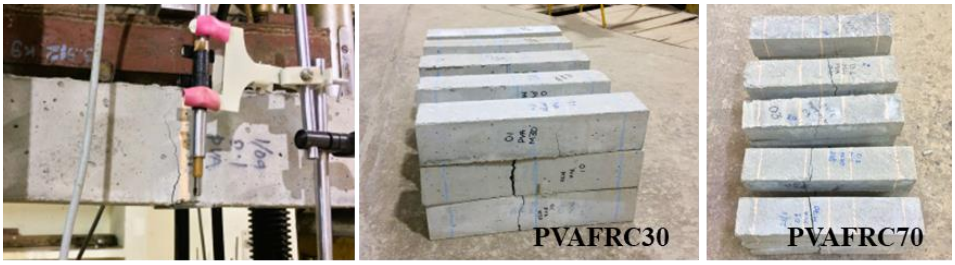

(b) PVAFRC

Figure 5.9 Failure of flexural strength specimens of PVAFRCs

5.2.5.4 Split tensile strength

The split tensile strength results of PVAFRC30 and PVAFRC70 are tabulated in Table 5.3. The effcet of increasing the PVA fiber content on the split tensile strengths of PVAFRC30 and PVAFRC70 mixes is graphically shown in Figure 5.10. Test results showed that the addition of PVA fibers significantly increased the split tensile strength of concrete. In PVAFRC30 and PVAFRC70, the specimens of PVAFRC mixes showed higher split tensile strengths than those of the respective control mix specimens. In two grades of PVAFRCs, the mixes with 0.3% PVA fiber content showed highest split tensile strength. In PVAFRC30, compared to control mix N-0PVA, the split tensile strength of N-0.3PVA mix increased by 35.41%, and similarly, in PVAFRC70, compared to control mix H-0PVA, the split tensile strength of H-0.3PVA mix increased by 17.81%. This is almost similar to the results reported by Noushini, Samali, et al. 2013a [43] earlier in the literature. The authors reported that when 0.25% volume fraction of 12 mm length PVA fibers were added to control mix, the split tensile strength of concrete increased by 27.02%. The specimens of mixes with 0.4% and 0.5% PVA fiber content in two grades of PVAFRCs have showed lower split tensile strengths than those of specimens of mixes with 0.3% fiber content. This is because the addition of PVA fibers exceeding a certain value would not show any positive influence on strength other than weakening the performance of the concrete [82]. The addition of a higher volume percent of PVA fibers leads to a balling effect that causes improper compaction of concrete, internal voids, and the formation of a weak

fiber–matrix interphase. Therefore, the mixes with higher PVA fiber content showed lower split tensile strength than mixes with 0.3% PVA fibers.

Failure mode of split tensile strength specimens

Under the test, before attaining ultimate load, a vertical crack initially appeared in the compression zone of the specimen along the direction of loading, as shown in Figure 5.11(a). Upon further increase of load these vertical cracks propagate from top phase to bottom phase and caused failure of the specimens. At ultimate load, the failure of PC specimens occurred by a sudden split, and the specimens failed in two halves, as shown in Figure 5.11(b). However, in the case of PVAFRC specimens, after attaining ultimate load, the vertical cracks became wider, and the load carrying capacity gradually decreased, and specimens did not completely fail into two halves as shown in Figure 5.11(c).

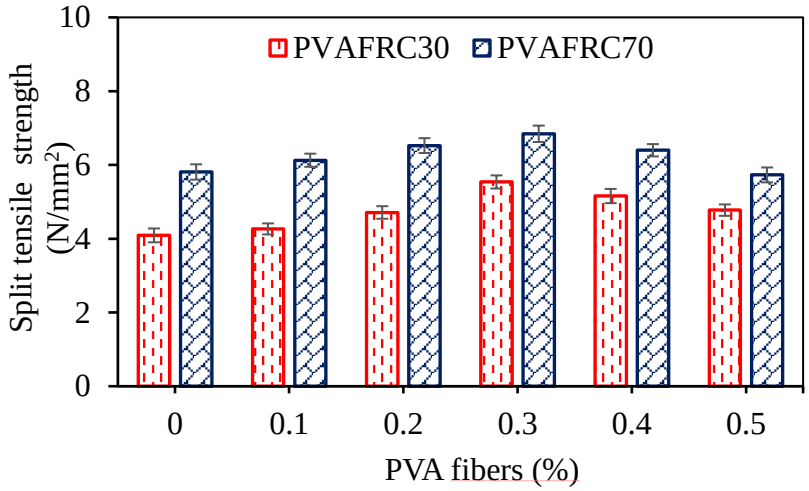

Figure 5.10 Split tensile strength of PVAFRCs

(a) (b) (c)

Figure 5.11 Failure of split tensile strength specimens: (a) crack at ultimate load, (b) plain concrete, (c) PVAFRC

5.2.5.5 Compressive stress–strain behavior

The experimental compressive stress-strain curves of PVAFRC30 and PVAFRC70 mixes obtained under uniaxial compression test are presented in Figure 5.12. These stress–strain

curves were plotted using data recorded in the DAC system. During the test, it was observed that up to 70–75% of the ultimate load, the load on the specimens increased at a high rate and then increased at a low rate until the ultimate load. After the ultimate load was obtained, testing on the specimens was continued until the ultimate load dropped to 60–65%. The behaviour of concrete specimens changed with addition of PVA fibers compared to the behaviour of the concrete specimens without any fibers. At 70–75% of ultimate load, several nonlinear vertical cracks appeared on the surface of the specimens. With further increase of load, the vertical cracks propagated from top phase to bottom phase along the direction of loading, and at the ultimate load, these cracks are scattered to the edges and caused failure of the specimens. From Figure 5.12, it was observed that the addition of PVA fibers had no significant influence on the ascending region of the stress–strain curves of PVAFRC specimens up to 50–70% of ultimate strength [163]. In the ascending region, the stress–strain curves of PVAFRC mixes initially behaved linear elastic up to nearly 60% of peak-stress and thereafter the path of the curve changed from linear behaviour to non-linear behaviour up to failure. Crack propagations, crack width increments, drop in load after the peak-stress, and post-peak behaviour of PVAFRC specimens were affected by the change in volume percentage of PVA fibers additions and the level of confinement they provided to concrete. A slow drop in stress values was observed along with increasing strains after the peak-stress. Compared to control mixes, the addition of PVA fibers enhanced the ductility behaviour of PVAFRC specimens of PVAFRC30 and PVAFRC70 by improving their post-peak behaviour [43]. The incorporated fibers in the concrete assist in increasing the volumetric strain capacity of the concrete after cracking by bridging the cracks and improving the post-peak behaviour of FRC [164,165]. In PVAFRC30, the increase in addition of PVA fibers from 0.1% to 0.3% slightly decreased the slope of stress–strain curve in the descending region compared to the slope of stress–strain curve in the descending region of PC. Further addition of PVA fibers (0.4% and 0.5%) increased the slope of stress–strain curves in the descending region compared to PVAFRC with 0.3% PVA fibers [163]. Same observation was noticed for specimens of PVAFRC70 mixes. The specimens of PVAFRC30 exhibited higher post-peak behaviour with low strain at peak-stress than specimens of PVAFRC70. In both PVAFRCs, specimens of PVAFRC30 mixes exhibited large post-peak behaviour, compared to specimens of PVAFRC70 mixes. For example, N-0.3PVA specimens showed larger post-peak behaviour then H-0.3PVA specimens. It was also observed from Figure 5.12 that the behaviour of PVAFRC specimens of PVAFRC30 mixes was more ductile than PVAFRC specimens of PVAFRC70 mixes. The crack propagation was more rapid for PVAFRC specimens of PVAFRC70 compared to PVAFRC specimens of PVAFRC30.

However, the effect of PVA fiber additions on the ultimate strength and post-peak behaviour of two grades of PVAFRCs was appreciable. The failure of PVAFRC specimens under uniaxial compression test is shown in Figure 5.13.

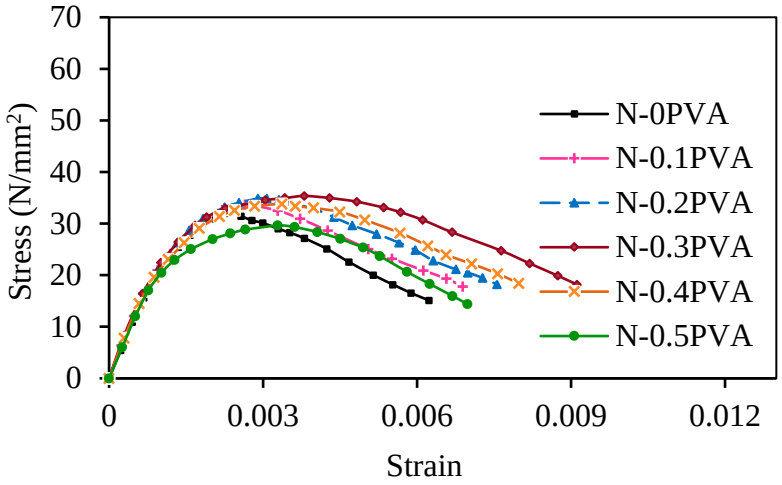

(a) PVAFRC30

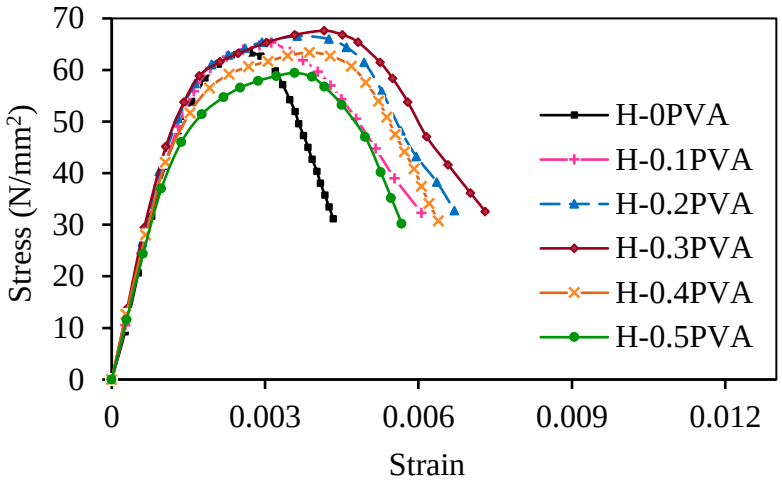

(b) PVAFRC70

Figure 5.12 Experimental compressive stress-strain curves of PVAFRCs

Figure 5.13 Failure of PVAFRCs specimens under the test of uniaxial compressive stress-strain behaviour

5.2.5.6 Energy absorption capacity

Previous researchers [166,167] found that the addition of fibers to concrete has a greater impact on energy absorption and crack controlling than increasing load bearing capacity. Therefore, improvement in the EAC of PVAFRC specimens of PVAFRC30 and PVAFRC70 mixes was assessed from the area under the experimental stress–strain curves and the results are presented in Tables 5.5. The change in EAC of specimens of PVAFRC30 and PVAFRC70 mixes with respect to percentage of PVA fibers additions is shown in Figure 5.14. It was observed from Figure 5.14 that the EAC of PVAFRC specimens of both PVAFRC30 and PVAFRC70 was higher than that of control mix specimens. This is because the incorporation of PVA fibers increased the post-peak behaviour of stress–strain curves and therefore increased the area under stress–strain curves [163]. The specimens of PVAFRC70 mixes exhibited higher EAC than specimens of PVAFRC30. The average EAC of all specimens of PVAFRC30 and PVAFRC70 mixes were 0.188 and 0.3, respectively. The specimens of PVAFRC70 showed higher EAC because of the accumulation of large areas under the stress–strain curves compared to that of the specimens of PVAFRC30. In both PVAFRCs, the specimens with 0.3% PVA fiber content exhibited higher EAC. In PVAFRC30, compared to control mix N-0PVA, the EAC of N-0.3PVA increased by 76.84%. In PVAFRC70, compared to the control mix of H-0PVA, the EAC of H-0.3PVA increased by 101.05%. This is because the specimens with 0.3% PVA fibers exhibited large post-peak behaviour compared to specimens with other percentages of PVA fibers, resulting in a higher area under the stress-strain curves. Therefore, the mixes with 0.3% PVA fibers had higher EAC compared to the mixes with other percentages of PVA fibers. The percentage increase or decrease in the EAC of PVAFRC mixes with respect to the addition of PVA fibers is shown in Table 5.6.

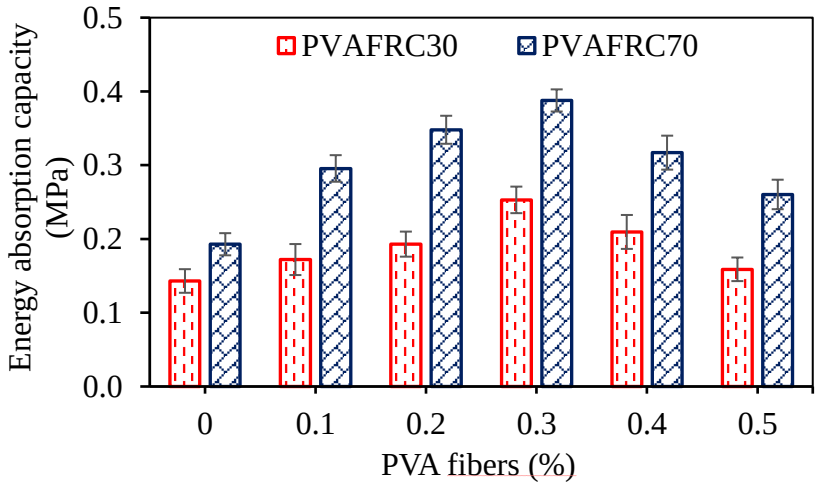

Figure 5.14 Energy absorption capacity of PVAFRCs

5.2.5.7 Young's modulus

Due to changes in the compressive strengths of PC with the addition of different percentages of PVA fibers, the change in Young's modulus of specimens of PVAFRC30 and PVAFRC70 mixes was evaluated according to ASTM C469 standards [144] and are presented in Tables 5.5. From Figure 5.15, it was observed that Young's modulus of PVAFRC specimens did not vary much with respect to addition of percentages of PVA fibers compared to that of respective to control mixes in each grade. As stated in section 5.2.5.5, the addition of PVA fibers had no significant influence on the ascending region of stress–strain curves of PVAFRC up to 50-70% of peak-stress. Because of that there was not much increment in Young's modulus values of PVAFRC specimens with an increase in the percentage of PVA fibers addition [82,168]. Compared to control mix, the percentage increase or decrease in Young's modulus of PVAFRC mixes with respect to addition of PVA fibers is shown in Table 5.6. In both grades, compared to control mix, the addition of PVA fibers by up to 0.4% slightly increased Young's modulus. In PVAFRC30, with the addition of PVA fibers from 0.1% to 0.4%, Young's modulus of N-0.1PVA, N-0.2PVA, N-0.3PVA, and N-0.4PVA mixes increased by 3.9%, 7.29%, 8.46%, and 5.42%, respectively, compared to control mix N-0PVA. In PVAFRC70, with the addition of PVA fibers from 0.1% to 0.4%, the Young's modulus of H-0.1PVA, H-0.2PVA, H-0.3PVA, and H-0.4PVA mixes increased by 5.60%, 9.96%, 15.34%, and 5.87%, respectively, compared to control mix H-0PVA. Similar observations have been previously reported by researchers [82] [43]. In both grades, the specimens of PVAFRC70 mixes exhibited higher Young's modulus than the specimens of PVAFRC30 mixes.

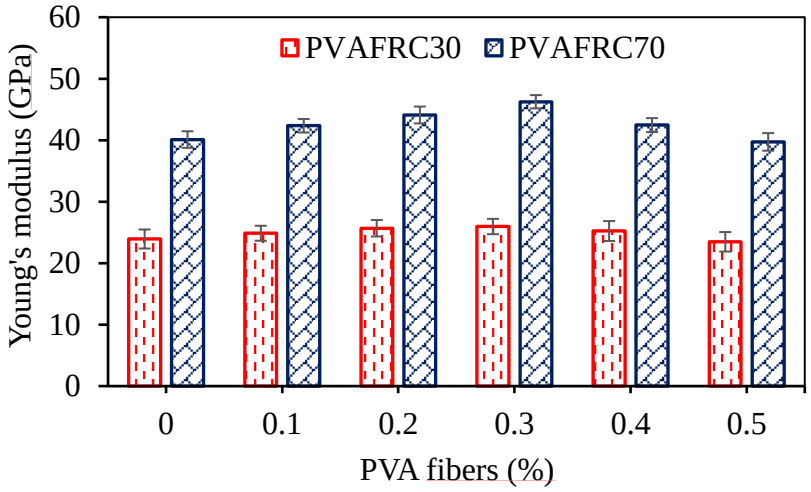

Figure 5.15 Young's modulus of PVAFRCs

Table 5.5 Compressive properties from experimental stress-strain curves of PVAFRCs

Mix name	MRI of PVA	PVAFRC30				PVAFRC70			
		Peak-stress (MPa)	Strain at peak-stress	EAC (MPa)	Young's modulus (GPa)	Peak-stress (MPa)	Strain at peak-stress	EAC (MPa)	Young's modulus (GPa)
0	0	31.99	0.00225	0.143	23.93	63.85	0.00260	0.193	40.10
0.1PVA	0.044	33.66	0.00265	0.172	24.86	65.36	0.00313	0.296	42.35
0.2PVA	0.088	34.84	0.00290	0.193	25.67	66.57	0.00363	0.348	44.10
0.3PVA	0.133	35.36	0.00380	0.253	25.95	67.61	0.00416	0.388	46.25
0.4PVA	0.177	33.82	0.00337	0.210	25.22	63.38	0.00387	0.317	42.45
0.5PVA	0.221	29.62	0.00328	0.159	23.47	59.44	0.00358	0.260	39.72

Table 5.6 Percentage increase or decrease in compressive properties of PVAFRC mixes compared to control mixes

Mix name	PVAFRC30				PVAFRC70			
	Peak-stress	Strain at peak-stress	EAC	Young's modulus	Peak-stress	Strain at peak-stress	EAC	Young's modulus
0	0.00	0.00	0.00	0.00	0.00	0.00	0.00	0.00
0.1PVA	5.23	17.82	20.30	3.90	2.37	20.02	53.26	5.61
0.2PVA	8.91	28.70	34.91	7.29	4.26	39.39	80.44	9.96
0.3PVA	10.53	68.91	76.84	8.47	5.89	59.63	101.06	15.34
0.4PVA	5.73	49.60	46.48	5.42	-0.73	48.46	64.31	5.87
0.5PVA	-7.40	45.88	11.06	-1.92	-6.91	37.60	34.99	-0.96

5.2.5.8 Micro-structure analysis of PVAFRCs

The micro-structural behaviour of PVAFRC specimens of two grades were studied through SEM and are presented in Figure 5.16. After determining the cube compressive strength, pieces of spalled crushed concrete from PVAFRC specimens were collected and prepared for SEM examination. From the SEM images, it was observed that the micro-structural characteristics of PVAFRC specimens of both PVAFRC30 and PVAFRC70 almost exhibited the same behaviour. The strong adhesion between PVA fibers and matrix was evident from the fiber–matrix interphase (refer Figure 5.16(a)). On the other hand, the development of balling effect with addition of higher volume fractions of PVA fibers resulted in weak fiber network like structures, poor adhesion between fiber and matrix, weak fiber–matrix interface and voids in matrix (refer Figure 5.16(b)). Figure 5.16(c) shows the scratches on PVA fiber caused by fiber–matrix interphase failure due to de-bonding and pull-out failure of PVA fiber. From Figure

5.16(d) and (e), on the fractured surface of the specimens, a half embedded PVA fiber in the matrix was observed. However, the other end of the fiber was pulled-out of the matrix and showed a deformity before the fracture. This indicates excellent embedment of PVA fibers in the matrix that improves the resistance against cracking [169]. The fiber–matrix interphase failure between PVA fiber and matrix is presented in Figure 5.16(f). However, some parts of the fracture separations from the PVA fiber are still bonded to the matrix. This shows the formation of strong bond between PVA fiber and matrix in case of mixes with lower volume fraction of PVA fibers [170]. The proper bonding between the PVA fiber and matrix can be observed through a matrix attached around the fiber in Figure 5.16(a). Hence, the fibers surrounded by matrix resulted in increased strength properties of the concrete from stress transfer mechanism between matrix and reinforced fiber [171]. As shown in Figure 5.16(h) and (i), the contortion, bridging and pull-out of PVA fibers indicates energy dissipation process and stress transformation to matrix [172-173]. The hole and slip trace created by the pulled-out of PVA fibers from the matrix is shown in Figures 5.16(d), (e), (g), (h), and (i). The pull-out failure of PVA fibers is due to the smaller development length of the fiber on one side of the crack and lower bond strength between fiber and matrix caused by heterogeneity of matrix due higher volume fraction of PVA fibers. The pull-out of PVA fibers from matrix has a positive effect on the tensile and flexural performance of the specimens. Since PVA fiber is a hydrophilic material [174], the pull-out of fiber from the matrix without rupturing increases the energy dissipation during the post-cracking process and thereby improves the tensile strength of PVAFRCs [175-177]. Figure 5.16(i) shows the bridging of meso-crack propagation and PVA fiber did not allow meso-crack to be propagated on the other side of the matrix. Furthermore, Figure 5.16(i) also shows proper bond development between PVA fiber and matrix, thereby enhancing the mechanical properties of PVAFRCs. As shown in Figure 5.16(j), after the debonding and fracture of PVA fiber, the meso-crack in the matrix propagated and transformed into macro-crack. From Figure 5.16(f), (i), and (j), it has been observed that PVA fibers are de-bonded from the matrix in some places due to the smooth surface of PVA fibers. Figure 5.16(c), (e), and (j) show the fractures on PVA fibers due to pull-out of fibers. The specimens with lower volume faction of PVA fibers demonstrated more fiber factures because of proper bond strength development with matrix. Compared to the specimens of PVAFRC30, due to higher matrix strength, on the fractured surface of PVAFRC70 specimens, more fractures of PVA fibers were observed instead of being pulled-out from the matrix [159]. The SEM images of specimens with lower volume fraction of PVA fibers showed proper fiber–matrix interphase bond strength, fracture of PVA fibers, deformation of PVA fibers before failure and pulled-out PVA fibers.

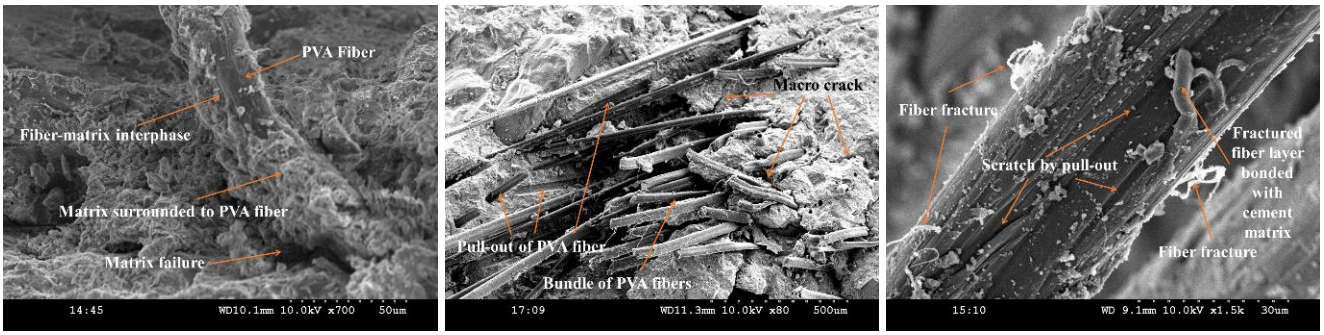

(a) (b) (c)

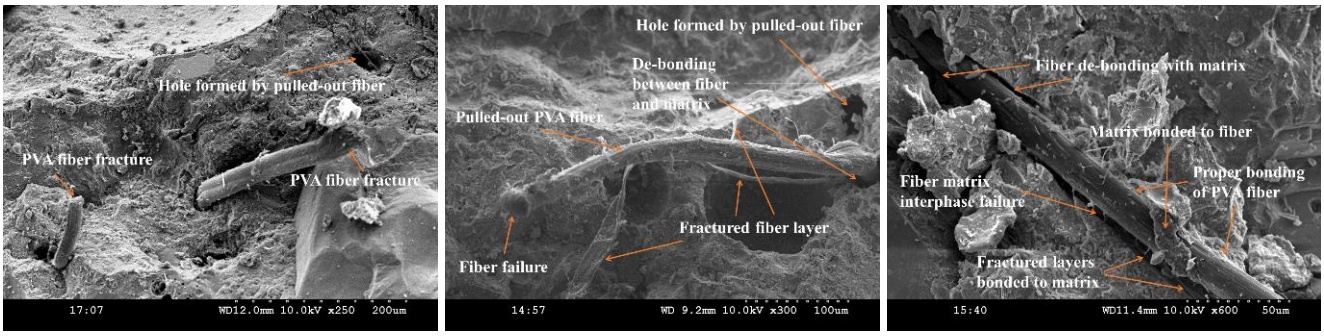

(d) (e) (f)

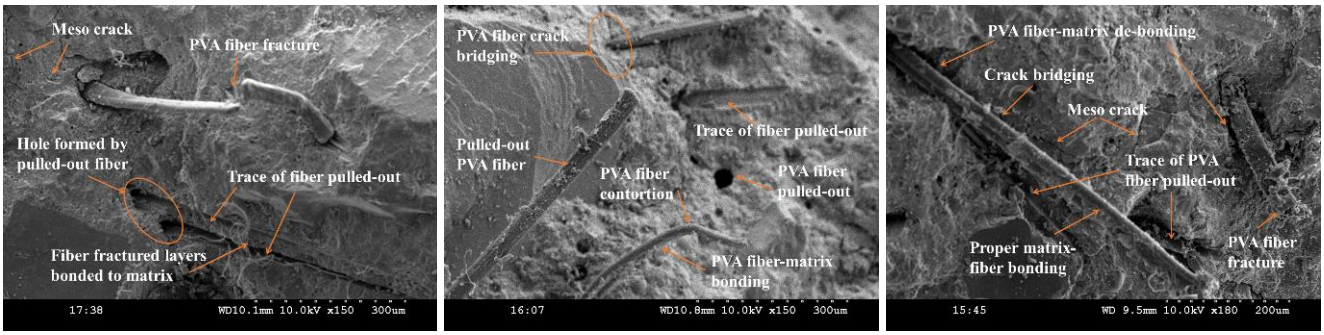

(g) (h) (i)

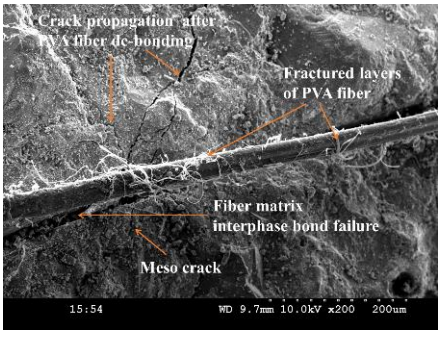

(j)

Figure 5.16 SEM images of PVAFRCs

5.2.6 Analytical Modelling of Compressive Stress-Strain Curves of PVAFRCs

5.2.6.1 Modified constitutive analytical model

The stress-strain relationship of concrete under compression is necessary for the analysis and design of concrete structures. The properties of fibers, aggregates, and cementitious materials, water to cementitious material ratio, testing conditions, loading rate, concrete/FRC strength, stiffness of the testing machine, and frictional resistance between the platens and specimens greatly affect the stress-strain behaviour of concrete/FRC especially in the post-peak region [178,179]. Therefore, it is necessary to establish a constitutive analytical model such that the stress–strain curves obtained in different conditions can be evaluated.

After examining various analytical stress–strain relationships proposed by the researchers in literature, the basic constitutive analytical model proposed by Carreira and Chu 1985 [180] to predict the stress–strain curves of PC, which was later adopted and revised by Ezeldin and Balaguru 1992 [181] to predict the stress–strain curves of steel FRC, was adopted and modified as shown in equation 5.1 for current study to analytically model the experimental stress–strain curves of specimens of PVAFRC30 and PVAFRC70.

$$f_c = f'_{cf}\left(\frac{\beta_n\left(\frac{\varepsilon_c}{\varepsilon_{of}}\right)}{\beta_n - 1 + \left(\frac{\varepsilon_c}{\varepsilon_{of}}\right)^{\beta_n}}\right) \qquad \text{Eq. (5.1)}$$

Where β_n is material parameter, f'_{cf} is cylindrical compressive strength of FRC, f_c and ε_c are stresses and strains on stress-strain curve, ε_{of} is strain related to cylindrical compressive strength of FRC. To predict the stress-strain behaviour of concrete from equation (5.1) for a given compressive strength values of FRC, only β_n and ε_{of} values are required.

5.2.6.2 Modified reinforcing index

The strength and stress-strain behaviour of a FRC composite is greatly influenced by the geometry, volume fraction, and mechanical properties of the fiber used, as well as matrix properties. Therefore, the effect of aspect ratio (l_f/d_f) and volume fraction (v_f) (or) weight fraction (w_f) of the fibers on strength and stress-strain behaviour of FRC was calculated through the factor reinforcing index (RI). In the literature many researchers have calculated RI values of fibers as a product of aspect ratio and volume fraction of fibers, as shown in below equation 5.2 [182-184], or as a product of aspect ratio and weight fraction of fibers, as shown in equation 5.3 [185-187]. But along with the aspect ratio, volume fraction or weight fraction of the fibers,

tensile strength, anchoring factor, and adhesion factor of fibers also play a major role in influencing the strength and stress-strain behaviour of FRC composites. Therefore, these factors need to be considered in calculation of RI values of fibers.

$$RI = v_f \times \frac{l_f}{d_f} \quad \text{Eq. (5.2)}$$

$$RI = w_f \times \frac{l_f}{d_f} \quad \text{Eq. (5.3)}$$

The relationships between RI and properties of stress-stain curves such as peak-stress, strain at peak-stress, and material parameter (β_n) are the main aspects required for analytical modelling of the stress-strain curve of the concrete. Therefore, the parameters in the modified constitutive analytical model (equation 5.1) are mainly related to RI, which is a major function to control the behaviour of stress-strain curve of FRC. In the present study, along with aspect ratio and volume fraction or weight fraction of the fibers, tensile strength, anchoring factor, and adhesion factor of PVA fibers were also considered in calculating RI values of fibers. For this, based on the fiber volume fraction, M. Khan et al. 2020 [171] proposed modified reinforcing index (MRI) expression shown in equation 5.4 was used to calculate RI values of PVA fibers. Thus, the calculated RI, i.e., MRI values for PVA fibers at 0%, 0.1%, 0.2%, 0.3%, 0.4%, and 0.5%, are tabulated in Tables 5.5 and 5.7. Then the relationships for peak-stress, strain at peak-stress and β_n with MRI values of various volume percentages of PVA fibers were developed for analytical modelling of compressive stress-strain curves of PVAFRC30 and PVAFRC70 mixes using the modified constitutive analytical model.

$$MRI = k_i k_a v_f \frac{l}{d} \left(\frac{\sigma_p}{\sigma_s}\right)^{\alpha} \quad \text{Eq. (5.4)}$$

where, k_i is the anchoring factor which is related to surface of the fiber that is smooth and straight. k_i value for PVA fiber is taken as 0.1 considering that the surface of the fibers is smooth and straight according to Cao et al. 2018 [175], Almusallam et al. 2016 [188], and Cao and Li 2018 [189]. k_a is the adhesion coefficient which depends on the chemical nature of the fiber. Based on the studies reported by researchers [83,190,191], the k_a value for PVA fiber is taken as 1.35. v_f, d and l are the volume fraction, diameter, and length of the fiber, respectively. σ_p is the tensile strength of PVA fiber and σ_s is the tensile strength of steel fiber. σ_s is taken as 1345 MPa according to M. Khan et al. 2020 [171]. α is the tension stiffening parameter that depends on the type of fiber used, for PVA fiber α value is taken as 0.5 according Cao et al. 2018 [175], Almusallam et al. 2016 [188], and Cao and Li 2018 [189].

5.2.6.3 Peak-stress relationships with MRI values of PVA fibers

The development of relationships for peak-stress and strain at peak-stress with MRI values of volume percentages of PVA fibers used are basic requirements for the analytical modelling of stress-strain curves of PVAFRC. The influence of addition of various volume percentages of PVA fibers on the peak-stress of PVAFRC specimens was calculated from the experimental stress–strain curves of the specimens of PVAFRC30 and PVAFRC70 and are presented in Tables 5.5. The peak-stress results of cylindrical specimens are found similar in trend to cube compressive strength results. In both PVAFRC30 and PVAFRC70, the increase in PVA fiber content from 0 to 0.3% slightly increased the peak-stress compared to strain at peak-stress, and with further additions of PVA fibers (0.4% and 0.5%), the increase in peak-stress and strain at peak-stress decreased. The addition of PVA fibers improved the peak-stress of specimens of PVAFRC30 mixes better than that of peak-stress of specimens of PVAFRC70 mixes. The percentage improvement in peak-stress with the addition of 0.3% PVA fibers was the highest among other percentage additions of PVA fibers compared to control mixes in both grades of PVAFRCs. In PVAFRC30, peak-stress of N-0.3PVA increased by 10.53% when compared to control mix N-0PVA. In PVAFRC70, peak-stress of H-0.3PVA increased by 5.89% when compared to control mix H-0PVA. The percentage of increase or decrease in the peak-stress of PVAFRC mixes with respect to addition of various volume percentages of PVA fiber is tabulated in Tables 5.6. To develop the relationships between peak-stress and MRI values of PVA fibers, appropriate regression analysis was carried out on the experimental data of PVAFRC30 and PVAFRC70 mixes. Thus, equation 5.5 for PVAFRC30, and equation 5.6 for PVAFRC70 mixes have been formulated to obtain the relationships for peak-stress of PVAFRC mixes with peak-stress of PC mixes.

$$f'_{cf} = -368.14MRI^2 + 74.383MRI + f_{cp} \quad \text{for PVAFRC30} \quad \text{Eq. (5.5)}$$

$$f'_{cf} = -449.21MRI^2 + 81.896MRI + f_{cp} \quad \text{for PVAFRC70} \quad \text{Eq. (5.6)}$$

In equations 5.5 and 5.6, f'_{cf} is cylindrical compressive strength of PVAFRC and f_{cp} is cylindrical compressive strength of PC.

5.2.6.4 Strain at peak-stress relationships with MRI values of PVA fibers

The influence of addition of different percentages of PVA fibers on the strain at peak-stress of PVAFRC specimens of PVAFRC30 and PVAFRC70 mixes was evaluated from the experimental stress–strain curves and are presented in Tables 5.5. From the strain at peak-stress values of N-0PVA and H-0PVA, it was observed that the strain corresponding to peak-stress

increased as the compressive strength of concrete increased. Same observation was also reported by Tasdemir et al. 1998 [192]. In both PVAFRC30 and PVAFRC70, compared to control mix, the addition of PVA fiber content from 0 to 0.5% increased the strain at peak-stress better than the peak-stress. Among all volume percentages of PVA fibers additions, at 0.3% PVA fiber addition, the increase in strain at peak-stress of N-0.3PVA and H-0.3PVA was more significant. The addition of 0.3% PVA fibers to PC mixes resulted in a 68.91% increase in strain corresponding to peak-stress of the N-0.3PVA, and 59.67% increase in strain corresponding to peak-stress of H-0.3PVA. The percentage increase in the strain at peak-stress of PVAFRC mixes with respect to the addition of PVA fiber percentages is presented in Table 5.6. According to this, the addition of PVA fibers significantly enhanced the strain-hardening behaviour of PVAFRC specimens when compared to control mix specimens [193,194]. PVAFRC specimens of PVAFRC70 exhibited better strain hardening behaviour than PVAFRC specimens of PVAFRC30. The relationships between strain at peak-stress to MRI values of PVA fibers were developed by performing suitable regression analysis on experimental data. Thus, equation 5.7 for PVAFRC30 and equation 5.8 for PVAFRC70 mixes were established to obtain the relationships for strain at peak-stress of PVAFRC mixes with strain at peak-stress of PC mixes.

$$\varepsilon_{of} = -0.0471MRI^2 + 0.0157MRI + \varepsilon_{cp} \quad \text{for PVAFRC30} \qquad \text{Eq. (5.7)}$$

$$\varepsilon_{of} = -0.066MRI^2 + 0.0195MRI + \varepsilon_{cp} \quad \text{for PVAFRC70} \qquad \text{Eq. (5.8)}$$

In equations 5.7 and 5.8, ε_{of} is strain at cylindrical compressive strength of PVAFRC, ε_{cp} is strain at cylindrical compressive strength of PC.

5.2.6.5 Material parameter relationships with MRI values of PVA fibers

In the present study, β_n in equation 5.1 is a function of MRI, which depends on the physical properties of stress-strain curve that is the slope of the inflection point at the ascending and descending phases of the stress-strain curves. The experimental stress–strain curves of the present study were divided into two regions as ascending region (from origin to peak-stress) and descending region (from peak-stress to failure). Therefore, β_n values were calculated from both ascending phase and descending phase of stress-strain curves. The β_n values calculated for ascending and descending phases of the stress-strain curves are denoted by β_a and β_d, respectively. Hence, β_a represents β_n value of ascending phase and β_d represents β_n value of descending phase. The calculated β_a and β_d values from the experimental stress-strain curves are presented in Table 5.7. The relationships developed between β_n and MRI values of PVA

fibers for both ascending and descending phases of the stress-strain curves of PVAFRC30 and PVAFRC70 mixes are shown in equations 5.9-5.12 below.

$\beta_a = 25.319MRI^2 - 9.3472MRI + 2.374$ for ascending region of PVAFRC30 Eq. (5.9)

$\beta_d = 22.509MRI^2 - 2.596MRI + 2.339$ for descending region of PVAFRC30 Eq. (5.10)

$\beta_a = 49.712MRI^2 - 14.443MRI + 2.348$ for ascending region of PVAFRC70 Eq. (5.11)

$\beta_d = 59.575MRI^2 - 7.698MRI + 4.184$ for descending region of PVAFRC70 Eq. (5.12)

Table 5.7 Material parameter (β_n) values of PVAFRCs

Mix name	MRI **values of PVA**	**β_a and β_d values calculated from experimental stress-strain curves**				**β_a and β_d values calculated from equations (5.9) - (5.12) using MRI values of PVA fibers for analytical modelling**			
		PVAFRC30		**PVAFRC70**		**PVAFRC30**		**PVAFRC70**	
		β_a	β_d	β_a	β_d	β_a	β_d	β_a	β_d
0	0	2.39	2.24	2.38	4.46	2.37	2.34	2.35	4.18
0.1PVA	0.044	1.97	2.44	1.76	3.49	2.01	2.27	1.81	3.96
0.2PVA	0.088	1.80	2.29	1.47	3.86	1.75	2.29	1.46	3.97
0.3PVA	0.133	1.49	2.40	1.28	4.59	1.58	2.39	1.31	4.21
0.4PVA	0.177	1.61	2.40	1.43	4.77	1.51	2.58	1.35	4.69
0.5PVA	0.221	1.51	2.97	1.54	5.24	1.54	2.86	1.58	5.39

5.2.6.6 Comparison of experimental stress-strain curves with analytical stress-strain curves of PVAFRCs

The β_a and β_d values calculated from equations 5.9-5.12 for analytical modelling of stress-strain curves of specimens of PVAFRC30 and PVAFRC70 mixes are tabulated in Table 5.7. The values obtained from equations 5.5, 5.7, 5.9 and 5.10 were substituted in equation 5.1 to get complete analytical stress-strain curves of specimens of PVAFRC30 mixes. The values obtained from equations 5.6, 5.8, 5.11, and 5.12 were substituted in equation 5.1 to get complete analytical stress-strain curves of specimens of PVAFRC70 mixes. Then all the analytically modelled stress-strain curves of specimens of PVAFRC30 and PVAFRC70 mixes were presented in the form of normalized stress versus normalized strain in Figure 5.17(a) and (b), respectively. In these figures, the comparison of analytically modelled stress-strain curves with experimental stress-strain curves are made to examine the accuracy of fit of the analytical stress-strain curves to experimental stress-strain curves. It was observed from Figure 5.17(a)-(b) that the analytically modelled stress-strain curves from the proposed modified analytical model showed good agreement with experimental stress-strain curves in both ascending and

descending regions. Additionally, the accuracy of fit of the analytical stress-strain curves to experimental stress-strain curves was examined in terms of parameters, root mean square error (RMSE) and absolute fraction of variance (AFV), as illustrated by researchers Ayub et al. 2019 [187] and U. Khan et al. 2013 [195]. The expressions for the calculation of RMSE and AFV are shown in equations 5.13 and 5.14, respectively. The RMSE values of each mix of PVAFRC30 and PVAFRC70 were calculated to estimate the difference between the predicted stress and corresponding experimental stress at the same strain level. The AFV values of each mix of PVAFRC30 and PVAFRC70 were calculated to have an idea about how far the predicted compressive stress results lie from the mean values. The calculated RMSE and AFV of two grades of PVAFRCs are presented in Table 5.8. The RMSE and AFV values were calculated by selecting the stress values obtained experimentally and the stress values predicted from the modified constitutive analytical model at the same strain level of experimental stress. These results indicated that analytical stress-strain curves modelled from the modified constitutive analytical model using peak-stress, strain at peak-stress and β_n relationships with MRI were very close to the experimental stress-strain curves, and good agreement between them existed.

$$RMSE = \sqrt{\frac{\Sigma(E_i - A_i)^2}{n}} \qquad \text{Eq. (5.13)}$$

$$AFV = 1 - \frac{\Sigma(E_i - A_i)^2}{\Sigma(A_i)^2} \qquad \text{Eq. (5.14)}$$

where E_i is experimental stress, A_i is analytically predicted stress at the same strain level of experimental stress, n is the total number of data points in each set of data.

Table 5.8 The RMSE and AFV values of PVAFRCs

Strength of PVAFRC	**Mix name**	**Parameter**	**Present study**	**Ezeldin and Balaguru, 1992** [181]	**Nataraja et al. 1999** [185]	**Ou et al. 2012** [183]	**Abbass et al. 2018** [196]
			$A_{\sigma-\varepsilon}$ curves	**$P_{\sigma-\varepsilon}$ curves**			
PVAFRC30	0	RMSE	0.9379	0.8101	0.8101	2.5724	0.8040
		AFV	0.9985	0.9989	0.9989	0.9871	0.9989
	0.1PVA	RMSE	0.9379	17.1296	16.1219	2.5921	0.7483
		AFV	0.9985	-0.4685	-0.2154	0.9869	0.9991
	0.2PVA	RMSE	0.9742	17.9872	16.6747	2.8227	1.1673
		AFV	0.9987	-0.2680	0.0458	0.9866	0.9980
	0.3PVA	RMSE	1.1193	17.2510	14.9592	3.7861	3.0813
		AFV	0.9984	-0.0292	0.3309	0.9780	0.9871
	0.4PVA	RMSE	0.7772	13.9218	12.4517	2.6709	2.2095
		AFV	0.9991	0.3983	0.5577	0.9883	0.9929
	0.5PVA	RMSE	0.9209	9.1163	8.3006	3.0596	3.3740
		AFV	0.9984	0.6911	0.7573	0.9804	0.9786
PVAFRC70	0	RMSE	2.6844	16.5467	16.5467	7.1958	9.4556
		AFV	0.9971	0.8029	0.8029	0.9807	0.9693
	0.1PVA	RMSE	1.5834	36.0948	30.4237	5.1331	6.3074
		AFV	0.9990	-0.4821	0.1565	0.9898	0.9859
	0.2PVA	RMSE	2.2162	33.3361	26.6917	8.3174	8.7634
		AFV	0.9981	-0.2762	0.3558	0.9723	0.9721
	0.3PVA	RMSE	2.0729	25.7609	19.8845	10.8461	11.1481
		AFV	0.9985	0.4750	0.7398	0.9569	0.9579
	0.4PVA	RMSE	2.1468	18.4069	14.0263	9.8210	10.6446
		AFV	0.9981	0.7377	0.8687	0.9630	0.9596
	0.5PVA	RMSE	1.2013	10.5301	9.5278	8.4455	8.7338
		AFV	0.9993	0.9282	0.9439	0.9684	0.9681

$A_{\sigma-\varepsilon}$ curves - Analytically modelled stress-strain curves; $P_{\sigma-\varepsilon}$ curves - Predicted stress-strain curves

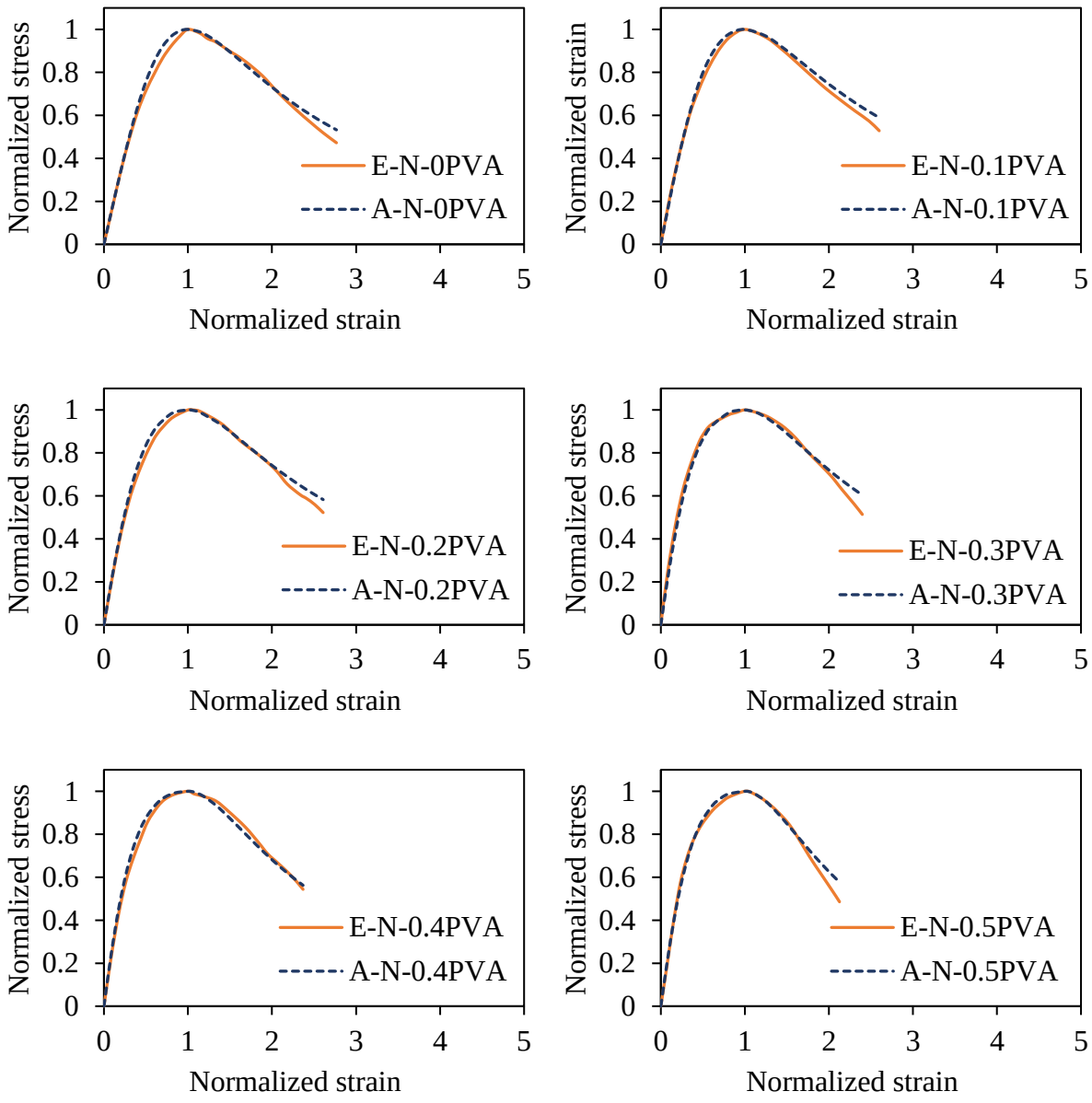

(a) PVAFRC30

Figure continues...

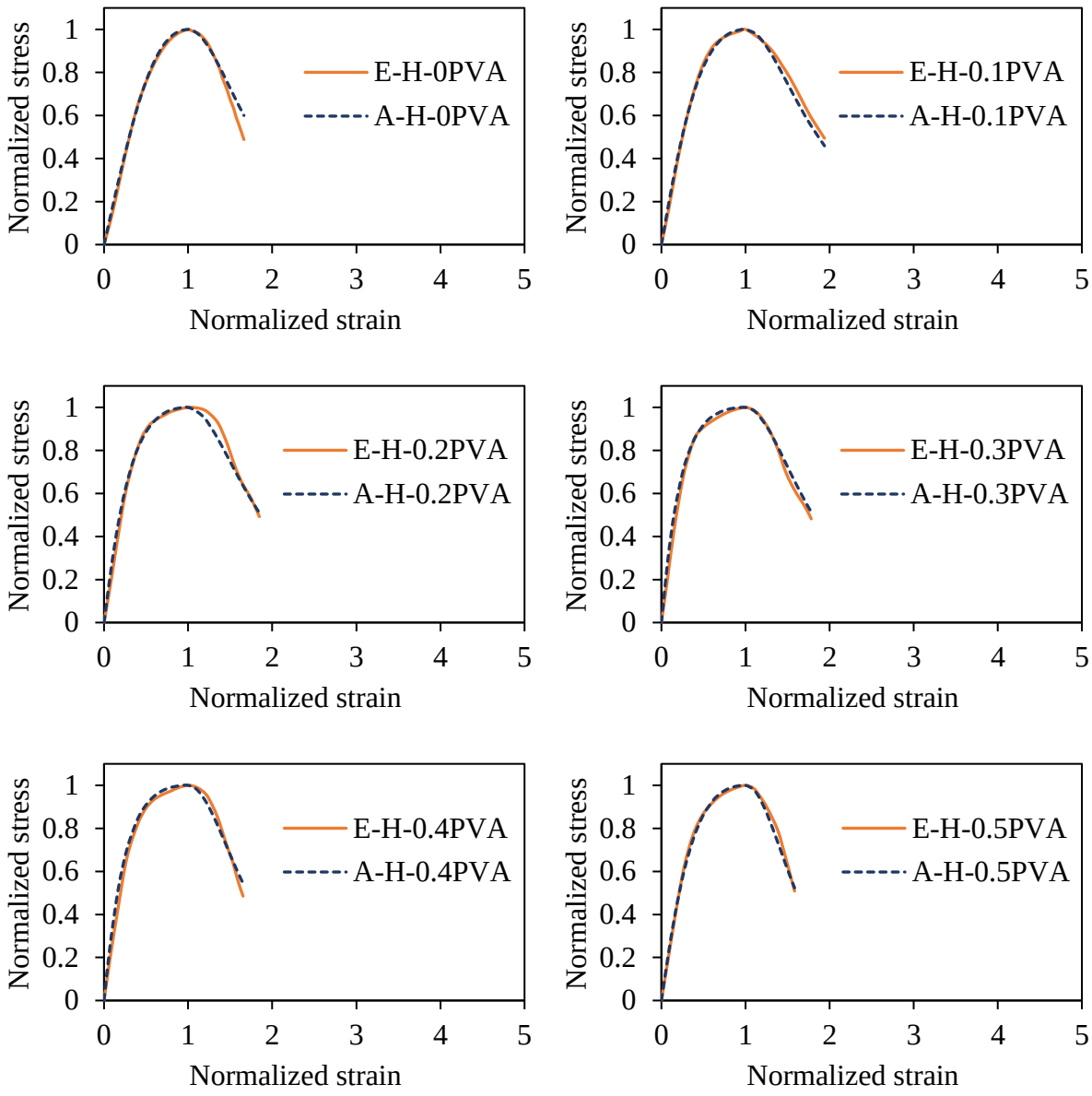

(b) PVAFRC70

Figure 5.17 Comparison of analytical stress-strain curves with experimental stress-strain curves of PVAFRCs

5.2.6.7 Application of existing stress-strain predictive models to experimental data of PVAFRCs

In the literature, Ezeldin and Balaguru 1992 [181], Nataraja et al. 1999 [185], Ou et al. 2012 [183] and Abbass et al. 2018 [196] used a constitutive analytical model and different expressions between material parameter (β) and RI for the analytical modelling of stress-strain curves of FRCs. The authors used constitutive analytical model shown in equation 5.15 and different relationships proposed between β and RI shown in Table 5.9. This constitutive analytical model and proposed relationships between β and RI were applied to the experimental data of PVAFRC30, and PVAFRC70 to examine how accurately they can predict stress-strain curves of PVAFRCs. To accomplish this, the values of β were calculated using the MRI values of PVA fibers from the relationships proposed by Ezeldin and Balaguru 1992 [181], Nataraja et al. 1999 [185], Ou et al. 2012 [183], and Abbass et al. 2018 [196] between β and RI. The calculated β values for 0 to 0.5% of PVA fibers are shown in Table 5.9. Thus, using β values, constitutive analytical model (equation 5.15) and the experimental data of the present study, the predicted stress-strain curves of each mix of PVAFRC30 and PVAFRC70 are presented in Figure 5.18 in normalized stress vs normalized strain form. Figure 5.18 also shows the comparison of normalized predicted stress-strain curves with normalized experimental and analytical stress-strain curves. The accuracy of the fit of these predicted stress-strain curves to the experimental stress-strain curves and analytical stress-strain curves is discussed below.

$$f_{cf} = f'_{cf}\left(\frac{\beta\left(\frac{\varepsilon_c}{\varepsilon_{of}}\right)}{\beta-1+\left(\frac{\varepsilon_c}{\varepsilon_{of}}\right)^{\beta}}\right) \qquad \text{Eq. (5.15)}$$

Table 5.9 β values calculated using MRI values of PVA fibers and relationships between β and RI given in literature

Reference	**Relationship between β and RI**	**MRI of values PVA fibers**	**β values calculated using MRI values of PVA fibers**	
Ezeldin and Balaguru, 1992 [181]	$\beta = 1.093 + 0.7132RI^{-0926}$ (RI = 0.75 to 2.5 for hooked steel fibers) $\beta = 1.093 + 0.74818ri^{-1.387}$, for ri = 2 to 5, where RI was estimated by weight of straight fibers. $\beta = (\frac{f_c'}{32.4})^3 + 1.55$ for plain concrete $\varepsilon_o = 0.002$ suggested in absence of data	0	N-0PVA	2.51
			H-0PVA	9.20
		0.044	58.05	
		0.088	22.87	
		0.133	13.37	
		0.177	9.35	
		0.221	7.17	
Nataraja et al. 1999 [185]	$\beta = 1.93RI^{-0.7406} + 0.5811$ where $RI \leq 3$ $\beta = (\frac{f_c'}{32.4})^3 + 1.55$ for plain concrete	0	N-0PVA	2.51
			H-0PVA	9.20
		0.044	20.09	
		0.088	12.26	
		0.133	9.18	
		0.177	7.54	
		0.221	6.48	
Ou et al. 2012 [183]	$\beta = 0.71RI^2 - 2RI + 3.05$ for RI up to 1.7	0	3.05	
		0.044	2.96	
		0.088	2.88	
		0.133	2.80	
		0.177	2.72	
		0.221	2.64	
Abbass et al. 2018 [196]	$\beta = 1.401RI^2 - 1.56RI + 2.42$ for RI up to 1.2	0	2.42	
		0.044	2.35	
		0.088	2.29	
		0.133	2.24	
		0.177	2.19	
		0.221	2.14	

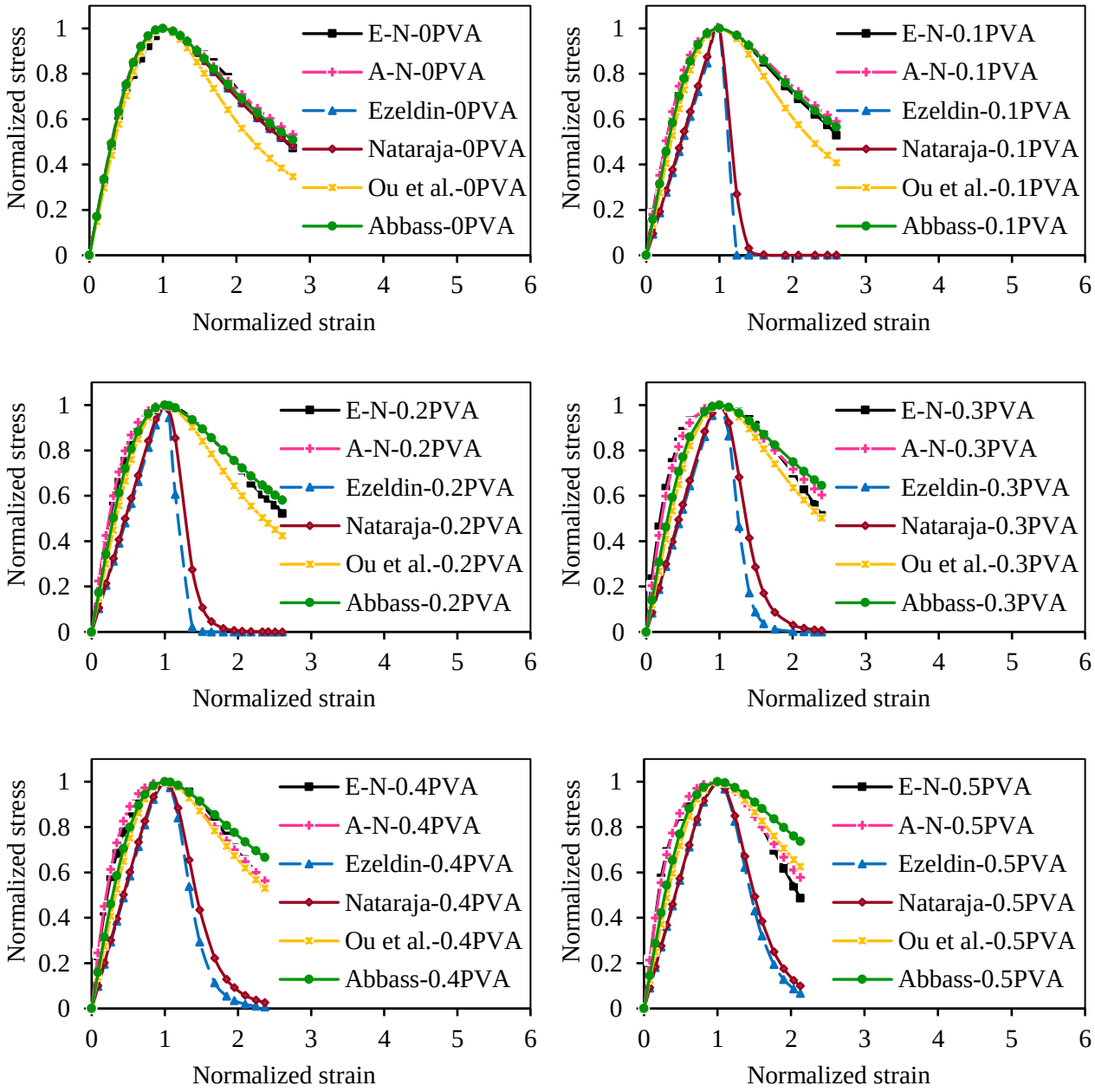

(a) PVAFRC30

Figure continues...

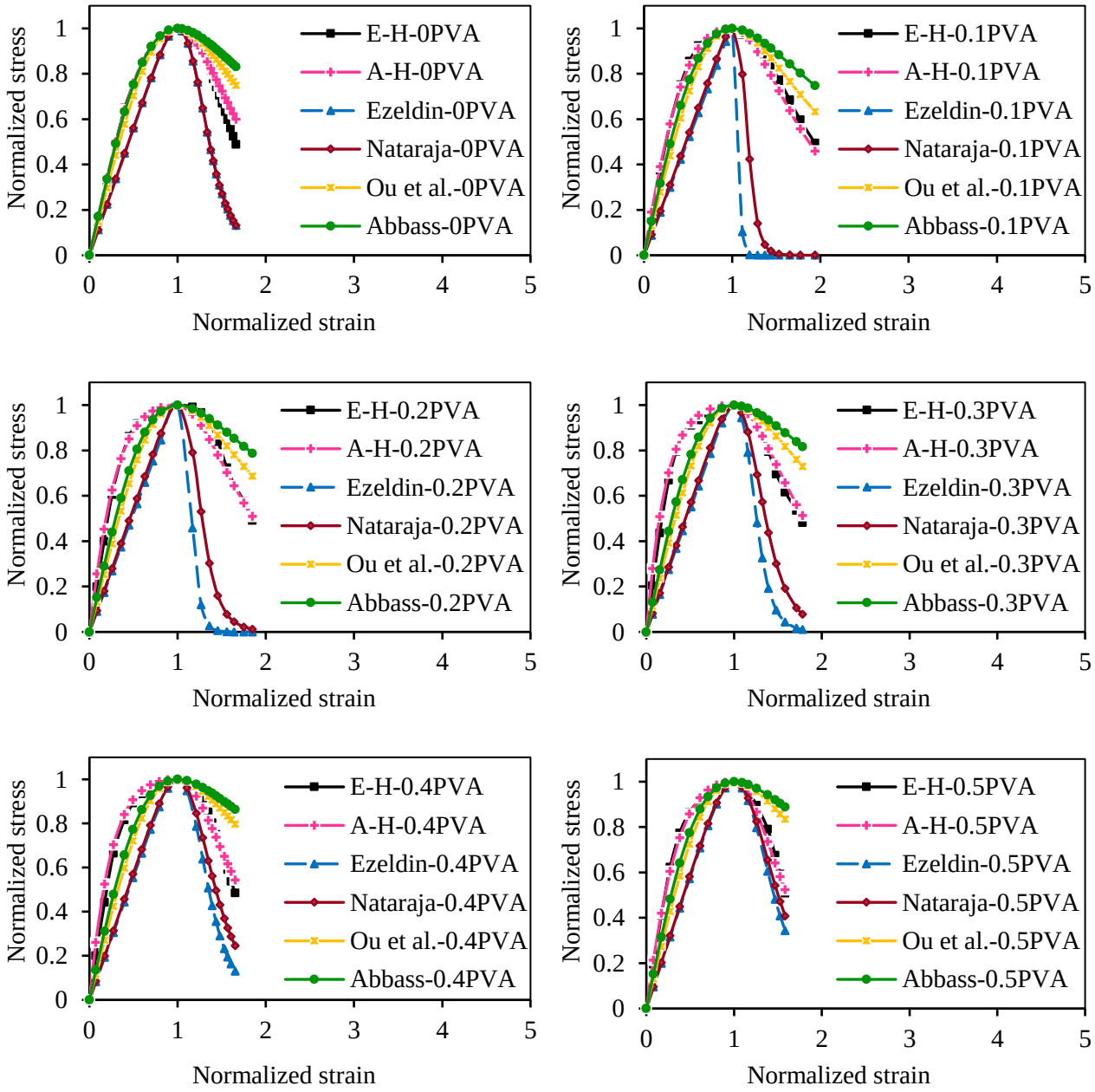

(b) PVAFRC70

Figure 5.18 Comparison of predicted stress-strain curves with experimental and analytical stress-strain curves of PVAFRCs

As shown in Figure 5.18, using Ezeldin and Balaguru's 1992 [181] proposed relationships between β and RI and a constitutive analytical model (equation 5.15), the predicted stress-strain curves of all PVAFRC30 and PVAFRC70 mixes showed disagreement with the experimental stress-strain curves and analytical stress-strain curves, except the N-0PVA mix. The predicted stress-strain curve of N-0PVA shows good agreement with the experimental and analytical stress-strain curve of the same mix. This is because the β value calculated using the MRI value of PVA fibers for N-0PVA from Ezeldin and Balaguru 1992 [181] proposed relationships between β and RI is close to the β_d value of N-0PVA mix calculated from equation 5.10 and the β_d value calculated from the experimental stress-strain curve of N-0PVA mix (refer Table 5.7). But in the case of H-0PVA mix, the calculated β value is not close to the β_d value calculated from equations 5.12 and the β_d value calculated from the experimental stress-strain curve of H-0PVA mix (refer Table 5.7 and 5.9). Therefore, using this β value in the modelling of stress-strain curve underestimated the stress values in both ascending and descending regions of stress–strain curves of H-0PVA mix compared to experimental data. This is also evident from the RMSE and AFV values of N-0PVA and H-0PVA mixes, shown in Table 5.8. The RSME and AFV values calculated from the predicted stress-strain curve of N-0PVA mix are near the RMSE and AFV values of the analytical stress-strain curve of N-0PVA mix, but in the case of H-0PVA mix they don't. This shows close agreement between predicted, analytical, and experimental stress-strain curves of N-0PVA mix. Further, the predicted stress-strain curve of all PVAFRC mixes of PVAFRC30 and PVAFRC70 showed disagreement with the experimental and analytical stress-strain curves. This is because the β values calculated for all percentages of PVA fibers using Ezeldin and Balaguru 1992 [181] proposed relationships between β and RI are very high compared to β_d values calculated from equations 5.10 and 5.12 and β_d values calculated from the experimental stress-strain curves of PVAFRC mixes of both PVAFRC30 and PVAFRC70 (Refer Table 5.7 and 5.9). Therefore, use of these β values in the prediction of stress-strain curves highly underestimates stress values in both ascending and descending regions of the stress–strain curves of PVAFRC mixes of PVAFRC30 and PVAFRC70 compared to experimental data. The relationship proposed by Ezeldin and Balaguru for calculating β values using RI is effective for RI range between 2 to 5. But due to lower MRI values of PVA fibers, the β values calculated using Ezeldin and Balaguru's proposed relationships β and RI were higher than the specified range. Therefore, the predicted stress–strain curves using higher β values have shown dis-agreement with experimental stress–strain curves of PVAFRCs. This is also evident from the RMSE and AFV values of PVAFRC30 and

PVAFRC70 mixes. From Table 5.8, it was observed that RMSE and AFV values calculated from the predicted stress-strain curves using Ezeldin and Balaguru 1992 proposed relationship between β and RI and the constitutive analytical model are not close to RMSE and AFV values calculated from the analytical stress-strain curves, except for N-0PVA mix.

From Figure 5.18, it was observed that, except for the H-0PVA mix, the behaviour of predicted stress-strain curves of PVAFRC30 and PVAFRC70 mixes using Nataraja et al. 1999 [185] proposed relationship between β and RI and the constitutive analytical model was found similar to the behaviour of predicted stress-strain curves using Ezeldin and Balaguru 1992 [181] proposed relationship between β and RI and the constitutive analytical model. As shown in Figure 5.18, using Nataraja et al. 1999 [185] proposed relationship and the constitutive analytical model, the predicted stress–strain curves of PVAFRC30 and PVAFRC70 mixes showed dis-agreement with the experimental stress–strain curves, except H-0PVA mix. The predicted stress-strain curve of H-0PVA showed good agreement with the experimental and analytical stress-strain curves because the β value calculated using the MRI value of PVA fiber content for H-0PVA mix from Nataraja et al. 1999 [185] proposed relationship was close to the β_d value of H-0PVA mix calculated from equation 5.12 and the β_d value calculated from the experimental stress-strain curve of H-0PVA mix (refer Table 5.7 and 5.9). Therefore, using this β value, the predicted stress-strain curve for the H-0PVA mix was shown to be in good agreement with the experimental and analytical stress-strain curves. This is also evident from the RMSE and AFV values from the predicted stress-strain curve of H-0PVA mix, which is close to the RMSE and AFV values of the analytical stress-strain curve of H-0PVA mix (refer Table 5.8). Similar to Ezeldin and Balaguru 1992 [181] proposed relationships between β and RI, Nataraja et al. 1999 [185] prosed relationships β and RI also underestimated the stresses in both ascending and descending regions of the predicted stress-strain curve, thereby showed disagreement between the predicted stress-strain curves of PVAFRC mixes in both PVAFRC30 and PVAFRC70. This is because the β values calculated using 0.1% to 0.5% of PVA fibers were obtained higher than β_d values calculated from equations 5.10 and 5.12 and β_d values calculated from the experimental stress-strain curves (refer Table 5.7 and 5.9). Therefore, the use of these β values in the prediction of stress-strain curves highly underestimates the stress values in both ascending and descending regions of the stress–strain curves of all PVAFRC30 and PVAFRC70 mixes, except for H-0PVA mix compared to experimental data. The relationships proposed by Nataraja et al. 1999 [185] for calculating β values using RI values are effective for RI $\leq$ 3. But the β values calculated by this relationship using MRI values of

PVA fibers are higher than the given RI range. Therefore, the predicted stress–strain curves using higher β values showed dis-agreement with the experimental stress–strain curves of specimens of two grades of PVAFRCs. This is also evident from the RMSE and AFV values of PVAFRC30 and PVAFRC70 mixes. From Table 5.8, it was observed that RMSE and AFV values calculated from the predicted stress-strain curves using Nataraja et al. 1999 [185] proposed relationships between β and RI and the constitutive analytical model was not close to RMSE and AFV values calculated from the analytical stress-strain curves, except for the H-0PVA mix.

As shown in Figure 5.18, using Ou et al. 2012 [183] proposed relationship between β and RI and a constitutive analytical model, the predicted stress-strain curves of PVAFRC30 mixes showed relative agreement with the experimental and analytical stress-strain curves of the same mixes in both the ascending and descending regions. This is because the calculated β values using MRI values of PVA fibers content for PVAFRC30 mixes from Ou et al. 2012 [183] proposed relationship between β and RI was near to β_d values calculated from equation 5.10 and β_d value calculated from the experimental stress-strain curve of PVAFRC30 mixes (refer Table 5.7 and 5.9). Therefore, using these β value for analytical modelling of stress-strain curve slightly underestimated stresses in the descending region of stress-strain curves of N-0PVA, N-0.1PVA, and N-0.2PVA mixes, and underestimated the stresses in the ascending region of stress-strain curves of N-0.3PVA, N-0.4PVA, and N-0.5PVA mixes compared to experimental data. Therefore, the predicted stress-strain curves of PVAFRC30 mixes showed relative agreement with experimental and analytical stress-strain curves. Similarly, using Ou et al. 2012 [183] proposed relationship between β and RI and a constitutive analytical model, predicted stress-strain curves of all PVAFRC70 mixes showed disagreement with the experimental and analytical stress-strain curves of the same mixes in both the ascending and descending regions. This is because the β values calculated using MRI values of 0.1% to 0.5% PVA fiber content for all mixes of PVAFRC70 from Ou et al. 2012 [183] proposed relationship between β and RI was lower than β_d values calculated from equation 5.12 and β_d values calculated from the experimental stress-strain curve of all PVAFRC70 mixes (refer Table 5.7 and 5.9). Therefore, use of these β values underestimated stresses in the ascending region and overestimated stresses in the descending region of predicted stress-strain curves of all PVAFRC70 mixes compared to the experimental and analytical stress-strain curves of the same mixes. This was also evident from the RMSE and AVF values. From Table 5.8, it was observed that the calculated RMSE

and AVF from the predicted stress-strain curves using Ou et al. 2012 [183] model was not close to the RMASE and AVF values calculated from analytical stress-strain curves.

As shown in Figure 5.18, using Abbass et al. 2018 [196] proposed relationship between β and RI and a constitutive analytical model, predicted stress-strain curves of N-0PVA, N-0.1PVA, and N-0.2PVA mixes showed good agreement with the experimental stress-strain curves and analytical stress-strain curves of the same mixes. This is because the β value calculated for N-0PVA, N-0.1PVA, and N-0.2PVA mixes using Abbass et al. 2018 [196] proposed relationship between β and RI was close to β_d values calculated from equation 5.10 and β_d values calculated from the experimental stress-strain curves of the same mixes (refer Table 5.7). Therefore, using these β values, the predicted stress-strain curves for N-0PVA, N-0.1PVA, and N-0.2PVA mixes showed good agreement with experimental and analytical stress-strain curves of the same mix. This is also evident from the RMSE and AFV values calculated from the predicted stress-strain curves of the N-0PVA, N-0.1PVA, and N-0.2PVA mixes using Abbass et al. 2018 [196] proposed relationship between β and RI and a constitutive analytical model, was close to RMSE and AFV values of the analytical stress-strain curves of N-0PVA, N-0.1PVA, and N-0.2PVA mixes (refer Table 5.8). Furthermore, the predicted stress-strain curves of N-0.3PVA, N-0.4PVA, N-0.5PVA, and all mixes of PVAFRC70 showed disagreement with the experimental and analytical stress-strain curves. This is because the β value calculated using MRI values of various volume percentages of PVA fibers for N-0.3PVA, N-0.4PVA, N-0.5PVA and all mixes of PVAFRC70 through Abbass et al. 2018 [196] proposed relationship between β and RI was higher than β_d values calculated from equations 5.10 and 5.12 and the β_d value calculated from the experimental stress-strain curves of the same mixes (refer Table 5.7 and 5.9). Therefore, use of these β values underestimated the stresses in the ascending region and overestimated the stresses in the descending region of the predicted stress-strain curves, which resulted in disagreement with the experimental and analytical stress-strain curves of N-0.3PVA, N-0.4PVA, N-0.5PVA, and all mixes of PVAFRC70. This is also evident from the RMSE and AFV values of mixes. From Table 5.8, it was observed that RMSE and AFV values calculated for N-0.3PVA, N-0.4PVA, N-0.5PVA and all mixes of PVAFRC70 from the predicted stress-strain curves using Abbass et al. 2018 [196] proposed expression between β and RI and the constitutive analytical model was not close to RMSE and AFV values calculated from the analytical stress-strain curves of the same mixes.

5.3 Part B: Study on Basalt Fiber Reinforced Concretes (BFRCs)

5.3.1 Materials Used for the Development of BFRCs

In accordance with the Bureau of Indian Standards, constituent materials used for the development of PVAFRC was same used for the development of BFRCs. As shown in Figure 5.19, filament-type short length basalt fibers of length 6 mm and diameter of 13 μm was used for the development of BFRCs. The properties of basalt fibers are presented in Table 5.10. A high-performance superplasticizer, Masterglenium Sky-8233, was used to improve the workability performance of concrete. The percentage of superplasticizer was taken to be the total weight of total binder materials.

Figure 5.19 Chopped basalt fibers

Table 5.10 Properties of basalt fiber

Properties	**Details**
Diameter	0.013 mm
Length	6 mm
Aspect ratio	461.5
Tensile strength	2700 N/mm^2
Density	2600 kg/m^3
Specific gravity	2.6
Elongation (%)	3.1
Fiber type	Filament

5.3.2 Mix Proportions and Mixes of BFRCs

Similar to Part-A, the effects of adding different percentages of basalt fiber on the mechanical, microstructural properties, and compressive stress-strain behavior of NSC of M30 grade and HSC of M70 grade were investigated. The mix proportions, constituent material quantities, and mix designations for all mixes of BFRC30 and BFRC70 are presented in Table 5.11. For each

strength of concrete, basalt fibers in quantities of 0%, 0.1%, 0.2%, 0.3%, 0.4%, and 0.5% of the volume of concrete were added. Based on the strength of the PC of NSC and HSC, the two mix proportions are designated as BFRC30 and BFRC70. In both BFRC30 and BFRC70, the mix containing 0% BFs is considered the PC mix or control mix. In the given mix designation, the first term stands for the strength of concrete, and the second term stands for the volume percentage of fibers added. For example, in N-0.3BF, N stands for the strength of concrete, and 0.3BF stands for the addition of 0.3% of basalt fibers.

Table 5.11 Mix proportions, mix designations and constituent materials quantities for BFRCs

Grade of concrete	**Mix designation**	**Basalt fibers (%)**	**Mix proportion**	**Constituent material (kg/m^3)**					**w/b ratio**	**SP**
				Binder material			**FA**	**CA**		
				OPC	**Fly ash**	**AF-1203**				
BFRC30 (Normal strength BFRC)	N-0BF	0	1:1.81:2.57	315	105	-	760	1080	0.4	0.25%
	N-0.1BF	0.1								
	N-0.2BF	0.2								
	N-0.3BF	0.3								
	N-0.4BF	0.4								
	N-0.5BF	0.5								
BFRC70 (High strength BFRC)	H-0BF	0	1:1.22:1.58	420	120	60	730	950	0.26	0.725%
	H-0.1BF	0.1								
	H-0.2BF	0.2								
	H-0.3BF	0.3								
	H-0.4BF	0.4								
	H-0.5BF	0.5								

w/b-water to binder ratio, SP-Superplasticizer, AF-1203-Alccofine-1203, FA-Fine aggregate, CA-Coarse aggregate

5.3.3 Mixing, Cast and Curing of BFRCs Specimens

According to the concrete mixing guidelines given in IS 456-2000 [133], all the raw constituent materials were mixed well in a pan mixer for 1 minute. Half of the measured water was added to the dry mix and mixed for 30 seconds. In the remaining water, a fixed quantity of superplasticizer was mixed thoroughly and then transferred to the wet mix, allowing it to be mixed for another 60 seconds. The pre-weighed basalt fibers were added to the PC mix and mixed for an additional 2 minutes to confirm the appropriate mix of fibers in the PC. The fiber mixing duration was increased with the increasing weight of basalt fibers. For each mix, 3 cylindrical specimens of size 200 mm in height and 100 mm in diameter were cast to study the compressive stress-strain behavior of concrete, 3 cube specimens of size 100 mm on each side

were cast to test the compressive strength of concrete, 3 cylindrical specimens of size 200 mm in height and 100 mm in diameter were cast to test the split tensile strength of concrete, and 3 prisms of size 500 mm in length, 100 mm in width, and 100 mm in depth were cast to test the flexural strength and flexural load-deflection behavior of concrete. Fresh concrete was filled into iron moulds and compacted with the help of a vibrating table. After 24 hours of casting, all the concrete specimens were removed from the iron moulds and immersed in water for curing for 28 days before being tested.

5.3.4 Test Methods for BFRCs

The workability, compressive strength, flexural strength, flexural load-deflection behavior, split tensile strength, and compressive stress-strain behavior of BFRCs were evaluated using the methods followed for the evaluation of PVAFRCs. The tests conducted on BFRC mixes are shown in Figure 5.20.

(a) Slump

(b) Compressive strength

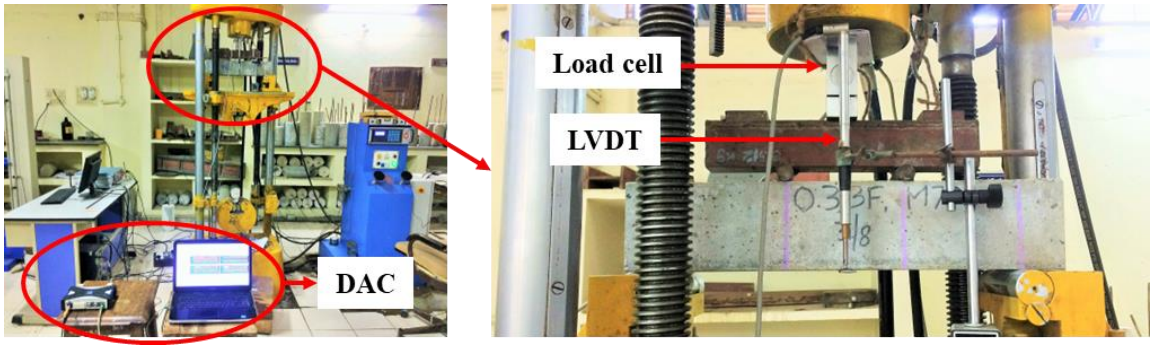

(c) Flexural strength and load-deflection behaviour

Figure continues...

(d) Split tensile strength

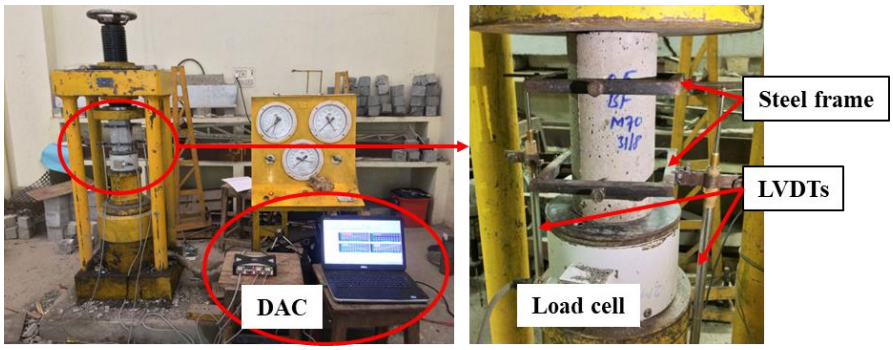

(e) Compressive stress-strain behavoiur

Figure 5.20 Tests on BFRC mixes

5.3.5 Results and Discussions

5.3.5.1 Workability

The slump cone test results of BFRC30 and BFRC70 mixes are graphically presented in Figure 5.21. It was observed that, at a predetermined water-to-binder ratio and superplasticizer dosage, the increase in the percentage of basalt fiber addition decreased slump values for BFRC30 and BFRC70 mixes [40,91,92]. The addition of 0.1% basalt fibers was evenly mixed into the concrete without causing balling, but it did reduce the slump values of N-0.1BF and H-0.1BF mixes. In the case of BFRC30, a minor balling effect was encountered with a 0.2% basalt fiber addition, and this effect partially increased when 0.3% of basalt fiber was added, becoming severe for further additions. The reduction in water content was observed with increasing percentages of basalt fibers. Consequently, the workability of N-0.3BF, N-0.4BF, and N-0.5BF mixes decreased. For BFRC70, the addition of 0.2% basalt fibers took some time to mix properly into the concrete to achieve homogeneous consistency. Furthermore, the mixing time of fibers into concrete slightly increased with the addition of 0.3% and 0.4% basalt fibers, and a decrease in water content was observed during mixing compared to previous mixes. Moreover, the addition of 0.5% fibers led to a balling effect, taking extra time to mix into the

concrete, resulting in the development of a harsh mix. Consequently, the workability of H-0.4BF and H-0.5BF mixes reduced, especially in the case of H-0.5BF compared to the control mix. For N-0.4BF, N-0.5BF, and H-0.5BF mixes, the balling effect of basalt fibers was very dominant. This difficulty during mixing resulted in the lowest slump values compared to the slump values of control mixes and other BFRC mixes. The balling effect in BFRC mixes may be attributed to the moisture absorption property of basalt fibers, and uneven dispersion of the higher volume percentage of basalt fibers added may also be due to the development of frictional forces during the mixing of constituent materials. For these reasons, the workability of fresh BFRC mixes decreased with an increase in the addition of various volume percentages of basalt fibers.

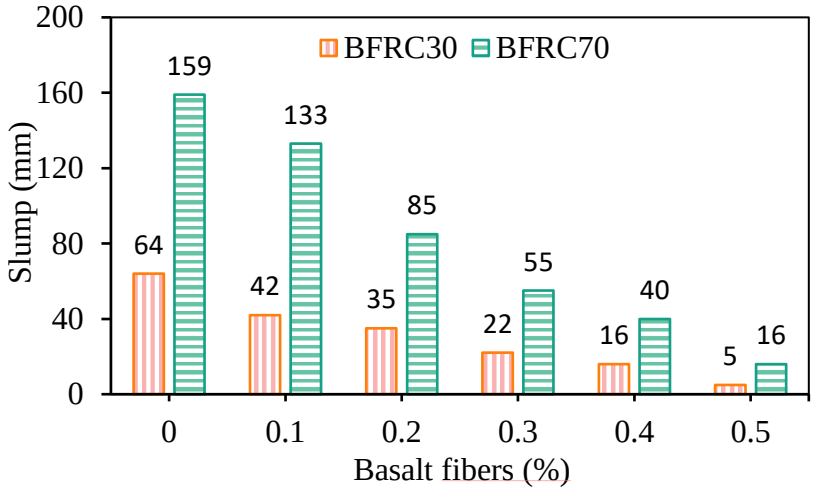

Figure 5.21 Workability of BFRCs mixes

5.3.5.2 Compressive strength

The cube compressive strength of PC partially increased with the addition of 0.1%, 0.2%, and 0.3% basalt fibers in two grades of BFRCs (BFRC30 and BFRC70). The compressive strength results of all mixes of BFRC30 and BFRC70 are presented in Table 5.12 and graphically shown in Figure 5.22. From the test results, it was observed that with the addition of 0.1%, 0.2%, and 0.3% basalt fibers, the compressive strength of BFRC30 mixes improved more than BFRC70 mixes. The compressive strength of concrete improved the most with 0.3% basalt fibers addition over all other percentages in both grades of BFRCs. Compared to control mixes, the compressive strength of N-0.3BF and H-0.3BF mixes improved by 10.79% and 2.48%, respectively. The addition of basalt fibers above 0.3% decreased the compressive strength of concrete in BFRC30 and BFRC70 mixes. The percentage change in compressive strength of BFRC mixes with respect to the addition of basalt fibers percentages is presented in Table 5.13.

The partial increase in the compressive strength of BFRC mixes may be attributed to the addition of a lower volume percentage of shorter-length basalt fibers, which leads to good interfacial bond strength with the matrix as they mix properly into PC, thereby playing an effective role in the crack arresting and crack bridging mechanism [159]. Also, a decrement in the compressive strength of BFRC mixes containing 0.4% and 0.5% fibers may be attributed to the addition of higher volume percentages of basalt fibers, which led to the development of fiber balling effects and improper distribution of fibers in the concrete. The balling effect of fibers leads to the development of a structure like a fiber network in concrete and also increases the pore concentration [43], resulting in the heterogeneity of the mix, ultimately reducing the strength of BFRCs [171]. Previously, at 0.3% basalt fibers addition, Zhou et al. 2020 [105], Biradar et al. 2020 [197], and Borhan 2013 [91] reported 5.07%, 9.82%, and 12.5% improvement in compressive strength of concrete compared to PC, and they also reported a decrease in compressive strength of concrete with further increase in the percentage of basalt fibers additions.

Failure mode of compressive strength specimens

During testing, a few cracks formed on the surface of BFRC specimens before reaching their maximum load. Once the specimens reached the ultimate load, the cracks widened and propagated further as the load decreased. The failure of these specimens was not as rapid as that of PC specimens. However, the specimens exhibited cracking, and there was minimal spalling of concrete. Despite this, the cross-sectional area was not crushed as in the case of PC specimens in the two strengths of BFRCs (see Figure 5.23).

Table 5.12 Strength properties of BFRCs mixes

Mix designation	BFRC30			BFRC70		
	CS (MPa)	FS (MPa)	STS (MPa)	CS (MPa)	FS (MPa)	STS (MPa)
0BF	38.57	4.27	4.09	80.33	6.22	5.81
0.1BF	39.98	4.68	4.30	81.17	7.45	6.21
0.2BF	41.21	5.56	4.65	82.14	8.57	6.43
0.3BF	42.73	6.58	5.44	82.62	9.15	6.75
0.4BF	37.97	6.11	5.22	79.13	8.79	6.21
0.5BF	33.78	5.12	5.03	75.29	8.13	5.93

CS: Compressive strength; FS: Flexural strength; STS: Split tensile strength

Table 5.13 Percentage increase or decrease in strength properties of BFRC mixes compared to control mix

Mix designation	BFRC30			BFRC70		
	CS	FS	STS	CS	FS	STS
0BF	-	-	-	-	-	-
0.1BF	3.64	9.60	5.06	1.05	19.83	6.85
0.2BF	6.84	30.21	13.62	2.25	37.88	10.68
0.3BF	10.79	53.98	33.07	2.84	47.19	16.16
0.4BF	-1.57	43.09	27.63	-1.50	41.34	6.85
0.5BF	-12.41	19.91	22.96	-6.28	30.70	2.12

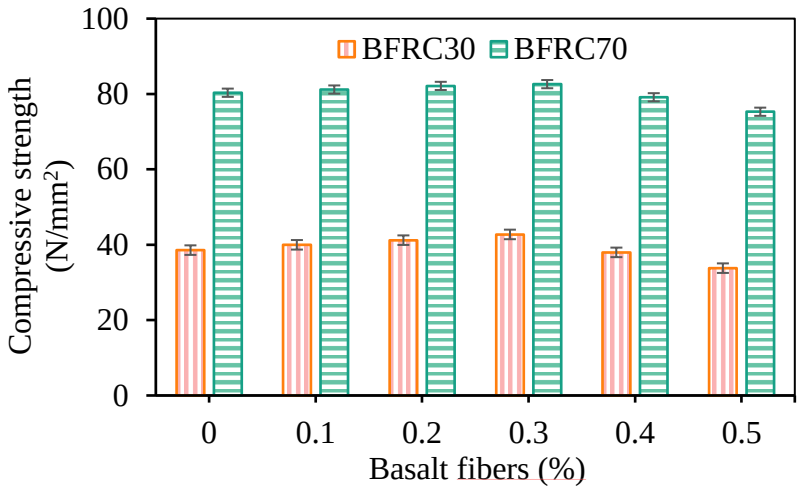

Figure 5.22 Compressive strength of BFRCs

Figure 5.23 Failure of compressive strength specimens of BFRCs

5.3.5.3 Flexural strength and flexural load-deflection behaviors

The flexural strength results of BFRC30 and BFRC70 mixes are presented in Table 5.12 and graphically illustrated in Figure 5.24. From the test results, it was observed that the enhancement of flexural strength of BFRC30 and BFRC70 mixes with the addition of basalt fibers of 0.1%, 0.2%, 0.3%, 0.4%, and 0.5% was significantly greater than the enhancement that occurred in the compressive strength. Earlier, D. Wang et al. 2019 [102] also observed an

effective improvement in the flexural strength of concrete compared to the compressive strength with the addition of basalt fibers. The flexural strength of concrete improved the most with the addition of 0.3% basalt fibers in both BFRC30 and BFRC70 grades. Compared to control mixes, the flexural strength of N-0.3BF and H-03BF mixes improved by 53.98% and 47.19%, respectively, with the addition of 0.3% basalt fibers. In both BFRCs, the increase in flexural strength slightly decreased for mixes with 0.4% and 0.5% basalt fibers compared to the mixes with 0.3% basalt fibers. However, the flexural strength of mixes containing 0.4% and 0.5% basalt fibers was higher than those of control mixes. This slight decrease in flexural strength may be attributed to the heterogeneity of the mixes caused by the addition of higher volume percentages of basalt fibers. The percentage increase in flexural strength of BFRC mixes with respect to the addition of basalt fibers is presented in Table 5.13. The effect of 0 to 0.5% of basalt fibers on deflection behavior of concrete was evaluated on flexural specimens of BFRCs, as shown in Figure 5.20(c). The experimental load-deflection curves obtained at the midspan of specimens are shown in Figure 5.25. It was observed from Figure 5.25 that the specimens of BFRC30 and BFRC70 mixes exhibited linear load-deflection behavior up to the point of failure. With respect to flexural strength, the deflection behavior of BFRC specimens improved the most with the addition of 0.3% basalt fibers compared to other percentages of basalt fibers. Compared to control mixes, the ultimate deflection of N-0.3BF and H-0.3BF mixes increased by 107.73% and 99.52%, respectively. Similarly to flexural strength, the ultimate deflection of specimens with 0.4% and 0.5% basalt fibers in both BFRCs was slightly lower than that of specimens with 0.3% basalt fibers. However, the percentage increase in ultimate deflections was higher than control mix specimens. Basalt fiber's excellent bonding mechanism and crack bridging effect against crack propagation were responsible for the improvement in deflection behavior of BFRC specimens. In previous literature, Biradar et al. 2020 [197] also reported an 18.83% improvement in flexural strength with the addition of 0.3% basalt fibers, and with the addition of 0.5% basalt fibers, the improvement in flexural strength decreased to 15.75% compared to the control mix. Jiang et al. 2014 [198] also reported that compared to the control mix, the flexural strength of concrete improved by 9.58% and 10.37% with the addition of 0.3% basalt fibers of 12 mm and 22 mm lengths, and the increase in flexural strength decreased slightly with the addition of 0.4% basalt fibers of both lengths.

Failure mode of flexural strength specimens

During testing, a small crack developed on the surface of BFRCs flexural specimens at the mid-span before reaching the ultimate load. As the load increased further, the crack extended from

the bottom phase to the top phase, ultimately causing the failure of the specimens in two halves after reaching the ultimate load, as shown in Figure 5.26.

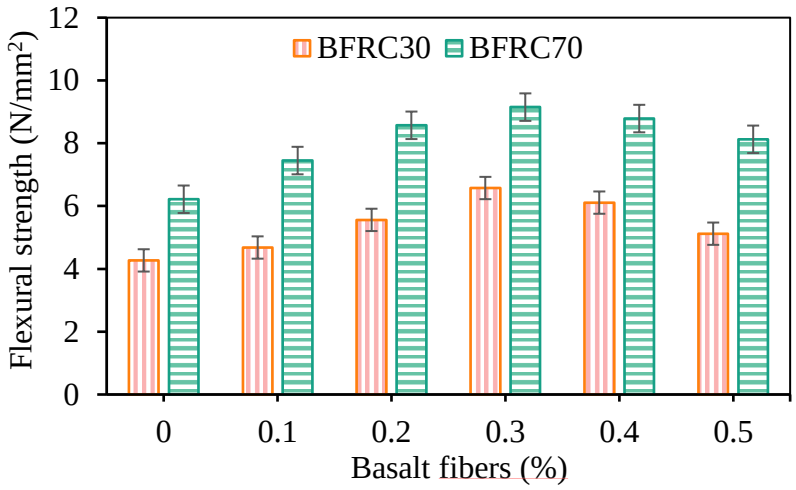

Figure 5.24 Flexural strength of BFRCs

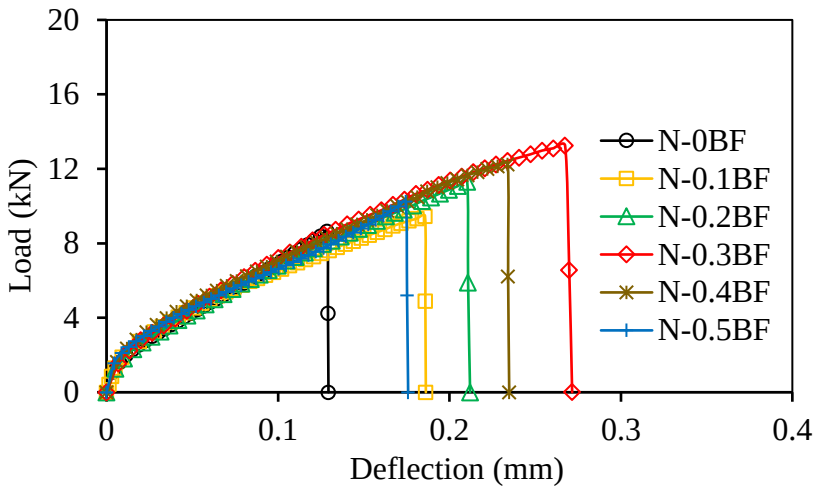

(a) BFRC30

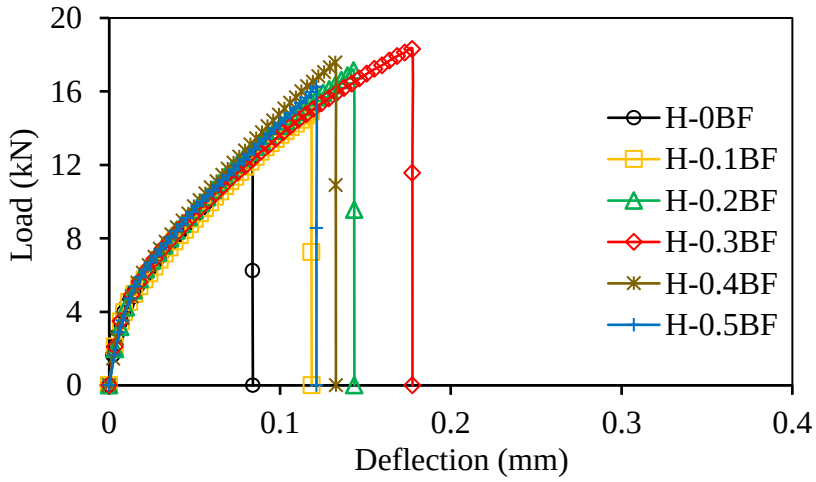

(c) BFRC70

Figure 5.25 Flexural load-deflection behaviour of BFRCs

Figure 5.26 Failure of flexural strength specimens of BFRCs

5.3.5.4 Split tensile strength

The split tensile strength results of BFRC30 and BFRC70 mixes are tabulated in Table 5.12 and graphically presented in Figure 5.27. The addition of basalt fibers (0.1%-0.5%) significantly improved the split tensile strength of BFRC mixes. From the test results, it was observed that basalt fibers more effectively improved the split tensile strength of BFRC30 mixes than that of BFRC70 mixes. In both strengths of BFRCs, the addition of 0.3% basalt fibers resulted in the highest split tensile strengths. The split tensile strengths of N-0.3BF and H-0.3BF mixes increased by 33.07% and 16.16%, respectively, compared to the control mixes. The increase in split tensile strength slightly decreased with the addition of 0.4% and 0.5% basalt fibers compared to the mixes with 0.3% basalt fibers. However, these mixes exhibited higher split tensile strength compared to the control mixes of both grades. X. Sun et al. 2019 [103] also previously reported a similar observation with 6 mm length basalt fibers. The percentage increase in split tensile strength of specimens from BFRC30 and BFRC70 mixes, with respect to control mixes, is presented in Table 5.13. The reason for the increase in split tensile strength of BFRC mixes is that the fibers in the cracked plains effectively prevent the spread of microcracks by inducing bridging action between the cracked surfaces. Furthermore, due to the strong bonding between the matrix and fibers, stresses are transferred to bridge fibers through bridging action, preventing the spread of macrocracks [100]. The balling effect of the fibers resulted in improper compaction of concrete, increasing internal pores and forming a weak matrix. This may be attributed to a slight decrease in the split tensile strength of concrete mixes incorporated with 0.4% and 0.5% basalt fibers. Previously, in the literature, Biradar et al. 2020 [197] and J. Wang and Zhang 2010 [199] also reported a similar observation. They noted a 36.70% and 22.5% improvement in the split tensile strength of concrete with the addition of 0.3% basalt fibers of lengths 12 mm and 30 mm, respectively. It was also reported that the increase in split tensile strength of concrete decreased to 23.12% and 15% with the addition of 0.5% basalt fibers of 12 mm length and 0.35% basalt fibers of 30 mm length, respectively, compared to the control mix.

Failure mode of split tensile strength specimens

During testing, a vertical crack developed in the compression zone of the specimen along the direction of the loading before reaching the ultimate load, as shown in Figure 5.28(a). As the load reached the ultimate point, a vertical crack started propagating from the upper phase to the bottom phase of the specimen. In the case of specimens with 0.1%-0.5% basalt fibers, after reaching the ultimate load, the vertical crack widened, and the load-carrying capacity of the specimens gradually decreased. The specimens did not fail completely into two halves, as shown in Figure 5.28.

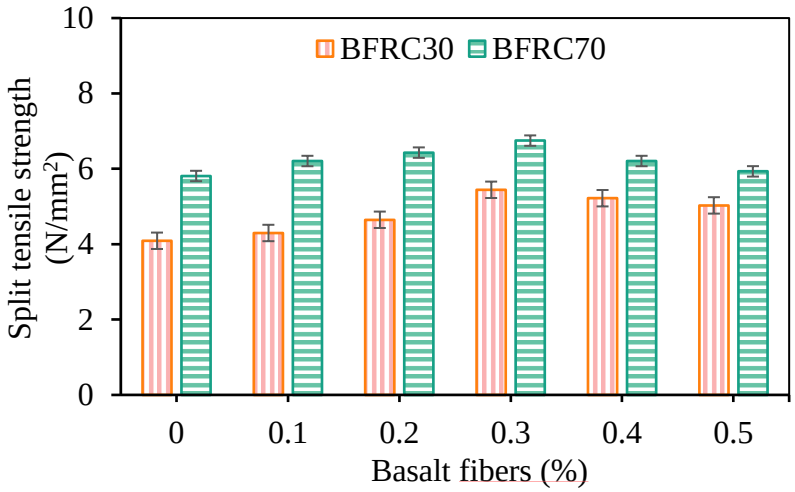

Figure 5.27 Split tensile strength of BFRCs

Figure 5.28 Failure of split tensile strength specimens of BFRCs

5.3.5.5 Compressive stress–strain behaviors

Under the uniaxial compression test, the experimental stress-strain curves obtained for BFRC30 and BFRC70 mixes are shown in Figure 5.29. It was observed from Figure 5.29 that the addition of basalt fibers to the PC mix had no significant influence on the initial stages of the ascending phase of the stress-strain curves of BFRCs. All the stress-strain curves of BFRCs showed a linear elastic response up to 60% of the ultimate strength in the ascending phase, and after that, the linear response turned nonlinear. The improvement in stress-strain behavior of BFRCs due to the addition of basalt fibers becomes noticeable after the linear elastic response phase of the

stress-strain curves. The addition of basalt fibers greatly influenced crack propagation, crack width increment, post-peak response, and the decrease in load after the peak stress of BFRCs mixes. In two grades of BFRCs, the addition of basalt fibers in dosages ranging from 0.1% to 0.5% improved the post-peak behavior of BFRC specimens compared to PC mixes. This enhancement may be attributed to the added fibers resisting crack propagation through the crack-bridging phenomenon, increasing the volumetric strain capacity even after the occurrence of several cracks [164,165]. The addition of 0.3% basalt fibers in the PC mix exhibited the highest improvement in both pre-peak and post-peak behavior of the stress-strain curve compared to other percentages of basalt fiber additions. BFRC30 mixes, with the addition of 0.1% to 0.5% basalt fibers, demonstrated larger post-peak behavior and higher failure strain than BFRC70 mixes. Consequently, specimens of BFRC30 mixes exhibited better ductility than those of BFRC70 mixes.

Failure mode of compressive stress-strain specimens

The increase in compressive strength of concrete usually indicates increased brittleness. During testing of PC cylindrical specimens, small microcracks formed on the surface before reaching the ultimate load. As the load approached the ultimate stage, these small cracks propagated further. Upon reaching the maximum load, a major crack occurred with a noise in the loading direction, leading to the crushing of the surrounding concrete and complete failure of the specimens, as shown in Figure 5.30(a). The failure mode of PC specimens was brittle, attributed to tensile splitting [186]. The loudness of noise increased for the PC specimens of HSC. On the other hand, small multiple non-linear vertical cracks commenced to appear on the surface of BFRC specimens before reaching the ultimate load. As the load increased further, these cracks propagated along the direction of loading from the top phase to the bottom phase of the specimens, as shown in Figure 5.30(b). After reaching the ultimate load, the load-carrying capacity of specimens gradually decreased due to crack widening and spreading to the edges, leading to crushing and spalling of the surrounding concrete and the failure of BFRC specimens [105]. The typical failure modes of some BFRC specimens are shown in Figure 5.30(c).

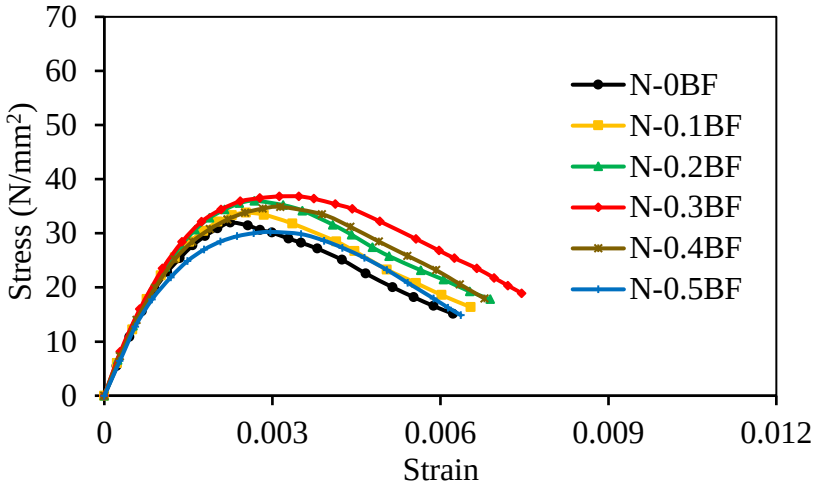

(a) BFRC30

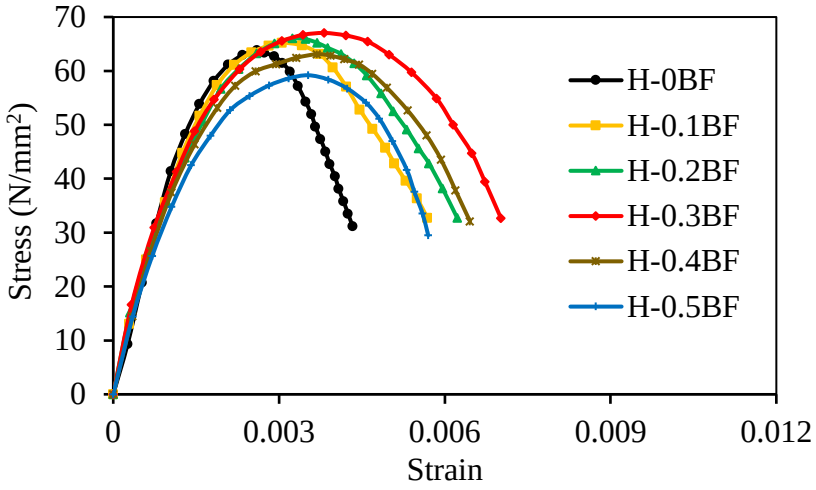

(b) BFRC70

Figure 5.29 Experimental compressive stress-strain behaviour of BFRCs

(a) (b) (c)

Figure 5.30 Failure of BFRCs specimens under the test of uniaxial compressive stress-strain behavior (a) plain concrete (b) cracking of BFRC (c) BFRC specimens

5.3.5.6 Energy absorption capacity

The toughness of concrete increases with the incorporation of small fibers [200,201]. Therefore, the change in the toughness of BFRC30 and BFRC70 concrete mixes, due to the addition of various volume percentages of basalt fibers, was measured in terms of EAC from the area under

stress-strain curves. The calculated EAC for BFRC30 and BFRC70 mixes is shown in Table 5.14, and the change in EAC with respect to the percentage of basalt fiber additions is illustrated in Figure 5.31. The test results indicate that the addition of 0.1% to 0.5% of basalt fibers to the control mix improved the EAC of the concrete. BFRC mixes with 0.3% basalt fibers showed a higher EAC than mixes with other percentages of basalt fibers in two strengths of BFRCs. Compared to control mixes, the addition of 0.3% basalt fibers increased the EAC of N-0.3BF and H-0.3BF mixes by 47.6% and 89.6%, respectively. The increase in EAC decreased for mixes with 0.4% and 0.5% basalt fibers in both grades compared to the EAC of mixes with 0.3% basalt fibers. However, these mixes exhibited higher EAC than that of control mixes. The percentage increase or decrease in EAC of BFRC mixes concerning the addition of basalt fibers, compared to control mixes, is presented in Table 5.15. The highest improvement in EAC of N-0.3BF and H-0.3BF was attributed to the significantly enhanced pre-peak and post-peak behavior of stress-strain curves with the addition of 0.3% basalt fibers. This improvement can be attributed to the strong fiber-matrix bond strength and crack bridging phenomena of basalt fibers. As a result, the large region accumulated below the stress-strain curves had a higher EAC compared to mixes with other percentages of basalt fibers. Among the two grades, BFRC70 mixes showed a higher EAC than BFRC30 mixes. Previously, W. Li and Xu 2009 [202] also reported the highest increment in EAC of concrete incorporated with the addition of 0.3% basalt fibers.

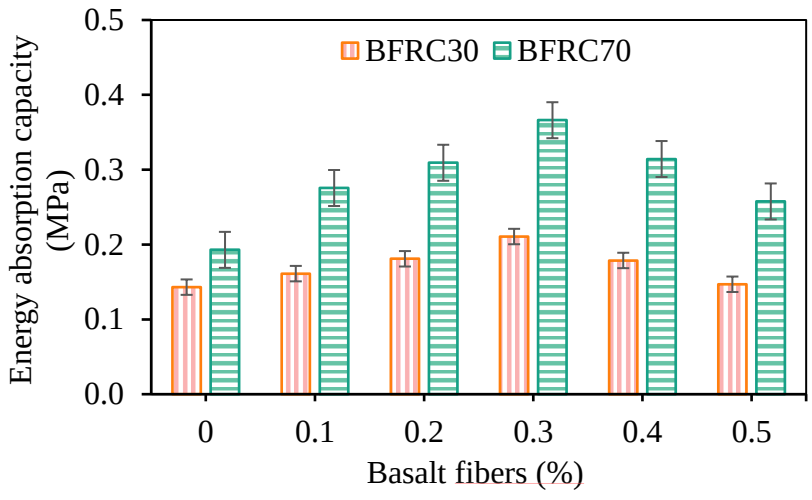

Figure 5.31 Energy absorption capacity of BFRCs

5.3.5.7 Young's modulus

Due to changes in the compressive strength of PC mixes with the addition of basalt fibers, the change in Young's modulus of BFRC30 and BFRC70 mixes was calculated from the

experimental stress-strain curves according to ASTM C469 standards [144]. The Young's modulus of specimens for BFRC30 and BFRC70 mixes concerning the addition of basalt fiber percentages is shown in Figure 5.32. The Young's modulus values for BFRC30 and BFRC70 are presented in Table 5.14. The test results show that the Young's modulus of BFRC specimens does not vary significantly concerning the percentage of basalt fiber addition. It can be seen from Figure 5.29 that the addition of basalt fibers has no significant effect on the ascending region of the stress-strain curves of BFRC specimens up to 50–70% of peak-stress. As a result, the Young's modulus values of BFRC mixes did not significantly increase with the proportion of basalt fiber additions. Compared to the control mix, the addition of basalt fiber up to 0.4% increased the Young's modulus of BFRC30 mixes. In the case of BFRC70 mixes, the addition of basalt fibers up to 0.3% enhanced the Young's modulus of the mixes. The percentage increase in Young's modulus for N-0.1BF, N-0.2BF, N-0.3BF, and N-0.4BF compared to the control mix N-0BF is 2.01%, 5.08%, 8.40%, and 3.10%, respectively. Similarly, the percentage increase in Young's modulus for H-0.1BF, H-0.2BF, and H-0.3BF compared to the control mix H-0BF was 4.85%, 7.26%, and 9.24%, respectively. Among the two strengths of BFRCs, BFRC70 mixes exhibited the highest Young's modulus compared to BFRC30 mixes.

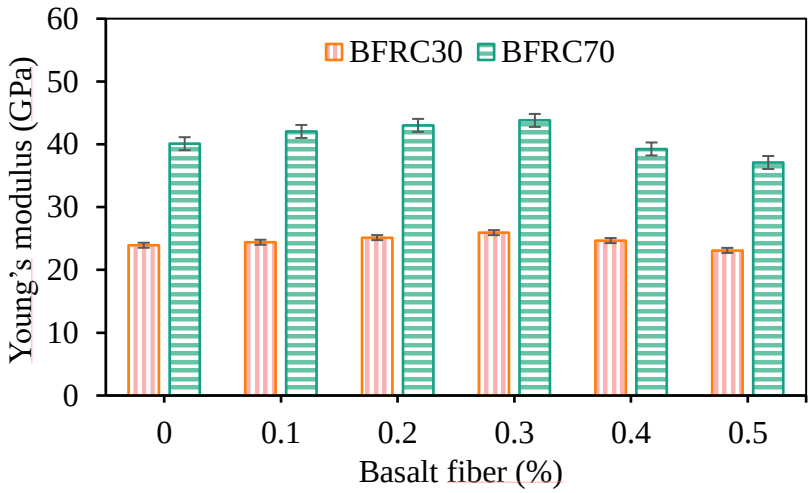

Figure 5.32 Young's modulus of BFRCs

Table 5.14 Compressive properties from experimental stress-strain curves of BFRCs

Mix name	MRI of BF	BFRC30				BFRC70			
		Peak-stress (MPa)	Strain at peak-stress	EAC (MPa)	Young's modulus (GPa)	Peak-stress (MPa)	Strain at peak-stress	EAC (MPa)	Young's modulus (GPa)
0	0	31.99	0.00225	0.143	23.93	63.85	0.00260	0.193	40.10
0.1BF	0.065	33.81	0.00253	0.161	24.41	65.23	0.00305	0.276	42.05
0.2BF	0.130	36.02	0.00268	0.181	25.14	66.01	0.00325	0.309	43.01
0.3BF	0.196	36.82	0.00347	0.211	25.94	67.04	0.00382	0.366	43.80
0.4BF	0.261	34.89	0.00314	0.179	24.67	63.10	0.00369	0.314	39.26
0.5BF	0.327	30.26	0.00297	0.147	23.11	59.20	0.00353	0.258	37.10

Table 5.15 Percentage increase or decrease in compressive properties of BFRC mixes compared to control mixes

Mix name	BFRC30				BFRC70			
	Peak-stress	Strain at peak-stress	EAC	Young's modulus	Peak-stress	Strain at peak-stress	EAC	Young's modulus
0	-	-	-	-	-	-	-	-
0.1BF	5.69	12.44	12.59	2.01	2.16	17.31	43.01	4.86
0.2BF	12.60	19.11	26.57	5.08	3.38	25.00	60.10	7.27
0.3BF	15.10	54.22	47.55	8.40	5.00	46.92	89.64	9.24
0.4BF	9.07	39.56	25.17	3.11	-1.17	41.92	62.69	-2.10
0.5BF	-5.41	32.00	2.80	-3.42	-7.28	35.77	33.68	-7.48

5.3.5.8 Micro-structure analysis of BFRCs

After completing the experimental study, SEM analysis was conducted to further characterize the microstructural properties of BFRC specimens and analyse the strength enhancement mechanism of basalt fibers in concrete. Following the determination of compressive strength on BFRC specimens, small pieces of spalled and crushed concrete were collected for SEM examination. The typical microstructural characteristics of fracture surfaces of BFRC specimens are shown in Figure 5.33. The microstructural properties of BFRC30 and BFRC70 mixes were almost identical. The development of a proper bond between the fiber and matrix can be observed in mixes incorporated with 0.1%, 0.2%, and 0.3% basalt fibers (refer to Figures 5.33(a), (e), (i)). Figures 5.33(b) and (h) show the crack arresting mechanism of basalt fiber, preventing the meso-crack from propagating to the other side of the matrix. The basalt bundles are separated into individual filaments and randomly distributed in the matrix, as shown in

Figures 5.33(c) and (e). The random distribution of basalt fibers plays an efficient role in preventing crack development [98,203]. During the initial stages of plastic shrinkage and hardening of BFRC, basalt fibers limit the expansion of small cracks and considerably reduce the probability of large pores forming in concrete. Under loading, the randomly distributed basalt fibers across cracks resist part of the stresses and absorb energy during the bridging of the cracks, which postpones the growth and widening of the cracks. Therefore, the strong fiber network formed in the core of the matrix makes BFRC tougher than PC [98].

The bond features between basalt fiber and the matrix are presented in Figures 5.33(a), (d), (e), and (i). The basalt fibers are well-embedded in the matrix and are coated with hydration products, as shown in Figures 5.33(a), (d), and (i). A lot of hydration products in the form of small, rice-shaped C-S-H gel crystals attach to the surface of the basalt fiber (refer to Figure 5.33(d)), indicating good cohesion between the fiber and matrix. This demonstrates the existence of a strong interfacial bond strength between the fiber and matrix. This could increase the pull-out friction between the basalt fiber and matrix, consequently enhancing the mechanical strength properties of the composite [156]. Due to the formation of a good interfacial bond between the fiber and matrix, more fibers are fractured than creating a hole by the complete pull-out failure of fibers (refer to Figure 5.33(e)). The slip trace created by the pull-out of fractured basalt fibers in the matrix is shown in Figures 5.33(c), (j), and (k). The reinforcement mechanism of basalt fibers in the matrix is depicted in Figure 5.33(c) and (e). The pull-out and rupture of basalt fibers are evident in Figure 5.33(c) and occur due to excessive shear friction and high energy consumption. The proper bonding of embedded basalt fiber with the matrix, crack propagation, and resistance to crack propagation by bridging across the crack are illustrated in Figure 5.33(f). The pull-out failure of basalt fibers is depicted in Figures 5.33(c) and (j). When the fibers are pulled out of the matrix, they consume energy against the frictional stress, which must be supplied to the progressing cracks. This further enhances the strength properties of FRC composites [204]. Figure 5.33(g) illustrates the fracture of a basalt fiber on one end. This may be due to a smaller development length of the fiber on one side of the crack. However, the other end of the basalt fiber is still embedded in the matrix, indicating the development of a strong bond with the matrix.

The strength of FRC composites is governed by controlling microcrack propagation in the matrix. As illustrated in Figure 5.33(h), meso-cracks formed in the matrix propagate further. When they reach the interface of the fiber, the reinforcing mechanism of the fiber prevents further crack propagation. Consequently, the crack continues to spread along the fiber-matrix

interface until the fiber fractures. Once the fiber fractures, the crack again spreads into the matrix and then moves to the next interface (refer to Figure 5.33(j)). This process continues until the complete failure of specimens [205]. After the failure of fibers, the meso-crack propagates and transforms into a macro-crack. Figures 5.33(g) and (k) show the interfacial bond failure between the matrix and fiber. The development of micro-cracks in the matrix depth and the cracks around the fibers, caused by pulling and the smooth surface of basalt fibers, may be potential reasons for the bond failure between fibers and the matrix.

In the case of BFRC70 mixes, replacing a portion of cement with alccofine-1203 resulted in the formation of additional C-S-H gel structures around basalt fibers, as illustrated in Figures 5.33(d) and (i). This structure promotes the development of a robust interfacial transition zone at the fiber-matrix interface, significantly enhancing the bond strength between the fiber and the matrix. Consequently, more fractured basalt fibers are observed on the fractured surface of specimens from BFRC70 mixes compared to BFRC30 mixes, as depicted in Figure 5.33(e). This result can positively impact the mechanical strength properties of BFRC70 mixes. In both grades of BFRCs, a uniform distribution of fibers was observed in the mix incorporated with 0.3% basalt fibers, showing the highest strength results compared to mixes with all other percentages of basalt fibers. The heterogeneity of the mixes caused by the addition of higher volume percentages (0.4% and 0.5%) of basalt fibers resulted in a fiber balling effect, a structure resembling a fiber network, uneven distribution of fibers, voids in the matrix, and improper bonding between fiber and matrix, as shown in Figure 5.33(l). The structure resembling a fiber network and uneven distribution of fibers may be attributed to entrapped voids and cracks in the matrix, weakening the BFRC composite. Additionally, due to the balling effect and improper bond between fiber and matrix, the fibers may not effectively play a role in the crack-bridging mechanism and may easily pull out from the matrix, ultimately reducing the strength of the concrete.

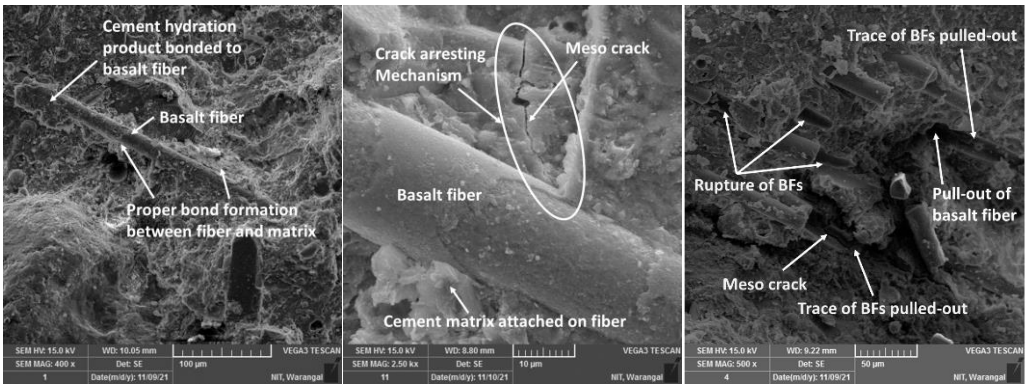

(a) (b) (c)

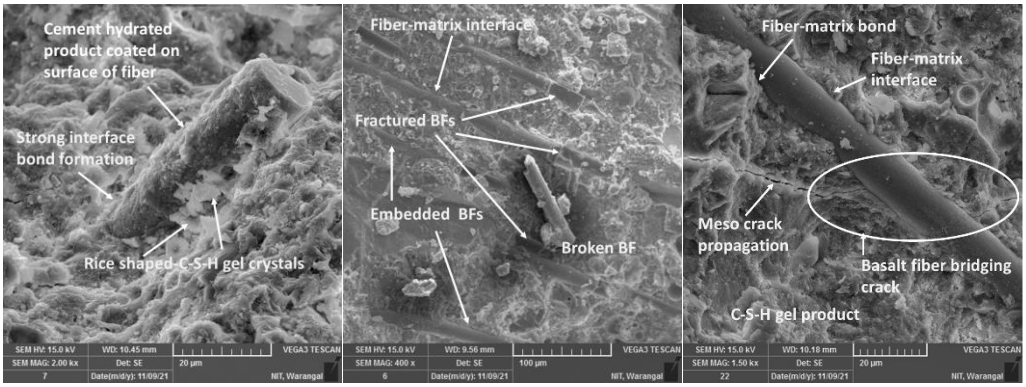

(d) (e) (f)

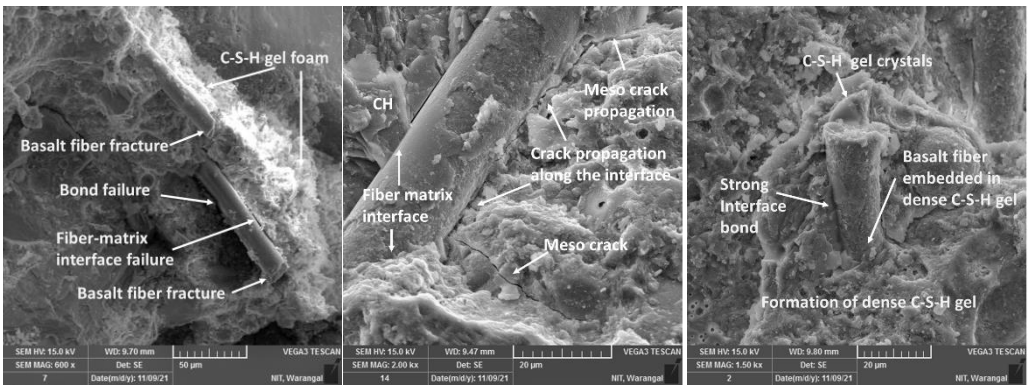

(g) (h) (i)

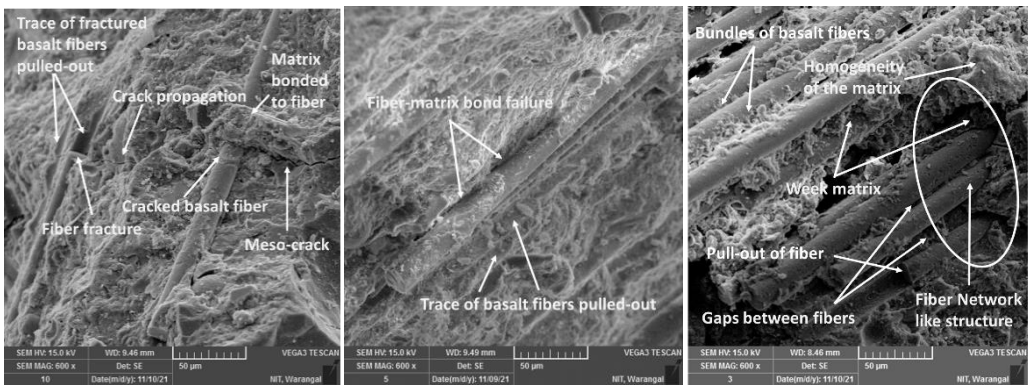

(j) (k) (l)

Figure 5.33 SEM images of BFRCs

5.3.6 Analytical Modelling of Compressive Stress-Strain Curves of BFRCs

5.3.6.1 Modified constitutive analytical model

The modified constitutive analytical model used for analytical modelling of compressive stress-strain curves of PVAFRC30 and PVAFRC70 was the same used for analytical modelling of compressive stress-strain curves of BFRC30 and BFRC70.

5.3.6.2 Modified reinforcing index

The relationships between RI and properties of stress-strain curves, such as peak-stress, strain at peak-stress, and the material parameter (β_n), are the main aspects required for the analytical modelling of stress-strain behavior of concrete. Hence, the parameters in the modified constitutive analytical model are mainly related to RI. To calculate RI values for 0.1%, 0.2%, 0.3%, 0.4%, and 0.5% basalt fibers, the modified reinforcing index expression proposed by M. Khan et al. 2020, as shown in equation 5.16, was used. The calculated RI values, i.e., MRI values, for various volume percentages of basalt fibers are presented in Tables 5.14 and 5.16.

$$MRI = b_i b_j v_f \frac{l}{d}\left(\frac{\sigma_b}{\sigma s}\right)^{\alpha} \quad \text{Eq. (5.16)}$$

Where b_i is anchoring factor, the value of b_i depends on type of fibers. Since the surface of basalt fibers is straight and smooth, the value of b_i was taken as 0.1 according to studies [171,175,189]. b_j is adhesion coefficient, the value of b_j depends on the chemical nature of basalt fiber, and it was taken as 1, as reported in previous studies [171,206,176]. l is length of fiber, v_f is volume fraction of fibers, and d is diameter of fiber. σ_b is the tensile strength of basalt fiber. σ_s is tensile strength of the steel fiber. The value of σ_s is taken as 1345 MPa, as reported by M. Khan et al. 2020. α is tension stiffening parameter, and due to the straight and smooth surface of basalt fiber, α value was taken as 0.5, as reported by researchers [171,175,189].

5.3.6.3 Peak-stress relationships with MRI values of basalt fibers

The peak-stress results obtained from the experimental stress-strain curves of BFRC30 and BFRC70 mixes specimens are summarized in Table 5.14. The addition of basalt fibers improved the peak-stress of BFRC30 mixes specimens, which were better than the peak-stress of BFRC70 mixes specimens. The percentage improvement in peak-stress at the addition of 0.3% basalt fibers was the highest among other percentage additions of basalt fibers compared to PC mixes in both BFRC30 and BFRC70. At 0.3% basalt fiber addition, the peak-stress of N-0.3BF and H-0.3BF increased by 15.1% and 4.99%, respectively. The peak-stress values of the

specimens of mixes with 0.4% and 0.5% basalt fibers were lower than the peak-stress values of PC specimens. The percentage increase in the peak-stress of BFRC mixes with respect to MRI values of basalt fibers is tabulated in Table 5.15. To develop the relationship between peak-stress and MRI values of basalt fibers, appropriate regression analysis was carried out on the experimental data of BFRC30 and BFRC70 mixes. Thus, equation 5.17 for BFRC30 mixes and equation 5.18 for BFRC70 mixes were developed to obtain the relationships for the compressive strength of BFRC mixes with the compressive strength of PC mixes.

f'_{cf} = -203.82MRI^2 + 64.639MRI + f_{cp} for BFRC30 Eq. (5.17)

f'_{cf} = -189.22MRI^2 + 49.366MRI + f_{cp} for BFRC70 Eq. (5.18)

where f'_{cf} is cylindrical compressive strength of BFRC and f_{cp} is cylindrical compressive strength of PC.

5.3.6.4 Strain at peak-stress relationships with MRI values of basalt fibers

The effect of basalt fiber addition on the strain at peak-stress of BFRC mixes was measured from the experimental data of stress-strain curves of BFRC30 and BFRC70 mixes and is summarized in Table 5.14. From the test results, it was observed that the strain at peak-stress of PC specimens increased with an increase in compressive strength of concrete [192]. The addition of basalt fibers from 0.1% to 0.5% improved the strain at peak-stress of BFRC mixes, and among all additions, the improvement in strain at peak-stress was more significant at the addition of 0.3% of basalt fibers in both strengths of BFRCs. The percentage increase in the strain at peak-stress of BFRC mixes with respect to the MRI values of basalt fibers is presented in Table 5.15. The addition of 0.3% basalt fibers to PC mix resulted in a 54.22% increase in the strain at peak-stress of N-0.3BF mix and a 46.92% increase in the strain at peak-stress of H-0.3BF mix. This indicates that the addition of basalt fibers is more effective in improving the strain at peak-stress when compared to compressive strength. The relationships between strain at peak-stress and MRI values of various percentages of basalt fibers additions were developed by conducting suitable regression analysis on experimental data. Thus, equation 5.19 for BFRC30 mixes and equation 5.20 for BFRC70 mixes were developed to obtain the relationships for strain at peak-stress of BFRC mixes with strain at peak-stress of PC mixes.

ε_{of} = -0.0175MRI^2 + 0.0084MRI + ε_{cp} for BFRC30 Eq. (5.19)

ε_{of} = -0.0181MRI^2 + 0.009MRI + ε_{cp} for BFRC70 Eq. (5.20)

Where ε_{of} is strain at cylindrical compressive strength of BFRC, ε_{cp} is strain at cylindrical compressive strength of PC.

5.3.6.5 Material parameter relationships with MRI values of basalt fibers

The β_n in the modified constitutive analytical model is a function of MRI. The experimental stress-strain curves of specimens of BFRC30 and BFRC70 mixes were divided into two phases, i.e., up to peak-stress as the ascending phase and subsequent descending phase. Therefore, β_n values were calculated for both the ascending phase and descending phase. β_n values calculated for the ascending phase are represented by β_a, and β_n values calculated for the descending phase are represented by β_d. The β_a and β_d values calculated from the experimental stress-strain curves of BFRCs are presented in Table 5.16. The relationships developed between β_n and MRI values of basalt fibers for both ascending and descending phases of stress-strain curves of BFRC30 and BFRC70 mixes are shown below in equations 5.21-5.24.

β_a = 8.0986MRI^2 - 4.6618MRI + 2.4155 for ascending region of BFRC30 Eq. (5.21)

β_d = -11.262MRI^2 + 5.5964MRI + 2.1893 for descending region of BFRC30 Eq. (5.22)

β_a = 7.673MRI^2 - 4.1611MRI + 2.3947 for ascending region of BFRC70 Eq. (5.23)

β_d = 59.023MRI^2 - 19.631MRI + 4.7162 for descending region of BFRC70 Eq. (5.24)

Table 5.16 Material parameter (β_n) values of BFRCs

Mix name	MRI **values of Basalt fibers**	**β_a and β_d values calculated from experimental stress-strain curves**				**β_a and β_d values calculated from equations (5.21) - (5.24) using MRI values of basalt fibers for analytical modelling**			
		BFRC30		**BFRC70**		**BFRC30**		**BFRC70**	
		β_a	β_d	β_a	β_d	β_a	β_d	β_a	β_d
0	0	2.39	2.24	2.38	4.74	2.42	2.19	2.24	4.72
0.1BF	0.065	2.14	2.47	2.10	3.65	2.15	2.51	2.00	3.68
0.2BF	0.130	2.09	2.60	2.19	3.13	1.94	2.73	1.83	3.16
0.3BF	0.196	1.62	2.99	1.73	3.22	1.81	2.85	1.72	3.14
0.4BF	0.261	1.82	2.91	1.79	3.57	1.75	2.88	1.68	3.62
0.5BF	0.327	1.76	2.77	1.90	4.61	1.76	2.82	1.70	4.61

5.3.6.6 Comparison of experimental stress-strain curves with analytical stress-strain curves of BFRCs

The β_a and β_d values calculated from equations 5.21-5.24 for analytical modelling of stress-strain curves of specimens of BFRC30 and BFRC70 mixes are tabulated in Table 5.16. The complete experimental stress-strain curves of the BFRC30 mixes were analytically modelled by substituting the values obtained from equations 5.17, 5.19, 5.21, and 5.22 into the modified constitutive analytical model (equation 5.1). Similarly, the complete experimental stress-strain curves of the BFRC70 mixes were analytically modelled by substituting the values obtained from equations 5.18, 5.20, 5.23, and 5.24 into the modified constitutive analytical model. All the analytically modelled stress-strain curves of BFRC30 and BFRC70 mixes are then presented in the form of normalized stress versus normalized strain curves in Figure 5.34. The comparison of analytical stress-strain curves of BFRCs with experimental stress-strain curves of BFRCs is also presented in Figure 5.34. This comparison was made to examine the accuracy of the fit of the analytical stress-strain curves to the experimental stress-strain curves of BFRCs, and good agreement between them was observed. Furthermore, the accuracy of the fit of the analytical stress-strain curves to experimental stress-strain curves was examined in terms of the parameters RMSE and AFV. The expressions for the calculation of RMSE and AFV are shown in equations 5.13 and 5.14, respectively. The RMSE and AFV values of both grades of BFRCs are presented in Table 5.17. These results indicate that the analytical stress-strain curves of BFRCs, modelled from the modified constitutive analytical model using peak-stress, strain at peak-stress, and β_n relationships with MRI of basalt fibers, were very close to the experimental stress-strain curves of BFRCs, and good agreement between them existed.

Table 5.17 The predicted RMSE and AFV values for BFRCs

Strength of BFRC	**Mix name**	**Parameter**	**Present study**	**Ezeldin and Balaguru, 1992** [181]	**Nataraja et al. 1999** [185]	**Ou et al. 2012** [183]	**Abbass et al. 2018** [196]
			$A_{\sigma-\varepsilon}$ **curves**	$P_{\sigma-\varepsilon}$ **curves**			
BFRC30	0	RMSE	1.3522	0.8101	0.8101	2.5723	0.8039
		AFV	0.9970	0.9988	0.9988	0.9871	0.9988
	0.1BF	RMSE	0.6281	15.9419	14.4192	1.7062	1.1917
		AFV	0.9994	-0.0065	0.3086	0.9949	0.9978
	0.2BF	RMSE	0.9604	16.4687	14.5026	1.3117	1.6954
		AFV	0.9987	0.1017	0.3910	0.9974	0.9962
	0.3BF	RMSE	1.1711	13.0602	11.5504	3.0719	3.8108
		AFV	0.9983	0.6069	0.7128	0.9880	0.9834
	0.4BF	RMSE	0.5705	8.4749	8.28202	2.2455	3.0481
		AFV	0.9995	0.8348	0.8438	0.9926	0.9877
	0.5BF	RMSE	0.9192	5.2359	6.00256	2.3214	3.1053
		AFV	0.9985	0.9272	0.8996	0.9901	0.9836
BFRC70	0	RMSE	1.2807	16.5466	16.5466	7.1957	9.4555
		AFV	0.9993	0.8028	0.8028	0.9807	0.9692
	0.1BF	RMSE	1.1159	34.5171	28.9065	4.9614	7.2782
		AFV	0.9995	-0.3981	0.2171	0.9904	0.9813
	0.2BF	RMSE	2.4811	29.3885	23.1168	4.1876	6.2532
		AFV	0.9978	0.2847	0.6297	0.9936	0.9869
	0.3BF	RMSE	3.1209	20.2465	16.9792	6.7097	7.7181
		AFV	0.9966	0.7373	0.8298	0.9837	0.9801
	0.4BF	RMSE	1.9255	10.5058	10.2113	6.3857	7.2426
		AFV	0.9986	0.9406	0.9444	0.9845	0.9812
	0.5BF	RMSE	1.9928	6.1029	6.4637	7.7742	8.5876
		AFV	0.9981	0.9794	0.97602	0.97404	0.97006

$A_{\sigma-\varepsilon}$ curves - Analytically modelled stress-strain curves; $P_{\sigma-\varepsilon}$ curves - predicted stress-strain curves

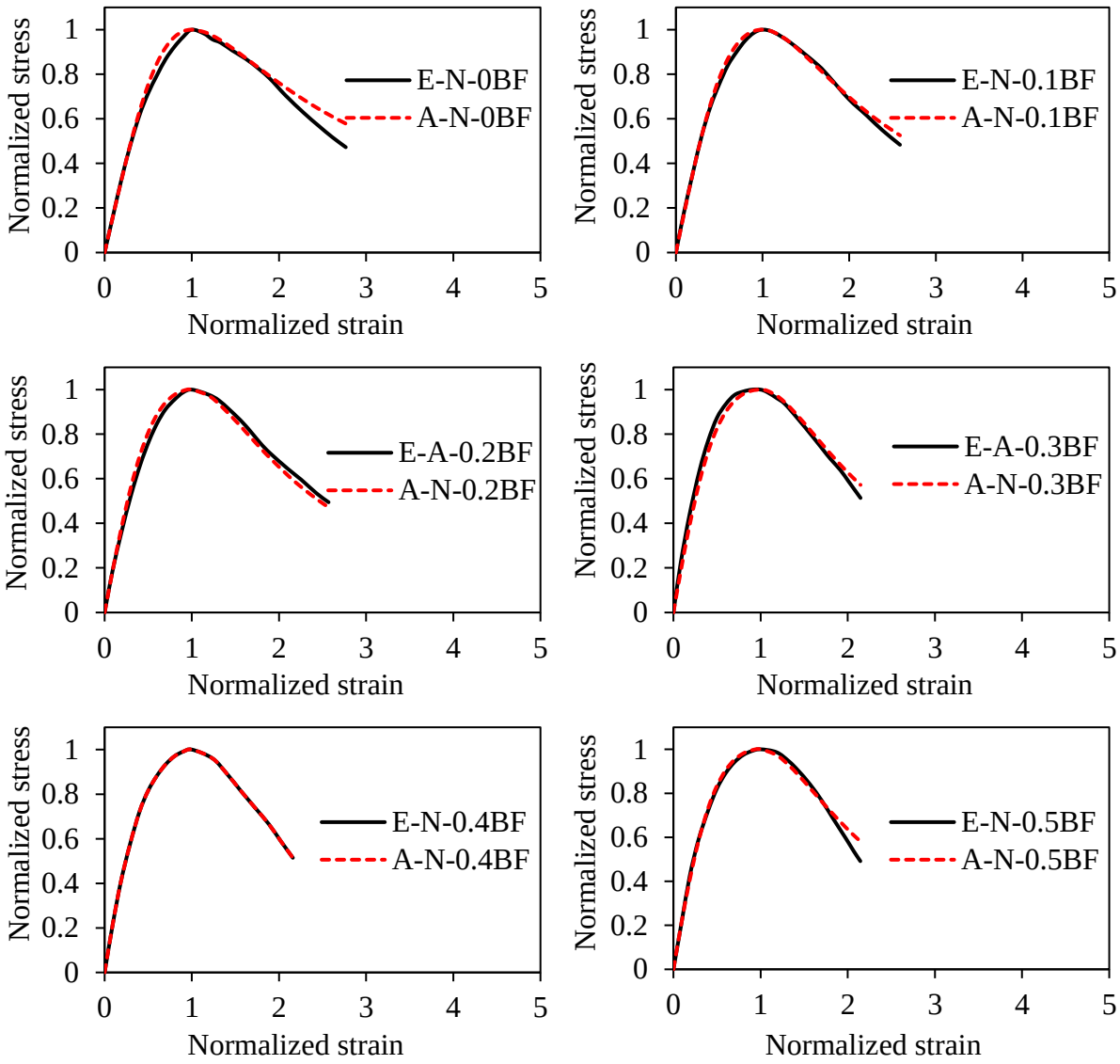

(a) BFRC30

Figure continues...

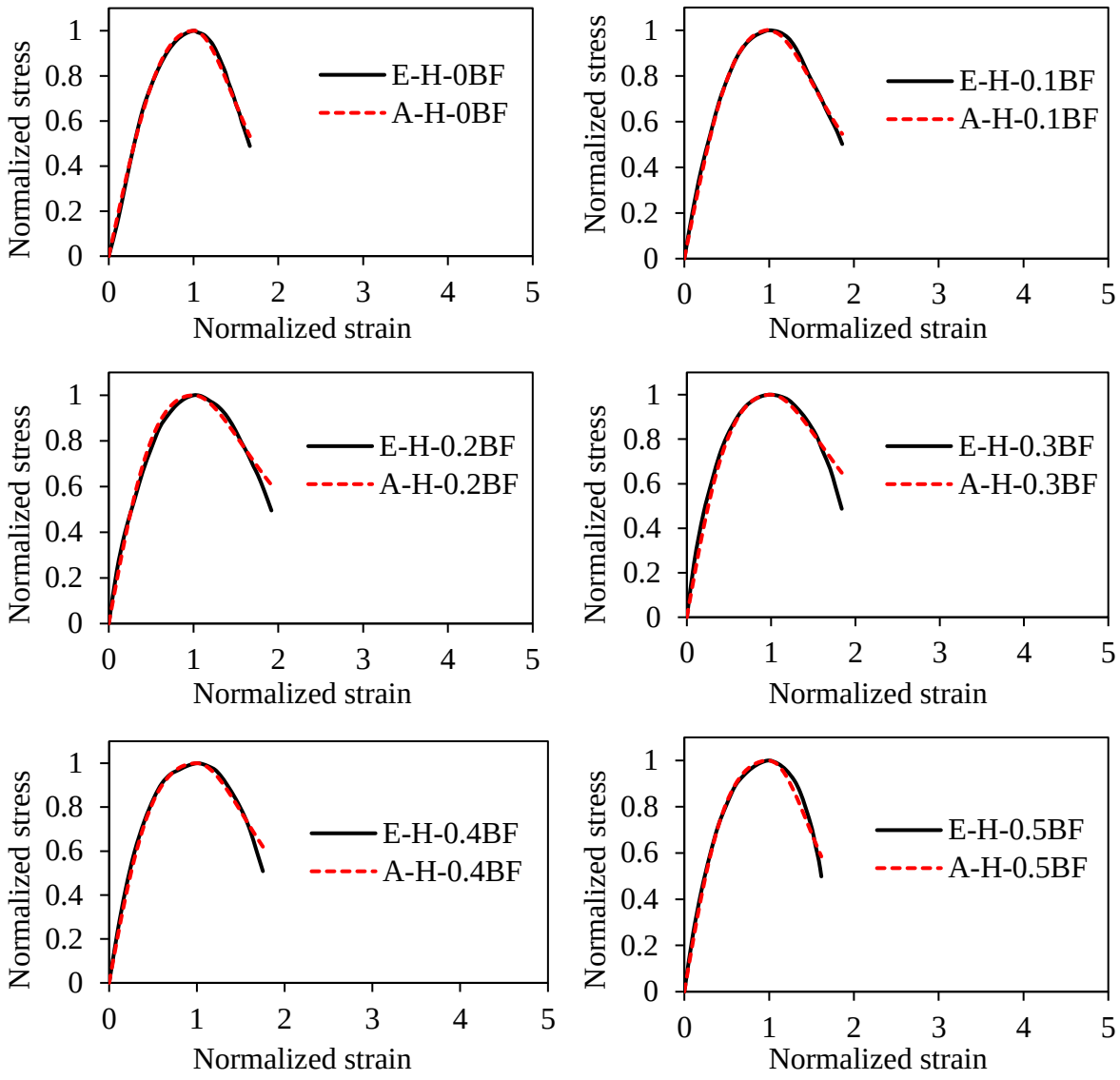

(b) BFRC70

Figure 5.34 Comparison of analytical stress-strain curves with experimental stress-strain curves of BFRCs

5.3.6.7 Application of existing stress-strain predictive models to experimental data of BFRC

The researchers, Ezeldin and Balaguru 1992 [181], Nataraja et al. 1999 [185], Ou et al. 2012 [183] and Abbass et al. 2018 [196] used a constitutive analytical model and relationships proposed between β and RI were applied to the experimental data of BFRC30 and BFRC70 to examine how accurately they can predict BFRC's stress-strain curves. For this, the β values were calculated from Ezeldin and Balaguru 1992 [181], Nataraja et al. 1999 [185], Ou et al. 2012 [183] and Abbass et al. 2018 [196] proposed expressions between β and RI using MRI values of basalt fibers and are tabulated in Table 5.18. Thus, using these β values and the

experimental data of BFRC30 and BFRC70, the predicted stress-strain curves of each mix were normalized and presented in Figure 5.35. The comparison of predicted stress-strain curves with normalized experimental and normalized analytical stress-strain curves of BFRCs is also presented in Figure 5.35. The accuracy in the fit of these predicted stress-strain curves to the experimental and analytical stress-strain curves is discussed below.

Table 5.18 β values calculated using MRI values of basalt fibers and relationships between β and RI given in literature

Reference	**MRI of values basalt fibers**	**β values calculated using MRI values of basalt fibers**	
Ezeldin and Balaguru, 1992 [181]	0	N-0BF	2.51
		H-0BF	9.20
	0.065	33.97	
	0.130	13.66	
	0.196	8.26	
	0.261	5.90	
	0.327	4.62	
Nataraja et al. 1999 [185]	0	N-0BF	2.51
		H-0BF	9.20
	0.065	15.13	
	0.130	9.29	
	0.196	7.03	
	0.261	5.79	
	0.327	5.00	
Ou et al. 2012 [183]	0	3.05	
	0.065	2.92	
	0.130	2.80	
	0.196	2.68	
	0.261	2.58	
	0.327	2.47	
Abbass et al. 2018 [196]	0	2.42	
	0.065	2.32	
	0.130	2.24	
	0.196	2.17	
	0.261	2.11	
	0.327	2.06	

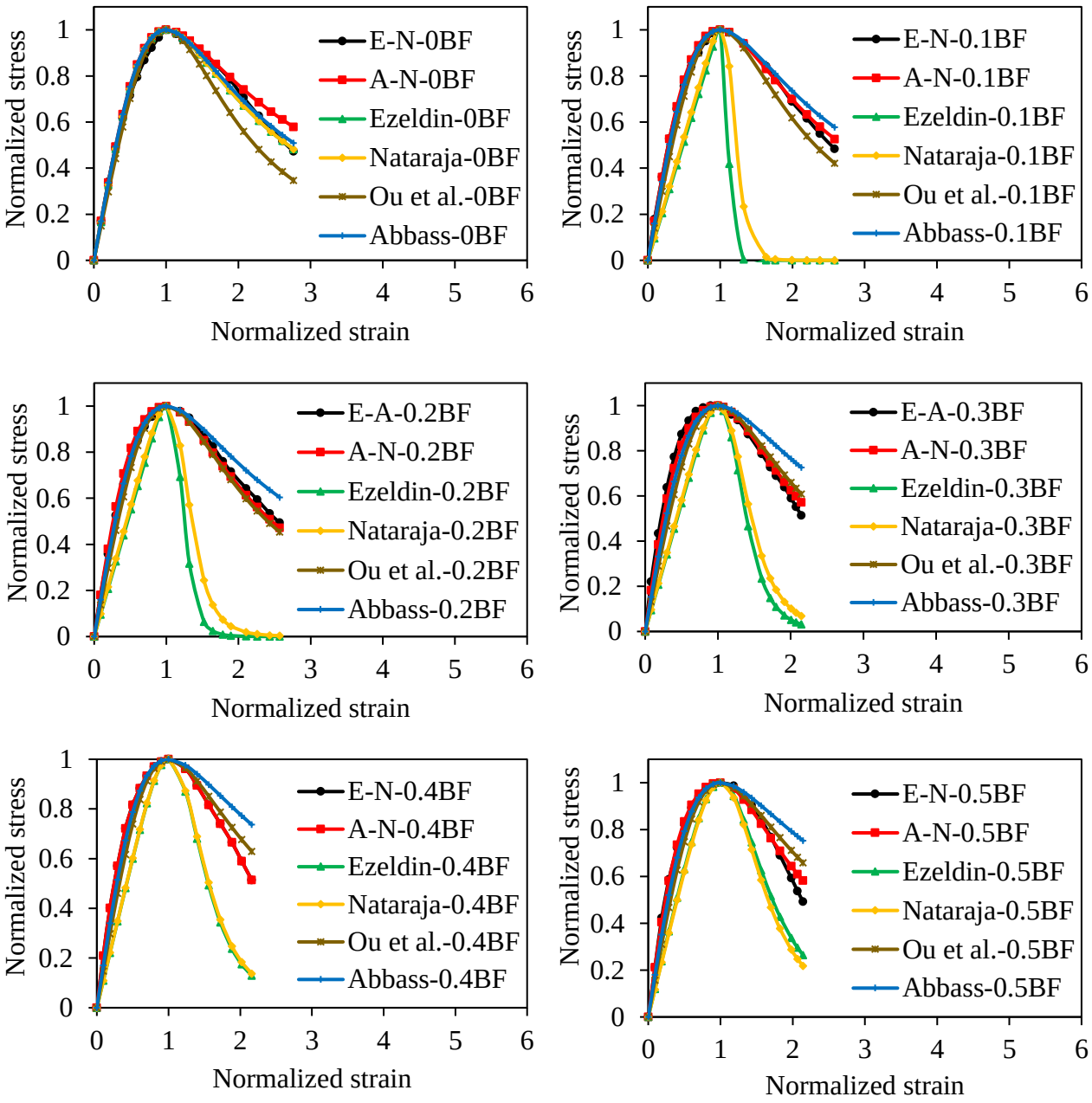

(a) BFRC30

Figure continues...

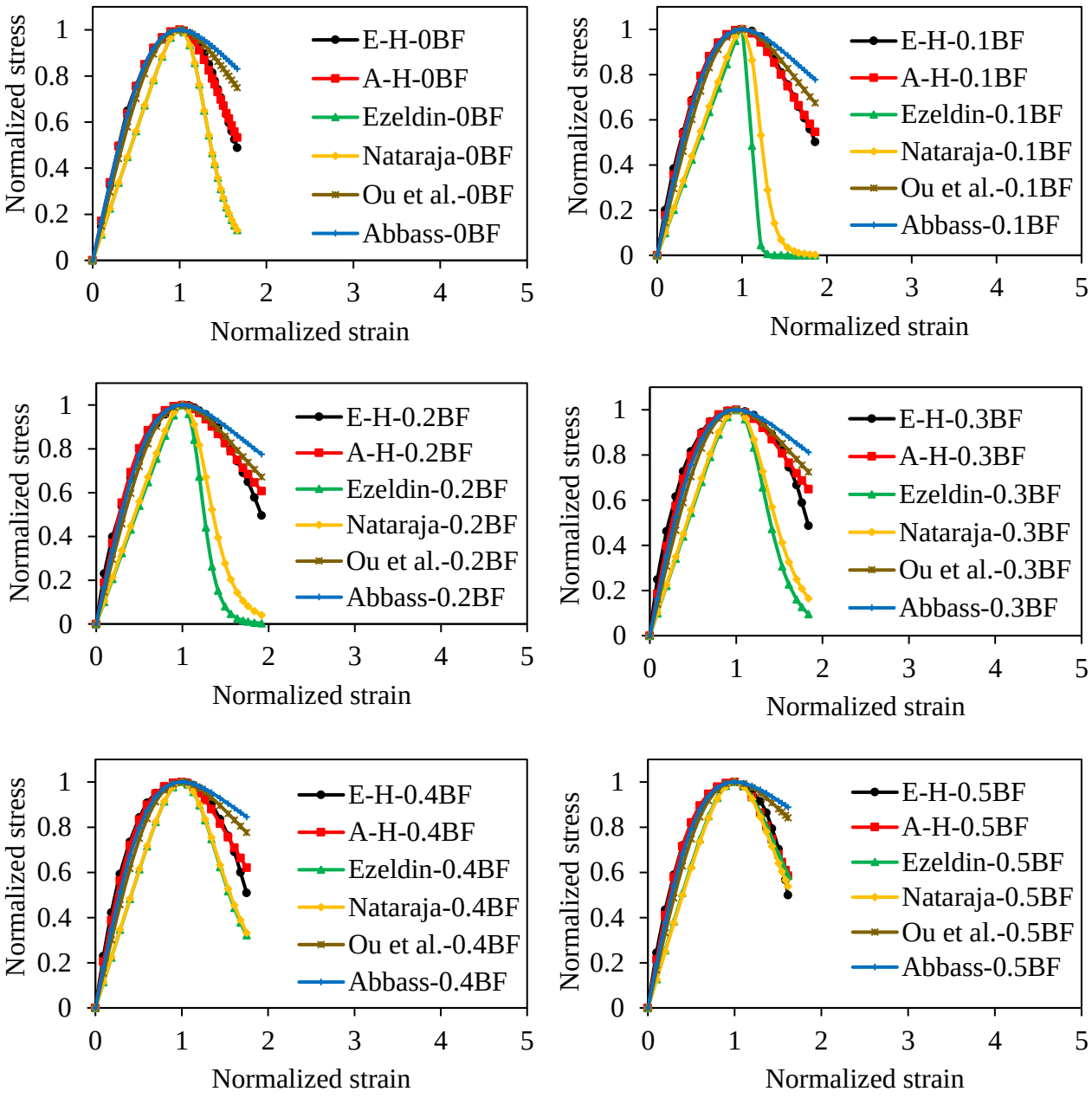

(b) BFRC70

Figure 5.35 Comparison of predicted stress-strain curves with experimental and analytical stress-strain curves of BFRCs.

As shown in Figure 5.35, using Ezeldin and Balaguru 1992 [181] proposed relationship between β and RI and the constitutive analytical model, the predicted stress-strain curve of the N-0BF showed good agreement with experimental stress-strain curve and analytical stress-strain curve of the same mix, but the predicted stress-strain curve of H-0BF mixes showed disagreement with experimental stress-strain curve and analytical stress-strain curves of same mix. This is because the calculated β value of control mix (N-0BF) using Ezeldin and Balaguru 1992 [181] proposed relationships between β and RI was near the β_d value of N-0BF mix calculated from equation 5.22 and from experimental stress-strain curve, but in the case of H-0BF mix, the calculated β value was not close to β_d values calculated from equation 5.24 and from experimental stress-strain curve (refer Tables 5.16 and 5.18). This is also evident from the calculated RMSE and AFV values of N-0BF and H-0BF mixes, shown in Table 5.17. The RSME and AFV values of N-0BF mix were close to RMSE and AFV values of analytical stress-strain curve of N-0BF mix but in the case of H-0BF mix it wasn't. This shows close agreement of the predicted stress-strain curve with analytical and experimental stress-strain curve of N-0BF mix. The reason for predicting steeper pre-peak and post-peak responses of the stress-strain curves of concrete mixes with 0.1%-0.5% of basalt fibers is the β values calculated using MRI values of basalt fibers from Ezeldin and Balaguru 1992 [181] proposed relationships was much higher than β_d values calculated from equations 5.22 and 5.24 and experimental stress-strain curves (refer Table 5.16 and 5.18). Therefore, using these higher β values, the predicted stress-strain curves of concrete mixes incorporated with basalt fibers highly underestimated stresses of the predicted stress-strain curves compared to experimental data. The Ezeldin and Balaguru 1992 [181] proposed relationships for calculating β using RI values of fibers was effective for steel fibers RI range 2 to 5. But using this relationship, β values calculated based on MRI values of basalt fibers were higher than the given range. Hence, using higher β values, the predicted stress-strain curves of BFRC30 and BFRC70 mixes incorporated with 0.1%-0.5% of basalt fibers showed disagreement with the experimental and analytical stress-strain curves. This is also evident in RMSE and AFV values calculated for BFRC30 and BFRC70 mixes incorporated with 0.1% to 0.5% basalt fibers. From Table 5.17, it was observed that RMSE and AFV values calculated from the predicted stress-strain curves using Ezeldin and Balaguru 1992 [181] proposed relationships between β and RI and constitutive analytical model was not close to RMSE and AFV values calculated from the analytical stress-strain curves of the BFRC mixes of both BFRC30 and BFRC70.

As shown in Figure 5.35, using Nataraja et al. 1999 [185] proposed relationships between β and RI and the constitutive analytical model, the predicted stress-strain curve of N-0BF showed good agreement with the experimental and analytical stress-strain curves of same mix, but the predicted stress-strain curve of H-0BF mix showed disagreement with the experimental and analytical stress-strain curves of the same mix. This is because the β value calculated for plain control mix (N-0BF) using Nataraja et al. 1999 [185] proposed relationship between β and RI was near to β_d value of the N-0BF calculated from equation 5.22 and experimental stress-strain curve; but in the case of H-0BF mix, the β values calculated were not close to β_d value calculated from equation 5.24 and experimental stress-strain curve (refer Table 5.16 and 5.18). This is also evident from the RMSE and AFV values of N-0BF and H-0BF mixes, shown in Table 5.17. The RSME and AFV values of N-0BF mix was close to RMSE and AFV values of analytical stress-strain curve of N-0BF mix, but in the case of H-0BF mix it wasn't. This shows close agreement between the predicted stress-strain curve and analytical stress-strain curve of N-0BF mix. In two strengths of BFRCs, the stresses of concrete mixes with 0.1%-0.5% BFs was underestimated in ascending and descending regions of the predicted stress-strain curves by the Nataraja et al. 1999 [185] proposed relationships and constitutive analytical model compared to the experimental and analytical stress-strain curves. The reason for this is the calculated β values based on MRI values of various volume percentage of basalt fibers using Nataraja et al. 1999 [185] proposed relationships between β and RI are much higher than the β_d value calculated from equations 5.22 and 5.24 and experimental stress-strain curve (refer Table 5.16 and 5.18). Therefore, use of these higher β values for the prediction of stress-strain curves of concrete mixes incorporated with basalt fibers has highly underestimated the stresses of the predicted stress-strain curves. Nataraja et al. 1999 [185] proposed relationships between β and RI is effective for the steel fiber RI range RI $\leq$ 3. But the calculated β values based on MRI values of basalt fibers using Nataraja et al. 1999 [185] proposed relationships was higher than the proposed range. Hence, using higher β values, the predicted stress-strain curves of BFRC30 and BFRC70 mixes incorporated with 0.1% to 0.5% of basalt fibers showed disagreement with the experimental and analytical stress-strain curves. This is also evident from the calculated RMSE and AFV values of BFRC30 and BFRC70 mixes. From Table 5.17, it was observed that the RMSE and AFV values calculated from the predicted stress-strain curves using Nataraja et al. 1999 [185] proposed relationships between β and RI and the constitutive analytical model are not close to RMSE and AFV values calculated from the analytical stress-strain curves of BFRC mixes of BFRC30 and BFRC70. Therefore, the predicted stress-strain

curves of mixes incorporated with 0.1%-0.5% basalt fibers showed disagreement with the experimental and analytical curves same mixes.

As shown in Figure 5.35, using Ou et al. 2012 [183] and Abbass et al. 2018 [196] proposed relationships between β and RI and constitutive analytical model, the predicted stress-strain curves of BFRC30 and BFRC70 mixes exhibited good agreement with experimental and analytical stress-strain curves in ascending phase of the stress-strain curves and predicted the stiff descending phase after peak-stress due to over-estimation of stress, and hence, showed disagreement with experimental and analytical stress-strain curves in descending phase. And the slope of the stiff descending phase of the predicted stress-strain curves of BFRC30 and BFRC70 mixes decreased as the strength of concrete increased. The reason for the predicted stresses showing good agreement with experimental and analytical stresses in ascending phase of the stress-strain curves is that the β values calculated based on MRI values of basalt fibers using Ou et al. 2012 [183] and Abbass et al. 2018 [196] proposed relationships between β based on RI which were close to $\beta_a$values calculated from equations 5.21 and 5.23 and experimental stress-strain curves (refer Table 5.16 and 5.18). Hence, using of these β values, the predicted stress-strain curves showed good agreement in ascending phase of stress-strain curves. The reason for showing disagreement with experimental and analytical stresses in descending phases of the predicted stress-strain curves is that the β values calculated based on MRI values of basalt fibers using Ou et al. 2012 [183] and Abbass et al. 2018 [196] proposed relationships between β and RI which were not close to β_d values calculated from equations 5.22 and 5.24 and from experimental stress-strain curves (refer Table 5.16 and 5.18). Hence, the predicted stress-strain curves using these higher β values showed disagreement with the experimental and analytical stress-strain curves in descending phase. This was also evident from RMSE and AFV values of BFRC30 and BFRC70 mixes. From Table 5.17, it was observed that the RMSE and AFV values assessed from the predicted stress-strain curves using Ou et al. 2012 [183] and Abbass et al. 2018 [196] proposed relationships between β and RI and the constitutive analytical model was not close to RMSE values and lower than AFV values calculated from analytical stress-strain curves of specimens of BFRC30 and BFRC70 mixes. This shows the disagreement of predicted stress-strain curves of BFRC mixes with experimental and analytical stress-strain curves.

5.4 Conclusions

This phase of the research presents the results from an experimental and analytical investigation conducted on PVAFRCs and BFRCs of M30 and M70 grades. The study assessed the mechanical and microstructural properties, compressive stress-strain behavior, EAC, Young's modulus, peak-stress, and strain at peak-stress. Additionally, relationships for compressive properties of stress-strain curves, such as peak-stress, strain at peak-stress, and β_n with MRI values of various volume percentages of PVA fibers and basalt fibers, were developed for the analytical modelling of compressive stress-strain curves of PVAFRCs and BFRCs of M30 and M70 grades using a proposed modified constitutive analytical model. Based on the presented results, the conclusions drawn from this chapter are:

- At a constant water-binder ratio, constituent material quantities, and superplasticizer dosage, the addition of PVA fibers and basalt fibers reduced the workability of concrete mixes. The balling effect of fibers became noticeable at a 0.4% addition, and it became more severe with a 0.5% addition in both grades of PVAFRCs and BFRCs.
- The compressive strength of the PVAFRCs and BFRCs partially increased with the addition of 0.1%, 0.2% and 0.3% of fibers and decreased with the addition of 0.4% and 0.5% of fibers.
- The addition of 0.1% to 0.5% PVA fibers and basalt fibers to NSC and HSC improved their flexural and split tensile strengths more significantly than the improvement in compressive strength.
- The addition of 0.3% PVA fibers and basalt fibers resulted in the highest improvement in compressive, flexural, and split tensile strengths of concrete compared to other percentages in two strengths of PVAFRCs and BFRCs.
- The percentage improvement in compressive, flexural, and split tensile strengths of concrete mixes with 0.3% fibers was greater in PVAFRC30 and BFRC30 than the improvement observed in PVAFRC70 and BFRC70.
- The addition of PVA and basalt fibers enhanced the post-peak behaviour of concrete by controlling the post-crack regime of the stress-strain curves, and this improvement was greatest for the PVAFRC30 and BFRC30 mixes compared to the PVAFRC70 and BFRC70 mixes.
- The improvement in the post-peak behavior of concrete was highest with the addition of 0.3% fibers in two strengths of PVAFRCs and BFRCs. As a result, the mixes with 0.3% PVA fibers and basalt fibers had the highest EAC. The improvement in EAC of

PVAFRC70 and BFRC70 mixes was greater than that of the PVAFRC30 and BFRC30 mixes.

- The Young's modulus of control mixes in two strengths of PVAFRCs and BFRCs improved the most with the addition of 0.3% PVA fibers and basalt fibers. The PVAFRC70 and BFRC70 mixes showed the highest Young's modulus compared to the PVAFRC30 and BFRC30 mixes.
- In two strengths of PVAFRCs and BFRCs, PVA and basalt fibers improved the strain at peak-stress more effectively than the peak-stress. PVAFRC30 and BFRC30 mixes with 0.3% PVA and basalt fibers exhibited the most significant improvement in both peak-stress and strain at peak-stress compared to PVAFRC70 and BFRC70 mixes.
- The addition of 0.3% PVA fibers to the control mix of PVAFRC30 and PVAFRC70 has improved the mechanical properties, load-deflection behavior, and post-peak behaviour and compressive properties of stress-strain curve better than the improvement shown by the addition of 0.3% basalt fibers to the control mix of BFRC30 and BFRC70.
- The reinforcing, crack arresting, and crack bridging mechanisms of PVA and basalt fibers were revealed from SEM images of the PVAFRCs and BFRCs. The fracture and pull-out failure of PVA and basalt fibers in the concrete show the development of a high-quality bond between the fiber and matrix, leading to an increase in the strength of PVAFRCs and BFRCs.
- The compressive stress-strain curves of PVAFRCs and BFRCs, predicted through the proposed modified constitutive analytical model using the relationships for peak-stress, strain at peak-stress, and material parameter (β_n) with MRI values of PVA and basalt fibers, showed good agreement with the experimental stress-strain curves.
- The goodness of fit of the analytically modelled stress-strain curves to the experimental stress-strain curves of PVAFRCs and BFRCs was also estimated in terms of RMSE and AFV, and the obtained results showed good agreement between them.
- The constitutive analytical model and relationships proposed between β and RI by various researchers have not been able to accurately predict the experimental stress-strain curves of PVAFRCs and BFRCs.

Chapter 6

Experimental Investigation on Flexural Response of BFRC and PVAFRC Beams Reinforced with BFRP Rebars

6.1 General

The current chapter investigates the flexural response of BFRP rebars reinforced PC, BFRC, and PVAFRC beams of NSC and HSC under experimental evaluation. For this investigation, PC of M30 and M70 grades has been developed. Then, based on the experimental results presented in Chapter 5, the optimum percentage of PVA fibers from PVAFRC30 and PVAFRC70 and the optimum percentage of basalt fibers from BFRC30 and BFRC70 were adopted to develop normal-strength and high-strength PVAFRC and BFRC for investigating the flexural response of BFRP-reinforced PC, BFRC, and PVAFRC beams. To evaluate the potential of BFRP rebars as a longitudinal reinforcement for flexural members, a singly reinforced beam with pure bending conditions was adopted and investigated under four-point bending test method. In this phase (Phase-III) of research work, the flexural response of under and over steel-reinforced PC beams of M30 and M70 grades is studied. Then, the flexural response of BFRP under- and over-reinforced PC beams was investigated and the test result were compared with that of steel under- and over-reinforced PC beams. Following this, the flexural behavior of BFRP under- and over-reinforced BFRC and PVAFRC beams is studied, and improvement in flexural behavior of these beams compared to BFRP under- and over-reinforced PC beams is discussed. The flexural response of the study includes evaluation of mid-point load-deflection behavior, moment-curvature relationships, ductility indices, crack pattern, and failure mode. The details of mix proportions, mix designations, constituent material quantities, physical properties of BFRP rebars and steel reinforcing bars, percentage of PVA fibers and basalt fibers used, reinforcement area, geometry of the beam, mixing of concrete, cast and curing of beams, test method, and discussions on of obtained results are presented in the following sections.

6.2 Materials

The constituent materials used for preparation of PC, BFRC and PVAFRC are in accordance with Bureau of Indian standards. Ordinary Portland cement of 53 grade, class-F fly ash, and alccofine-1203 were used as binder materials. Natural river sand confirming to Zone-II was used as fine aggregates, and crushed granite of maximum size 16 mm was used as coarse aggregates. Masterglenium SKY-8233, a polycarboxylic ether based high-performance

superplasticizer was used to enhance the workability of concrete. The helical wound sand coated BFRP rebars of 8 mm, 10 mm, and 12 mm in diameter, as shown in Figure 6.1, were used for the present investigation. Steel reinforcing bars of 6 mm, 8 mm, 10 mm, 12 mm and 16 mm in diameter were used for steel under- and over-reinforced PC beams. Fe500 grade steel was used for this study. The filament type short length basalt fibers of length 6 mm and diameter of 13 μm were used for the development of BFRC. The filament type kuralon (REC15) PVA fibers with a length of 12 mm and a diameter of 40 μm were used for the development of PVAFRC.

Figure 6.1 Helical wound sand coated BFRP rebars

6.3 Reinforcement and Cross Section Details of the Beams

A total of twelve BFRP-reinforced concrete (PC, BFRC and PVAFRC) beams of M30 and M70 grades were prepared to study the flexural response under static loading. In addition to this, four steel-reinforced PC beams were also prepared and tested to compare the changes in flexural response BFRP RC (PC, BFRC and PVAFRC) beams from flexural response of steel-reinforced PC beams. All the beams were designed to fail in flexure. All the beams were 1800 mm long and had a cross section of 100×150 mm^2. The details of dimension of the tested beams are shown in Figure 6.2 and the reinforcement and cross section details of the beams are shown in Figure 6.3. The C-R, T-R, and S-R in Figure 6.3 stand for compression reinforcement, tensile reinforcement, and shear reinforcement.

BFRP RC beams were designed as under-reinforced and over-reinforced beams according to ACI 440.1R-15 [22]. 80 percent of the balanced reinforcement ratio was taken as the percentage of reinforcement to design BFRP under-reinforced beams, and 140 percent of the balanced reinforcement ratio was taken as the percentage of reinforcement to design BFRP over-reinforced beams according to ACI 440.1R-15 [22]. The steel under- and over-reinforced PC beams were designed according to IS 456-2000 [133]. All the BFRP RC beams and steel-

reinforced PC beams consist of a single layer of BFRP rebars as longitudinal reinforcement in the tension zone of the beam. In addition, 6 mm diameter mild steel reinforcing bars were used as stirrups, and 4 mm galvanized iron (GI) wire, in accordance with IS 280-2006 [207], was used as detailing reinforcement in the compression zone of all BFRP RC beams as well as steel-reinforced PC beams.

Based on the grade of concrete, all the tested beams were divided into two series, i.e., M30 and M70 series. For each series, a total of 8 beams were cast and tested in four phases. In Phase I, steel under- and over-reinforced PC beams of M30 series and M70 series were cast and tested. In Phase II, BFRP under- and over-reinforced PC beams of M30 and M70 series were cast and tested. In Phase III, BFRP under- and over-reinforced BFRC beams of M30 and M70 series were cast and tested. Finally, in Phase IV, BFRP under- and over-reinforced PVAFRC beams of M30 and M70 series were cast and tested. Reinforcement cage for M30 and M70 series BFRP RC beams and steel-reinforced PC beams are presented in Figure 6.4.

The names and reinforcement details of all the tested BFRP RC beams and steel-reinforced PC beams are given in Table 6.1. To improve the flexural performance of BFRP-reinforced PC beams, basalt fibers and PVA fibers were added separately, and the percentage details of fibers added are presented in Table 6.1. In addition to this, Table 6.1 also shows the compressive strength of concretes used to cast the beams, which was determined using cube specimens of size 100×100×100 mm. All the beams were named based on area of longitudinal tensile reinforcement provided, fiber type used, type RC section, and grade of concrete. In Phase I, SUR30 and SUR70 stand for steel under-reinforced M30 and M70 grade PC beams, SOR30 and SOR70 stand for steel over-reinforced M30 and M70 grade PC beams. In Phase II, BUR30 and BUR70 stand for BFRP under-reinforced M30 and M70 grade PC beams, BOR30 and BOR70 stand for BFRP over-reinforced M30 and M70 grade PC beams. In Phase III, BBUR30 and BBUR70 stand for BFRP under-reinforced M30 and M70 grade BFRC beams, BBOR30 and BBOR70 stand for BFRP over-reinforced M30 and M70 grade BFRC beams. In Phase IV, BPUR30 and BPUR70 stand for BFRP under-reinforced M30 and M70 grade PVAFRC beams, BPOR30 and BPOR70 stand for BFRP over-reinforced M30 and M70 grade PVAFRC beams. Steel-reinforced PC beams of Phase-I were used as control beams to compare the flexural response of BFRP-reinforced PC beams of Phase II. Further, BFRP-reinforced PC beams were used as control beams to observe improvement in flexural behaviour of BFRP-reinforced BFRC and PVAFRC beams of Phase III and Phase IV.

Table 6.1 Name and reinforcement details of BFRP-reinforced PC, BFRC, and PVAFRC beams

Series	Phase	Beam name	Type of section	Reinforcement area (mm^2)		Tensile reinforcement	Fiber (%) and type	CS (MPa)
				Required	Provided			
M30	I	SUR30	UR	137	100.5	2-8 mm	-	38.57
		SOR30	OR		185	2-10 mm, 1-6 mm	-	38.57
	II	BUR30	UR	132	100.5	2-8 mm	-	38.57
		BOR30	OR		206.5	2-10 mm, 1-8 mm	-	38.57
	III	BBUR30	UR	132	100.5	2-8 mm	0.3% BF	41.52
		BBOR30	OR		206.5	2-10 mm, 1-8 mm	0.3% BF	41.52
	IV	BPUR30	UR	132	100.5	2-8 mm	0.3% PVA	42.73
		BPOR30	OR		206.5	2-10 mm, 1-8 mm	0.3% PVA	42.73
M70	I	SUR70	UR	309	235.6	3-10 mm	-	80.33
		SOR70	OR		402	2-16 mm	-	80.33
	II	BUR70	UR	210	191	1-12 mm, 1-10 mm	-	80.33
		BOR70	OR		304.5	2-12 mm, 1-10 mm	-	80.33
	III	BBUR70	UR	210	191	1-12 mm, 1-10 mm	0.3% BF	82.62
		BBOR70	OR		304.5	2-12 mm, 1-10 mm	0.3% BF	82.62
	IV	BPUR70	UR	210	191	1-12 mm, 1-10 mm	0.3% PVA	84.18
		BPOR70	OR		304.5	2-12 mm, 1-10 mm	0.3% PVA	84.18

UR - Under-reinforced, OR – Over-reinforced, BF – Basalt fibers, PVA – PVA fibers, CS- Compressive strength of cube

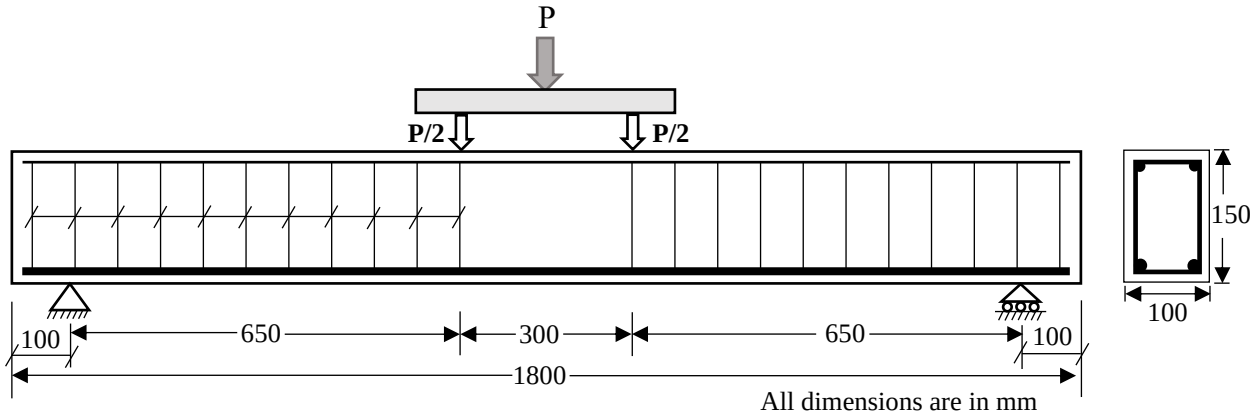

Figure 6.2 Dimensions of all the beams

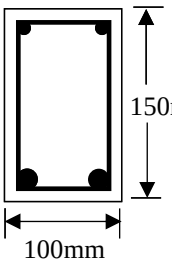

Under Reinforced section
C-R – 2- 4mm
T-R – 2- 8mm
S-R – 6mm @ 90mm c/c
Concrete cover- 20mm

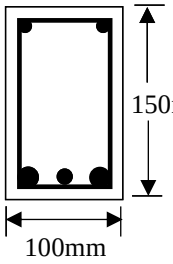

Over Reinforced section
C-R – 2- 4mm
T-R – 2- 10mm + 1- 6mm
S-R – 6mm @ 90mm c/c
Concrete cover- 20mm

Phase I → M30 series Steel-reinforced PC beams

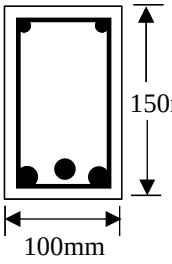

Under Reinforced section
C-R – 2- 4mm
T-R – 3- 10mm
S-R – 6mm @ 80mm c/c
Concrete cover- 20mm

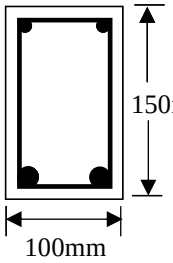

Over Reinforced section
C-R – 2- 4mm
T-R – 2- 16mm
S-R – 6mm @ 60mm c/c
Concrete cover- 20mm

Phase I → M70 series Steel-reinforced PC beams

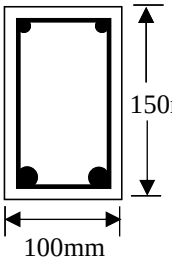

Under Reinforced section
C-R – 2- 4mm
T-R – 2- 8mm
S-R – 6mm @ 60mm c/c
Concrete cover- 20mm

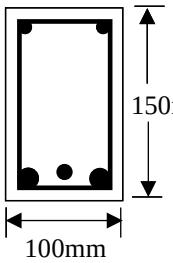

Over Reinforced section
C-R – 2- 4mm
T-R – 2- 10mm+ 1-8mm
S-R – 6mm @ 60mm c/c
Concrete cover- 20mm

Phase II, III and IV → M30 series BFRP-reinforced PC, BFRC, and PVAFRC beams

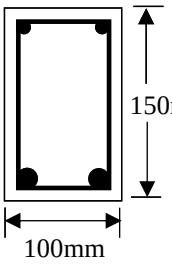

Under Reinforced section
C-R – 2- 4mm
T-R – 1- 12mm + 1-10mm
S-R – 6mm @ 60mm c/c
Concrete cover- 20mm

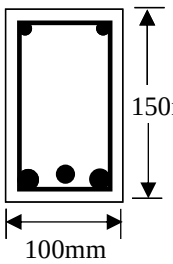

Over Reinforced section
C-R – 2- 4mm
T-R – 2- 12mm + 1-10mm
S-R – 6mm @ 50mm c/c
Concrete cover- 20mm

Phase II, III and IV → M70 series BFRP-reinforced PC, BFRC, and PVAFRC beams

Figure 6.3 Cross-section and reinforcement details of beams

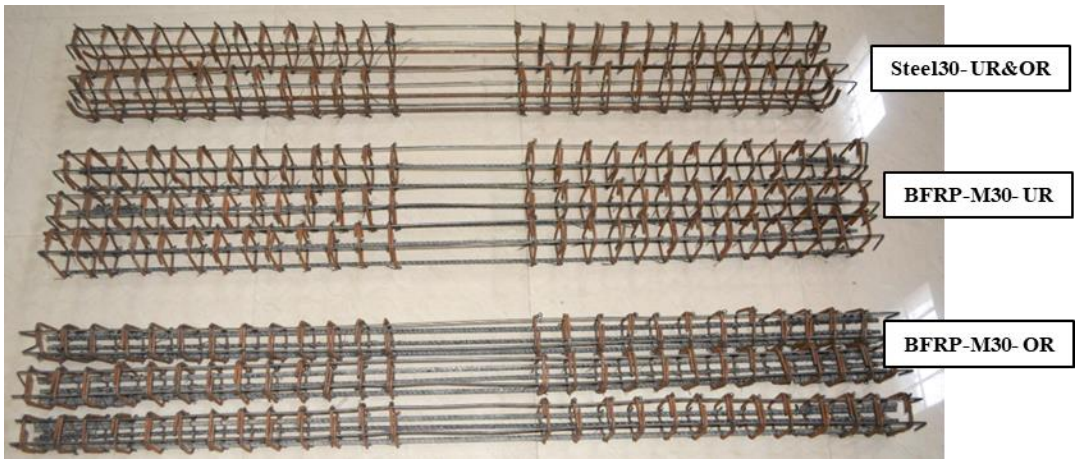

(a) Steel reinforcement

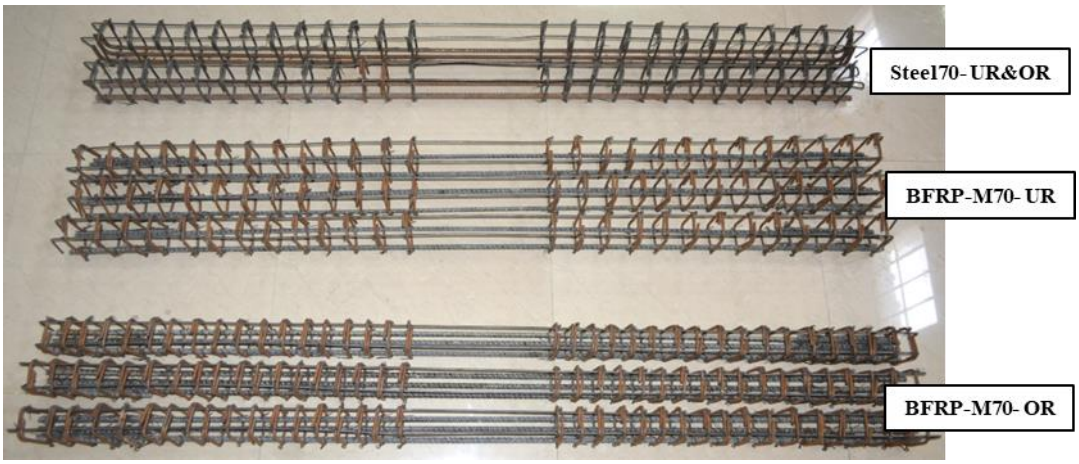

(b) BFRP reinforcement

Figure 6. 4 Reinforcement cages for reinforced concrete beams

6.4 Tensile Test on BFRP and Steel Reinforcing Bars

The conventional method used for the tensile test of steel reinforcing bars was the same used for the tensile test of BFRP rebars. Under the tensile test, the failure of a steel reinforcing bar generally occurs at the provided gauge length. But in the case of BFRP rebar, the same use of BFRP rebar for tensile testing as that of steel reinforcing bars may lead to the crushing failure of the rebar at the bar-holding jaw of the tensile testing machine. This is because BFRP rebar is a composite material and not a homogeneous material like steel reinforcing bars. Therefore, to avoid such crushing failure and to ensure tensile failure at the provided gauge length, as shown in Figure 6.5, steel casings are provided at either end of BFRP rebars used for tensile testing. The gauge length and grip length provided to the BFRP rebars is shown in Figure 6.5.

To carry out tensile tests on 8 mm BFRP rebar, internally helically wound steel tubes with 16 mm inner diameter are used for casing BFRP rebars on either side. Then, to develop high bond strength between BFRP rebar and steel tubes, polyester-based high-strength epoxy resin was

used. The steel tubes were closed at one end, then epoxy resin was filled up to 1/3rd of steel tubes. BFRP rebar was then inserted into the steel tube in a clockwise rotation up to its grip length. To develop high bond strength between rebar, epoxy resin and steel tubes, the epoxy resin filled steel tube inserted with BFRP rebar was hold on tightly and uniform tamping was done. Then the specimen was kept in an undisturbed position for 24 hours, and the same procedure is followed for the other end of BFRP rebar. In the same manner, 10 and 12 mm BFRP rebars were prepared and tested for stress-strain behaviour evaluation. The tensile test on BFRP rebars and steel reinforcing bars was carried out using a universal testing machine of 1000 kN capacity. The tensile test on BFRP rebars was carried in accordance with ASTM D7205/D7205M-06 [208]. Tensile tests on the steel reinforcing bars were conducted in IS 1608 (Part 1)-2018 [209]. The tensile test carried on BFRP rebar, and the failure that occurred at gauge length is showed in Figure 6.6.

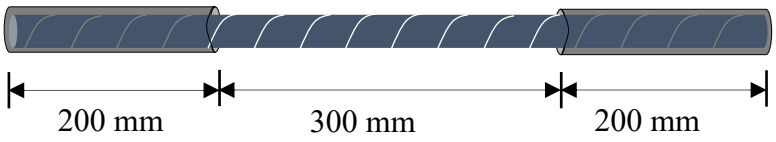

Figure 6.5 A schematic depiction of BFRP rebar prepared for tensile testing.

Figure 6.6 Tensile test on BFRP rebar

6.5 Mix Proportions, Mixing, Cast and Curing of BFRP-Reinforced Concrete Beams

The constituent material quantities used for the development of PC, BFRC and PVAFRC of M30 and M70 grade are presented in Table 6.2. To improve the flexural response of BFRP-reinforced PC beams, 0.3% of basalt fibers and 0.3% of PVA fibers were used to reinforce the PC. The concrete mixing guidelines given in IS 456-2000 [133], was followed for preparation

of PC and PVAFRC and BFRC. Then, immediately after preparation of concrete, a layer (equal to the concrete cover) of fresh PC/BFRC/PVAFRC was filled in the bottom of the oiled iron mould and then a reinforcement cage was placed and the remaining fresh PC/BFRC/PVAFRC was transferred to the iron mould and compacted with the help of a concrete needle vibrator. After 24 hours of cast, all the beams were taken out from the iron mould and kept in water curing for 28days. Figure 6.7 shows the preparation of concrete/FRC and cast of BFRP RC beams.

Table 6.2 Constituent material quantities for BFRP-reinforced concrete beams

Series	**Type concrete**	**Constitutive materials (kg/m^3)**					**w/b ratio**	**fibers used (%)**		**SP (%)**
		Binder materials			**Fine agg.**	**Coarse agg.**				
		Cement	**Fly ash**	**AF-1203**				Basalt fiber	PVA fiber	
M30	PC	315	105	-	760	1080	0.4	-	-	0.25
M30	BFRC	315	105	-	760	1080	0.4	0.3	-	0.25
M30	PVAFRC	315	105	-	760	1080	0.4	-	0.3	0.25
M70	PC	420	120	60	730	950	0.26	-	-	0.725
M70	BFRC	420	120	60	730	950	0.26	0.3	-	0.725
M70	PVAFRC	420	120	60	730	950	0.26	-	0.3	0.725

w/b-water to binder ratio, SP-Superplasticizer, AF-1203- Alccofine-1203

Figure 6.7 Cast of BFRP-reinforced concrete beams

6.6 Test Procedure of BFRP-Reinforced Concrete Beams

The experimental test setup of the beams tested is shown in Figure 6.8. To develop the moment-curvature relationships, the applied load and corresponding deformations developed in the compression and tension zones of the beams during testing were recorded using the DAC system with the help of a 2 MN capacity load cell and LVDTs, as shown in Figure 6.8. To

develop load-deflection curves at the midspan of the beams, the deflections exhibited by the beams under the loading were noted with the help of dial gauges provided under the beams. All the beams were tested under static loading conditions. The tests on the beams were carried out on a Tinius Olsen Testing machine with a maximum capacity of 3000 kN.

Figure 6.8 Experimental testing of BFRP-reinforced concrete beams

6.7 Results and Discussions

6.7.1 Stress-Strain Behaviour of BFRP and Steel Reinforcing Bars

The typical stress-strain plot for BFRP and steel reinforcing bars used in the present study is shown in Figure 6.9. Table 6.3 presents a summary of the tensile test results of BFRP rebars and steel reinforcing bars used for the investigation. Under tensile load, BFRP rebars exhibited linear stress-strain behavior, whereas steel reinforcing bars showed bi-linear stress-strain behavior. Due to basalt fiber's high tensile stress-carrying capacity, the ultimate tensile stress of BFRP rebars was higher than that of the steel reinforcing bars, and the ultimate tensile strain at rupture failure was found to be nearly 7 to 8 times lower than the ultimate tensile strain of steel reinforcing bars. This clearly indicates the negligible elongation of BFRP rebars due to their brittleness and low Young's modulus.

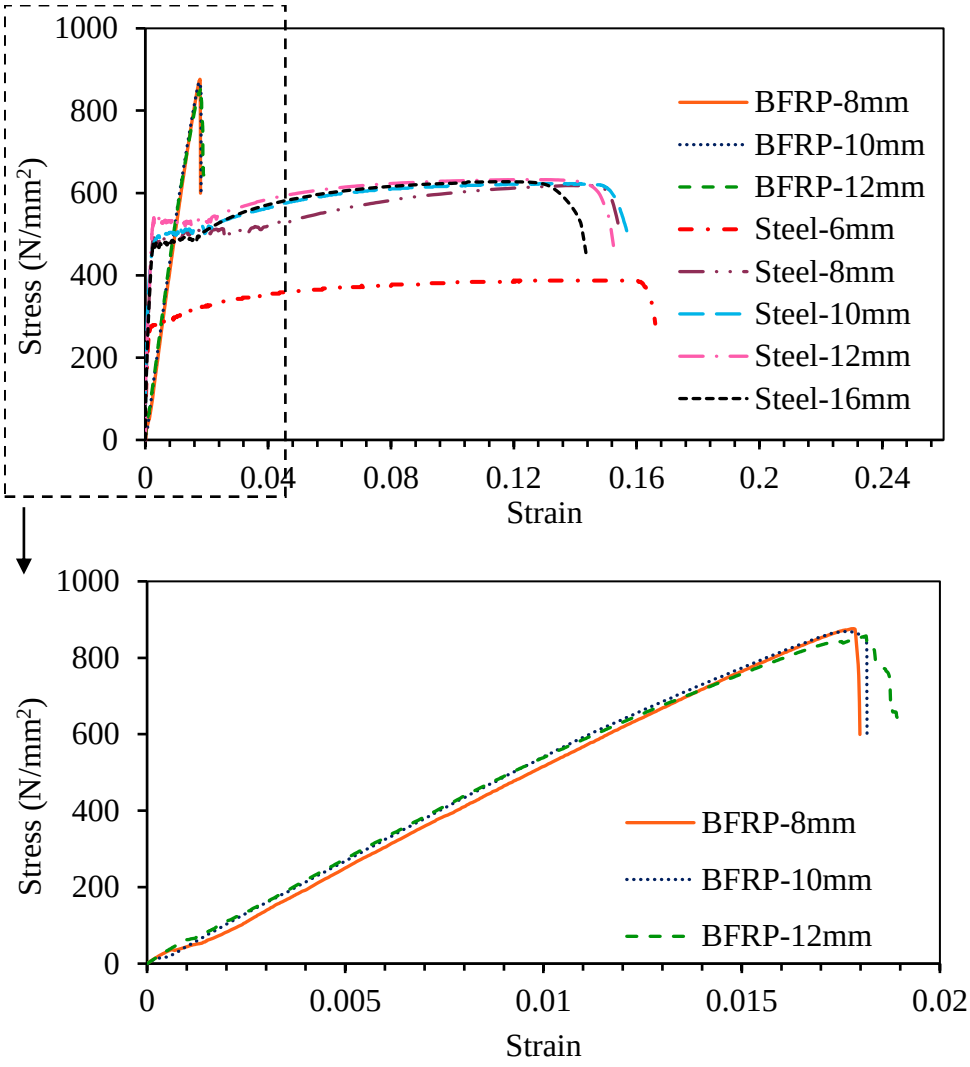

Figure 6.9 Stress-strain curves of BFRP and steel reinforcing bars

Table 6.3 Tensile properties of BFRP and steel reinforcing bars

Reinforcing bar	**Diamter of bar**	**Ultimate load (kN)**	**Ultimate Tensile strength (N/mm²)**	**Strain at ultimate failure**	**Yield strength (N/mm²)**	**Young's modulus (GPa)**	**Elangation (%)**
BFRP	8 mm	44.04	876.16	0.0178	-	56	1.78
	10 mm	68.25	868.79	0.0176	-	55	1.76
	12 mm	96.92	857.04	0.0181	-	56	1.81
steel	6 mm	10.95	387.18	0.1489	266.58	205	14.89
	8 mm	31.07	618.20	0.1434	486.74	195	14.34
	10 mm	48.91	622.71	0.1373	484.80	198	13.73
	12 mm	71.52	632.41	0.1283	528.40	199	12.83
	16 mm	126.14	627.39	0.1185	477.76	200	11.85

6.7.2 Load-Deflection Behavior of BFRP-Reinforced Concrete Beams

The load-deflection behavior of all tested beams of M30 and M70 series is illustrated in Figures 6.10 to 6.13. The deflections at the first cracking load and ultimate load of all tested beams are tabulated in Table 6.4. The stiffness of the tested beams calculated before and after cracking from the load-deflection curves is presented in Table 6.5. The steel-reinforced PC beams and BFRP RC beams showed distinct behavior in load-deflection curves. The pre-cracking load-deflection behavior of steel-reinforced PC beams and BFRP RC beams was similar. However, the post-cracking behavior of these beams was clearly different. The load-deflection curves of steel-reinforced PC beams showed three different stages before complete failure: the first stage was from the point of loading to the first cracking of concrete in the tension zone of the beam, the second stage was from cracking of concrete to yielding of the steel reinforcement, and the third stage was from yielding of steel reinforcement to the crushing of concrete at the compression zone at ultimate load. The load-deflection curves of BFRP-reinforced PC, BFRC, and PVAFRC beams exhibited bilinear load-deflection behavior with two different stages before complete failure: the first stage was from the point of loading to the first cracking of concrete in the tension zone of the beam, and the second stage was from the cracking of concrete to the crushing of concrete in the compression zone at ultimate load. In both steel-reinforced PC beams and BFRP RC beams, concrete crushing or rupture failure of reinforcing bars is referred to as the ultimate strength of the beam. The pre-cracking stiffness of beams was measured at a load value equal to 10% of the ultimate load; the post-cracking stiffness of the test beams was measured at a load value equal to 75% of the ultimate load.

6.7.2.1 Load-deflection behavior of steel-reinforced PC beams

The experimental load-deflection curves of steel-reinforced PC beams tested in Phase I of the M30 and M70 series are shown in Figure 6.10.

First stage of the load-deflection curve

From Figure 6.10, it was observed that from the beginning of loading to cracking, all the tested steel-reinforced PC beams (SUR30, SOR30, SUR70, and SOR70) exhibited linear load-deflection behavior with greater stiffness in the first stage compared to the second stage of the load-deflection curves. The slope of the curves for both M30 and M70 series beams was nearly the same at this stage. The steel over-reinforced PC beams showed slightly higher load and deflection at cracking than steel under-reinforced PC beams. The pre-cracking stiffness of beams, calculated from the first stage of the load-deflection curves, shows that in both series,

SOR30 and SOR70 beams exhibited higher stiffness than SUR30 and SUR70 beams due to the higher steel reinforcement area. In the first stage of load-deflection curves, M70 series steel-reinforced PC beams showed higher load and deflection values at cracking, as well as higher pre-cracking stiffness compared to M30 series beams.

Second stage of the load-deflection curve

In the second stage of load-deflection curves, all the steel-reinforced PC beams exhibited linear load-deflection behavior even after cracking, but the slope of the curves reduced compared to the slope of the curve in the first stage. This indicates a decrease in the stiffness of the beam because of cracking. The stiffness values of the beams after cracking are tabulated in Table 6.5. At the end of the second stage of the load-deflection curves, the steel over-reinforced PC beams in both series showed higher load and deflection compared to under-reinforced beams. Therefore, similar to the first stage, the steel over-reinforced beams showed higher post-cracking stiffness in the second stage of load-deflection curves compared to the steel under-reinforced PC beams in both M30 and M70 series. The beams of the M70 series showed higher loads and deflections at the start of yielding of steel rebar, as well as higher post-cracking stiffness compared to SUR30 and SOR30 beams.

Third stage of the load-deflection curve

In the third stage, the slope of the load-deflection curves of steel-reinforced PC beams decreased largely due to the yielding of steel reinforcing bars, as well as crack widening and propagation. The large drop in the slope of the load-deflection curves indicates the maximum decrease in the stiffness of the beams. At this stage, as expected, the yielding of steel reinforcement in under-reinforced beams and the cracking and crushing of concrete in over-reinforced beams caused a plateau in the load-carrying capacity, but the deflection of beams increased continuously with a limited increase in load until flexural tension or flexural compression failure occurred. In both series, at the ultimate load, steel over-reinforced PC beams showed higher strength and lower deflections compared to steel under-reinforced PC beams. Therefore, in the third stage, steel over-reinforced PC beams showed comparatively better stiffness than steel under-reinforced PC beams.

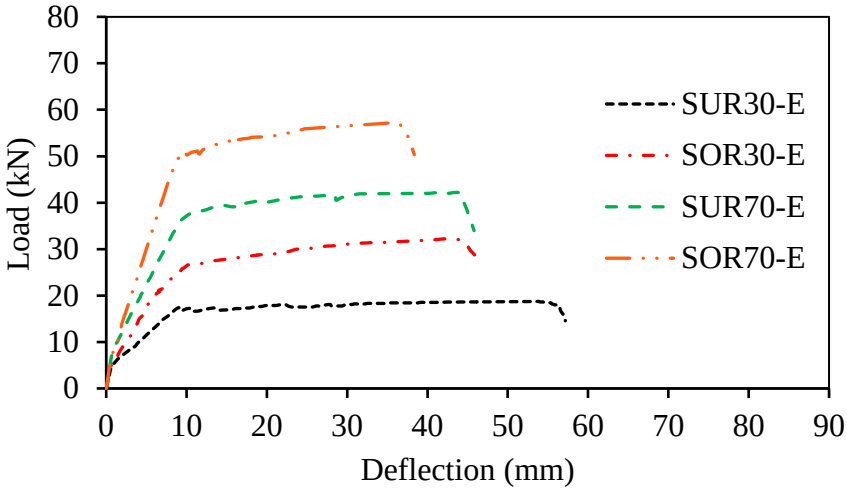

Figure 6.10 Experimental load-deflection curves of steel-reinforced PC beams

6.7.2.2 Load-deflection behavior of BFRP-reinforced PC beams

The experimental load-deflection curves of the BFRP-reinforced PC beams tested in Phase II of M30 and M70 series are shown in Figure 6.11, in comparison with experimental load-deflection curves of steel-reinforced PC beams.

First stage of the load-deflection curve

The pre-cracking load-deflection behavior of all BFRP-reinforced PC beams in the first stage of the load-deflection curve is linear, similar to the pre-cracking load-deflection behavior of steel-reinforced PC beams. The BFRP over-reinforced PC beams had higher load and deflection values at cracking compared to BFRP under-reinforced PC beams. The pre-cracking stiffness, calculated from the first stage of the load-deflection curves, shows that in both the series, BOR30 and BOR70 beams showed higher pre-cracking stiffness than BUR30 and BUR70 beams because of a higher BFRP reinforcement area. Compared to M30 series BFRP-reinforced PC beams, M70 series BFRP-reinforced PC beams had higher load and deflection at cracking, as well as higher stiffness in the first stage of the load-deflection curves.

All the BFRP-reinforced PC beams showed load and deflection values at cracking that were almost the same as the load and deflection values at cracking of steel-reinforced PC beams. But compared to the steel-reinforced PC beams, the BFRP-reinforced PC beams had lower stiffness (refer to Table 6.5). BFRP over-reinforced PC beams showed greater stiffness with higher slope values than BFRP under-reinforced PC beams prior to beam cracking. The BFRP-reinforced PC beams of the M70 series had higher stiffness and slope before cracking when compared to BFRP-reinforced PC beams of the M30 series. This is attributed to higher concrete strength and a larger reinforcement ratio. The BFRP under- and over-reinforced PC beams of the M70 series

had stiffness of 10.26 kN/mm and 10.83 kN/mm in the first stage of the load-deflection curve, whereas BFRP under- and over-reinforced PC beams of the M30 series have stiffness values of 7.40 kN/mm and 7.53 kN/mm.

Second stage of the load-deflection curve

It can be observed from Figure 6.11 that the post-cracking stiffness of BFRP-reinforced PC beams decreased considerably in the second stage of load-deflection curves and had a gentler slope than steel-reinforced PC beams. After cracking, the deflection of BFRP-reinforced PC beams increased linearly with respect to the load until ultimate failure occurred. In both series, as expected, BFRP under-reinforced PC beams showed higher deflection for lower loads, and BFRP over-reinforced PC beams showed lower deflections for higher loads. In the M30 series, BUR30 exhibited a deflection of 41.25 mm at an ultimate load of 28.41 kN, whereas BOR30 exhibited a deflection of 34.03 mm at an ultimate load of 46.02 kN. In the M70 series, BUR70 exhibited a deflection of 38.70 mm at an ultimate load of 54.35 kN, whereas BOR70 exhibited a deflection of 30.65 mm at an ultimate load of 70.77 kN.

All the BFRP-reinforced PC beams exhibited higher flexural strengths than steel-reinforced PC beams. The BFRP under- and over-reinforced PC beams of the M30 series had 51.6% and 42.9% higher ultimate loads, and BFRP under- and over-reinforced PC beams of the M70 series had 28.64% and 23.63% higher ultimate loads compared to steel-reinforced PC beams because of the high tensile force carrying capacity of BFRP rebars. The flexural strength results show that BFRP rebars improved the flexural strength of M30 series BFRP-reinforced PC beams more significantly compared to BFRP-reinforced PC beams of the M70 series. At the ultimate load, BFRP under- and over-reinforced PC beams exhibited lower deflection than steel-reinforced PC beams in both series.

Figure 6.11 shows that after cracking, all the BFRP-reinforced PC beams exhibited linear behavior in the second phase of the load-deflection curve until the ultimate failure of the beam occurred. The post-cracking stiffness of all the BFRP-reinforced PC beams was significantly lower compared to the pre-cracking stiffness of steel-reinforced PC beams. Similar to the first stage, BFRP over-reinforced PC beams had better stiffness and slope than BFRP under-reinforced PC beams in the second stage of the load-deflection curve. The M70 series beams showed higher post-cracking stiffness and slope compared to M30 series beams in the second stage. The post-cracking stiffness of BFRP-reinforced PC beams reduced compared to the post-cracking stiffness of steel-reinforced PC beams. This is attributed to the lower Young's modulus

and stiffness of BFRP rebars than the Young's modulus and stiffness of steel reinforcing bars (refer to Table 6.5).

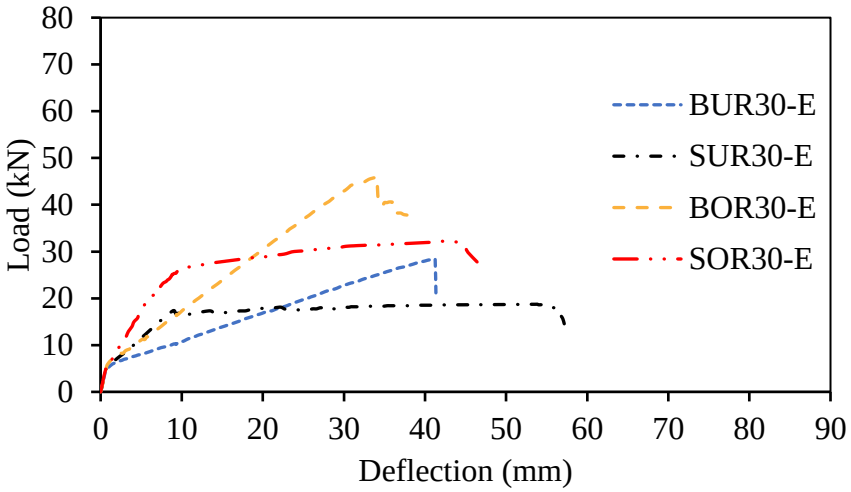

(a) M30 series

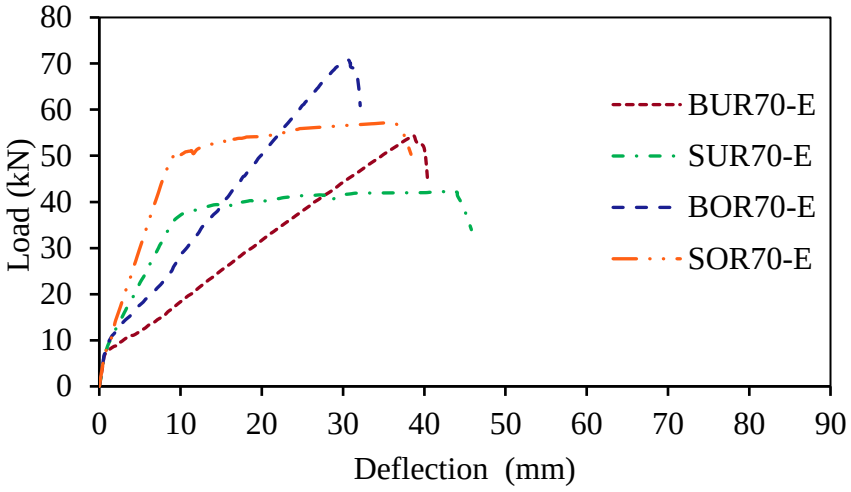

(b) M70 series

Figure 6.11 Experimental load-deflection curves of BFRP-reinforced PC beams

6.7.2.3 Load-deflection behavior of BFRP-reinforced BFRC beams

The experimental load-deflection curves of BFRP-reinforced BFRC beams tested in Phase III of M30 and M70 series are illustrated in Figure 6.12, in comparison with the experimental load-deflection curves of BFRP-reinforced PC beams.

First stage of the load-deflection curve

The pre-cracking load-deflection behavior of all BFRP-reinforced BFRC beams was linear, similar to that of steel-reinforced PC beams and BFRP-reinforced PC beams. The incorporation of basalt fibers marginally enhanced the cracking load and deflection at cracking of BFRP under- and over-reinforced BFRC beams in both series compared to BFRP-reinforced PC

beams and steel-reinforced PC beams. BFRP under- and over-reinforced BFRC beams of M30 showed higher load and deflection at cracking than BFRP-reinforced PC beams and steel-reinforced PC beams, whereas BFRP-reinforced BFRC beams of M70 series showed higher load and deflection at cracking than BFRP-reinforced PC beams but exhibited almost equal cracking load and corresponding deflection to the steel-reinforced PC beams. In both series, BFRP over-reinforced BFRC beams showed higher load and deflection values at cracking compared to BFRP under-reinforced BFRC beams. The pre-cracking stiffness of BFRP-reinforced BFRC beams increased partially with the addition of basalt fibers compared to BFRP-reinforced PC beams and steel-reinforced PC beams (refer to Table 6.5). Similar to steel-reinforced PC beams and BFRP-reinforced PC beams, before cracking, BFRP over-reinforced BFRC beams showed higher pre-cracking stiffness with better slope values than BFRP under-reinforced BFRC beams. Compared to M30 series BFRP-reinforced BFRC beams, M70 series BFRP-reinforced BFRC beams exhibited higher stiffness and slope before the first crack.

Second stage of the load-deflection curve

It can be observed from Figure 6.12 that in the second stage of load-deflection curves of BFRP-reinforced BFRC beams, the post-cracking stiffness decreased compared to pre-cracking stiffness, similar to the case of steel-reinforced PC beams and BFRP-reinforced PC beams. In the second phase, BFRP-reinforced BFRC beams had a gentler slope compared to steel-reinforced PC beams. The addition of basalt fibers slightly improved post-cracking stiffness of BFRP under-reinforced BFRC beams compared to BFRP under-reinforced PC beams. The addition of basalt fibers did not show much effect in improving the stiffness of the BFRP over-reinforced BFRC beam. However, BFRP-reinforced BFRC beams have lower stiffness than steel-reinforced PC beams.

After cracking, the deflections of BFRP-reinforced BFRC beams increased linearly with respect to load until reaching the ultimate load. The BFRP under- and over-reinforced BFRC beams of the M30 series exhibited higher deflections at ultimate loads than BFRP-reinforced PC beams but lower deflections than steel-reinforced PC beams. The BFRP under- and over-reinforced BFRC beams of the M70 series exhibited higher deflections at ultimate load than BFRP-reinforced PC beams and steel-reinforced PC beams. In both series, compared to BFRP over-reinforced BFRC beams, BFRP under-reinforced BFRC beams showed higher deflection at ultimate load, and compared to BFRP under-reinforced BFRC beams, BFRP over-reinforced BFRC beams showed higher ultimate loads. All the BFRP-reinforced BFRC beams exhibited higher flexural strengths than BFRP-reinforced PC beams and steel-reinforced PC beams. The

BFRP under- and over-reinforced BFRC beams of the M30 series have 4.44% and 3.70% higher ultimate loads, and BFRP under- and over-reinforced BFRC beams of the M70 series have 1.27% and 3.17% higher ultimate loads compared to BFRP-reinforced PC beams. This may be attributed to reinforcing PC with 0.3% basalt fibers.

Figure 6.12 shows that after cracking, all the BFRP-reinforced BFRC beams exhibited linear load-deflection behavior in the second phase of the load-deflection curve until the ultimate failure of the beam. The post-cracking stiffness of all BFRP-reinforced BFRC beams was considerably lower compared to the pre-cracking stiffness, similar to the case of steel-reinforced PC beams and BFRP-reinforced PC beams. Similar to the first stage, BFRP over-reinforced BFRC beams had better stiffness and slope values than BFRP under-reinforced BFRC beams in the second stage. The M70 series beams showed higher post-cracking stiffness and slope values compared to M30 series beams at this stage. The BBUR70 and BBOR70 showed post-cracking stiffness of 1.94 kN/mm and 2.36 kN/mm, whereas BBUR30 and BBOR30 showed post-cracking stiffness of 0.80 kN/mm and 1.35 kN/mm. The addition of basalt fibers slightly improved post-cracking stiffness of BFRP under- and over-reinforced BFRC beams compared to BFRP under- and over-reinforced PC beams. However, BFRP-reinforced BFRC beams had lower post-cracking stiffness than steel-reinforced PC beams in both series (refer to Table 6.5). The flexural strength results show that the addition of basalt fibers improved the flexural strength of M30 series BFRP-reinforced BFRC beams more than M70 series BFRP-reinforced BFRC beams.

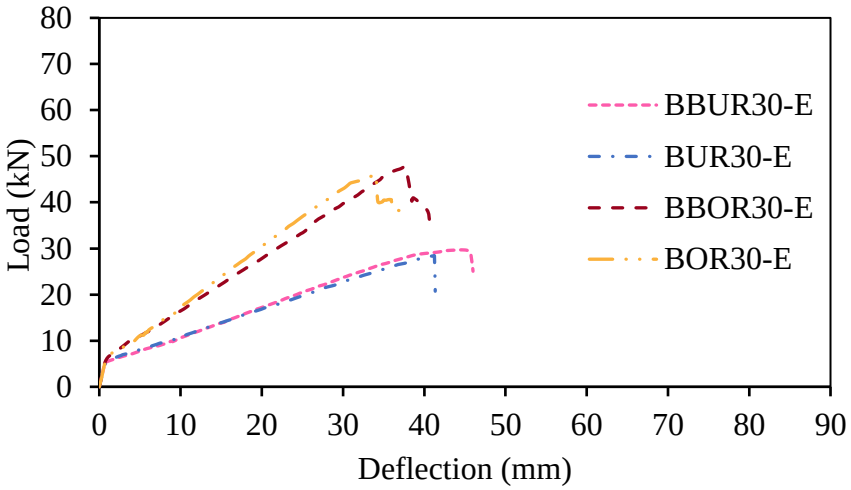

(a) M30 series

Figure continues...

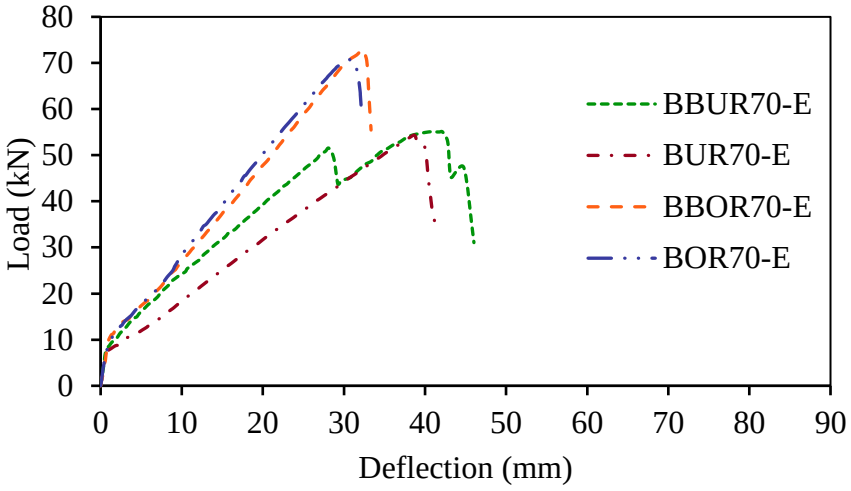

(b) M70 series

Figure 6.12 Experimental load-deflection curves of BFRP-reinforced BFRC beams

6.7.2.4 Load-deflection behavior of BFRP-reinforced PVAFRC beams

The experimental load-deflection curves of BFRP-reinforced PVAFRC beams tested in Phase IV of M30 and M70 series are illustrated in Figure 6.13, in comparison with experimental load-deflection curves of BFRP-reinforced BFRC beams.

First stage of the load-deflection curve

The pre-cracking load-deflection behavior of all BFRP-reinforced PVAFRC beams was linear, the same as the pre-cracking load-deflection behavior of BFRP-reinforced BFRC and PC beams and steel-reinforced PC beams. The deflection at the cracking of BFRP-reinforced PVAFRC beams in both M30 and M70 series was nearly the same as the deflection at cracking of BFRP-reinforced BFRC beams. However, the load at cracking of BFRP-reinforced PVAFRC beams in both series improved with the incorporation of PVA fibers compared to BFRP-reinforced BFRC beams (refer to Table 6.4). The BFRP over-reinforced PVAFRC beams showed higher load and deflection values at cracking compared to BFRP under-reinforced PVAFRC beams. The addition of PVA fibers increased the pre-cracking stiffness of BFRP-reinforced PVAFRC beams more than BFRP-reinforced BFRC and PC beams (refer to Table 6.5). Similar to the beams of Phases I, II, and III, before cracking, BFRP over-reinforced PVAFRC beams showed higher pre-cracking stiffness with better slope values than the BFRP under-reinforced PVAFRC beams. Compared to M30 series BFRP-reinforced PVAFRC beams, M70 series BFRP-reinforced PVAFRC beams exhibited higher pre-cracking stiffness and a higher slope before the first crack.

Second stage of the load deflection curve

It can be observed from Figure 6.13 that in the second stage of load-deflection curves of BFRP-reinforced PVAFRC beams, the post-cracking stiffness of the beams decreased compared to pre-cracking stiffness. In the second phase of the load-deflection curves, BFRP-reinforced PVAFRC beams had a lower slope compared to steel-reinforced PC beams. The addition of PVA fibers slightly improved post-cracking stiffness of BFRP over-reinforced PVAFRC beams compared to BFRP over-reinforced BFRC beams. The addition of PVA fibers did not show much effect in improving the stiffness of BFRP under-reinforced PVAFRC beams. However, BFRP-reinforced PVAFRC beams had lower stiffness than steel-reinforced PC beams.

After the cracking of the beam, the deflections of BFRP-reinforced PVAFRC beams increased linearly with respect to the load until the failure of the beams. The BFRP under- and over-reinforced PVAFRC beams of the M30 series exhibited higher deflections at ultimate loads than BFRP-reinforced BFRC and PC beams but showed lower deflections than steel-reinforced PC beams. The BFRP under- and over-reinforced PVAFRC beams of the M70 series exhibited higher deflections at ultimate load than BFRP-reinforced BFRC and PC beams and steel-reinforced PC beams. In both series, compared to BFRP over-reinforced PVAFRC beams, BFRP under-reinforced PVAFRC beams showed higher deflection at ultimate load, and compared to BFRP under-reinforced PVAFRC beams, BFRP over-reinforced PVAFRC beams showed higher ultimate loads (refer to Table 6.4). All the BFRP-reinforced PVAFRC beams exhibited higher flexural strengths than BFRP-reinforced BFRC and PC beams as well as steel-reinforced beams. The BFRP under- and over-reinforced PVAFRC beams of the M30 series had 8.80% and 11.51% higher ultimate loads, and the BFRP under- and over-reinforced PVAFRC beams of the M70 series had 2.91% and 4.94% higher ultimate loads compared to the BFRP-reinforced PC beams. This may be attributed to the increase in concrete flexural strength properties with the toughening effect of incorporated PVA fibers.

Figure 6.13(a) and (b) show that after cracking, all the BFRP-reinforced PVAFRC beams exhibited linear load-deflection behavior in the second phase of the load-deflection curve until the ultimate failure of the beam. The post-cracking stiffness of all BFRP-reinforced PVAFRC beams decreased compared to pre-cracking stiffness. Similar to the first stage, BFRP over-reinforced PVAFRC beams had better stiffness and slope values than BFRP under-reinforced PVAFRC beams in the second stage of the load-deflection curve. The M70 series beams showed higher post-cracking stiffness and slope values compared to M30 series beams at this stage. In the second phase of load-deflection curves, BFRP-reinforced PVAFRC beams had a

gentler slope compared to steel-reinforced PC beams. The addition of PVA fibers improved the post-cracking stiffness of BFRP over-reinforced PVAFRC beams slightly compared to BFRP over-reinforced BFRC and PC beams. The addition of PVA fibers did not show much effect in improving the post-cracking stiffness of BFRP under-reinforced PVAFRC beam. However, BFRP-reinforced PVAFRC beams had lower post-cracking stiffness than steel-reinforced PC beams in both series (refer to Table 6.5). The flexural strength results show that the addition of PVA fibers improved the flexural strength of M30 series BFRP-reinforced PVAFRC beams more than M70 series BFRP-reinforced PVAFRC beams.

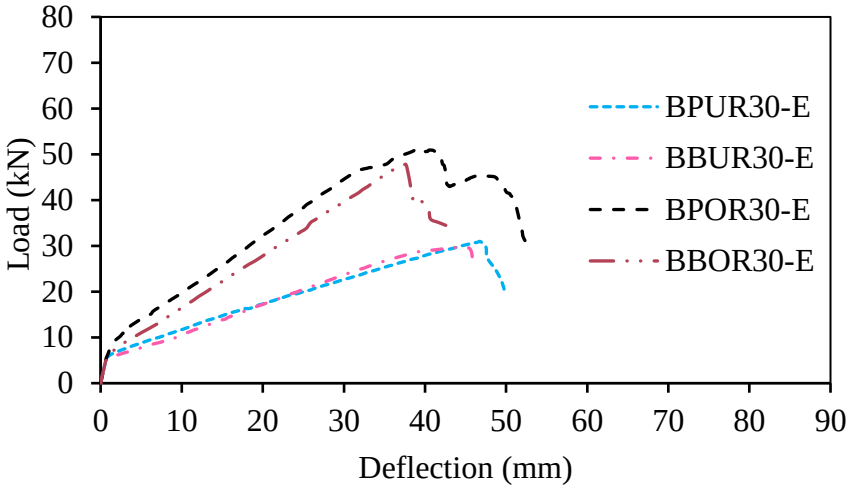

(a) M30 series

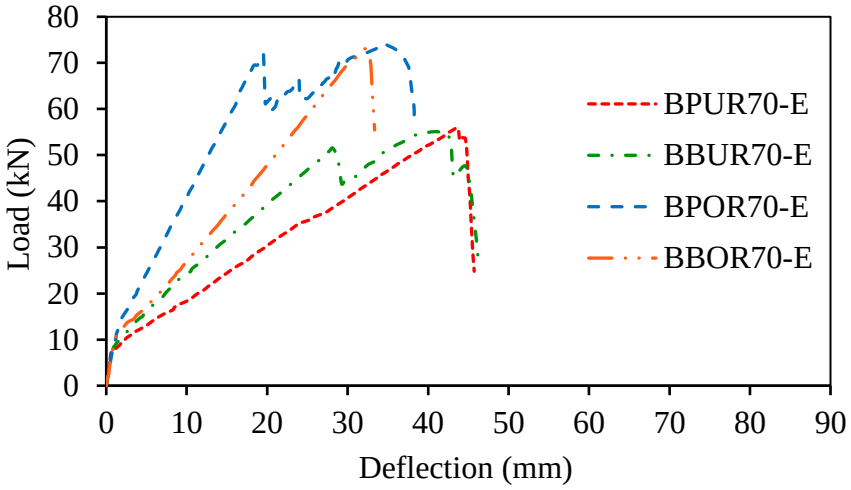

(b) M70 series

Figure 6.13 Experimental load-deflection curves of BFRP-reinforced PVAFRC beams

Table 6.4 Experimental load-deflection results of BFRP-reinforced concrete beams

Series	Beam name	First cracking load (P_{FCL}) (kN)	Deflection at first cracking load (δ_{FCL}) (mm)	Ultimate load (P_{UL}) (kN)	Deflection at max. load (δ_{UL}) (mm)
M30	SUR30	4.87	0.67	18.74	53.87
	SOR30	5.50	0.75	32.20	42.01
	BUR30	4.81	0.67	28.41	41.25
	BOR30	5.47	0.75	46.02	34.04
	BBUR30	5.27	0.74	29.67	45.00
	BBOR30	5.70	0.80	47.72	37.66
	BPUR30	5.57	0.75	30.91	46.85
	BPOR30	5.94	0.82	51.31	39.30
M70	SUR70	7.13	0.74	42.25	42.25
	SOR70	7.65	0.81	57.24	35.85
	BUR70	7.04	0.72	54.35	38.70
	BOR70	7.61	0.77	70.77	30.65
	BBUR70	7.39	0.74	55.04	41.33
	BBOR70	7.90	0.82	73.01	32.25
	BPUR70	7.56	0.81	55.93	43.65
	BPOR70	8.04	0.86	74.26	34.32

Table 6.5 Experimental stiffness results of BFRP-reinforced concrete beams

Series	Beam name	10% of ultimate load	Deflection at 10% of ultimate load (kN)	Stiffness before cracking (kN/mm)	75% to ultimate load	Deflection at 70% of ultimate load (kN)	Stiffness after cracking (kN/mm)
M30	SUR30	1.87	0.25	7.48	14.05	6.61	2.13
	SOR30	3.22	0.39	8.22	24.15	8.46	2.86
	BUR30	2.84	0.38	7.40	21.31	27.51	0.77
	BOR30	4.60	0.61	7.53	34.51	23.13	1.49
	BBUR30	2.97	0.39	7.68	22.25	27.81	0.80
	BBOR30	4.77	0.62	7.72	35.79	26.53	1.35
	BPUR30	3.09	0.40	7.74	23.18	31.05	0.75
	BPOR30	5.13	0.65	7.96	38.49	25.08	1.53
M70	SUR70	4.22	0.41	10.38	31.69	7.80	4.06
	SOR70	5.72	0.53	10.87	42.93	7.44	5.77
	BUR70	5.43	0.53	10.26	40.76	27.18	1.50
	BOR70	7.08	0.65	10.83	53.08	21.32	2.49
	BBUR70	5.50	0.52	10.59	41.28	21.30	1.94
	BBOR70	7.30	0.66	11.14	54.76	23.17	2.36
	BPUR70	5.59	0.50	11.08	41.95	31.06	1.35
	BPOR70	7.43	0.65	11.39	55.70	14.44	3.86

6.7.3 Moment-Curvature Relationships of BFRP-Reinforced Concrete Beams

The experimental moment-curvature relationships of all tested beams are shown in Figures 6.14 to 6.17. The moments and curvatures at cracking and ultimate stages of all the beams are presented in Table 6.6. Curvature is a crucial term indicating the deformation of a structure under applied load. It was determined at the mid-section through a section analysis using experimental concrete and BFRP strains. The moment-curvature relationships of all tested beams were found to be similar to the load-deflection relationship of beams because the curvature of beams closely resembled the pattern of concrete and BFRP strains, as well as the mid-point deflection of beams. The cracking moment and ultimate moment of the beams were determined by the load at the first crack and the load at the ultimate failure of the beams. The steel-reinforced PC beams and BFRP RC beams exhibited moment-curvature relationships of the same behavior up to the cracking moment. However, beyond the cracking moment, steel-reinforced PC beams and BFRP RC beams showed different moment-curvature relationships, as depicted in Figures 6.14 to 6.17. Test data indicates that at cracking and ultimate load, the over-reinforced beams of Phases I, II, III, and IV of both M30 and M70 series showed higher moments and lower curvature values compared to under-reinforced beams.

6.7.3.1 Moment-curvature relationships of steel-reinforced PC beams

The experimental moment-curvature relationships of the steel-reinforced PC beams of M30 and M70 series are shown in Figure 6.14. The test results indicate that the steel under-reinforced PC beam exhibited a larger curvature at lower cracking and ultimate moments, whereas steel over-reinforced PC beams exhibited lower curvature at higher cracking and ultimate moments (refer to Table 6.6). In both series, steel-reinforced PC beams showed cracking moments and curvature at cracking moments that were higher than those of BFRP-reinforced PC beams. This is attributed to an increase in the gross cross-sectional inertia and stiffness of the beams by reinforcing with steel reinforcing bars. The steel reinforcing bars had a higher Young's modulus and stiffness than BFRP rebars. Thus, the area of steel reinforcement provided, and their stiffness significantly impact the cracking moment. In both M30 and M70 series, steel-reinforced PC beams of M70 series had higher moments but lower curvatures at cracking and ultimate failure of the beams compared to steel-reinforced beams of M30 series. This is due to M30 series beams showing higher deflection under applied load than those of M70 series beams.

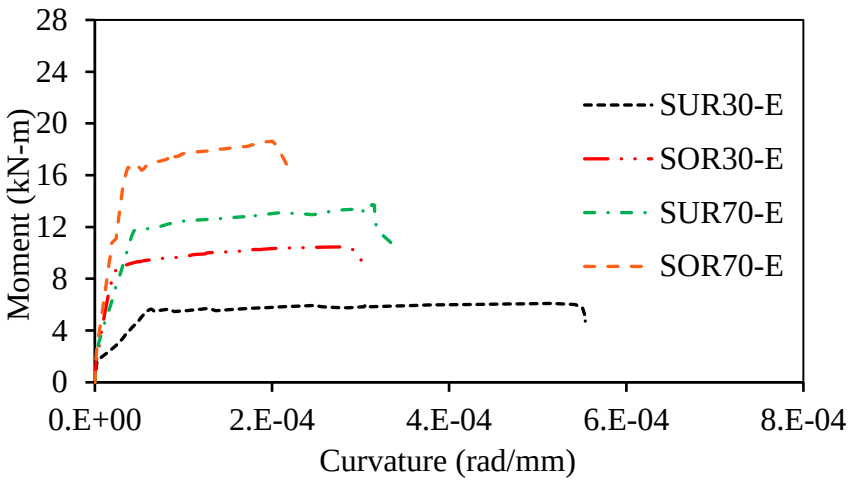

Figure 6.14 Experimental moment-curvature relationships of steel-reinforced PC beams

6.7.3.2 Moment-curvature relationships of BFRP-reinforced PC beams

The experimental moment-curvature relationships of all the BFRP-reinforced PC beams evaluated in Phase II of M30 and M70 series are shown in Figures 15, in comparison with the experimental moment-curvature relationships of all steel-reinforced PC beams. All the BFRP-reinforced PC beams showed a cracking moment near that of the steel-reinforced PC beams, but the curvature at the cracking moment of BFRP-reinforced PC beams was lower than the curvature at the cracking moment of steel-reinforced PC beams (refer to Table 6.6). This difference was due to the development of lower strain values in BFRP rebars compared to the development of strains in steel reinforcing bars at cracking. In both series, BFRP-reinforced PC beams showed lower curvature and higher ultimate moments compared to steel-reinforced PC beams. The BFRP rebar had a higher strength carrying capacity and underwent only a small percentage of elongation before failure, whereas the steel reinforcing had a lower strength carrying capacity and underwent substantial deformation before failure due to yielding. Therefore, BFRP rebars developed lower strain values at higher loads, and steel reinforcing bars developed higher strain values at lower loads until they reached their maximum tensile strength. Because of this, all the BFRP-reinforced PC beams showed lower curvature and higher ultimate moments than steel-reinforced PC beams. The test data shows that similar to the behavior of steel under-reinforced PC beams, BFRP under-reinforced PC beams also exhibited larger curvature at lower cracking and ultimate moments, whereas BFRP over-reinforced PC beams exhibited lower curvature at higher cracking and ultimate moments. In both M30 and M70 series, BFRP-reinforced PC beams of M30 series showed a large curvature at lower cracking and ultimate moments compared to BFRP-reinforced PC beams of M70 series. This was due to the development of large strain values in BFRP rebars and concrete of BUR30 and

BOR30 beams compared to the development of strain values in BFRP rebars and concrete of BUR70 and BOR70 beams, respectively.

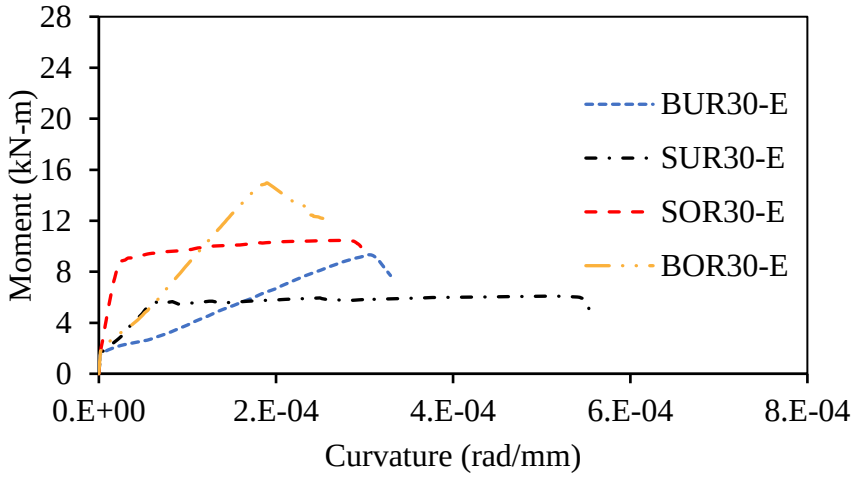

(a) M30 series

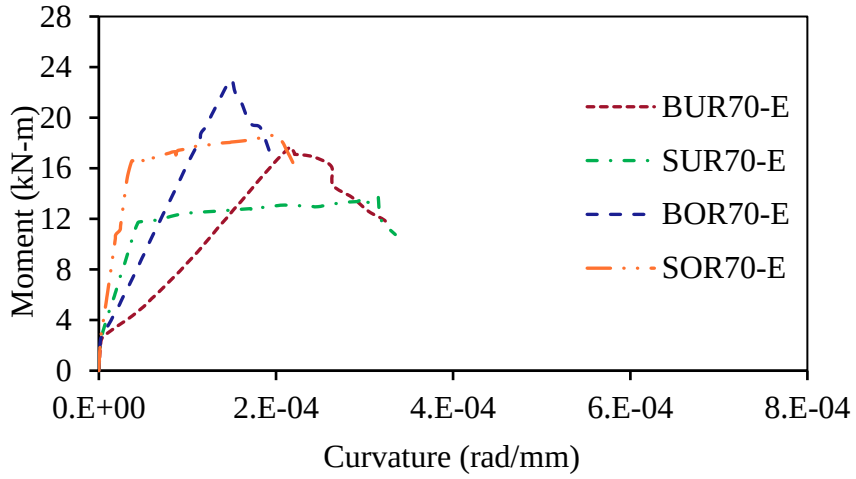

(b) M70 series

Figure 6.15 Experimental moment-curvature relationships of BFRP-reinforced PC beams

6.7.3.3 Moment-curvature relationships of BFRP-reinforced BFRC beams

The experimental moment-curvature relationships of BFRP-reinforced BFRC beams tested in Phase III of the M30 and M70 series are shown in Figure 6.16. The moment at cracking and ultimate load, along with their corresponding curvature, increased with the addition of basalt fibers in all BFRP-reinforced BFRC beams. These beams exhibited higher cracking and ultimate moments than both BFRP-reinforced PC beams and steel-reinforced PC beams. The incorporation of basalt fibers increased the strength of concrete at the cracking and ultimate stages by inducing a crack-bridging effect and consuming fracture energy against crack propagation and widening. Therefore, it increased the strength of the concrete, resulting in

higher cracking moments and ultimate moments compared to BFRP-reinforced PC beams and steel-reinforced PC beams. In comparison to steel-reinforced PC beams, the curvature that decreased in PC beams by reinforcing with BFRP rebars increased with the addition of basalt fibers. Thus, all BFRP-reinforced BFRC beams showed higher curvature at cracking and ultimate moments than those of the curvature at cracking and ultimate moments of BFRP-reinforced PC beams. This was due to the development of additional strain values in BFRC with the incorporation of basalt fibers compared to the development of strain values in PC. However, all BFRP-reinforced BFRC beams had lower curvature at cracking and ultimate moment compared to the curvature at cracking and ultimate moment of steel-reinforced PC beams (refer to Table 6.6). The test data shows that BFRP under-reinforced BFRC beams exhibited larger curvature at lower cracking and ultimate moments, whereas BFRP over-reinforced BFRC beams exhibited lower curvature at higher cracking and ultimate moments. BFRP-reinforced BFRC beams of M30 series showed higher curvature at lower cracking moments and ultimate moments compared to BFRP-reinforced BFRC beams of M70 series. This was due to the development of large strain values in BFRP rebars and concrete of BBUR30 and BBOR30 beams compared to the development of strain values in BFRP rebars and concrete of BBUR70 and BBOR70 beams, respectively.

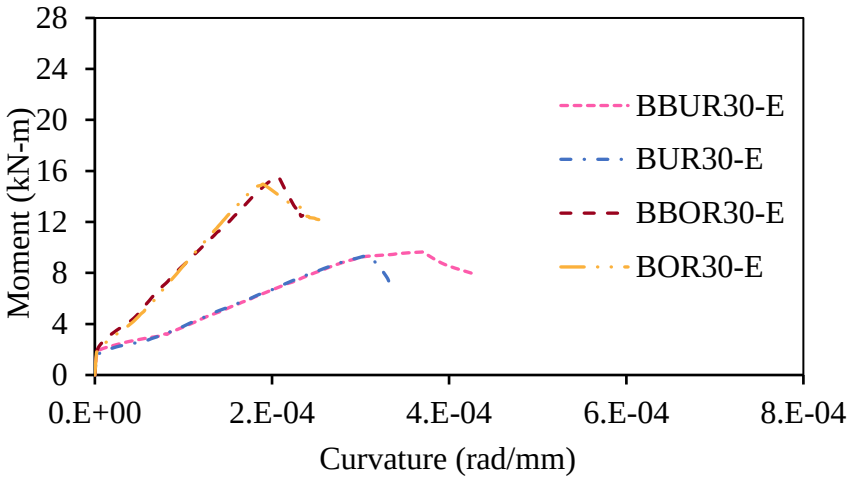

(a) M30 series

Figure continues...

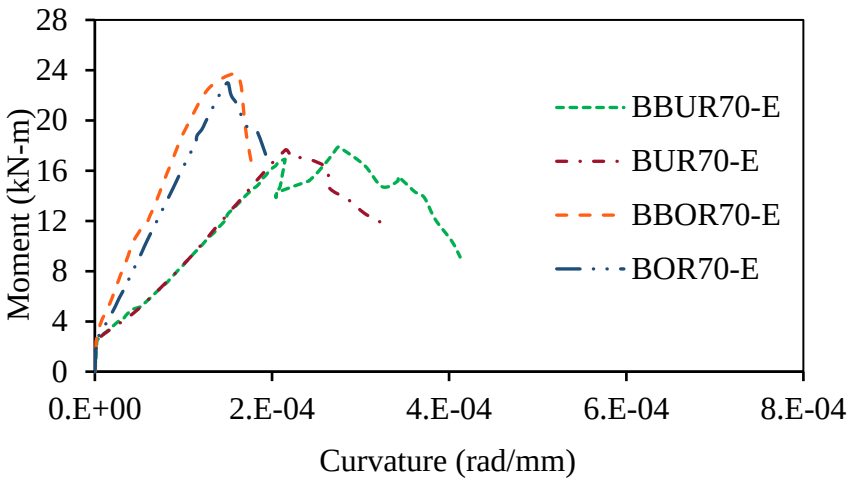

(b) M70 series

Figure 6.16 Experimental moment-curvature relationships of BFRP-reinforced BFRC beams

6.7.3.4 Moment-curvature relationships of BFRP-reinforced PVAFRC beams

The experimental moment-curvature relationships of BFRP-reinforced PVAFRC beams tested in Phase IV of the M30 and M70 series are shown in Figure 16.17(a) and (b), respectively, in comparison with the experimental moment-curvature relationships of BFRP-reinforced BFRC beams. The cracking moment, ultimate moment, and their corresponding curvatures of all BFRP-reinforced PVAFRC beams increased with the addition of PVA fibers. All the BFRP-reinforced PVAFRC beams showed higher cracking and ultimate moments than the cracking and ultimate moments of BFRP-reinforced BFRC and PC beams, as well as steel-reinforced PC beams. The incorporation of PVA fibers increased the strength of concrete by inducing a crack-bridging effect to hold the cracked planes together and consuming more fracture energy to resist the propagation and widening of cracks. Therefore, all the BFRP-reinforced PVAFRC beams showed higher cracking moments and ultimate moments than those of BFRP-reinforced BFRC and PC beams, and steel-reinforced PC beams. Compared to steel-reinforced PC beams, the curvature, which decreased in BFRP-reinforced PC beams, increased more effectively with the addition of PVA fibers than with basalt fibers. Thus, all the BFRP-reinforced PVAFRC beams showed higher curvature at cracking and ultimate moments than those of the curvature at cracking and ultimate moments of BFRP-reinforced BFRC beams (refer to Table 6.6). This may be attributed to the development of higher strain values in PVAFRC compared to the development of strain values in BFRC. However, the BFRP-reinforced PVAFRC beams of the M30 series have lower curvature at cracking and ultimate moments compared to the curvature at cracking and ultimate moment of steel-reinforced beams of the M30 series. The BFRP-

reinforced PVAFRC beams of the M70 series have shown almost equal curvature at cracking and ultimate moment compared to steel-reinforced beams of the M70 series.

The test data shows that BFRP under-reinforced PVAFRC beams exhibited larger curvature at lower cracking and ultimate moments, whereas BFRP over-reinforced PVAFRC beams exhibited lower curvature at higher cracking and ultimate moments. The BFRP-reinforced PVAFRC beams of the M30 series showed slightly higher curvature at lower moments during cracking and ultimate failure of the beams compared to BFRP-reinforced PVAFRC beams of the M70 series. This is due to the development of higher strain values in BFRP rebars and concrete of BPUR30 and BPOR30 beams compared to the development of strain values in BFRP rebars and concrete of BPUR70 and BPOR70 beams, respectively.

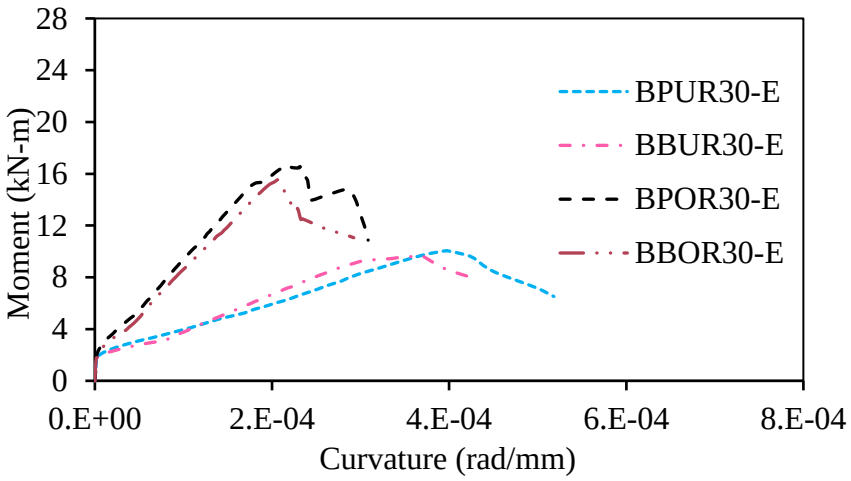

(a) M30 series

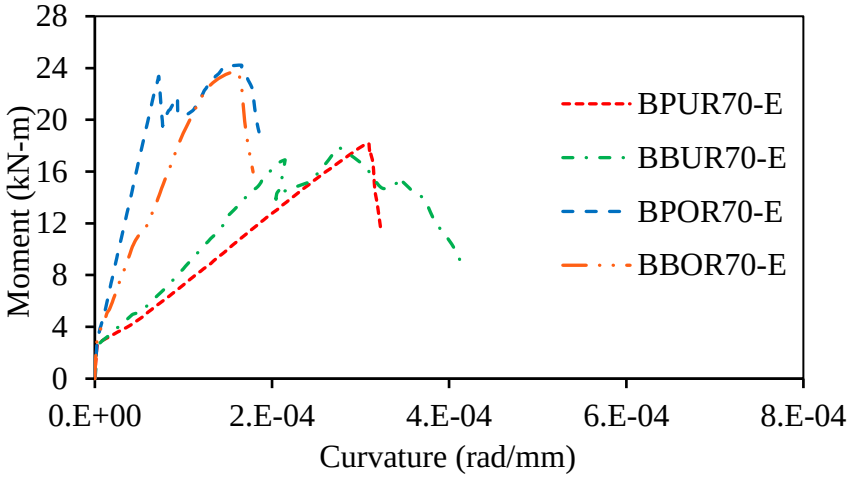

(a) M70 series

Figure 6.17 Experimental moment-curvature relationship of BFRP-reinforced PVAFRC beams

Table 6.6 Experimental moment-curvature results of BFRP-reinforced concrete beams

Series	Specimens Name	Cracking Moment (M_{FCL}) (kN-m)	Curvature at cracking × 10^{-6} (φ_{FCL}) (rad/mm)	Ultimate Moment (M_{UL}) (kN-m)	Curvature at ultimate × 10^{-4} (φ_{UL}) (rad/mm)
M30	SUR30	1.58	2.389	6.09	5.103
	SOR30	1.79	2.092	10.47	2.827
	BUR30	1.56	2.246	9.23	3.104
	BOR30	1.78	1.981	14.96	1.904
	BBUR30	1.71	2.294	9.64	3.690
	BBOR30	1.85	2.042	15.51	2.075
	BPUR30	1.81	2.340	10.05	3.956
	BPOR30	1.93	2.081	16.68	2.178
M70	SUR70	2.32	2.401	13.73	3.132
	SOR70	2.49	2.081	18.60	1.981
	BUR70	2.29	2.244	17.66	2.163
	BOR70	2.48	1.880	23.00	1.496
	BBUR70	2.40	2.268	17.89	2.754
	BBOR70	2.57	2.036	23.73	1.574
	BPUR70	2.46	2.438	18.18	3.091
	BPOR70	2.62	2.194	24.22	1.653

6.7.4 Ductility Indices of the BFRP-Reinforced Concrete Beams

The capacity of a structural member to absorb energy without failing is known as ductility, and it is usually measured in terms of the amount of inelastic deformation that occurs before complete failure [9]. For steel-reinforced PC beams, ductility is defined as the ratio of the curvature or deformation under flexural strength to that under the yielding load [210]. The calculated ductility indices of the steel-reinforced PC beams of the M30 and M70 series are presented in Table 6.7. However, in the case of BFRP RC beams, this approach is not suitable since BFRP rebar has linear elastic behavior until failure without any yield, unlike steel reinforcing bars. Therefore, the approach for evaluating the ductility of the BFRP RC beams is different from that of the steel-reinforced PC beams. The energy-based method and deformability-based method are two common approaches to evaluate the ductility of FRP RC beams, as neither of the two approaches considers the yielding of rebars. The energy-based ductility index method was proposed by Jeong and Naaman in 1995 [211], and it is calculated from the load-deflection curve as a ratio of the total energy absorbed to elastic energy. The energy-based ductility index (μ_E) can be calculated as follows:

$$\mu_E = \frac{1}{2}\left(\frac{E_T}{E_e} + 1\right) \qquad \text{Eq. (6.1)}$$

Where, E_T is total absorbed energy, which is equal to A1+A2 in Figure 6.18, and E_e is absorbed energy in the elastic region, which is equal to A1 in Figure 6.18.

The idealized load-deflection curve proposed by Jeong and Naaman in 1995 [211] is illustrated in Figure 6.18, showing the energies to be determined for evaluating the ductility of FRP RC beams. In Figure 6.18, P1 is the initial peak load or cracking load, S1 is the initial slope, P2 is the secant peak load, and S2 is the secant slope of the load-deflection curve. The secant peak load (P2) can be considered as the ultimate load (Pu) since the load-deflection curve of FRP RC beams is bilinear. In Figure 6.18, S is the unloading slope, which is calculated as follows:

$$S = \frac{P1S1+(P2-P1)S2}{P2} \qquad \text{Eq. (6.2)}$$

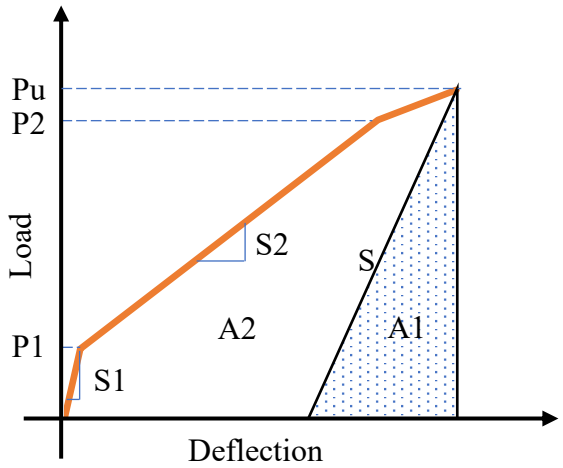

Figure 6.18 Schematic diagram of the load-deflection curve showing calculated energies [211]

The deformability-based ductility index method was proposed by Jaejar et al. 1997 [212] and it considers the moments as well as curvature or deflection for ductility evaluation. The deformability-based ductility index is defined as ratio of the ultimate moment and curvature or displacement to moment and curvature or deflection at a concrete compressive strain of 0.001 $\mu\varepsilon$. The inelastic energy dissipation of concrete is to begin at a compressive strain of 0.001 $\mu\varepsilon$. Because FRC varies from concrete not only in Young's modulus but also in ultimate compressive strain capacity, a deformation-based ductility index may not be suitable for evaluating ductility FRP-reinforced FRC elements. Therefore, in the present study, energy absorption-based ductility index method was used to evaluate the ductility indices of the BFRP-reinforced PC, BFRC and PVAFRC beams. The calculated ductility indices from the experimental load-deflection behaviour of the BFRP RC beams of M30 and M70 series are presented in Table 6.7.

Table 6.7 The ductility indices of BFRP-reinforced concrete beams

Series	Specimens ID	E_T is total absorbed energy	E_e is absorbed energy in the elastic region	Ductility indices
M30	SUR30	906.20	100.71	8.998
	SOR30	1140.49	181.20	6.294
	BUR30	706.51	236.59	1.993
	BOR30	896.09	544.19	1.323
	BBUR30	846.32	254.76	2.161
	BBOR30	1047.91	612.14	1.356
	BPUR30	906.10	267.29	2.195
	BPOR30	1234.31	693.42	1.390
M70	SUR70	1546.07	195.78	7.897
	SOR70	1732.59	285.72	6.064
	BUR70	1180.43	627.19	1.441
	BOR70	1229.44	849.55	1.224
	BBUR70	1459.36	653.31	1.617
	BBOR70	1364.79	911.25	1.249
	BPUR70	1400.21	667.11	1.549
	BPOR70	1770.74	994.52	1.390

The results show that the ductility of beams decreased with an increase in the longitudinal reinforcement ratio for M30 and M70 series beams. The ductility indices of the M30 series steel-reinforced PC beams, BFRP-reinforced PC beams, BFRC beams, and PVAFRC beams are higher than those of M70 series beams. This is because, after attaining peak strength, in the strain-hardening phase, reinforcing bars of NSC beams produced higher strain values than reinforcing bars of HSC beams. Hence, NSC beams exhibited a larger area in post-peak behavior than that of the HSC beams; therefore, ductility indices of M30 series beams are higher than those of the M70 series beams. Irrespective of the reinforcement ratio, reinforcing the PC with BFRP rebars decreased the ductility of beams significantly compared to steel-reinforced concrete beams in both series due to the low Young's modulus of BFRP rebars. Compared to steel under- and over-reinforced PC beams of the M30 series, the BFRP under- and over-reinforced PC beams had 77.85% and 78.59% lower ductility. Similarly, in the M70 series, compared to the steel under- and over-reinforced PC beams, BFRP under- and over-reinforced PC beams had 81.75% and 79.82% lower ductility.

The addition of basalt fibers to the PC slightly improved the ductility of BFRP under- and over-reinforced PC beams in both M30 and M70 series. The improvement in ductility indices of BFRP under-reinforced BFRC beams was better compared to the improvement in ductility indices of BFRP over-reinforced BFRC beams in both the series. Compared to the ductility

indices of BFRP under- and over-reinforced PC beams in M30 series, BFRP under- and over-reinforced BFRC beams ductility indices improved by 7.77% and 2.41%, respectively with the addition of basalt fibers. Similarly, compared to the ductility indices of BFRP under- and over-reinforced PC beams of M70 series, the ductility indices of BFRP under- and over-reinforced BFRC beams improved 10.88% and 2.02%.

In addition to this, the addition of PVA fibers to PC improved the ductility of BFRP under- and over-reinforced PC beams better than that of basalt fibers for both M30 and M70 series. This was because of PVA fibers' lower density, large volume of fibers to be accumulated in the same volume of concrete compared to basalt fibers. Therefore, a greater number of fibers can play an effective role in crack bridging phenomena and consume more energy against concrete fracture to increase flexural strength of concrete beams. Compared to the ductility of BFRP under- and over-reinforced PC beams in M30 series, the ductility indices of BFRP under- and over-reinforced PVAFRC beams improved by 9.20% and 4.80%, respectively. Compared to the ductility indices of BFRP under- and over-reinforced PC beams of M70 series, the ductility indices of BFRP under- and over-reinforced PVAFRC beams improved by 7.0% and 11.99%, respectively. In both M30 and M70 series, steel-reinforced PC beams showed higher ductility. And for BFRP RC beams, in both the series, BFRP under- and over-reinforced PVAFRC beams showed higher ductility indices compared to BFRP under- and over-reinforced BFRC and PC beams. All the under-reinforced concrete beams showed better ductility index than over-reinforced concrete beams in both the series.

6.7.5 Cracking Pattern and Failure Modes of the BFRP-Reinforced Concrete Beams

All the steel-reinforced PC and BFRP-reinforced PC, BFRC, and PVAFRC beams were designed as singly reinforced beams and tested under a four-point bending test. Shear reinforcement in the constant moment region was avoided to achieve a pure bending condition. Consequently, all the tested beams failed in flexure due to the development of several flexural cracks on the tension face and the crushing of concrete on the compression face in the constant moment region. The rupture of BFRP rebars in the tension region and the crushing of concrete in the compression region are two different flexural failure modes that caused the failure of the tested beams. The failure pattern of all the tested beams in Phase I, II, III, and IV of M30 and M70 series under flexural loading is shown in Figure 6.19. The crack propagation in the tested beams followed the traditional flexural-cracking patterns observed in simply supported beams. The crack pattern and failure mechanism of each specimen are discussed below.

6.7.5.1 Steel-reinforced PC beams

Beam: SUR30

During testing of SUR30, an initial vertical crack developed in the tension face at the middle of the constant moment region of the beam at a load value of 4.87 kN. As the load increased, a couple of cracks developed on either side of the initially developed crack. With an increase in load, these cracks started widening and propagating from the tension face to the compression face of the beam. The development of cracks spread outward from the constant moment region into the shear span at higher loads, and cracks in the shear span began to propagate from the bottom face of the beam vertically up towards the top support. As the beam approached ultimate strength, deformation increased and led to yielding of steel reinforcement in the sagging region. Due to this, compressive stresses developed in the compression face of the midspan, inducing the crushing of concrete at the top compression fiber of the constant moment region of the beam. The failure of SUR30 occurred due to the yielding of steel reinforcement in the sagging region followed by the crushing of concrete in the compression face. Therefore, the failure of SUR30 was categorized as a flexural-tension failure. As evident in Figure 6.19 of SUR30, major flexural cracks causing the failure of beams developed at the constant moment region and very few in the shear span of the beams. The cracks in the shear span in steel-reinforced PC beams with stirrups were much steeper than those in BFRP RC beams.

Beam: SUR70

The first crack for SUR70 beam occurred at a load value of 7.13 kN. The crack pattern and failure mode of the SUR70 beam were the same as that of the SUR30 beam. However, in comparison to the SUR30, the SUR70 beam exhibited a few more cracks in the shear span. This could be attributed to the higher flexural strength and stiffness of the beam.

Beam: SOR30

The first crack for SOR30 beam occurred at a load value of 5.50 kN. The development of cracks and crack pattern were the same as that of the SUR30 beam. But the failure of SOR30 beam occurred due to the crushing of concrete in compression face of the constant moment region followed by a slight yielding of steel reinforcement in tension face. SOR30 exhibited a certain amount of deformation before reaching ultimate strength. Due to this the compressive stress developed in the top compression fiber induced the crushing of concrete at the top compression face of the constant moment region. The failure mode of SOR30 was categorized as flexural-compression failure. Similar to SUR30 and SUR70 beams, for SOR30 major flexural cracks

developed in the constant moment region and compared to SUR30 and SUR70, more cracks developed in shear span of SOR30 and SOR70 beams as shown in Figure 6.19 of the beams.

Beam: SOR70

The first crack for SOR70 beam occurred at a load value of 7.65 kN. The cracking pattern of SOR70 was the same as that of SOR30. However, the failure of the beam occurred purely due to the crushing of concrete in the top compression fiber at ultimate load. The compressive stress developed in the top compression fiber, induced by the applied load, led to the crushing of concrete. Hence, the failure mode of SOR70 was categorized as concrete crushing failure. Even though SOR70 was cracked and damaged in the compression face, the beam returned to its original position upon unloading after the completion of the test. This may be attributed to the higher axial stiffness and unyielding nature of the tensile steel reinforcement provided.

6.7.5.2 BFRP-reinforced concrete beams

From Figures 6.19, all BFRP RC beams of M30 and M70 series experienced a higher number of flexural-tensile cracks than steel-reinforced PC beams. This is possibly due to low Young's modulus and low stiffness of BFRP rebars. All the BFRP-reinforced PC beams failed in a brittle manner, especially under-reinforced beams PC beams. In case of BFRP-reinforced BFRC and PVAFRC beams, a warning of complete failure of the beams was observed. Similar to steel-reinforced PC beams of M30 and M70 series, for all the tested BFRP-reinforced PC, BFRC and PVAFRC beams an initial vertical flexural crack began to occur in extreme tension fibers of concrete in the constant moment region. As the load increased, with increasing deformation of beam, more flexural cracks developed gradually along the constant moment region in the tension face and propagated up towards the compression face. With further increase of load, the development of cracks spread outward from midspan into shear span. The cracks in shear spans began to form and propagate from the bottom face of the beam diagonally up towards the top supports [55]. As these cracks propagated upward, the incline of the cracks increased and moved toward the applied load. The cracks that were formed at higher load had a higher slope from the vertical axis. This is typical behavior due to the increased curvature of the beam with the applied load.

The cracks in BFRP RC beams showed significant branching near the location of tensile reinforcement (bottom third of the beams) approximately from 70% of the maximum load. At higher loading stages, the rate of formation of new cracks significantly decreased and the existing cracks grown wider, especially the first formed cracks. At the higher stress levels,

branches of small cracks were developed to the initially formed cracks due to the development of higher strains in BFRP rebars [213]. However, the number and spacing of flexural cracks above the mid-depth of the beam in the constant moment region were similar in both BFRP RC beams and steel-reinforced PC beams [55]. The development of cracks at higher loading in the shear span was significantly greater for BFRP RC beams than steel-reinforced PC beams. The shear cracks in BFRP RC beams varied from 40 to 60 degrees approximately and spread close to the end support [55].

Beam: BUR30

The first crack for BUR30 occurred at a load value of 4.81 kN. The cracking pattern of BUR30 beam was the same as explained above. As BUR30 beam approaching ultimate strength, the cracks that were formed at low load began to widen, especially the cracks developed in constant moment region. At failure, the BFRP reinforcement rebars ruptured at a region of maximum bending moment. This caused the flexural cracks around the mid-span to widen significantly, causing concrete cover to spall off in tension with a loud noise as shown in Figure 6.19. The failure of BUR30 was sudden, brittle manner. The concrete on top surface remained undamaged at the time of failure. Therefore, the failure of BUR30 was categorized as BFRP rupture failure.

Beam: BBUR30

The first crack for BBUR30 occurred at a load value of 5.27 kN. The cracking pattern and failure mode of BBUR30 beam were observed to be the same as that of beam BUR30. Hence, the failure mode of BBUR30 was BFRP rupture failure. Due to the addition of basalt fibers, there were no big changes in cracking pattern and failure mode of the beam. The effect of basalt fiber on performance of BBUR30 was seen from improvement in flexural strength and toughness characteristics of the beam.

Beam: BUR70

The first crack for BUR70 occurred at a load value of 7.04 kN. The cracking pattern of BUR70 was the same as explained in section 6.7.5.2. The failure of the beam occurred purely by the crushing of concrete in the top compression fiber of the constant moment region. When the imposed load on the beam approached the ultimate load capacity, the beam exhibited higher deformation because of the loss of stiffness due to the widening and rapid propagation of cracks from the tension face to the compression face. This developed higher compressive stress in the compression fiber at mid-span leading to a small concrete compression zone due to an upward shift of the neutral axis, resulting in the crushing of concrete in the compression face at ultimate

load. Therefore, BUR70 failed in concrete crushing before attaining BFRP rebar rupture. The failure mode of BUR70 was concrete crushing failure.

Beam: BOR30

The first crack for BOR30 occurred at a load value of 5.47 kN. The crack pattern and failure mode of BOR30 beam were the same as that of BUR70. Hence, the failure mode of BOR30 was concrete crushing failure.

Beam: BOR70

The first crack occurred at a load of 7.61 kN. The cracking pattern and failure of BOR70 were the same as that of beam BUR70. The failure mode of BOR70 was concrete crushing failure.

Beam: BBUR70

The first crack for BBUR70 occurred at a load value of 7.39 kN. The cracking pattern and failure mode of BBUR70 beam were the same as that of BUR70. Crushing of concrete in the compression face led to complete failure of the beam before attaining BFRP rebar rupture. Therefore, BBUR70 failed in concrete crushing before attaining BFRP bar rupture. The failure mode of BBUR70 was categorized as concrete crushing failure. Due to the addition of basalt fibers, there was no significant change in the cracking pattern and failure mode of the beam.

Beam: BPUR30

The first crack for BPUR30 occurred at a load value of 5.57 kN. The cracking pattern of BPUR30 was the same as explained in section 6.7.5.2. BPUR30 showed an identical failure mode of pure flexural failure among all tested beams. There was no damage to the concrete in the compression face and spalling of concrete in the tension face. Under loading, BPUR30 exhibited many vertical flexural cracks along the constant moment region and a few cracks in the shear span. The branching cracks at the level of tensile reinforcement occurred at the constant moment region due to the development of higher tensile stress in BFRP rebars. The developed cracks led to a decrease in the resistance of the beam against the applied load. Therefore, this type of failure is classified as flexural failure. There was no spalling of concrete at the tension face due to the presence of PVA fibers.

Beam: BPOR30

The first crack for BPOR30 occurred at a load of 5.94 kN. The cracking pattern and failure mode of BPOR30 were the same as that of BUR70. BPOR30 failed in concrete crushing before attaining BFRP rebar rupture. Therefore, the failure mode of BPOR30 was categorized as

concrete crushing failure. Due to the addition of PVA fibers, there was no significant change in the cracking pattern and failure mode of the beam.

Beam: BPOR70

The first crack for BPOR70 occurred at a load value of 8.04 kN. The behavior, cracking pattern, and failure mode of BPOR70 were the same as that of BPOR30. Therefore, BPOR70 failed in concrete crushing before attaining BFRP rebar rupture. The failure mode of BPOR70 was categorized as concrete crushing failure. There was no significant change in the crack pattern and failure mode of BPOR70 due to the presence of PVA fibers. The effect of PVA fibers addition was clearly seen in the improved flexural strength and toughness of the beam.

Beams: BBOR30 and BBOR70

The first crack for BBOR30 and BBOR70 occurred at a load of 5.70 kN and 7.90 kN. The cracking pattern for BBOR30 and BBOR70 was the same as explained in section 6.7.5.2, and both beams showed a similar kind of failure mode. BBOR30 and BBOR70 failed due to the crushing of concrete in compression followed by the rupture of BFRP rebar. The shear failure of concrete occurred in the middle of the constant moment region, as shown in Figure 6.19. The compressive stress developed at the top compression face due to deformation and the rapid propagation and widening of the cracks at higher loads led to a smaller concrete compression zone due to the upward shift of the neutral axis. This resulted in the crushing of concrete in the compression face and the development of higher stress in BFRP tensile reinforcement. At the ultimate load, after the crushing of concrete in the compression face, BFRP rebar rupture took place, leading to the complete failure of concrete in shear. Therefore, the failure of BBOR30 and BBOR70 was categorized as compressive flexural-shear failure [214]. The effect of basalt fibers on the crack pattern and failure mode of BBOR30 and BBOR70 was not significant.

Beam: BPUR70

The first crack for BPUR70 occurred at a load value of 7.56 kN. The crack pattern and failure mode of BPUR70 beam were the same as that of BBOR30 and BBOR70 beams. Therefore, the failure of BPUR70 was categorized as compressive flexural-shear failure. The presence of PVA fibers didn’t make any significant change in the crack pattern and failure mode of BPUR70.

Though the addition of basalt fibers and PVA fibers did not fully improve the ductility of the beam, the fibers reduced the brittle failure mode of the beam. Clear formation, propagation, widening, and crushing of concrete in the compression face were achieved before BFRP rebars reinforced FRC beams fail completely when compared to BFRP-reinforced PC beams.


S-UR-30
SUR30
BFRP-UR-M30
BUR30
BBUR30
BFRP-UR-30
BPUR30
S-OR-30
S-OR-30
SOR30
BFRP OR 30
BOR30
BFRP BF OR-M30
BBOR30
BFRP PVA OR-30
BPOR30

(a) M30 series

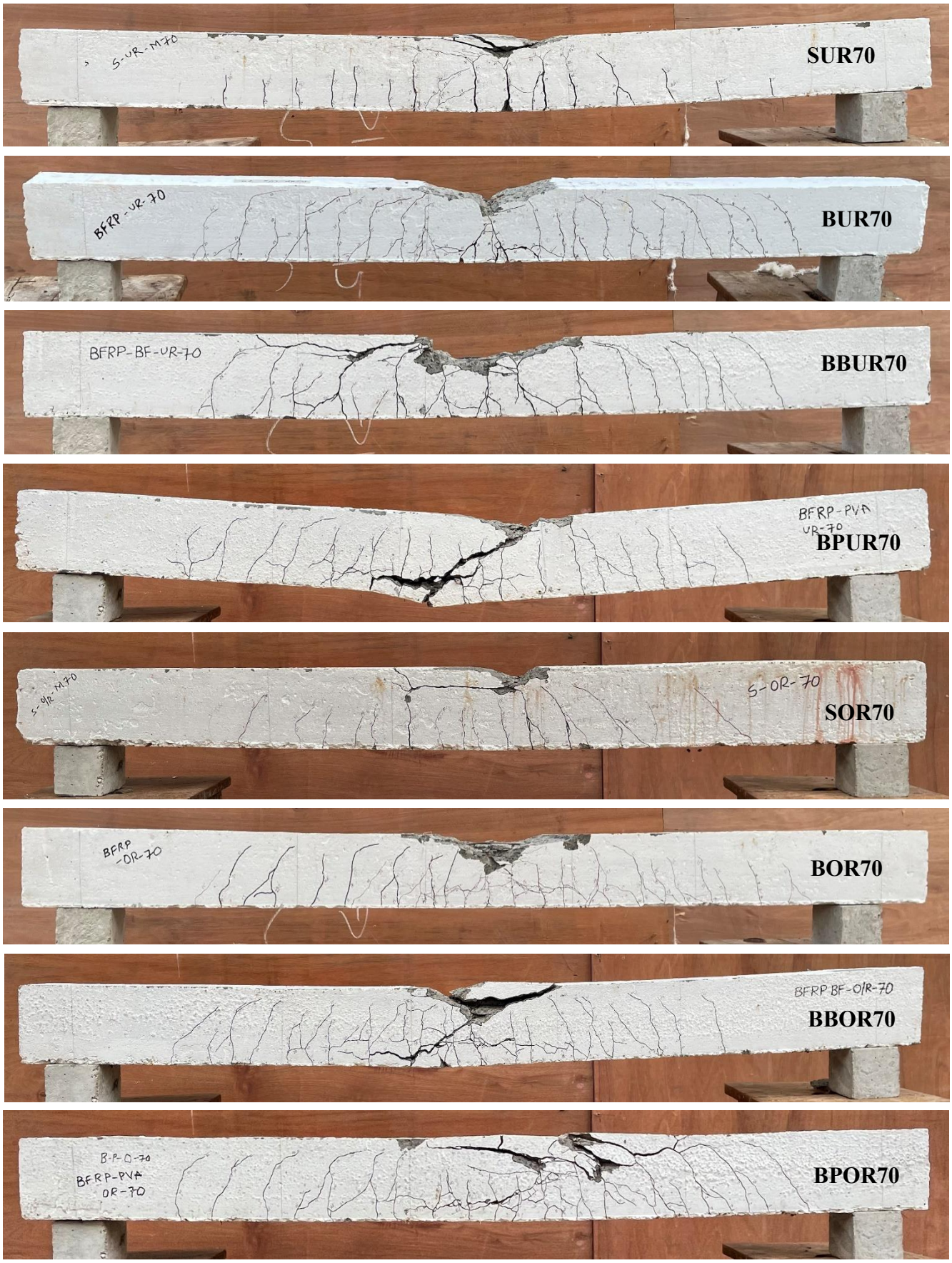

(b) M70 series

Figure 6. 19 Cracking pattern and failure modes of BFRP-reinforced concrete beams

6.8 Conclusions

The flexural behavior of BFRP-reinforced PC, BFRC, and PVAFRC beams, and steel-reinforced PC beams of NSC (M30 series) and HSC (M70 series), has been experimentally evaluated in this chapter. The load-deflection behavior, moment-curvature relationships, flexural strength, first cracking load, ultimate load-carrying capacity, deflection at first crack and ultimate load, curvature at cracking moment and ultimate moment, stiffness of the beam, ductility indices, and crack pattern and failure modes of the beams were evaluated experimentally. From the results presented in this chapter, the following conclusions are drawn:

- The results of tensile tests on BFRP rebars proved that it is a non-yielding composite material that carries a higher tensile stress under minimal strains. BFRP rebars had a linear tensile stress-strain curve with abrupt tensile destruction failure.
- The flexural behaviour of BFRP RC beams completely differed from the flexural behaviour of steel-reinforced PC beams due to the difference in stress-strain behaviour of basalt rebars and steel reinforcing bars.
- The load-deflection behaviour and moment-curvature relationships of BFRP-reinforced PC, BFRC, and PVAFRC beams exhibited two phases which bound the cracking point, whereas steel-reinforced PC beams exhibited three phases which bound the cracking and yielding points.
- Although BFRP rebar is a brittle material with no clear yielding point, BFRP RC beams exhibited more deformation and curvature prior to failure during testing.
- The steel-reinforced PC beams showed higher deflection and curvature at ultimate load and moment and had greater stiffness, and ductility indices than the BFRP-reinforced PC, BFRC and PVAFRC beams.
- Reinforcing the PC beams with BFRP rebars resulted in a decrement in deflections and curvatures at cracking and ultimate strength, and lower stiffness and ductility indices than the steel-reinforced PC beams.
- The amount of deflection, curvature, stiffness, and ductility exhibited by BFRP-reinforced PC beams was partially countered by reinforcing PC with basalt fibers and PVA fibers. However, due to higher bond strength and a better strain-softening behavior, PVA fibers improved the flexural behavior of BFRP RC beams better than the basalt fibers.

- ❖ Under flexural loading, all the BFRP RC beams exhibited a higher number of flexural tensile cracks than steel-reinforced PC beams, attributed to the lower Young's modulus of BFRP rebars.
- ❖ All the BFRP RC beams exhibited the branching of flexural tensile cracks before reaching their ultimate load, attributed to the development of higher tensile stress in both concrete and BFRP rebars.
- ❖ The average crack spacing and maximum crack width of the BFRP RC beams were greater than those of steel-reinforced PC beams, but the development of cracking and crack patterns was almost identical.
- ❖ Flexural-tension failure, flexural-compression failure, crushing of concrete in compression zone, rupture of BFRP rebars in tension zone, and compression flexural-shear failure indicate the failure patterns of BFRP RC beams.

Chapter 7

Numerical Investigation on Flexural Response of BFRC and PVAFRC Beams Reinforced with BFRP Rebars

7.1 General

The load-deflection behavior, moment-curvature relationships, ductility indices, crack patterns, and failure modes of BFRP RC beams were studied experimentally in the previous chapter. Numerical modelling helps decrease the number of specimens cast and tested, which need to be studied for various parameter considerations influencing concrete behavior. For the present numerical study, load-deflection behavior, moment-curvature relationships, and ductility indices of BFRP-reinforced PC, BFRC, and PVAFRC beams were investigated in this chapter using the finite element method (FEM). The numerical modelling results were used to validate the experimental results and are discussed in this chapter.

7.2 Non-Linear Finite Element Analysis

At present, finite element analysis (FEA) has become an important tool in design and research. It is being used for various applications in engineering to study the effects of heat, blast, fluid flow, wind, accidents, and more. The main benefit of FEA is its capability to simulate costly tests and provide simple solutions to very difficult problems. By utilizing various loads, different element types, boundary conditions, and material properties, FEA can be applied to a wide range of diverse engineering applications [215]. Thus, implementing FEA modelling to study the flexural behavior of FRP RC beams is the best tool for the preparation and testing of large beams in budget research.

The FEM is a numerical simulation approach that evaluates the behavior of a component under a given load by estimating important structural parameters (such as stresses, strains, etc.). FEM analyses a problem by discretizing and then integrating all the elements. In this study, to model the flexural behavior of BFRP-reinforced PC, BFRC, and PVAFRC beams, as well as steel-reinforced PC beams, a non-linear FEM analysis software, ABAQUS v6.14/CAE, was used. ABAQUS has become popular in research and academic institutions due to its competence in simulating even multi-dimensional problems and its extensive library of elements and materials [215].

The load-deflection behavior of the beam is regarded as the most important part in analysing beam behavior since it includes response parameters such as first crack load, ultimate load, as well as deflection at first crack and ultimate loads. Therefore, correlating the load-deflection

behavior of simulated beams with the load-deflection behavior of experimentally tested beams is considered an effective means to validate the non-linear model. In addition to this, using the numerical results, moment-curvature relationships of all the tested beams were also developed and correlated with those of the experimental moment-curvature relationships. To further validate the non-linear model, the ductility indices of the beams were also calculated from the numerical load-deflection curves and correlated with those of the ductility indices of the beams calculated from experimental load-deflection curves.

7.3 Concrete Damage Plasticity Model

In the present study, the concrete damaged plasticity (CDP) model was used for simulating the PC, BFRC, and PVAFRC beams reinforced with BFRP rebars, and also for simulating the steel-reinforced PC beams. The CDP model was used in this study because it has the capability of simulating the complete inelastic behavior of concrete, including compressive crushing and tensile cracking with damage properties. This model uses the concept of isotropic damaged elasticity in combination with isotropic tensile and compressive plasticity to signify the inelastic behavior of concrete [216]. The CDP model is intended for problems where the concrete is exposed to static, dynamic, monotonic, and/or cyclic loads under low-confining pressure.

The CDP model presents five various factors for defining characteristics such as the yield surface, concrete brittleness, viscoplastic regularization, and a non-associated flow rule with multi-variable hardening plasticity. As a result, the CDP model is totally adaptable for simulating concrete under various loading conditions. Compression crushing of the concrete and tension cracking are the prime failure mechanisms in the CPD model. The combined behavior of BFRP/steel and concrete is replicated using the embedded element technique.

7.3.1 Plasticity Modelling

The definition of a flow rule, an initial yield surface, and a hardening rule are necessary components of a plasticity model. The particular components of the plasticity model employed by the CDP model inside ABAQUS are detailed here.

Plastic Flow

The CDP model assumes non-associated potential plastic flow. This model uses the Drucker-Prager hyperbolic function as the flow potential, G.

$$G = \sqrt{(\varepsilon\sigma_{to}\tan\psi)^2 + \bar{q}^2} - \bar{p}\tan\psi \qquad \text{Eq. (7.1)}$$

where, σ_{to} is the uniaxial tensile stress at failure

$\bar{p}$ is the hydrostatic pressure stress

$\bar{q}^2$ is the mises equivalent effective stress

ψ is the dilation angle measured in the p-q plane at high confining pressure

ε is the eccentricity

This flow potential assumes that a unique flow direction is defined always and is also smooth and continuous. At high confining pressure, it approaches the linear Drucker-Prager flow potential asymptotically and intersects the hydrostatic pressure axis at 90°. In ABAQUS, ε = 0.1 is the default value for flow potential eccentricity.

The dilation angle (ψ) also affects the flow potential function. This angle is a material property. It is a measure of the angle at which the flow potential function is inside the meridional plane in relation to the axis of the hydrostatic pressure when high confining pressures are present (see Figure 7.1). Smaller values of the dilation angle will result in brittle behaviour, while larger values will result in a more ductile behavior [217]. Based on the parametric study conducted, the dilation angle was taken as 45 degrees for modelling all types of RC beams in the present study.

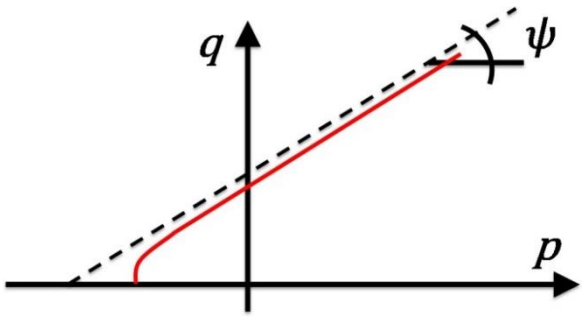

Figure 7.1 Hyperbolic Drucker-Prager flow potential function [55].

Yield Function

The concrete strength under uniaxial tension and compression determines the shape of flow potential and the corresponding load surfaces. A modified yield function of Lubliner et al. 1989 [218], by Lee and Fenves 1998 [219] was utilised by this model to account for evolution of strength under tension and compression. The hardening variables, $\tilde{\varepsilon}_t^{pl}$ and $\tilde{\varepsilon}_c^{pl}$, control the evolution of the yield surface. The yield function is defined as the following under effective stresses:

$$F = \frac{1}{1-\alpha}(\bar{q} - 3\alpha\bar{p} + \beta(\tilde{\varepsilon}^{pl})\langle\hat{\bar{\sigma}}_{max}\rangle - \gamma\langle\hat{\bar{\sigma}}_{max}\rangle) - \bar{\sigma}_c(\tilde{\varepsilon}_c^{pl}) = 0, \qquad \text{Eq. (7.2)}$$

With

$$\alpha = \frac{(\sigma_{b0}/\sigma_{c0})-1}{2(\sigma_{b0}/\sigma_{c0})-1}; \quad 0 \le \alpha \le 0.5, \qquad \text{Eq. (7.3)}$$

$$\beta = \frac{\bar{\sigma}_c\left(\tilde{\varepsilon}_c^{pl}\right)}{\bar{\sigma}_t\left(\tilde{\varepsilon}_t^{pl}\right)}(1-\alpha) - (1+\alpha), \qquad \text{Eq. (7.4)}$$

$$\gamma = \frac{3(1-K_c)}{2K_c-1}. \qquad \text{Eq. (7.5)}$$

Where,

$\hat{\bar{\sigma}}_{max}$ is maximum principal effective stress

$\bar{\sigma}_t\left(\tilde{\varepsilon}_t^{pl}\right)$ is effective tensile cohesion stress

$\bar{\sigma}_c\left(\tilde{\varepsilon}_c^{pl}\right)$ is effective compressive cohesion stress

σ_{b0}/σ_{c0} is ratio of initial equi-biaxial compressive yield stress to initial uniaxial compressive yield stress (the default value is 1.16).

The CDP model has been changed such that the failure surface considered in the deviatoric plane is no longer required to be a circle, as seen in Figure 7.2. and the shape of deviatoric plane is given by a parameter K_c. The value of K_c must satisfy the condition $0.5 \le K_c \le 1.0$. As recommended by user's manual of ABAQUS, the failure surface for K_c = 2/3 is used in the analysis.

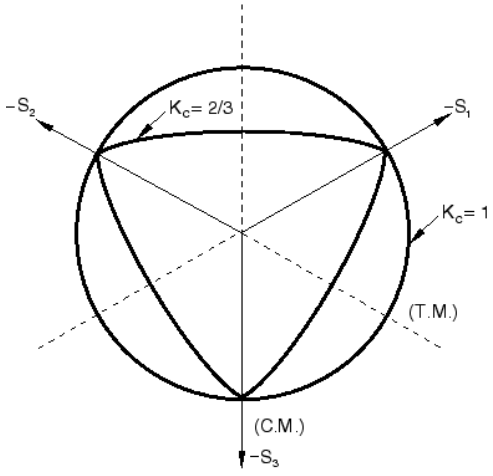

Figure 7.2 CDP deviatoric plane for different values of K_c [220]

Viscoplastic regularization

In implicit analysis programmes like ABAQUS, material models indicating stiffness degradation and softening behaviour usually have convergence difficulties. Viscoplastic regularisation of the constitutive equations is a common method for overcoming such

convergence difficulties. This causes the consistent tangent stiffness to become positive for adequately small-time increments. In ABAQUS, the CDP model may be regularised by using viscoplasticity and by enabling stresses to exist outside of the yield surface.

The use of viscoplastic regularization for the viscosity parameter with a small value (small when compared to the characteristic time-increment) generally helps in improving the convergence rate of the model in the softening regime, without any compromise in result. The value of the viscosity parameter can be specified as part of the CDP material behaviour definition. In ABAQUS, for the viscoplastic regularization not to be performed, zero is given as the default value for the viscosity parameter (μ) [220].

7.3.2 Uniaxial Tension and Compression Stress-Strain Behaviour of Concrete for CDP Model

The characterization of the response of concrete in uniaxial compressive and uniaxial tensile tests are assumed to be done by damaged plasticity as depicted in Figure 7.3. A linear elastic relationship is followed in stress-strain response under uniaxial tension until the failure stress, σ_{to}, is reached. The failure stress marks the beginning of micro-cracking in the concrete material. A macroscopic representation of the formation of micro-cracks, beyond the failure stress, is done with a softening stress-strain response. This softening induces strain localization. Similarly, the response under uniaxial compression is linear until the initial yield, σ_{co}. In the plastic region the response is generally considered as stress-hardening followed by strain-softening post the ultimate stress, σ_{cu}. This illustration, though slightly simplified, captures the key features of the concrete's response.

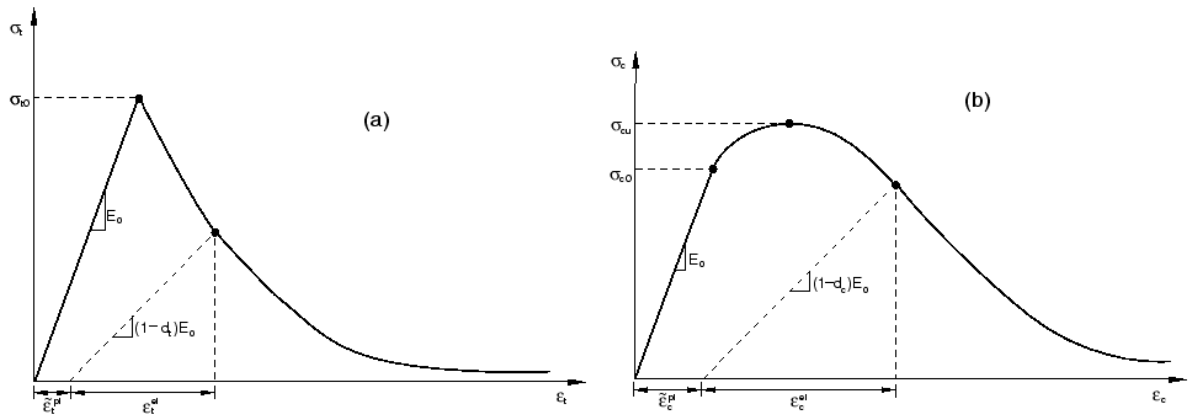

Figure 7.3 Response of concrete to uniaxial loading in (a) tension and (b) compression [220]

The input parameters used in the analysis by CDP constitutive models are shown in Tables 7.1, 7.2 and 7.3.

Table 7.1 Input parameter used in CDP model

ψ	Dilatation angle	45°
ε	Eccentricity	0.1
F	σ_{b0}/σ_{c0}	1.16
K_c	$q_{(TM)}/q_{(CM)}$	2/3
μ	Viscosity parameter	0

Table 7.2 Input parameters used for concrete damage in CDP model for M30 series beams

Concrete compression damage						**Concrete tension damage**					
Damage parameter (C)			**Inelastic strain**			**Damage parameter (T)**			**Cracking strain**		
PC	**BFRC**	**PVAFRC**	**PC**	**BFRC**	**PVAFRC**	**PC**	**BFRC**	**PVAFRC**	**PC**	**BFRC**	**PVAFRC**
0	0	0	0	0	0	0	0	0	0	0	0
0.09303	0.06328	0.03130	0.00104	0.00096	0.00102	0.53055	0.45741	0.44913	0.00085	0.00078	0.00077
0.29463	0.21367	0.13199	0.00242	0.00209	0.00231	0.64423	0.62390	0.61817	0.00185	0.00228	0.00227
0.52742	0.48617	0.48613	0.00398	0.00398	0.00532	0.81311	0.78399	0.78070	0.00985	0.00978	0.00977

Table 7.3 Input parameters used for concrete damage in CDP model for M70 series beams

Concrete compression damage						**Concrete tension damage**					
Damage parameter (C)			**Inelastic strain**			**Damage parameter (T)**			**Cracking strain**		
PC	**BFRC**	**PVAFRC**	**PC**	**BFRC**	**PVAFRC**	**PC**	**BFRC**	**PVAFRC**	**PC**	**BFRC**	**PVAFRC**
0	0	0	0	0	0	0	0	0	0	0	0
0.03725	0.06044	0.09075	0.00046	0.00118	0.00109	0.52488	0.45082	0.43867	0.00084	0.00078	0.00076
0.18619	0.18173	0.30387	0.00098	0.00204	0.00200	0.67067	0.61934	0.63828	0.00234	0.00228	0.00276
0.51166	0.51276	0.51795	0.00173	0.00320	0.00325	0.81085	0.78137	0.77653	0.00984	0.00978	0.00976

7.4 ABAQUS Simulation: Modelling of BFRP-Reinforced PC, BFRC and PVAFRC Beams

The numerical modelling for flexural behaviour of BFRP-reinforced PC and BFRC and PVAFRC beams, and steel-reinforced PC beams were performed on a simply supported beam tested for four-point bending test under static loading. A total of 16 beams were modelled for both the M30 and M70 series. For each series, 8 beams were modelled. The dimensions, reinforcement area, type of concrete (PC, BFRC, and PVAFRC) and their strengths, type of RC (under-reinforced and over-reinforced), and boundary conditions used in the experimental evaluation of BFRP-reinforced PC, BFRC, and PVAFRC beams, and steel-reinforced PC beams are the same used in numerical modelling. To model the beams, 3-D (three-dimensional) finite element models of RC beam were developed and determined for load-deflection behaviour, moment-curvature relationships, ductility indices, and damage pattern. Each step concerned with simulation is explained below in detail.

7.4.1 Concrete Beam Modelling: Beam Parts and Section Assignments, Element Type and Material Properties

The modelling was done in three-dimensions for each beam geometry using the interface of ABAQUS. In ABAQUS, a model consists of many “Parts”. A “Section” is assigned to each part and every part created as an independent geometry. All the details about the properties of a “Part” are contained in a section and the properties dependent on the type of part are considered. Also, a material is assigned to the part through section. A name is assigned to each material which is independent of any particular section and similarly, a name is assigned to each section which is independent of any particular part [217]. A 3D “Deformable” body was used to define a concrete part. An extrusion formulation was used to create the concrete area of the rectangular beam. In this method, a two-dimensional profile is defined first, after which specifying the third dimension creates three-dimensional geometry. A "homogeneous solid" section was assigned to the concrete part. This section is usually used for solid regions since it defines a single material.

To simulate the non-linear behavior of all types of concrete beams (PC, BFRC, and PVAFRC) in the M30 and M70 series, C3D8R elements with a size of 15mm (approximately) have been used to mesh the concrete beams. Since the concrete beams are modelled with rectangular cross sections, the use of C3D8R elements for meshing enhances the efficiency of the analysis of the beams [217]. Figures 7.4 and 7.5 show the element shape, type, and technique used to mesh

concrete regions. The mechanical properties of PC, BFRC, and PVAFRC used in the FEA analysis of RC beams were adopted from experimental data and are presented in Tables 7.4.

While modelling the concrete part, the density of the concrete is used as 2400 kg/m³ in accordance with IS 456-2000 [133]. Before testing the cube specimens for compressive strength, all PC, BFRC, and PVAFRC specimens are weighed, and the average cube weight is calculated as 2.405 ± 0.01 kg. In the development of BFRC and PVAFRC, 0.3% of the volume of the concrete is considered as the weight of the fibers. Consequently, the weight of the fibers in each cube specimen is negligible when compared to the weight of the concrete. Therefore, the change in concrete density with the inclusion of a smaller volume percentage of fibers is neglected. Based on the average weight of the cube specimens, the density of the concrete is used constant at 2400 kg/m³ for all BFRP-reinforced concrete beams.

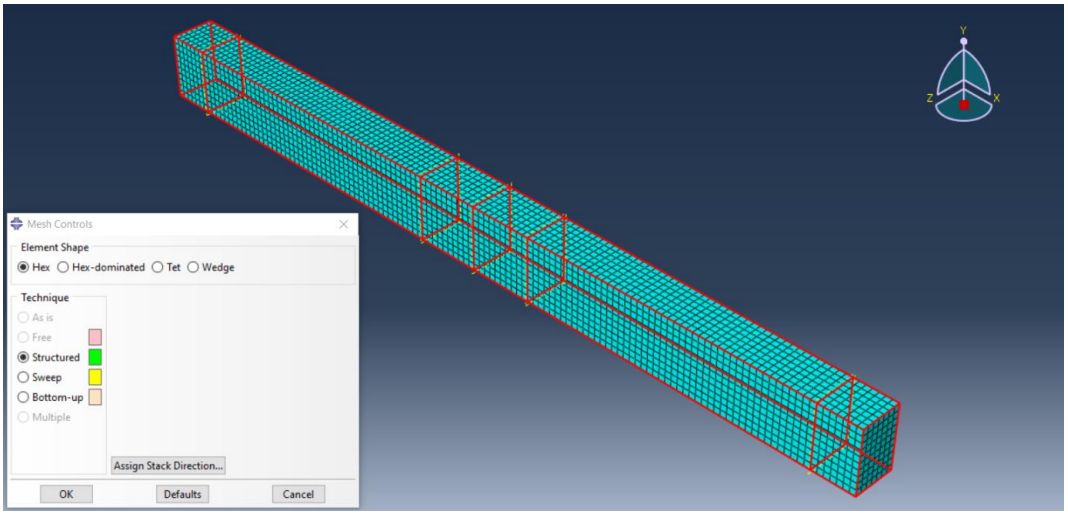

Figure 7.4 Beam with element shape and technique used in meshing

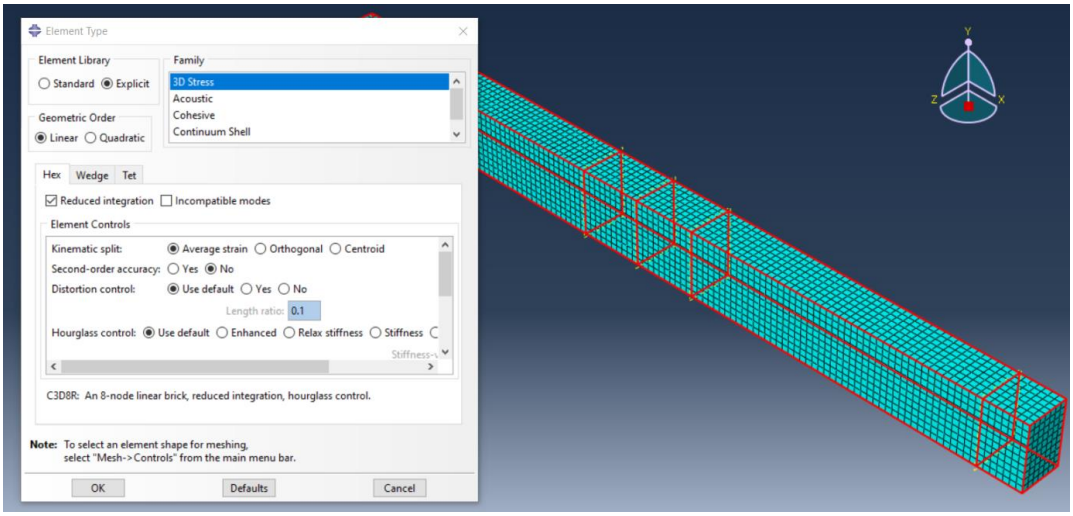

Figure 7.5 Beam with Element type used in meshing

Table 7.4 Mechanical input parameters of concrete for ABAQUS modelling

Grade of concrete	Concrete type	Concrete mechanical properties				
		Compressive strength (MPa)	Tensile strength (MPa)	Young's modulus (GPa)	Poisons ratio	Density of the concrete (kg/m^3)
M30	PC	38.57	4.27	31.05	0.18	2400
	BFRC	42.73	6.58	32.68	0.18	2400
	PVAFRC	41.52	6.70	32.22	0.18	2400
M70	PC	80.33	6.22	44.81	0.18	2400
	BFRC	82.62	9.15	45.45	0.18	2400
	PVAFRC	84.18	9.71	46.87	0.18	2400

The stress-strain relationship for PC, BFRC and PVAFRC under uniaxial compression is defined in both elastic and plastic ranges. The compressive behavior within the linear elastic range is defined by the modulus of elasticity and Poisson's ratio. The modulus of elasticity of all three types of concrete were calculated using equation, $5000\sqrt{f_{ck}}$, according to IS 456-2000 [133]. In plastic range, compressive stress is defined as a function of non-elastic strain, and also in the plastic range damage parameters were given. There were a total of five plastic damage parameters included in the CDP model, they being flow potential eccentricity (ε), dilation angle (ψ), the ratio of initial biaxial compressive yield stress to initial uniaxial compressive yield stress (σ_{b0}/σ_{c0}), viscosity parameter (μ), and the ratio of the second stress invariant on the tensile meridian to that on the compressive meridian ($q_{(TM)}/q_{(CM)}$). The values of all five plastic damage parameters considered in the modelling of non-linear behaviour of PC, BFRC, and PVAFRC are presented in Table 7.1. The stress-strain behavior of PC, BFRC and PVAFRC under compression was modelled with the proposed modified constitutive analytical model (equation 5.1 of Chapter 5). The stress-strain behavior of PC, BFRC and PVAFRC of M30 and M70 series modelled under compression are shown in Figure 7.6.

The tensile stress-strain behaviour of PC, BFRC, and PVAFRC were modelled by using Tamai et al. 1987 [221] proposed equations 7.6(a) and 7.6(b). The equation 7.6(a) was used to model the linear elastic stress-strain behaviour of concrete up until the crack started. After crack initiation, the tensile load-carrying capacity of concrete decreases. Thus, the stress at crack initiation is referred to as the peak tensile stress carrying capacity of concrete. The equation, $0.7\sqrt{f_{ck}}$, given in IS 456-2000 [133], was used to find the peak tensile strength of concrete. The stress-strain behaviour of concrete in the post-cracking stage was then modelled using

equation 7.6(b). All the modelled tensile stress-strain behaviour of PC, BFRC, and PVAFRC of M30 and M70 series are shown in Figure 7.7.

$\sigma_t = E_c \varepsilon_t$ for $\varepsilon_t \leq \varepsilon_{cr}$ Eq. (7.6(a))

$\sigma_t = f_t (\frac{\varepsilon_{cr}}{\varepsilon_t})^{0.4}$ for $\varepsilon_t \leq \varepsilon_{cr}$ Eq. (7.6(b))

Where ε_t is the tensile strain in concrete, ε_{cr} is strain in concrete at peak-stress (stress at first cracking), and f_t is tensile strength of concrete (peak-stress).

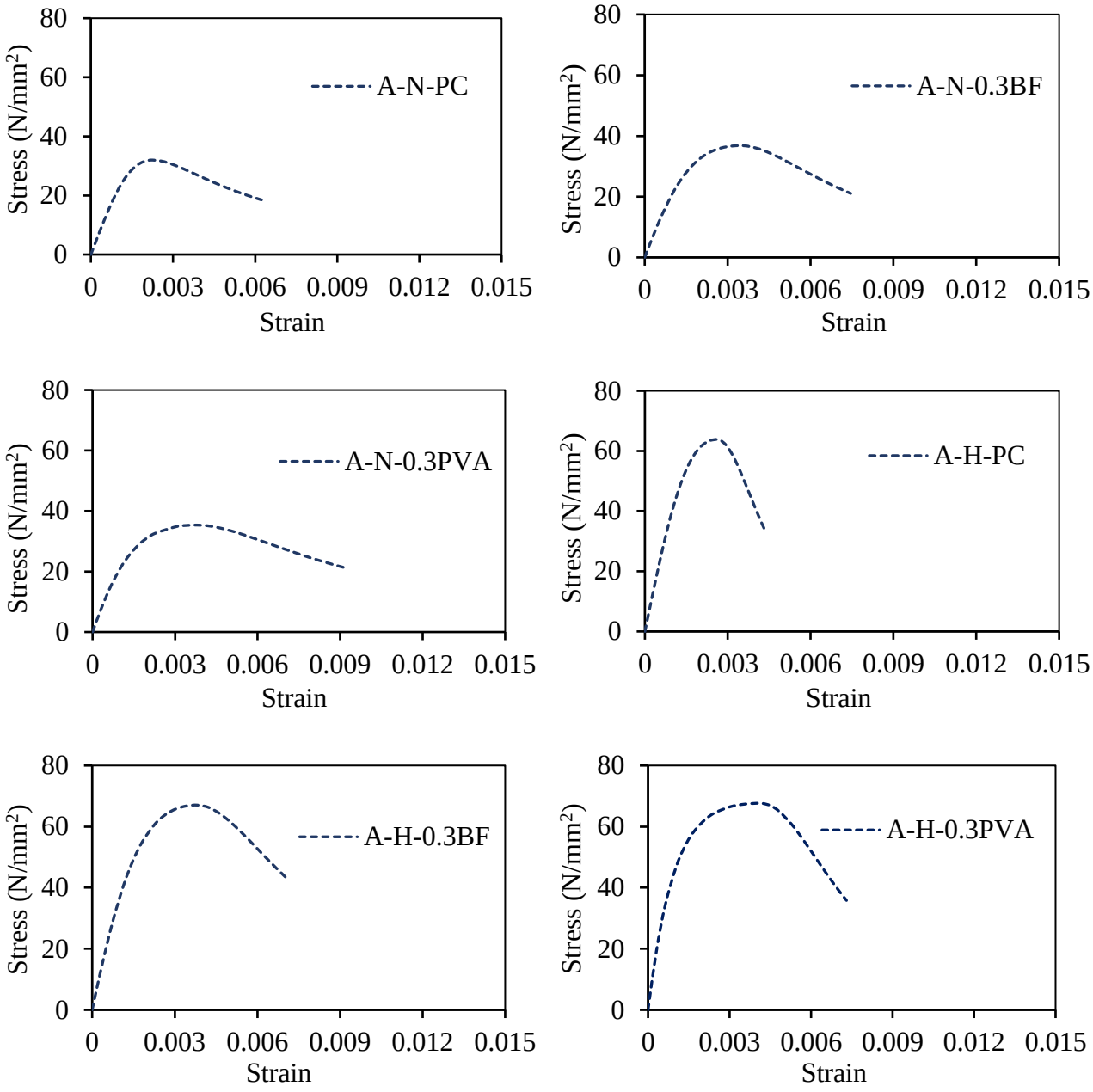

Figure 7.6 Stress-strain curves of PC, BFRC and PVAFRC of M30 and M70 series modelled under compression for ABAQUS input data

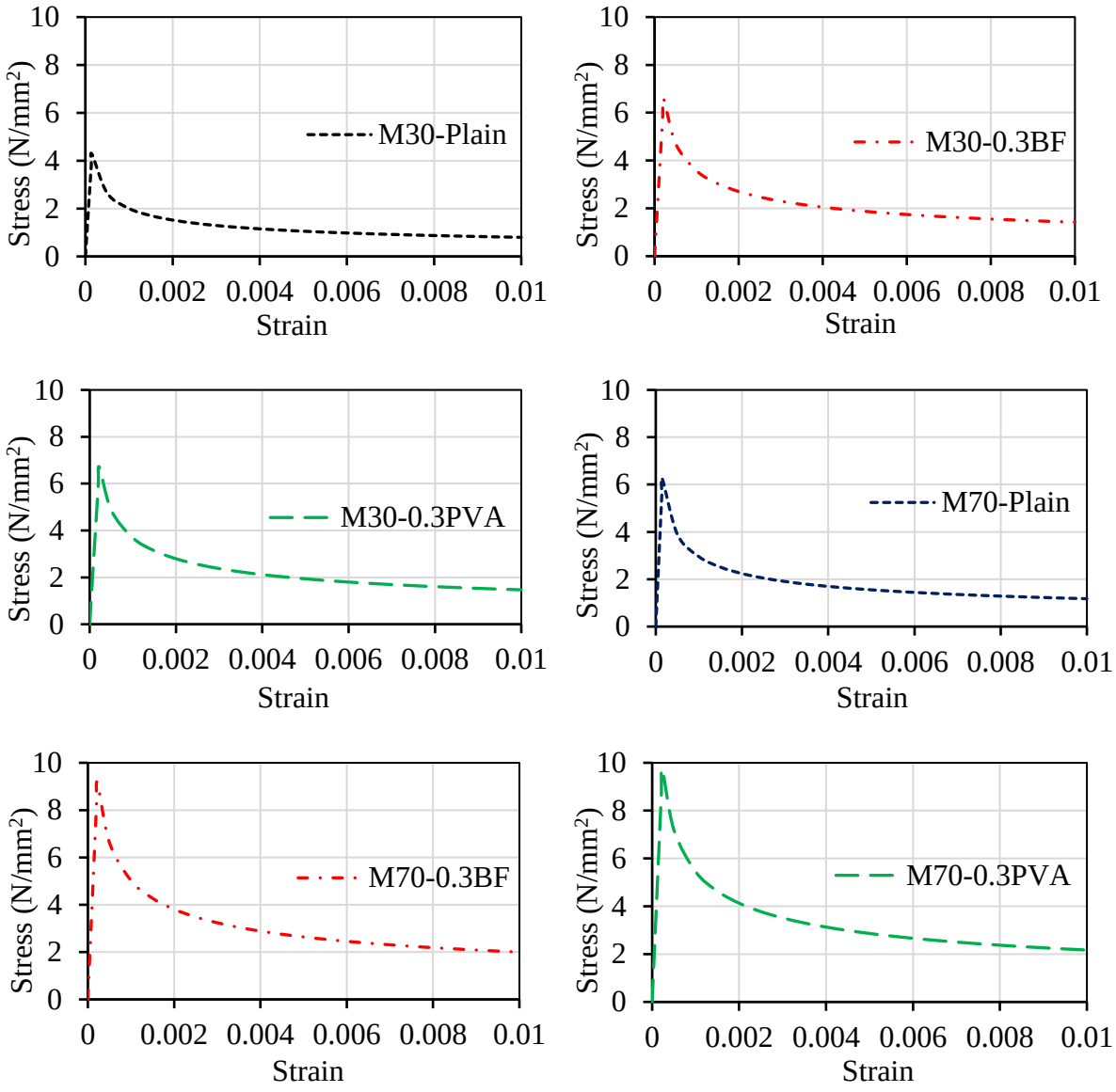

Figure 7.7 Stress-strain curves of PC, BFRC and PVAFRC of M30 and M70 series modelled under tension for ABAQUS input data

7.4.2 BFRP and Steel Rebars Modelling: Rebar Parts and Section Assignments, Element Type and Material Properties

The reinforcing bars were created using individual truss sections. Each longitudinal rebar was modelled as a one-dimensional rod. The deformable 'wire' type was used to define the 'Part' for the rebar. In ABAQUS, a wire is drawn as a line and is usually used to model a solid whose length is much larger compared to other dimensions. For assigning a property to this wire part, a 'truss' section is used. Truss sections provide only axial stiffness and define the cross-sectional area and material properties [217]. As the axial stiffness and cross-sectional area were the only two parameters of interest for each reinforcing bar, the truss section was applied to each wire part. Truss elements were used to mesh the discrete rods. Truss elements are long, slender

structural members that can transmit only axial force and do not transmit moments. In ABAQUS, a two-node straight truss element with a constant stress is available. It makes use of linear interpolation for displacement and position. A sufficient number of linear elements were adequate to capture the strain distribution within each reinforcing bar. Therefore, three-dimensional 2-node first-order truss elements, T3D2, were used to model the BFRP and steel reinforcing bars. The reinforcing bar meshed with truss elements is shown in Figure 7.8.

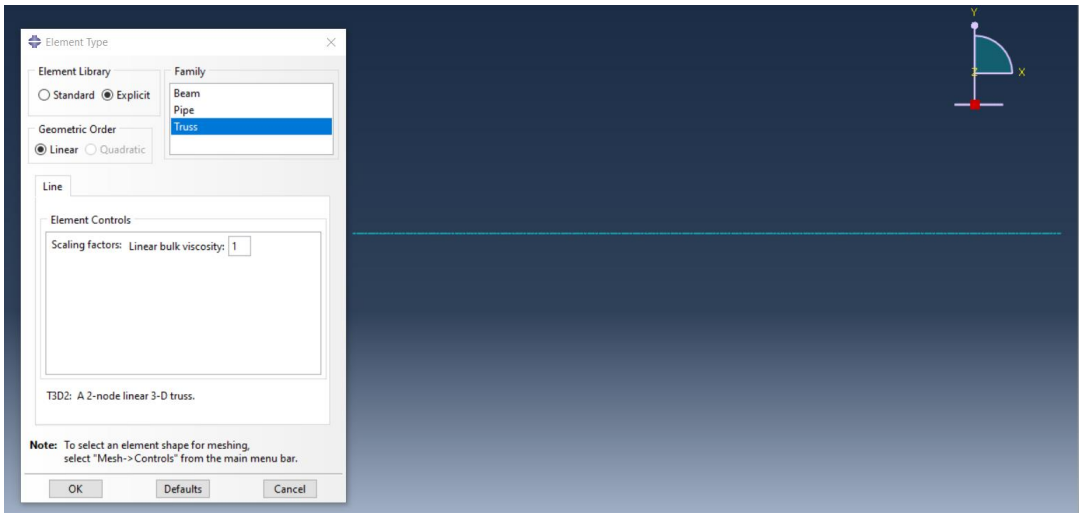

Figure 7.8 Reinforcing bar meshed with truss element

The stress-strain behavior of BFRP rebars is assumed to be linear-elastic up to failure. The longitudinal BFRP rebars were modelled as a brittle elastic isotropic material, as shown in Figure 7.9. A bilinear elastic–plastic model was used to simulate the longitudinal and transverse steel reinforcing bars, as shown in Figure 7.9. The nonlinear stress-strain behavior of the steel reinforcing bar was modelled as linear elastic up to the yield stage, beyond which it is fully plastic. In the linear elastic stage, the behavior was defined by the modulus of elasticity and Poisson's ratio, whereas in the plastic range, it was modelled according to the Von Mises criterion defined through the yield strength and the ultimate plastic strain (0.2). The input parameters for modelling BFRP and steel rebars were assigned according to the experimental data given in Table 7.5. The Poisson's ratio for BFRP rebar was taken as approximately 0.3 [222]. The Poisson's ratio for GI wire was taken as approximately 0.29 according to ASTM A653/A653M-23 galvanized steel [223].

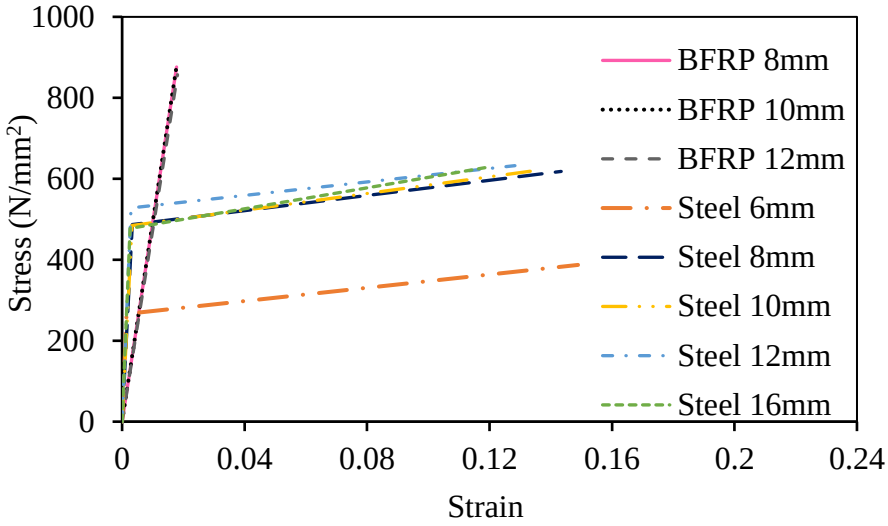

Figure 7.9 Stress-strain behaviour of BFRP and steel reinforcing bars used in the ABAQUS modelling

Table 7.5 Mechanical properties of BFRP and steel reinforcing bars used as input parameters for ABAQUS modelling

Rebar type	**Diameter (mm)**	**Density (kg/m^3)**	**Ultimate stress (MPa)**	**Strain at ultimate stress**	**Yield stress (MPa)**	**Poison's ratio**	**Young's modulus (GPa)**
BFRP	8	2100	876.16	0.0178	-	0.3	56
	10	2100	868.79	0.0176	-	0.3	55
	12	2100	857.04	0.0181	-	0.3	56
Steel	4	7850	610.65	0.1489	595.39	0.29	16
	6	7850	387.18	0.1434	266.58	0.3	205
	8	7850	618.20	0.1373	486.74	0.3	195
	10	7850	622.71	0.1283	484.80	0.3	198
	12	7850	632.41	0.1185	528.40	0.3	199
	16	7850	627.39	0.0178	477.76	0.3	200

7.4.3 Assembling of Concrete and Rebar Models and Interaction

The interaction between reinforcing bars (steel and BFRP) and concrete was established using the 'Embedded Region' constraint in ABAQUS. Using embedded region constraints tab, the individually modelled BFRP and steel reinforcing bars were embedded in concrete with the same degrees of freedom. The bond between rebars and concrete was considered based on the assumption that no slip is encountered for BFRP and steel rebars. Therefore, both fractional and absolute exterior tolerance were considered in embedded region constraint to ensure that perfect bond between concrete and both the rebars. Figure 7.10 presents the interaction between concrete and rebars.

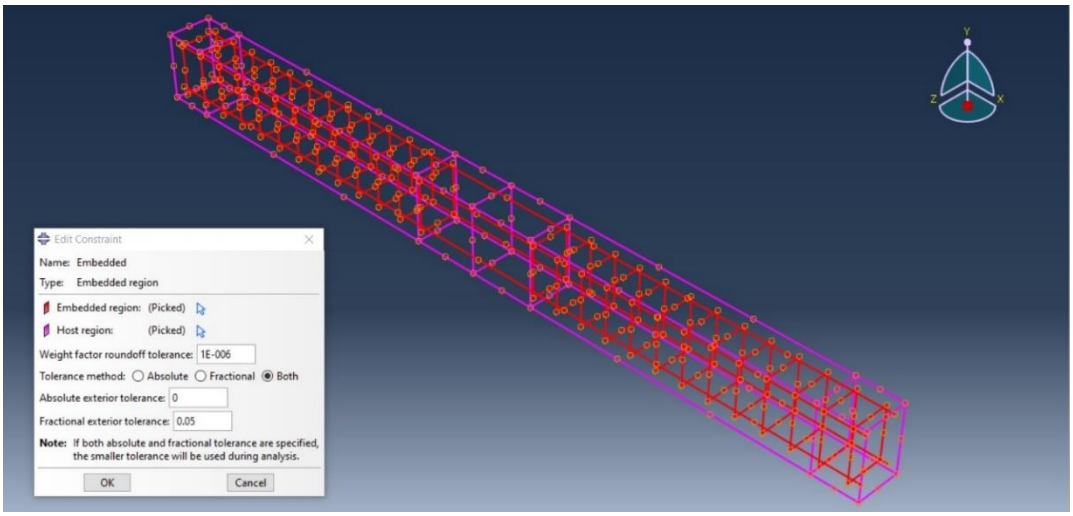

Figure 7.10 Interaction between rebars and concrete

7.4.4 Boundary Conditions

The boundary conditions used for all beams are shown in Figure 7.11. The boundary conditions are defined with respect to the directional axis 1, 2, and 3. '1' represents X-axis (the direction parallel to the beam's longitudinal), '2' represents Y-axis (the direction transverse to the beam's longitudinal axis), and '3' represents Z-axis (the out-of-plane direction). "U" represents displacements while "UR" represents rotations. Hence, U1 and UR2 refer to displacement in the 1-axis and rotation about the 2-axis respectively. The beams were tested with simple supports. The roller and pinned support boundary condition was prescribed on both the sides of RC beam at 100 mm from the edges. Also, applicator is constrained to move only in the direction of loading. One support provided restraint to only vertical displacement while allowing longitudinal displacement and rotations about out-of-plane axis (roller support). To model these conditions, a displacement of zero was prescribed in the Y-axis to a line of nodes at the support (U2 = 0), thereby allowing for rotations and longitudinal displacements. The other support provided restraint to both longitudinal and vertical displacements while allowing rotations about the out-of-plane axis (pin support). To model these conditions, a displacement of zero was prescribed in the X and Y axis to a line of node at the support (U1 = 0, U2 = 0), thus allowing only rotational displacements. To ensure stability of the model, the out-of-plane translations were restrained at the nodes of both the support (U3 = 0).

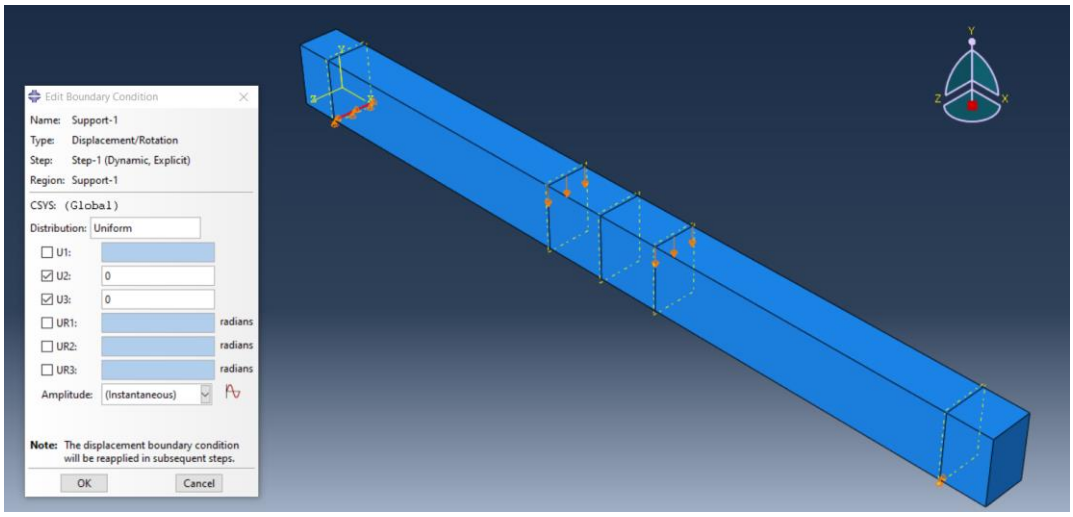

Figure 7.11 Beam with boundary conditions

7.4.5 Meshing

Meshing is the process of generating nodes and elements. A mesh is generated by defining nodes and connecting them to define the elements. Meshing helps in discretizing the member in order to solve the finite element model. Meshing was done for individual part with C3D8R 8-node element for concrete beams and T3D2 2-node element for BFRP and steel rebars. Figure 7.12 shows the meshing of the assembled model. To determine optimum mesh size, mesh sensitivity analysis was performed based on different mesh sizes. The obtained optimum mesh size was then considered for all the models of the study to have uniformity in meshing. The obtained optimum mesh size resulted in better convergence in all models.

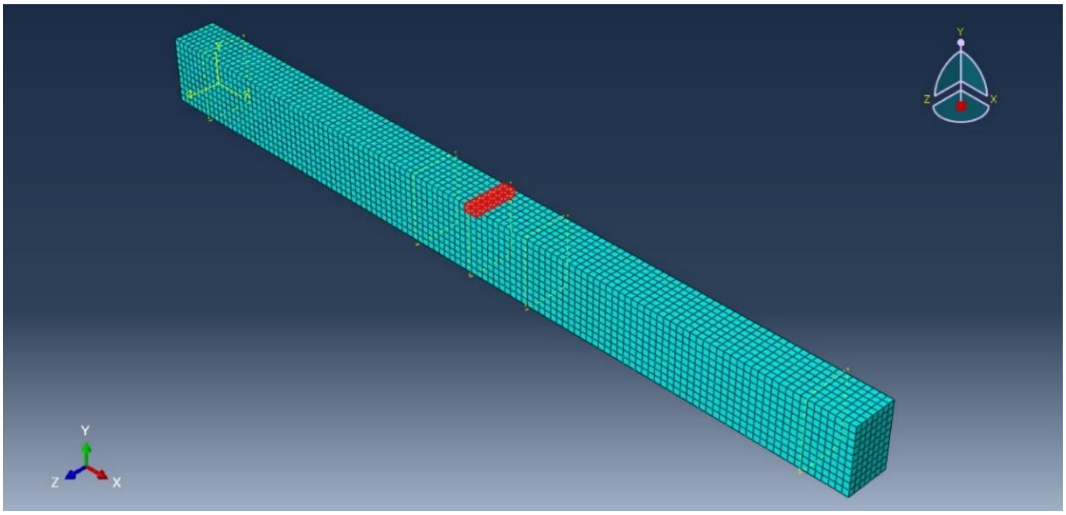

Figure 7.12 Meshing of the assembled model

7.4.6 Selection of Rebar and Concrete Nodes and Elements

Nodes and elements at various locations were grouped as sets to obtain the post analysis results. Nodes at supports were used to obtain the load and nodes at midspan bottom were used to obtain deflection. The elements at midspan top were used to obtain compressive strain in concrete and truss elements at midspan were used to obtain strain in rebar, as shown in Figure 7.13(a) and (b), respectively. The sum of reaction force at load nodes was taken as total load and the average of displacement (U2) at midspan nodes was considered as midspan deflection. To compute the strains in concrete and rebar, average of strains in midspan top elements and truss elements was considered respectively. The moments (M) were determined by multiplying reaction force with shear span distance and curvature (φ) was computed using equation 7.7 [22].

$$\varphi = \frac{\varepsilon_c + \varepsilon_f}{d} \qquad \text{Eq. (7.7)}$$

where, φ is curvature, ε_c is compressive strain in concrete, ε_f is strain in basalt rebar or steel rebar, and d is the effective depth.

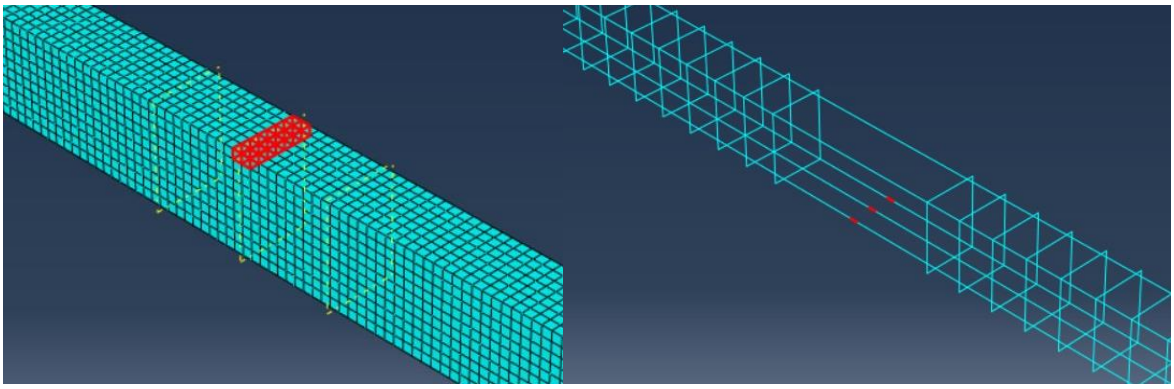

(a) Concrete (b) Rebars

Figure 7.13 Elements considered on concrete and rebars for M-φ response

7.4.7 Load Application

The displacement control loading approach has been used for the nonlinear simulation of the all the modelled beams [215]. This approach effectively overcomes convergence difficulties associated with concrete cracking, commonly encountered when employing a general static approach to solve nonlinear structures and provides the static solution with sufficient accuracy [224]. The loading was established by prescribing a downwards vertical displacement boundary condition to all the nodes under the loads (refer Figure 7.14.) The magnitude of this displacement was set large enough to ensure that failure of each beam occurs. A smooth step in amplitude function, with uniform distribution, was defined to establish the prescribed

displacement (refer Figure 7.15). Dynamic and explicit were defined for analysis as step-1 with a total time of 1 second as “Time period” and automatic increment. As the simulations were performed on three-dimensional beams, the reaction forces were distributed to multiple nodes. Therefore, the reaction forces outputted at both support nodes were summed to determine the total applied load at any given time. For convenience of applying boundary conditions, loadings and extracting data, sets (node set) were created for each support, point of loading and mid-span of the beam. The load application on the model under static loading conditions was employed using dynamic explicit features to overcome convergence difficulties and ensure the accurate attainment of results.

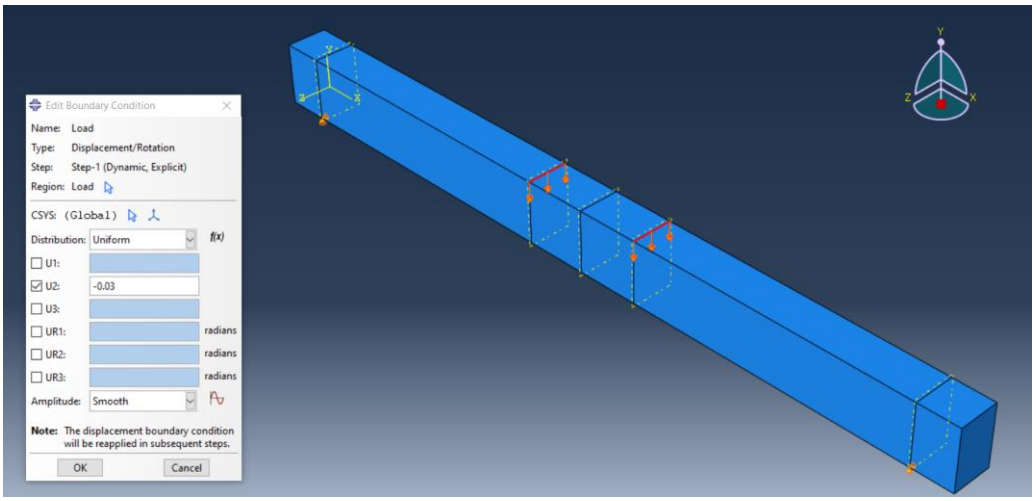

Figure 7.14 Beam with Loading condition

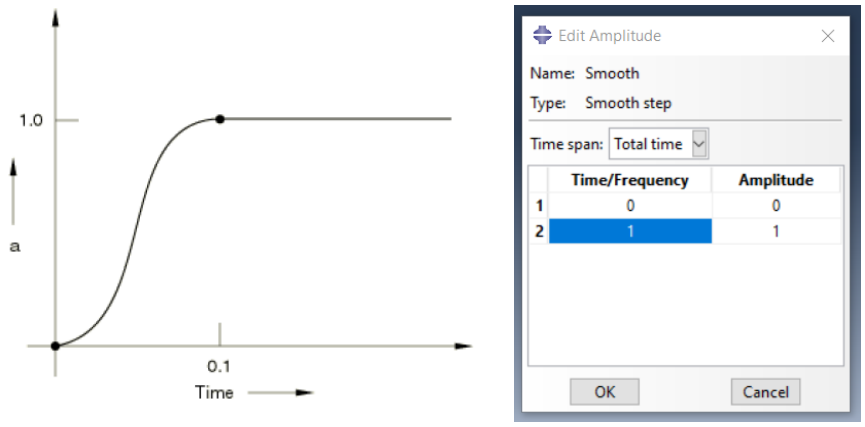

Figure 7.15 Amplitude function in ABAQUS

7.4.8 Assigning Job

Once all the input data was given to the assembled model, the model was run for analysis in job segment. Before starting the analysis by ABAQUS, it checks all the input parameters, assigned properties and meshing. If any missing data was observed, it shows an error.

7.4.9 Visualization and Extracting Output

Once the analysis was completed by ABAQUS, the results were extracted from the output data and visualized analytically and graphically. The required plots, such as load-deflection curves and moment-curvature relationships, were generated using XY data in visualization.

7.5 Results and Discussions

The deflections at the end of the analysis for the entire beam and reinforcements within is shown in Figure 7.16. Comparisons of simulation results with conventional mid-span deflection, moment-curvature response, ductility indices, crack pattern, and failure modes were carried out. The agreement of numerical results with experimental results and the percentage of error between them are discussed below.

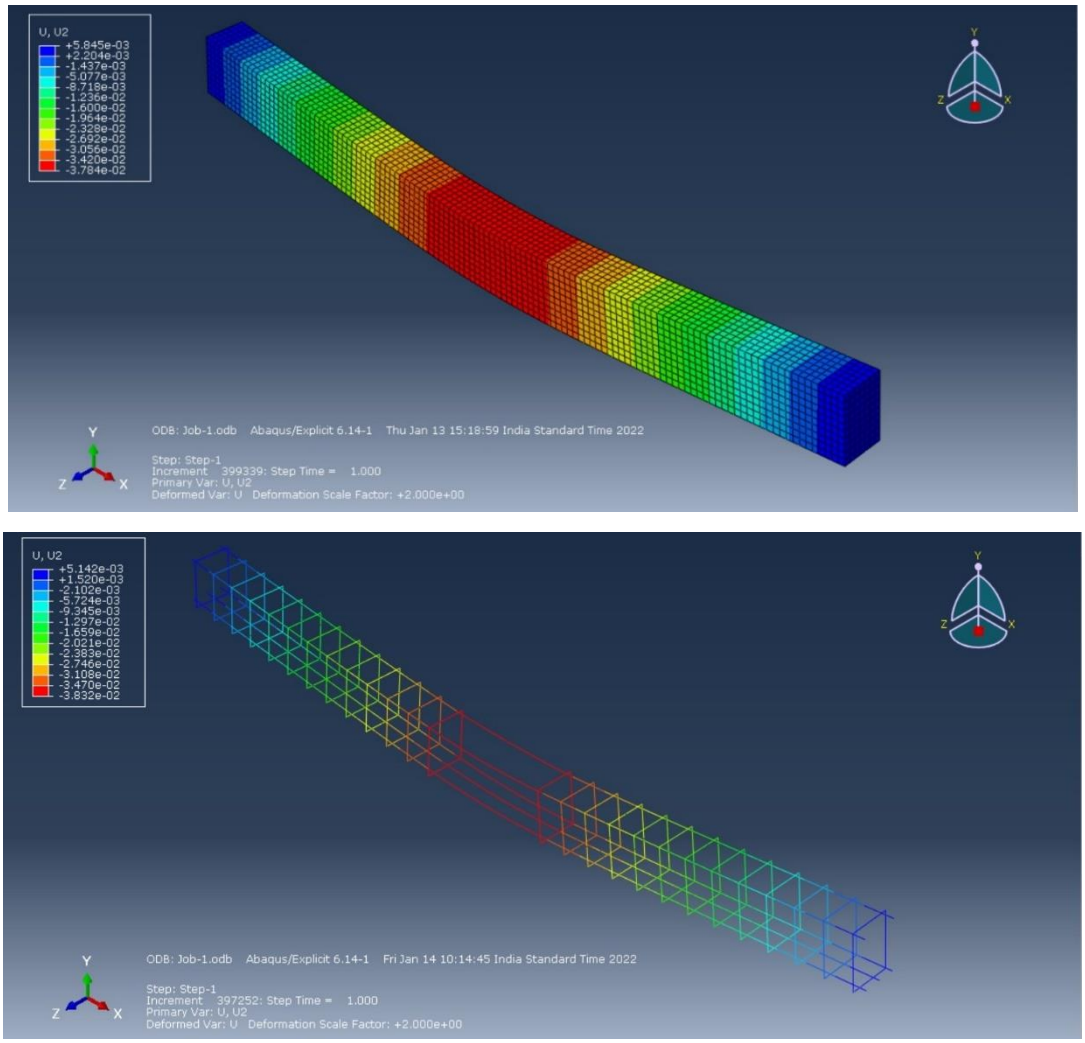

Figure 7.16 Deflection profile of reinforced concrete beam using ABAQUS software

7.5.1 Comparison of Numerical and Experimental Load-Deflection Curves

The graphical comparison between numerical load-deflection curves and experimental load-deflection curves is presented in Figure 7.17 for each beam. Two significant points on the load-deflection curves were selected to evaluate the percentage error between the load and deflection values of numerical and experimental results. The significant points chosen for comparative analysis are the first crack load and ultimate load.

The load and deflection values obtained at the first crack load and ultimate load from numerical and experimental results are shown in Table 7.6, and the percentage of error between numerical values and experimental values is also presented in Table 7.6. In the M30 series, a maximum error of 8.97% between numerical and experimental first crack load was obtained for beam BPOR30, while for deflection at the first crack load, a maximum error of 8.23% existed for SUR30 beam. In the M30 series, a maximum error of 9.34% between numerical and experimental ultimate load and a maximum of 6.94% error between numerical and experimental deflection at ultimate load were obtained for beam BOR30. In the M70 series, a maximum error of 8.22% between numerical and experimental first crack load and a maximum of 8.02% error between numerical and experimental deflection at the first crack load were obtained for beam SUR70. In the M70 series, a maximum error of 8.55% between numerical and experimental ultimate load was obtained for beam BBUR70, while for deflection at ultimate load, a maximum error of 8.64% existed for BOR70 beam.

From Table 7.6, it is evident that in the M30 series, the mean absolute error percentage between numerical and experimental first crack load was 7.36%, and in the case of deflection at the first crack load, the mean absolute error percentage between numerical and experimental results reduced to 6.46%. At the ultimate stage, the mean absolute error percentage between numerical and experimental load was 7.66%, and in the case of deflection, the mean absolute error percentage was reduced to 5.76%. In the M70 series, the mean absolute error percentage between numerical and experimental first crack load was 6.76%, and in the case of deflection at the first crack load, the mean absolute error percentage between numerical and experimental results was reduced to 6.59%. At the ultimate stage, the mean absolute error percentage between numerical and experimental load is 6.75%, and in the case of deflection, the mean absolute error percentage is reduced to 6.46%. The calculated percentage of error between numerical and experimental results is within the range of 10%. Therefore, based on Figure 7.17 and Table 7.6, it can be concluded that the obtained numerical results are in good accordance with the experimental results.

Table 7.6 Percentage of error between the numerical and experimental results of load-deflection behaviour of BFRP-reinforced concrete beams

Beam name	**Experimental values**				**Numerical values**				**% Error between experimental and numerical values**			
	At first crack load		**At ultimate load**		**At first crack load**		**At ultimate load**		**At first crack load**		**At ultimate load**	
	P_{FCL} **(kN)**	δ_{FCL} **(mm)**	P_{UL} **(kN)**	δ_{UL} **(mm)**	P_{FCL} **(kN)**	δ_{FCL} **(mm)**	P_{UL} **(kN)**	δ_{UL} **(mm)**	P'_{FCL}	δ'_{FCL}	P'_{UL}	δ'_{UL}
SUR30	4.87	0.67	18.74	53.87	5.298	0.731	19.98	57.12	8.14	8.23	6.23	5.70
SOR30	5.50	0.75	32.20	42.01	5.962	0.815	34.970	44.30	7.82	7.94	7.92	5.17
BUR30	4.81	0.67	28.41	41.25	5.081	0.711	30.56	43.22	5.36	6.40	7.04	4.56
BOR30	5.47	0.75	46.02	34.04	5.79	0.80	50.76	36.57	5.52	6.31	9.34	6.94
BBUR30	5.27	0.74	29.67	45.00	5.667	0.783	31.91	48.25	6.97	6.13	7.01	6.73
BBOR30	5.70	0.80	47.72	37.66	6.214	0.821	52.57	40.27	8.26	3.21	9.22	6.49
BPUR30	5.57	0.75	30.91	46.85	6.040	0.816	33.63	49.61	7.86	8.09	8.10	5.57
BPOR30	5.94	0.82	51.31	39.30	6.527	0.870	54.84	41.33	8.97	5.34	6.42	4.90
Mean absolute error of M30 series beams									7.36	6.46	7.66	5.76
SUR70	7.13	0.740	42.25	42.25	7.77	0.804	44.98	45.57	8.22	8.02	6.07	7.29
SOR70	7.65	0.811	57.24	35.85	8.29	0.863	62.02	37.16	7.75	6.07	7.70	3.52
BUR70	7.04	0.718	54.35	38.70	7.48	0.77	58.03	42.12	5.80	6.85	6.33	8.11
BOR70	7.61	0.771	70.77	30.65	8.12	0.83	75.81	33.55	6.31	6.97	6.65	8.64
BBUR70	7.39	0.74	55.04	41.33	7.96	0.80	60.18	43.90	7.12	7.49	8.55	5.86
BBOR70	7.90	0.82	73.01	32.25	8.37	0.86	77.07	34.75	5.61	4.57	5.27	7.20
BPUR70	7.56	0.81	55.93	43.65	8.14	0.86	61.09	45.61	7.20	6.08	8.45	4.30
BPOR70	8.04	0.86	74.26	34.32	8.56	0.93	78.17	36.80	6.09	6.70	4.99	6.75
Mean absolute error of M70 series beams									6.76	6.59	6.75	6.46

P_{FCL}= Load at first crack; δ_{FCL}= Deflection at first crack load; P_{UL}= Ultimate load; δ_{UL}= Deflection at ultimate load; P'_{FCL}= Percentage of error in first crack load; δ'_{FCL}= Percentage of error in deflection at first crack load; P'_{UL}= Percentage of error in ultimate load; δ'_{UL}= Percentage of error in deflection at ultimate load.

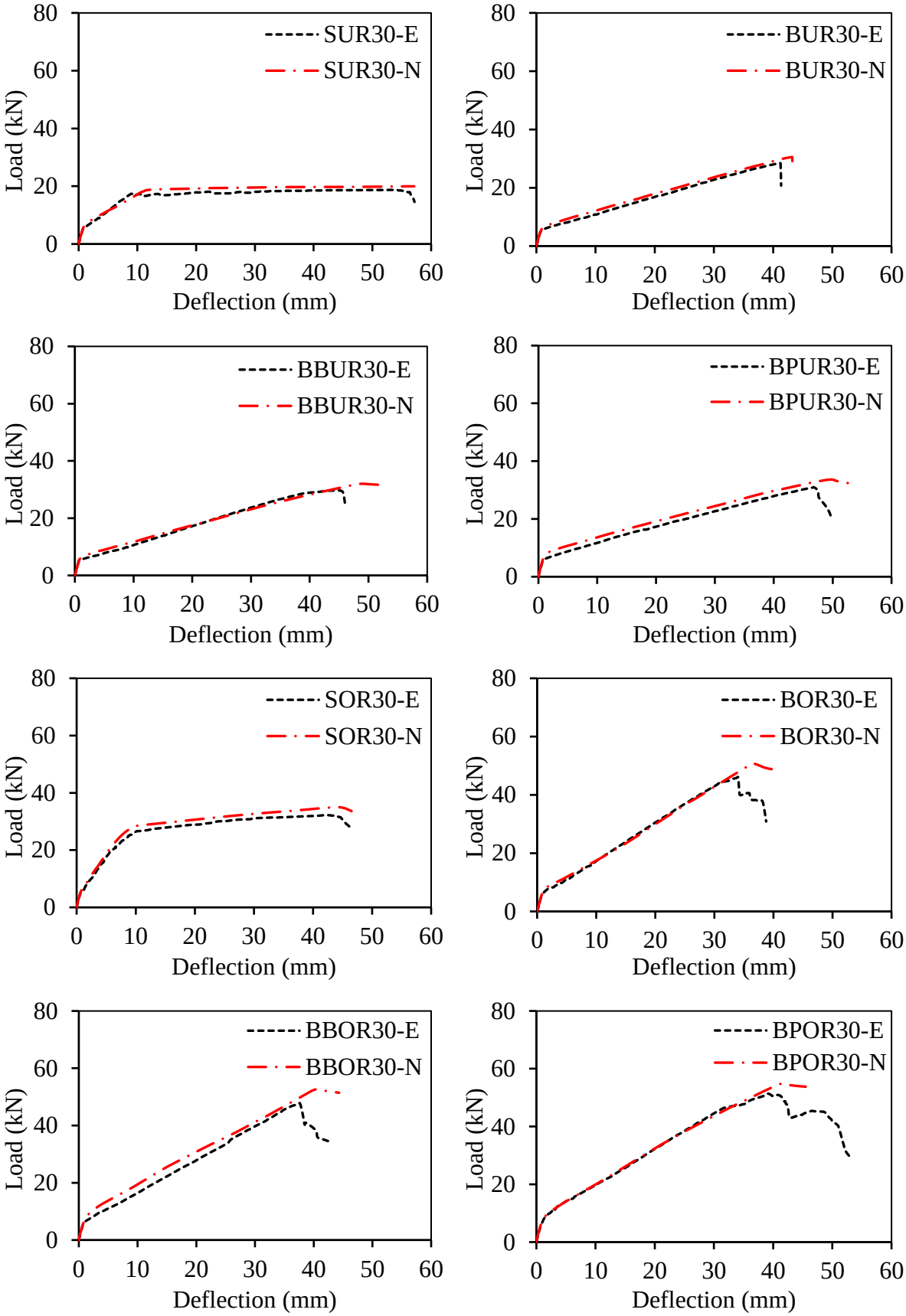
SUR30-E
SUR30-N
BUR30-E
BUR30-N
BBUR30-E
BBUR30-N
BPUR30-E
BPUR30-N
SOR30-E
SOR30-N
BOR30-E
BOR30-N
BBOR30-E
BBOR30-N
BPOR30-E
BPOR30-N
Load (kN)
Deflection (mm)
0
20
40
60
80
0
10
20
30
40
50
60

(a) M30 series

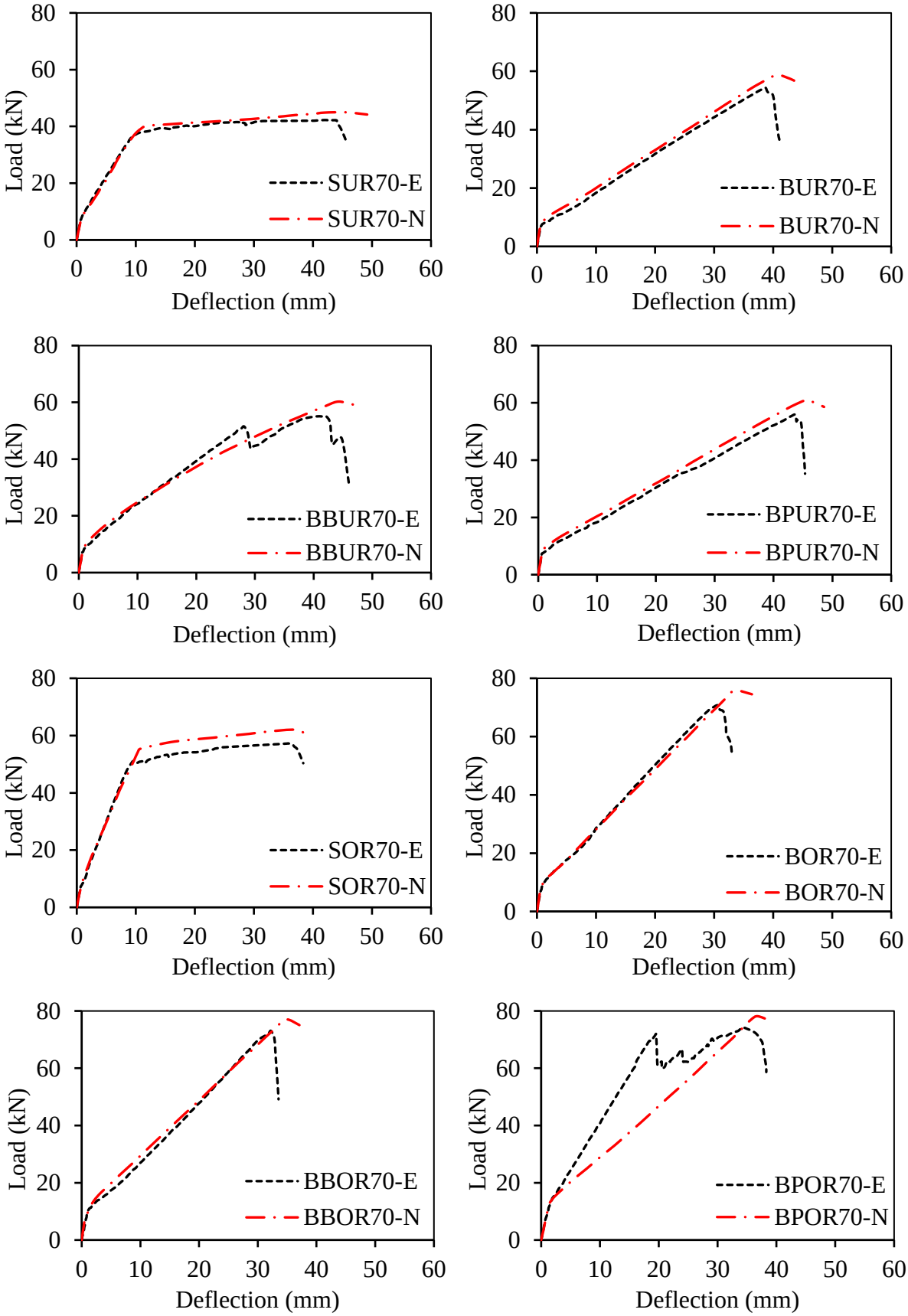

(b) M70 series

Figure 7.17 Comparison between numerical and experimental load-deflection curves of BFRP-reinforced concrete beams.

7.5.2 Comparison of Numerical and Experimental Moment-Curvature Relationships

The graphical comparison of numerical moment-curvature relationships with experimental moment-curvature relationships for each beam of Phase I, II, III, and IV of M30 and M70 series is shown in Figure 7.18. Two significant points on the moment-curvature relationship were selected to evaluate the percentage of error between the numerical and experimental moment and curvature results. The significant points chosen for comparative analysis are the first crack moment and ultimate moment. The moment and curvature values obtained at first crack load and ultimate loads from numerical and experimental results are shown in Table 7.7 along with the percentage of error between numerical and experimental results. For the M30 series, the highest error between the numerical and experimental moment at the first crack load was 8.97% for beam BPOR30, while the maximum error for curvature at the first crack moment was 10.06% for beam SUR30. Similarly, in the M30 series, the highest error between numerical and experimental ultimate moment was 9.34% for beam BPOR30, while the maximum error of curvature at ultimate moment was 10.06% for beam SUR30. For the M70 series, the maximum error between the numerical and experimental moment at the first crack load was 8.22% for beam SUR70, while the maximum error of curvature at the first crack moment was 9.07% for beam BOR70. Similarly, in the M70 series, the highest error between numerical and experimental ultimate moment was 8.55% for beam BBUR70, while the maximum error for curvature at the ultimate moment was 9.66% for beam BPOR70.

From Table 7.7, it is evident that in the M30 series, the mean absolute error percentage between numerical and experimental moment at the first crack load was 7.37%, and for curvature at the first cracking moment, the mean absolute error percentage increased to 8.30%. At the ultimate stage, the mean absolute error percentage between numerical and experimental ultimate moment was 7.66%, and for curvature at the ultimate moment, the mean absolute error percentage reduced to 7.13%. Similarly, in the M70 series, the mean absolute error percentage between numerical and experimental first cracking moment was 6.68%, and for curvature at the first cracking moment, the mean absolute error percentage increased to 7.29%. At the ultimate stage, the mean absolute error percentage between numerical and experimental ultimate moment was 6.84%, and in the case of curvature at the ultimate moment, the mean absolute error percentage increased to 7.0%. The calculated percentage of error between numerical and experimental results was a maximum of 10%. Therefore, from Figure 7.18 and Table 7.7, it can be concluded that the numerical moment-curvature results are in good accordance with experimental moment-curvature results.

Table 7.7 Percentage of error between the numerical and experimental results of moment-curvature relationships of BFRP-reinforced concrete beams

Beam name	Experimental values				Numerical values				% Error between experimental and numerical values			
	At first crack load		At ultimate load		At first crack load		At ultimate load		At first crack load		At ultimate load	
	M_{FC}	φ_{FCM}	M_U	φ_{UM}	M_{FC}	φ_{FC}	M_U	φ_{UM}	M'_{FCL}	φ'_{FCL}	M'_{UL}	φ'_{UL}
SUR30	1.58	2.389	6.09	5.103	1.72	2.656	6.49	5.376	8.14	10.06	6.23	5.08
SOR30	1.79	2.092	10.47	2.827	1.94	2.292	11.37	2.993	7.82	8.72	7.92	5.56
BUR30	1.56	2.246	9.23	3.104	1.65	2.462	9.93	3.345	5.36	8.78	7.05	7.21
BOR30	1.78	1.981	14.96	1.904	1.88	2.159	16.50	2.003	5.53	8.27	9.34	4.93
BBUR30	1.71	2.294	9.64	3.690	1.84	2.422	10.37	4.084	6.97	5.28	7.02	9.64
BBOR30	1.85	2.042	15.51	2.075	2.02	2.185	17.09	2.293	8.27	6.55	9.22	9.51
BPUR30	1.81	2.340	10.05	3.956	1.96	2.570	10.93	4.260	7.87	8.95	8.10	7.13
BPOR30	1.93	2.081	16.68	2.178	2.12	2.307	17.82	2.368	8.96	9.80	6.43	8.02
Mean absolute error of M30 series beams									7.37	8.30	7.66	7.13
SUR70	2.32	2.401	13.73	3.132	2.52	2.607	14.62	3.228	8.22	7.88	6.07	2.97
SOR70	2.49	2.081	18.60	1.981	2.70	2.228	20.16	2.152	7.76	6.63	7.70	7.95
BUR70	2.29	2.244	17.66	2.163	2.43	2.404	19.08	2.328	5.81	6.63	7.41	7.12
BOR70	2.48	1.880	23.00	1.496	2.64	2.068	24.64	1.569	5.92	9.07	6.65	4.65
BBUR70	2.40	2.268	17.89	2.754	2.59	2.450	19.56	2.990	7.12	7.41	8.55	7.91
BBOR70	2.57	2.036	23.73	1.574	2.72	2.235	25.05	1.684	5.61	8.93	5.27	6.56
BPUR70	2.46	2.438	18.18	3.091	2.65	2.597	19.85	3.404	7.21	6.12	8.45	9.20
BPOR70	2.62	2.194	24.22	1.653	2.78	2.325	25.40	1.830	5.77	5.65	4.66	9.66
Mean absolute error of M70 series beams									6.68	7.29	6.84	7.00

M_{FC}= Moment at first crack (kNm); φ_{FCM}= Curvature at first crack moment × 10^{-6} (rad/mm); M_U = Ultimate moment (kNm); φ_{UM}= Curvature at ultimate moment × 10^{-4} (rad/mm); M'_{FC}= Percentage of error in first crack moment; φ'_{FCM}= Percentage of error in curvature at first crack moment; M'_{UM}= Percentage of error in ultimate moment; φ'_{UM}= Percentage of error in curvature at ultimate moment.

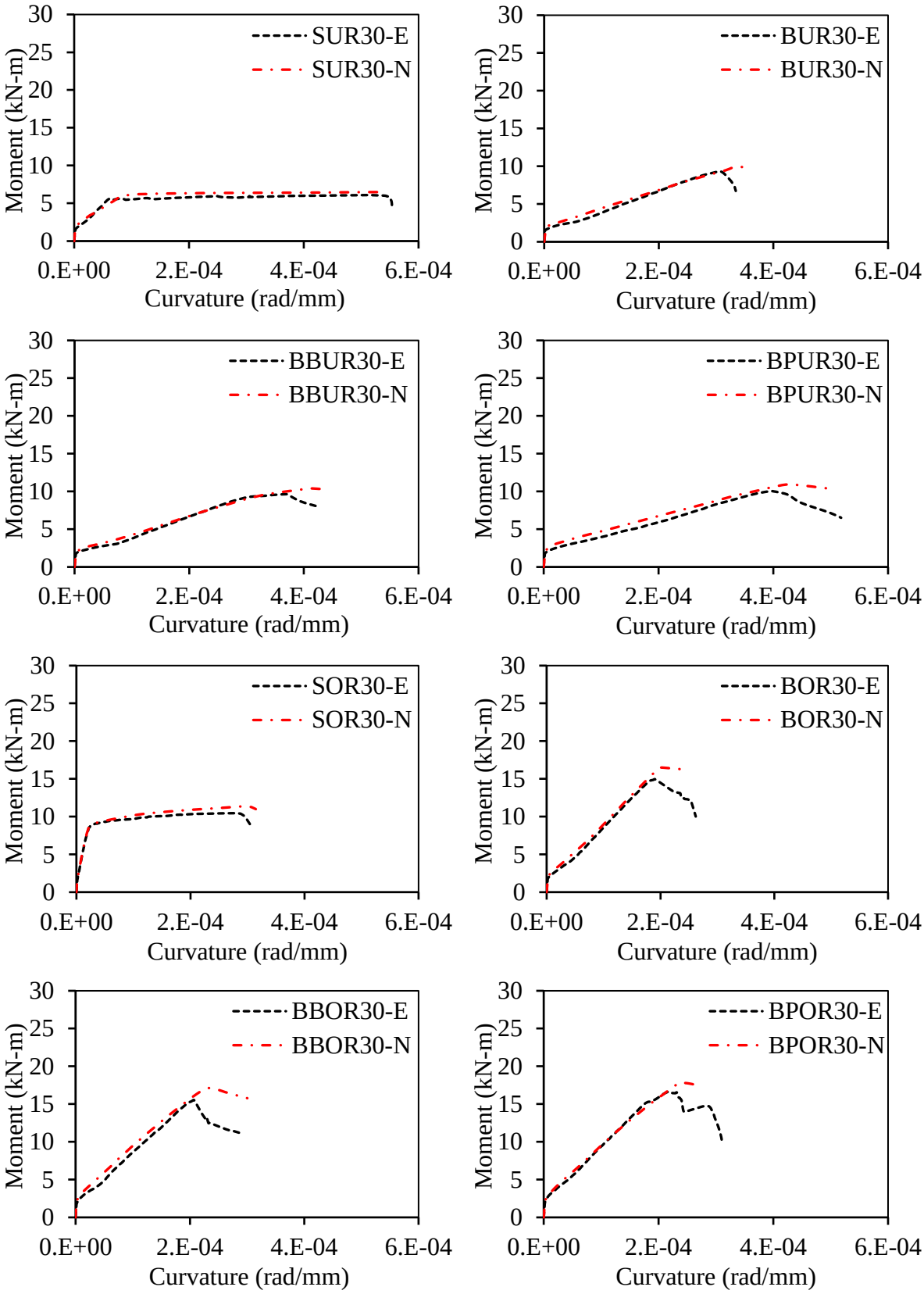
SUR30-E
SUR30-N
BUR30-E
BUR30-N
BBUR30-E
BBUR30-N
BPUR30-E
BPUR30-N
SOR30-E
SOR30-N
BOR30-E
BOR30-N
BBOR30-E
BBOR30-N
BPOR30-E
BPOR30-N
Moment (kN-m)
Curvature (rad/mm)
0
5
10
15
20
25
30
0.E+00
2.E-04
4.E-04
6.E-04

(a) M30 series

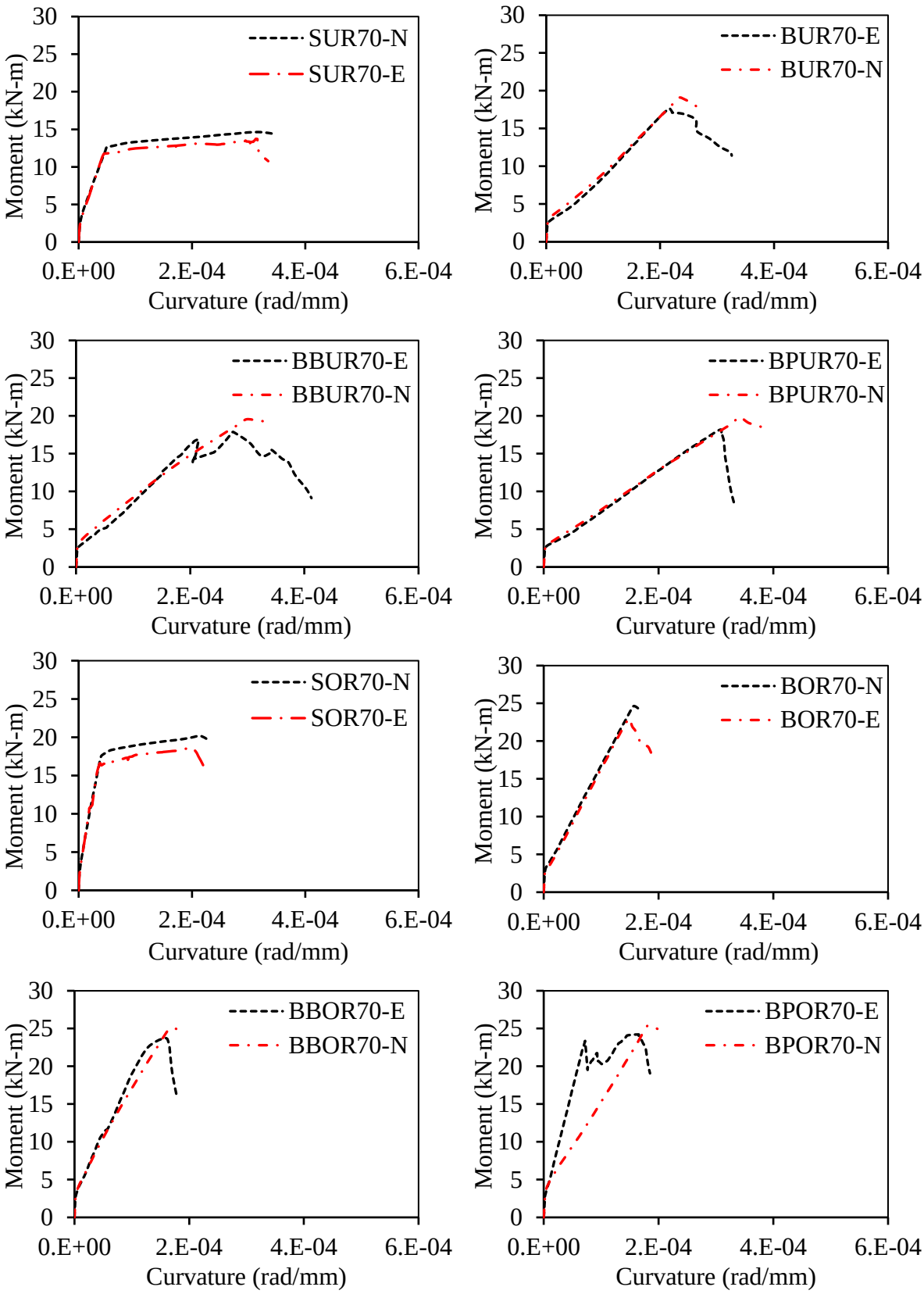

(b) M70 series

Figure 7.18 Comparison between numerical and experimental moment-curvature curves of BFRP-reinforced concrete beams.

7.5.3 Comparison of Numerical and Experimental Ductility Indices

The ductility indices values calculated from the area under the experimental load-deflection curves were compared with the ductility indices values calculated from the area under the numerical load-deflection curves. The calculated numerical and experimental ductility indices and the percentage error between them are presented in Table 7.8. From the results presented in Table 7.8, it was noticed that the ductility indices results of numerically simulated beams were found to be similar to the ductility indices results of experimentally evaluated beams.

Due to the yielding and higher Young's modulus of steel reinforcement compared to BFRP rebars, reinforcing PC with steel reinforcement showed the highest experimental and numerical ductility indices in both M30 and M70 series. In the case of BFRP RC beams, due to the low Young's modulus and linear stress-strain behaviour of BFRP rebars, reinforcing PC, BFRC, and PVAFRC beams with BFRP rebars led to low ductility in the beam compared to steel-reinforced PC beams. In the M30 series, the BOR30 beam showed the lowest experimental and numerical ductility indices with an error percentage of 1.83% between them. In the M70 series, the BOR70 beam showed the lowest experimental and numerical ductility indices with an error percentage of 4.97% between them. In both series, under-reinforced beams showed better ductility behavior than over-reinforced beams. The use of BFRC and PVAFRC slightly improved the ductility behavior of BFRP RC beams. This can be observed clearly from results presented in Table 7.8. The BFRP-reinforced PC beams showed the lowest ductility indices in both series. From numerical ductility results, it was noticed that BFRP-reinforced BFRC and PVAFRC beams showed better ductility indices compared to BFRP-reinforced PC beams. The use of PVA fibers showed better improvement in ductility indices of BFRP-reinforced beams compared to BFRP-reinforced BFRC beams.

From the calculated percentage of error, the difference between numerical ductility indices and experimental ductility indices was very low with an average error of 6.07%, a standard deviation of 7.04 for the M30 series, and 6.87% with a standard deviation of 6.57 for the M70 series. The highest difference between numerical and experimental ductility indices occurred for the SUR30 beam in the M30 series and the SUR70 beam in the M70 series. The lowest difference between numerical and experimental ductility indices occurred for BOR30 in the M30 series and BOR70 in the M70 series. Except for SUR30 and SUR70 beams, the calculated percentage of error between numerical and experimental ductility indices values was within 10%. As a result, the ductility indices values of numerically simulated beams were in good agreement with the experimental ductility indices values, with 90-98% accuracy.

Table 7.8 Percentage of error between the numerical and experimental results of ductility indices BFRP-reinforced concrete beams

Series	Beam name	Experimental ductility indices ($E-\mu_E$)	Numerical Ductility indices ($N-\mu_E$)	Percentage of error in ductility indices (μ'_E)
M30 series	SUR30	9.00	6.96	22.66
	SOR30	6.29	6.50	3.22
	BUR30	1.99	1.96	1.85
	BOR30	1.32	1.35	1.83
	BBUR30	2.16	2.22	2.70
	BBOR30	1.36	1.42	4.25
	BPUR30	2.19	2.40	8.60
	BPOR30	1.39	1.44	3.44
M70 series	SUR70	7.90	6.10	22.70
	SOR70	6.06	5.72	5.61
	BUR70	1.44	1.55	7.02
	BOR70	1.22	1.29	4.97
	BBUR70	1.62	1.58	2.07
	BBOR70	1.25	1.32	5.19
	BPUR70	1.55	1.50	3.29
	BPOR70	1.39	1.33	4.13

7.5.4 Damage Pattern of Simulated Beams

Damage patterns of steel-reinforced PC beams and BFRP-reinforced PC, BFRC, and PVAFRC beams were identical. The damage pattern of all numerically simulated beams is shown in Figure 7.19. In Figure 7.19, for each beam, the compression damage (CD) profile and tension damage (TD) profile are shown separately. All the numerically simulated beams failed in tensile compression failure. The development of cracks in the tension zone and failure of the compression zone of each beam is clearly presented in the damage profiles.

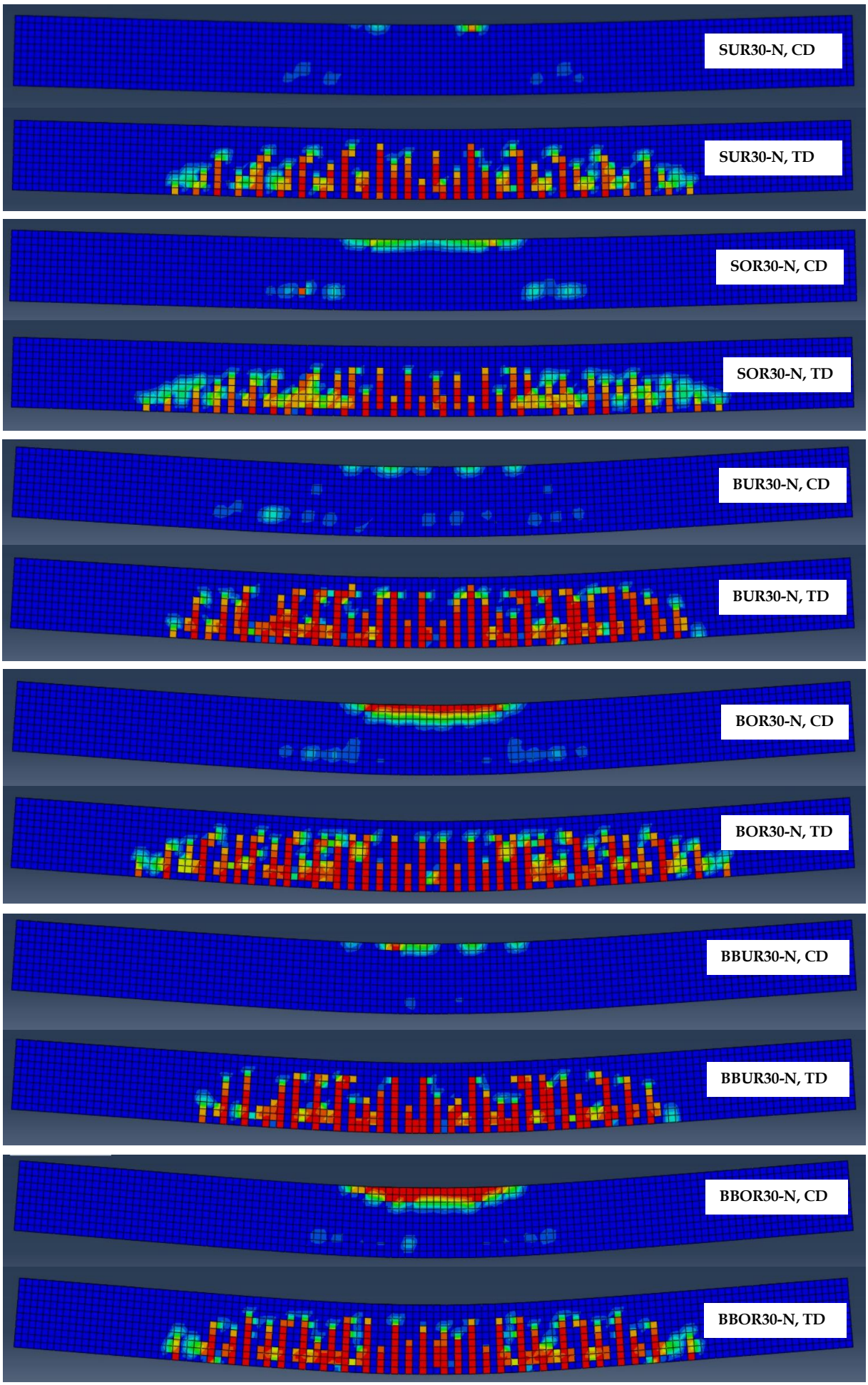
SUR30-N, CD
SUR30-N, TD
SOR30-N, CD
SOR30-N, TD
BUR30-N, CD
BUR30-N, TD
BOR30-N, CD
BOR30-N, TD
BBUR30-N, CD
BBUR30-N, TD
BBOR30-N, CD
BBOR30-N, TD

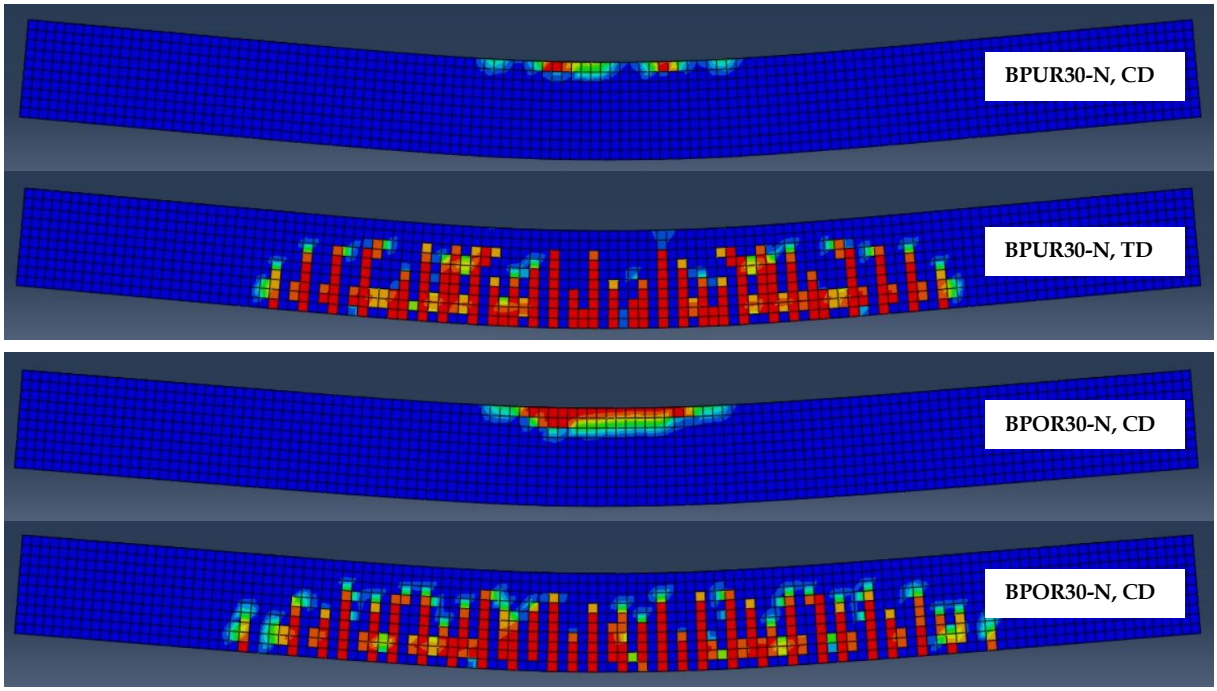

(a) M30 series beam

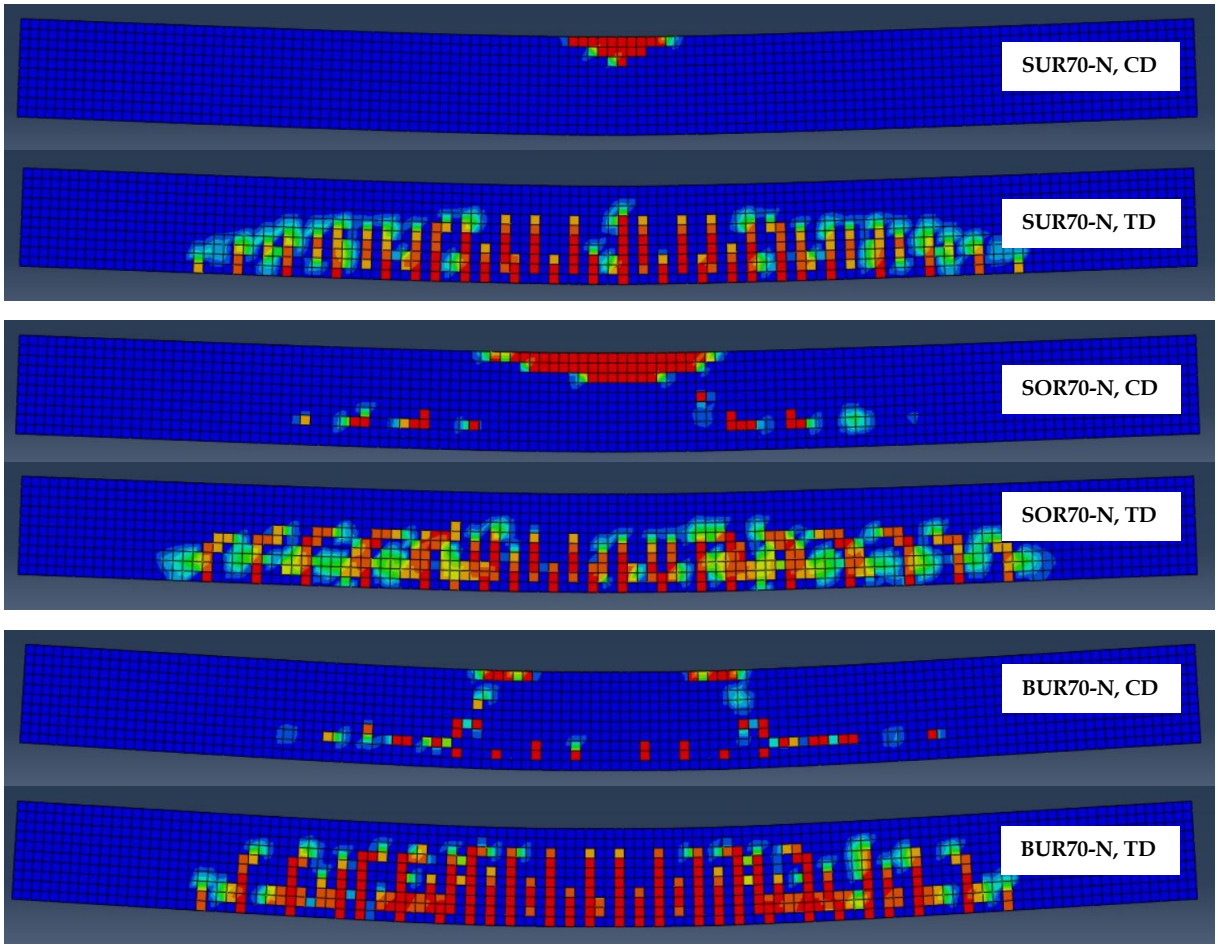

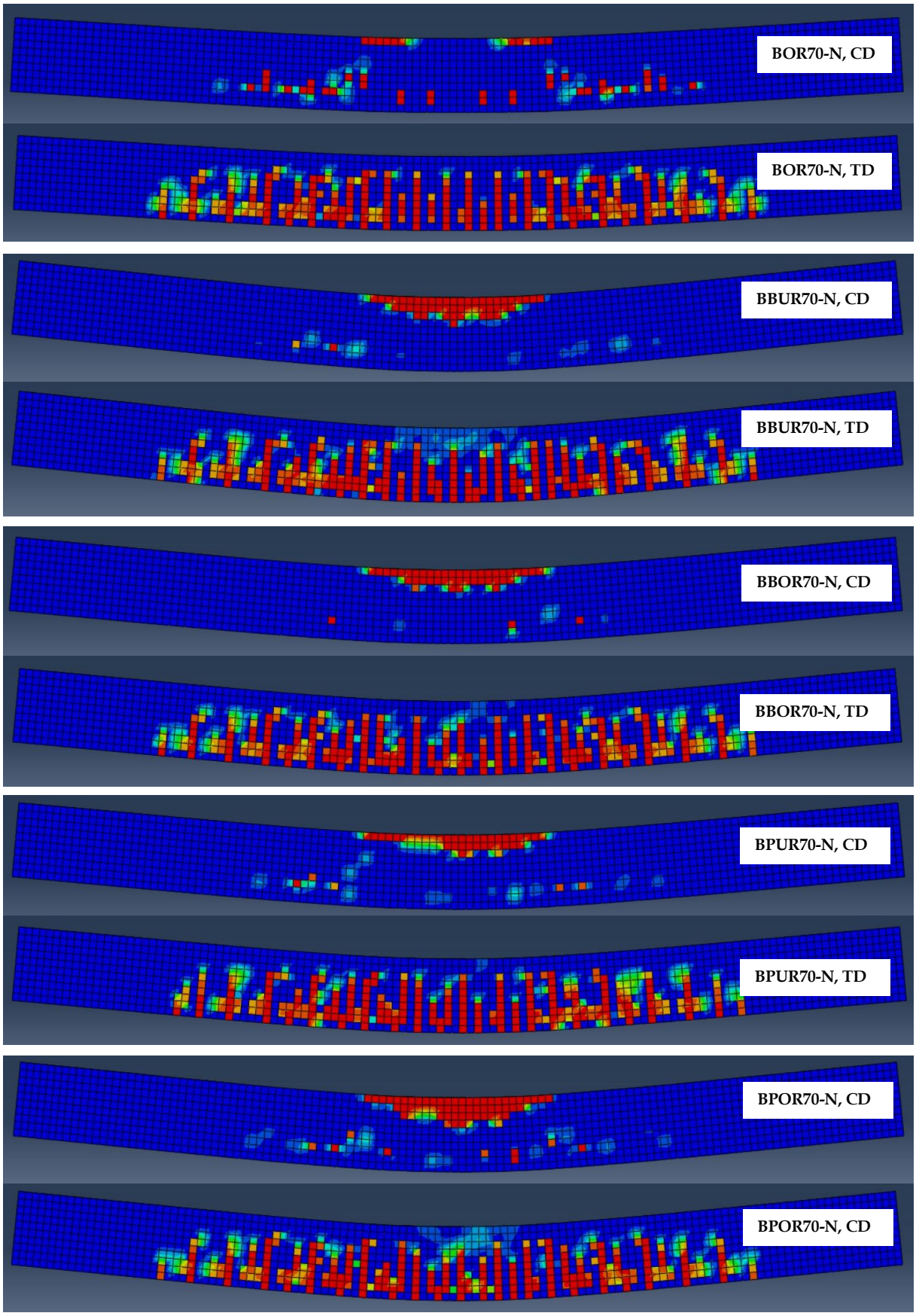

b) M70 series beams

Figure 7.19 Cracking pattern and failure modes of numerically simulated beams

7.6 Conclusions

In this chapter, the flexural behavior of PC, BFRC, PVAFRC beams reinforced with BFRP rebars and PC beams reinforced with steel reinforcing bars was investigated with the nonlinear finite element method to validate the experimental results of the tested beams. All the experimentally tested beams were simulated using the finite element method based ABAQUS software. Based on the results presented, the following conclusions are drawn:

- A total of 16 3D nonlinear finite element models (12 BFRP RC beams and 4 steel-reinforced PC beams) was developed for the M30 and M70 series to simulate the flexural response of BFRP-reinforced PC, BFRC, and PVAFRC beams, and steel-reinforced PC beams.
- The effect of different parameters, including the percentage of longitudinal reinforcement, compressive strength of concrete and FRC, and the addition of basalt fibers and PVA fibers, on the flexural response of simulated beams was investigated.
- The numerical models developed using ABAQUS demonstrated great capability in simulating the overall experimental results and flexural behaviour.
- All the numerically simulated beams behaved in a similar manner to the experimental results. The simulated BFRP-reinforced PC, BFRC, and PVAFRC beams' load-deflection behaviour and moment-curvature relationship had a bi-linear response bound by a cracking point. On the other hand, the load-deflection behaviour and moment-curvature response of the simulated steel-reinforced PC beams had three stages of response that were bound with the cracking of concrete and yielding of steel reinforcing bar.
- The percentage of error between experimental and numerical results of load, deflection, moment, and curvature at first cracking and ultimate strength and ductility indices of the BFRP-reinforced PC, BFRC, and PVAFRC were found within 10%. This shows good agreement of the numerical load-deflection behavior and moment-curvature relationships and ductility indices of BFRP-reinforced PC, BFRC, and PVAFRC beams with experimental results.
- The damage pattern of concrete in compression and tension and the crack pattern of the beams in tension were accurately illustrated by numerical models in a way similar to that of experimental crack pattern and the damage pattern of concrete in compression and tension.

Chapter 8
Conclusions and Scope for Future Research

8.1 Conclusions

The main objective of this thesis was to improve the flexural behavior of BFRP-reinforced concrete beams by reinforcing PC with basalt fibers and PVA fibers. The flexural behavior of BFRP-reinforced concrete beams was investigated in two concrete grades: NSC (M30 grade) and HSC (M70 grade). In the Phase-I of research work, the development of HSC using alccofine-1203 as a partial replacement to cement was investigated. Based on the performance of various alccofine-1203 based concrete mixes, the optimum percentage of alccofine-1203 to be used as a replacement for cement for the development of HSC of M70 grade was determined. Then, in the Phase-II of research work, a study was carried out to improve the strength properties of PC of M30 and M70 grades by reinforcing them with various percentages of basalt fibers and PVA fibers separately. Based on the results of BFRC and PVAFRC mixes, the optimum percentage of basalt fibers and PVA fibers was identified. Then, in the third phase of research work, BFRP under- and over-reinforced PC, BFRC, and PVAFRC beams of M30 and M70 grades were investigated experimentally to evaluate flexural strength, load-deflection behavior, moment-curvature relationships, stiffness, ductility, and cracking pattern and failure modes. The results of these beams were compared with steel under- and over-reinforced PC beams. To develop BFRC and PVAFRC for Phase-III work, the optimum percentage of fibers obtained from Phase-II of research work was used. In the Phase-IV of research work, numerical modelling of BFRP under- and over-reinforced PC, BFRC, and PVAFRC beams as well as steel under- and over-reinforced PC beams was done to validate the results of experimentally tested BFRP under- and over-reinforced PC, BFRC, and PVAFRC beams as well as steel under- and over-reinforced PC beams.

From the results of experimental, analytical, and numerical studies presented in the thesis, the following conclusions were drawn:

Experimental and Microstructural Investigations on Alccofine-1203 Based HSC

- The use of alccofine-1203 in the development of HSC was investigated through evaluating fresh properties and hardened properties which include mechanical and microstructural properties and compressive stress-strain behaviour of alccofine-1203 based concrete mixes.

- Among the replacement of 4%, 6%, 8%, 10%, 12% and 14% cement with alccofine-1203 from the control mix binder (80% cement and 20% fly ash), the highest improvement in mechanical properties and stress-strain behaviour of concrete was observed at 10% replacement level. Beyond 10% replacement, alccofine-1203 incorporation led to negative effect on strength improvement of concrete.
- The HSC binder mix containing 10% alccofine-1203 exhibited superior microstructural characteristics, such as the formation of additional C-S-H gel and dense core structure and the lowest Ca/Si ratio, indicating the development of HSC with the higher strength properties. Therefore, 10% replacement of cement with alccofine-1203 could be the best percentage to develop HSC with superior strength properties.
- At a constant water-binder ratio, aggregate weights and superplasticizer dosage, the incorporation of alccofine-1203 can lower the water demand of the mix needed since the workability of HSC mixes increased with an increase in percentage of cement replacement with alccofine-1203.
- The setting time of the alccofine-1203 incorporated concrete mixes decreased compared to the control mix. This could be advantageous in climate conditions where early hardening of HSC needed.

Experimental, Microstructural, and Analytical Studies on PVAFRCs and BFRCs

- At a constant water-binder ratio, superplasticizer dosage, and aggregate weights, the workability of concrete mixes decreased with the addition of basalt fibers and PVA fibers. This may be attributed to the moisture-absorbing property of the fibers.
- The mechanical, microstructural properties, and stress-strain behavior of concrete showed the highest improvement with the addition of 0.3% basalt fibers and PVA fibers in two strengths of BFRCs and PVAFRCs.
- The incorporated basalt and PVA fibers improved the flexural and split tensile strength of the concrete highest than the compressive strength.
- The addition of basalt fibers and PVA fibers beyond 0.3% showed a negative effect on the strength improvement and on the behavior of compressive stress-strain curves in two strengths of BFRCs and PVAFRCs.
- The basalt and PVA fibers improved the post-peak behavior of BFRCs and PVAFRCs by controlling the post-crack regime. This led to an increase in EAC of the concrete.

- The mechanical properties and stress-strain behavior of PVAFRC30 and BFRC30 mixes were improved the most with the addition of PVA fibers and basalt fibers compared to the PVAFRC70 and BFRC70 mixes.
- The percentage improvement in mechanical properties and compressive stress-strain behavior of M30 and M70 grade concretes with the incorporation of PVA fibers was greater than the improvement shown by the basalt fibers.
- The reinforcing, crack-arresting, crack-bridging mechanism, and balling effect of PVA and basalt fibers were observed in SEM images of PVAFRCs and BFRCs. The fracture and pull-out failure of PVA and basalt fibers in the concrete matrix show the development of a high-quality bond between the fiber and matrix, enhancing the strength of PVAFRCs and BFRCs.
- To predict the compressive stress-strain curves of PVAFRCs and BFRCs, a modified analytical constitutive model was proposed based on the Ezeldin and Balaguru's constitutive analytical model.
- The stress-strain curves of PVAFRCs and BFRCs modelled using modified constitutive analytical model and proposed relationships of peak-stress, strain at peak-stress and material parameter (β_n) with MRI values of PVA fibers and basalt fibers showed good agreement with experimental stress-strain curves.
- The constitutive analytical model and relationships proposed between β and RI by various researchers were unable to accurately predict the experimental stress-strain curves of PVAFRCs and BFRCs.

Experimental Investigation on Flexural Response of BFRP-Reinforced PC, BFRC, and PVAFRC Beams

- All the BFRP RC (PC, BFRC, and PVAFRC) beams showed higher flexural strength than steel-reinforced PC beams.
- The BFRP RC beams exhibited more deformation, curvature, and cracks during testing before beam fails due to lower Young's modulus of BFRP rebars.
- The PC beams reinforced with BFRP rebars showed low deflections, curvature at cracking, and ultimate load. Additionally, the stiffness and ductility of the beams decreased significantly compared to steel-reinforced PC beams.
- The decrement in stiffness of the beams after cracking was more significant for BFRP RC beams compared to steel-reinforced PC beams.

- The amount of deflection and curvature at cracking and ultimate strength exhibited by BFRP-reinforced PC beams, as well as the decrease in their stiffness, and ductility indices were countered by reinforcing PC with basalt and PVA fibers.
- Reinforcing PC with PVA fibers enhanced the flexural response of BFRP-reinforced PVAFRC beams better than the enhancement attributed to BFRP-reinforced BFRC beams by reinforcing PC with basalt fibers.
- The cracking and crack pattern of BFRP RC beams were almost similar to steel-reinforced PC beams. However, before BFRP RC beams reached ultimate failure, they exhibited a higher number of flexural tensile cracks and crack branches due to the development of higher stress in BFRP rebar and concrete.
- The steel under-reinforced PC beams failed due to the yielding of steel reinforcement in the tension zone, while steel over-reinforced PC beams failed due to the crushing of concrete in the compression zone. For BFRP RC beams, rupture failure of BFRP rebars in the tension zone, crushing of concrete in the compression zone, and compression-flexural-shear failure were the observed failure patterns during the experimental study.

Numerical Investigation on Flexural Response of BFRP-Reinforced PC, BFRC, and PVAFRC Beams

- The numerical load-deflection, moment-curvature, and ductility indices results are in the same pattern as experimental results and showed good agreement with them.
- Modelling the concrete beams using the stress-strain curves of BFRCs and PVAFRCs improved the flexural strength, deflection, curvature, stiffness, and ductility response of the numerically modelled BFRP RC beams.
- A maximum of 10% error difference was obtained between experimental and numerical load, deflection, moment, and curvature at first cracking and ultimate strength, as well as the ductility indices of BFRP RC beams. This shows good agreement of the numerical results of BFRP RC beams with the experimental results.
- Modeling BFRP RC beams using PVAFRC's stress-strain curves improved the flexural performance of BFRP-reinforced PVAFRCs more effectively than the improvement observed when modeling BFRP-reinforced BFRC beams using the stress-strain curves of BFRCs.
- The cracking in the tension zone and the damage pattern of concrete in the compression zone of numerically modelled beams closely resembled the experimental cracking and damage patterns.

8.2 Significant Contribution from Research Work

- A novel supplementary cementitious material alccofine-1203 based high strength concrete was developed.
- A constitutive model was developed for modelling of compressive stress-strain curves of PVA fiber-reinforced concrete and basalt fiber-reinforced concrete.
- Evaluated the flexural behaviour of normal-strength and high-strength PC, basalt fiber- and the PVA fiber- reinforced concrete beams reinforced with BFRP rebars.
- The experimental behaviour of the above concrete beams is validated by conducting numerical analysis using FEM based software.
- A sustainable reinforcing system for enhancing structural performance of BFRP-reinforced PC beams was developed to counter back the undesirable behaviour of the beams associated with brittleness of BFRP rebars. This system includes alccofine-1203-based HSC, basalt fibers, PVA fibers, and BFRP rebars, aiming to improve the structural behavior of the beams.

8.3 Scope for Future Research

- Feasibility of using BFRP rebars in association with other engineering cementitious materials.
- The performance of BFRP rebars reinforced structural concrete members under biaxial compression can be explored.
- The investigation on shear behavior of FRC beams reinforced with BFRP rebars with BFRP rebars stirrups can be explored.
- The investigation on flexural response of BFRP-reinforced concrete beams under dynamic loading conditions can be explored.
- Application of BFRP rebars as pre-stressing tendons can be investigated.
- Application of BFRP rebars as dowel and tie bars for the reinforced concrete pavement can be investigated.

8.4 Limitations of the Research

- The replacement of 10% of cement with alccofine-1203 and 20% with fly ash resulted in the highest mechanical, microstructural, and compressive stress-strain properties. These outcomes may vary with changes in concrete mix proportions and other percentage combinations of alccofine-1203 and fly ash.

- The study on alccofine-1203 based high-strength concrete lacks comprehensive exploration of long-term durability factors associated with the developed concrete mixes.
- The results obtained from the investigation of BFRCs and PVAFRCs are confined to basalt fibers (6mm length, 13μm diameter) and PVA fibers (12mm length, 40μm diameter) at various volume percentages (0.1, 0.2, 0.3, 0.4, and 0.5%). The highest mechanical, microstructural, and compressive stress-strain properties were achieved at the 0.3% fiber addition. However, it is acknowledged that these outcomes may vary with changes in concrete mix proportions and fiber characteristics, such as length, diameter, and volume fractions.
- The relations proposed between the compressive stress-strain response and MRI values of PVA fibers for analytical modelling of compressive stress-strain curves of PVAFRC are applicable for the range of MRI values 0 to 0.221.
- The relations proposed between the compressive stress-strain properties and MRI values of PVA fibers for the analytical modelling of compressive stress-strain curves of PVAFRCs are applicable for the range of MRI values from 0 to 0.221.
- The relations proposed between the compressive stress-strain properties and MRI values of basalt fibers for the analytical modelling of compressive stress-strain curves of BFRCs are applicable for the range of MRI values from 0 to 0.327.
- For the analytical modelling of the compressive stress-strain curves of PVAFRCs and BFRC, different relations for ascending and descending phases of the stress-strain curve were proposed between material parameter (β_n) and MRI values of the fibers.
- The study assessed the flexural response of BFRP-reinforced PC, BFRC, and PVAFRC beams, employing both under and over singly reinforced beams with a pure bending region under four-point static loading. The obtained results are confined to the strength of the concrete and reinforcing materials such as helical wound sand-coated BFRP rebars, basalt fibers, and PVA fibers. It is noted that the results of the study may vary when using different types of surface-configured BFRP rebars, FRCs, and loading conditions.
- Steel bars are used as transverse reinforcement for all the beams, as BFRP rebar loses its strength when bent into a rectangular stirrup due to its composite nature. BFRP rebars are used only as longitudinal reinforcement in the tension regions of the BFRP-RC beams.

Bibliography

[1] A. Sarja, *Integrated life cycle design of structures*. Finland: CRC Press, 2002.

[2] D. Pawłowski and M. Szumigała, "Flexural behaviour of full-scale basalt FRP RC beams - Experimental and numerical studies," in *Procedia Engineering, 7th Scientific-Technical Conference Material Problems in Civil Engineering (MATBUD'2015)*, 2015, vol. 108, pp. 518–525.

[3] J. Cai, J. Pan, and X. Zhou, "Flexural behavior of basalt FRP reinforced ECC and concrete beams," *Construction and Building Materials*, vol. 142, pp. 423–430, 2017.

[4] P. C. Association, "Types and causes of concrete deterioration," *ortland Cement Association, Skokie, IL, USA*, 2002.

[5] A. Lapko and M. Urbański, "Experimental and theoretical analysis of deflections of concrete beams reinforced with basalt rebar," *Archives of Civil and Mechanical Engineering*, vol. 15, no. 1, pp. 223–230, 2015.

[6] H. Zhu, S. Cheng, D. Gao, S. M. Neaz, and C. Li, "Flexural behavior of partially fiber-reinforced high-strength concrete beams reinforced with FRP bars," *Construction and Building Materials*, vol. 161, pp. 587–597, 2018.

[7] G. Nkurunziza, A. Debaiky, P. Cousin, and B. Benmokrane, "Durability of GFRP bars: A critical review of the literature," *Progress in Structural Engineering and Materials*, vol. 7, no. 4, pp. 194–209.

[8] P. Banibayat and A. Patnaik, "Creep rupture performance of basalt fiber-reinforced polymer bars," *Journal of Aerospace Engineering*, vol. 28, no. 3, p. 04014074, 2013.

[9] F. Elgabbas, P. Vincent, E. A. Ahmed, and B. Benmokrane, "Experimental testing of basalt-fiber-reinforced polymer bars in concrete beams," *Composites Part B: Engineering*, vol. 91, pp. 205–218, 2016.

[10] B. Tighiouart, B. Benmokrane, and P. Mukhopadhyaya, "Bond strength of glass FRP rebar splices in beams under static loading," *Construction and Building Materials*, vol. 13, no. 7, pp. 383–392, 1999.

[11] D. Tomlinson and A. Fam, "Performance of Concrete Beams Reinforced with Basalt FRP for Flexure and Shear," *Journal of Composites for Construction*, vol. 19, no. 2, p.

4014036, 2015.

[12] F. Elgabbas, E. A. Ahmed, and B. Benmokrane, “Physical and mechanical characteristics of new basalt-FRP bars for reinforcing concrete structures,” *Construction and Building Materials*, vol. 95, pp. 623–635, 2015.

[13] F. Yuan, J. Pan, and C. K. Y. Leung, “Flexural Behaviors of ECC and Concrete / ECC Composite Beams Reinforced with Basalt Fiber-Reinforced Polymer,” *Journal of Composites for Construction*, vol. 17, pp. 591–602, 2013.

[14] E. Korol, J. Tejchman, and Z. Mróz, “Experimental and numerical assessment of size effect in geometrically similar slender concrete beams with basalt reinforcement,” *Engineering Structures*, vol. 141, pp. 272–291, 2017.

[15] I. Ahmed, T. Manzur, I. H. EFAZ, and T. Mahmood, “Experimental study on bond performance of epoxy coated bars and uncoated deformed bars in concrete,” Bangladesh University of Engineering & Technology (BUET), 2017.

[16] Austroads, “Service life prediction of reinforced concrete structures,” in *Austroads Project No. N.T&E.9813*, Sydney, Australia, 2000.

[17] E. Cosenza, G. Manfredi, and R. Realfonzo, “Behavior and Modeling of Bond of FRP Rebars to Concrete,” *Journal of Composites for Construction*, vol. 1, no. 2, pp. 40–51, 1997.

[18] I. F. Kara, A. F. Ashour, and M. A. Köroğlu, “Flexural behavior of hybrid FRP/steel reinforced concrete beams,” *Composite Structures*, vol. 129, pp. 111–121, 2015.

[19] C. Soriano and A. Alfantazi, “Corrosion behavior of galvanized steel due to typical soil organics,” *Construction and Building Materials*, vol. 102, pp. 904–912, 2016.

[20] B. Saikia, J. Thomas, A. Ramaswamy, and K. S. Nanjunda Rao, “Performance of hybrid rebars as longitudinal reinforcement in normal strength concrete,” *Materials and Structures*, vol. 38, no. 284, pp. 857–864, 2005.

[21] J. P. Won, C. G. Park, H. H. Kim, S. W. Lee, and C. I. Jang, “Effect of fibers on the bonds between FRP reinforcing bars and high-strength concrete,” *Composites Part B: Engineering*, vol. 39, no. 5, pp. 747–755, 2008.

[22] ACI 440.1R-15, “Guide for the Design and Construction of Structural Concrete

Reinforced with Fiber-Reinforced Polymer (FRP) Bars," American Concrete Institute, Farmington Hills, 2015.

[23] M. Urbanski, A. Lapko, and A. Garbacz, "Investigation on concrete beams reinforced with basalt rebars as an effective alternative of conventional R/C structures," in *Procedia Engineering, 11th International Conference on Modern Building Materials, Structures and Techniques, MBMST 2013*, 2013, vol. 57, pp. 1183–1191.

[24] M. A. Issa, T. Ovitigala, and Mustapha Ibrahim, "Shear Behavior of Basalt Fiber Reinforced Concrete Beams with and without Basalt FRP Stirrups," *Journal of Composites for Construction*, vol. 20, no. 4, 2016.

[25] W. Zhishen, W. Xin, and W. Gang, "Advancement of structural safety and sustainability with basalt fiber reinforced polymers," in *Poceedings of CICE 2012 6th International Conference on FRP Composites in Civil Engineering*, 2012, p. 29.

[26] S. Gopinath, A. R. Murthy, and H. Patrawala, "Near surface mounted strengthening of RC beams using basalt fiber reinforced polymer bars," *Construction and Building Materials*, vol. 111, pp. 1–8, 2016.

[27] X. Wang, Z. Wang, Z. Wu, and F. Cheng, "Shear behavior of basalt fiber reinforced polymer (FRP) and hybrid FRP rods as shear resistance members," *Construction and Building Materials*, vol. 73, pp. 781–789, 2014.

[28] C. High, H. M. Seliem, A. El-Safty, and S. H. Rizkalla, "Use of basalt fibers for concrete structures," *Construction and Building Materials*, vol. 96, pp. 37–46, 2015.

[29] J. Wu, H. Li, and G. Xian, "Influence of elevated temperature on the mechanical and thermal performance of BFRP rebar," *Advances in FRP Composites in Civil Engineering*, 2011, pp. 69–72.

[30] W. Ge, J. Zhang, D. Cao, and Y. Tu, "Flexural behaviors of hybrid concrete beams reinforced with BFRP bars and steel bars," *Construction and Building Materials*, vol. 87, pp. 28–37, 2015.

[31] X. Fan and M. Zhang, "Behaviour of inorganic polymer concrete columns reinforced with basalt FRP bars under eccentric compression: An experimental study," *Composites Part B: Engineering*, vol. 104, pp. 44–56, 2016.

[32] A. El Refai, M.-A. Ammar, and R. Masmoudi, "Bond Performance of Basalt Fiber-

Reinforced Polymer Bars to Concrete," *Journal of Composites for Construction*, vol. 19, no. 3, p. 04014050, 2014.

[33] X. Fan and M. Zhang, "Experimental study on flexural behaviour of inorganic polymer concrete beams reinforced with basalt rebar," *Composites Part B: Engineering*, vol. 93, pp. 174–183, 2016.

[34] Gohnert, M., Van Gool, R. & Benjamin. m., "BFRP reinforced in concrete beams in flexure," *The Structural Engineer*, pp. 38–43, 2014.

[35] A. Bentur and S. Mindess, *Fibre reinforced cementitious composites*. Crc Press, 2006.

[36] Perumalsamy N. Balaguru and S. P. Shah, *Fiber-reinforced Cement Composites*. New York: McGraw-Hill, 1992.

[37] P. K. Mehta and P. J. M. Monteiro, *Concrete: microstructure, properties, and materials*, 2006.

[38] Y. Mohammadi, S. P. Singh, and S. K. Kaushik, "Properties of steel fibrous concrete containing mixed fibres in fresh and hardened state," *Construction and Building Materials*, vol. 22, no. 5, pp. 956–965, 2008.

[39] A. Caggiano, M. Cremona, C. Faella, C. Lima, and E. Martinelli, "Fracture behavior of concrete beams reinforced with mixed long/short steel fibers," *Construction and Building Materials*, vol. 37, pp. 832–840, 2012.

[40] P. Iyer, S. Y. Kenno, and S. Das, "Mechanical Properties of Fiber-Reinforced Concrete Made with Basalt Filament Fibers," *Journal of Materials in Civil Engineering*, vol. 27, no. 1998, pp. 1–8, 2015.

[41] J. Branston, S. Das, S. Y. Kenno, and C. Taylor, "Mechanical behaviour of basalt fibre reinforced concrete," *Construction and Building Materials*, vol. 124, pp. 878–886, 2016.

[42] T. Horikoshi, A. Ogawa, T. Saito, and H. Hoshiro, "Properties of polyvinyl alcohol fiber as reinforcing materials for cementitious composites," in *In Proceedings of the International RILEM Workshop on High Performance Fiber Reinforced Cementitious Composites in Structural Applications*, 2006, pp. 145–153.

[43] A. Noushini, B. Samali, and K. Vessalas, "Effect of polyvinyl alcohol (PVA) fibre on dynamic and material properties of fibre reinforced concrete," *Construction and Building*

Materials, vol. 49, pp. 374–383, 2013.

[44] S. Wang and V. C. Li, "Polyvinyl alcohol fiber reinforced engineered cementitious composites: material design and performances," *In Proceedings of the International Workshop on HPFRCC Structural Applications, Hawaii*, 2005.

[45] V. C. Li, S. Wang, and C. Wu, "Tensile strain-hardening behavior of polyvinyl alcohol engineered cementitious composite (PVA-ECC)," *Materials Journal*, vol. 98, no. 6, pp. 483–492, 2001.

[46] A. Kumar, O. Parihar, R. Chaudhary, and S. P. Singh, "Use of alccofine 1206 to achieve high performance durable concrete," *SSRG International Journal of Civil Engineering (SSRG-IJCE)*, vol. 3, no. 5, pp. 181–185, 2016.

[47] P. Jangra, D. Singhal, and B. B. Jindal, "Preparation of Geopolymer Concrete (GPC) Using High-Silica Rice Husk Ash (RHA) Incorporating Alccofine," *Advanced Science, Engineering and Medicine*, vol. 9, no. 5, pp. 370–376, 2017.

[48] S. Gupta, S. Sharma, and E. D. Sharma, "A Review on Alccofine : A supplementary cementitous material," *International Journal of Modern Trends in Engineering and Research*, vol. 2, no. 8, pp. 114–119, 2015.

[49] B. B. Jindal, Praveen, D. Singhal, and A. Goyal, "Predicting Relationship between Mechanical Properties of Low Calcium Fly Ash-Based Geopolymer Concrete," *Transactions of the Indian Ceramic Society*, vol. 5456, pp. 258–265, 2017.

[50] D. Soni, S. Kulkarni, and V. Parekh, "Experimental Study on High-Performance Concrete , with Mixing of Alccofine and Flyash," *Indian Journal of Research*, vol. 3, no. 4, pp. 84–86, 2013.

[51] B. Huo, G. Yang, and X. Zhang, "Research on the flexural behavior of BFRP Concrete Beams," *Advanced Materials Research*, vol. 598, pp. 351–355, 2012.

[52] M. Inman, E. R. Thorhallsson, and K. Azrague, "A Mechanical and Environmental Assessment and Comparison of Basalt Fibre Reinforced Polymer (BFRP) Rebar and Steel Rebar in Concrete Beams," in *Energy Procedia, 8th International Conference on Sustainability in Energy and Buildings, SEB-16*, 2017, vol. 111, pp. 31–40.

[53] F. Elgabbas, E. A. Ahmed, and B. Benmokrane, "Flexural Behavior of Concrete Beams Reinforced with Ribbed Basalt-FRP Bars under Static Loads," *Journal of Composites*

for Construction, vol. 21, no. 3, p. 04016098, 2016.

[54] T. Ovitigala, M. A. Ibrahim, and M. A. Issa, "Serviceability and ultimate load behavior of concrete beams reinforced with basalt fiber-reinforced polymer bars," *ACI Structural Journal*, vol. 113, no. 4, pp. 757–768, 2016.

[55] J. Duic, S. Kenno, and S. Das, "Performance of concrete beams reinforced with basalt fibre composite rebar," *Construction and Building Materials*, vol. 176, pp. 470–481, 2018.

[56] CSA-S6-19, "Canadian highway bridge design code," Canadian Standard Association, Ontario, Canada, 2019.

[57] T. Younes, A. Al-Mayah, and T. Topper, "Fatigue performance of prestressed concrete beams using BFRP bars," *Construction and Building Materials*, vol. 157, pp. 313–321, 2017.

[58] F. Abed and A. Rahman, "Effect of basalt fi bers on the fl exural behavior of concrete beams reinforced with BFRP bars," *Composite Structures*, vol. 215, pp. 23–34, 2019.

[59] W. Qu, X. Zhang, and H. Huang, "Flexural Behavior of Concrete Beams Reinforced with Hybrid (GFRP and Steel) Bars," *Journal of Composites for Construction*, vol. 13, no. 5, pp. 350–359, Oct. 2009.

[60] A. El Refai, F. Abed, and A. Al-Rahmani, "Structural performance and serviceability of concrete beams reinforced with hybrid (GFRP and steel) bars," *Construction and Building Materials*, vol. 96, pp. 518–529, 2015.

[61] H. G. Harris and W. Somboonsong, "New ductile hybrid FRP reinforcing bar for concrete structure," *Journal of Composites for Construction*, vol. 2, pp. 28–37, 1998.

[62] M. Ju, S. Lee, and C. Park, "Response of Glass Fiber Reinforced Polymer (GFRP)-Steel Hybrid Reinforcing Bar in Uniaxial Tension," *International Journal of Concrete Structures and Materials*, vol. 11, no. 4, pp. 677–686, Dec. 2017.

[63] S. Gopinath, P. Nachiappan, A. R. Murthy, and N. R. Iyer, "Use of basalt fiber reinforced polymer bars in the development of hybrid beam - Investigations on the flexural response," *Indian Journal of Engineering and Materials Sciences*, vol. 24, no. 2, pp. 153–161, 2017.

[64] M. S. Akiel, T. El-Maaddawy, and A. El Refai, "Serviceability and moment redistribution of continuous concrete members reinforced with hybrid steel-BFRP bars," *Construction and Building Materials*, vol. 175, pp. 672–681, 2018.

[65] F. Abed, A. El Refai, and S. Abdalla, "Experimental and finite element investigation of the shear performance of BFRP-RC short beams," *Structures*, vol. 20, no. July, pp. 689–701, 2019.

[66] T. T. Tran, T. M. Pham, and H. Hao, "Effect of hybrid fibers on shear behaviour of geopolymer concrete beams reinforced by basalt fiber reinforced polymer (BFRP) bars without stirrups," *Composite Structures*, vol. 243, no. March, p. 112236, 2020.

[67] F. Abed, M. K. Sabbagh, and A. S. Karzad, "Effect of basalt microfibers on the shear response of short concrete beams reinforced with BFRP bars," *Composite Structures*, vol. 269, no. May, p. 114029, 2021.

[68] A. El Refai, W. Alnahhal, A. Al-Hamrani, and S. Hamed, "Shear performance of basalt fiber-reinforced concrete beams reinforced with BFRP bars," *Composite Structures*, vol. 288, no. February, p. 115443, 2022.

[69] S. Hamoush, T. Abu-lebdeh, and T. Cummins, "Deflection behavior of concrete beams reinforced with PVA micro-fibers," *Construction and Building Materials*, vol. 24, no. 11, pp. 2285–2293, 2010.

[70] M. R. Bangi and T. Horiguchi, "Effect of fibre type and geometry on maximum pore pressures in fibre-reinforced high strength concrete at elevated temperatures," *Cement and Concrete Research*, vol. 42, no. 2, pp. 459–466, 2012.

[71] W. Hu, X. Yang, J. Zhou, H. Xing, and J. Xiang, "Experimental Research on the Mechanical Properties of PVA Fiber Reinforced Concrete," *Research Journal of Applied Sciences, Engineering and Technology*, vol. 5, no. 18, pp. 4563–4567, 2013.

[72] A. Noushini, B. Samali, and K. Vessalas, "Influence of polyvinyl alcohol fibre addition on fresh and hardened properties of concrete," in *Proceedings of the 13th East Asia-Pacific Conference on Structural Engineering and Construction, EASEC-2013*, 2013.

[73] M. F. Nuruddin, S. U. Khan, N. Shafiq, and T. Ayub, "Strength development of concrete incorporating metakaolin and PVA fibres," *The Scientific World Journal*, vol. 567, 2014.

[74] M. K. Yew, H. Bin Mahmud, B. C. Ang, and M. C. Yew, "Effects of low volume fraction

of polyvinyl alcohol fibers on the mechanical properties of oil palm shell lightweight concrete," *Advances in Materials Science and Engineering*, vol. 2014, 2015.

[75] A. Noushini, K. Vessalas, and B. Samali, "Rheological Properties and Compressive Strength Behaviour of Polyvinyl Alcohol Fibre-Reinforced Concrete," *Australian Journal of Structural Engineering*, vol. 15, no. 1, pp. 77–88, 2015.

[76] M. F. Nuruddin, S. U. Khan, N. Shafiq, and T. Ayub, "Strength Prediction Models for PVA Fiber-Reinforced High-Strength Concrete," *Journal of Materials in Civil Engineering*, vol. 27, no. 12, pp. 1–16, 2015.

[77] M. Devi, L. Kannan, M. G. kumar, and T. S. V. achalam, "Flexural Behavior of Polyvinyl Alcohol Fiber Reinforced Concrete," *SSRG International Journal of Civil Engineering (SSRG-IJCE)*, vol. 4, no. 6, pp. 26–30, 2017.

[78] F. Xu, X. Deng, C. Peng, J. Zhu, and J. Chen, "Mix design and flexural toughness of PVA fiber reinforced fly ash-geopolymer composites," *Construction and Building Materials*, vol. 150, pp. 179–189, 2017.

[79] H. R. Pakravan, M. Jamshidi, and M. Latifi, "The effect of hydrophilic (polyvinyl alcohol) fiber content on the flexural behavior of engineered cementitious composites (ECC)," *The Journal of The Textile Institute*, vol. 109, no. May 2017, pp. 79–84, 2018.

[80] C. Zhu, J. Zhang, J. Peng, W. Cao, and J. Liu, "Physical and mechanical properties of gypsum-based composites reinforced with PVA and PP fibers," *Construction and Building Materials*, vol. 163, pp. 695–705, 2018.

[81] Z. P. Loh, K. H. Mo, C. G. Tan, and S. H. Yeo, "Mechanical characteristics and flexural behaviour of fibre-reinforced cementitious composite containing pva and basalt fibres," *Sadhana*, vol. 44, no. 4, pp. 1–9, 2019.

[82] R. Zhang, L. Jin, Y. Tian, G. Dou, and X. Du, "Static and dynamic mechanical properties of eco-friendly polyvinyl alcohol fiber-reinforced ultra-high-strength concrete," *Structural Concrete*, vol. 20, no. 3, pp. 1051–1063, 2019.

[83] L. Hong, Y. D. Chen, T. D. Li, P. Gao, and L. Z. Sun, "Microstructure and bonding behavior of fiber-mortar interface in fiber-reinforced concrete," *Construction and Building Materials*, vol. 232, 2020.

[84] S. H. Ghasemzadeh Mosavinejad, M. A. M. Langaroudi, J. Barandoust, and A.

Ghanizadeh, “Electrical and microstructural analysis of UHPC containing short PVA fibers,” *Construction and Building Materials*, vol. 235, p. 117448, 2020.

[85] F. R. Souza, V. N. Lima, D. C. T. Cardoso, and F. A. Silva, “Experimental Study of Polyvinyl Alcohol (PVA) Fiber Reinforced Concrete under Cyclic Loading,” in *CILAMCE-PANACM-2021 Proceedings of the XLII Ibero-Latin-American Congress on Computational Methods in Engineering and III Pan-American Congress on Computational Mechanics, ABMEC-IACM*, 202.

[86] P. Zhang, X. Han, Y. Zheng, J. Wan, and D. Hui, “Effect of PVA fiber on mechanical properties of fly ash-based geopolymer concrete,” *Reviews on Advanced Materials Science. Sci.*, vol. 60, no. 1, pp. 418–437, 2021.

[87] G. Prashanth Naik, K. Hemalatha, and S. Konik, “Flexural performance of Hybrid Fiber Reinforced Polymer Concrete using PVA fiber,” in *E3S Web of Conferences*, 2021, vol. 309.

[88] Q. Xiao, L. Feng, Y. Xia, and F. Xu, “Characterization of PVA Fiber-Reinforced Pervious Concrete with Blended Recycled Ceramic Aggregates and Natural Aggregate,” *Advances in Materials Science and Engineering*, vol. 2022, 2022.

[89] T. Zych and W. Krasodomski, *Study on the properties of cement mortars with basalt fibres*. In *Brittle Matrix Composites 10*, 2012, pp. 155–166.

[90] F. Chen, “An Experimental Study on Mechanical Properties of Basalt Fiber Reinforced Concrete,” *Applied Mechanics and Materials*, vol. 405–408, pp. 2767–2770, 2013.

[91] T. M. Borhan, “Thermal and Mechanical Properties of Basalt Fibre Reinforced Concrete,” *World Academy of Science, Engineering and Technology International Journal of Civil and Environmental Engineering*, vol. 7, no. 4, pp. 334–337, 2013.

[92] N. Shafiq, M. F. Nuruddin, A. E. A. Elshekh, and A. F. M. Salih, “Effect of chopped basalt fiber on the fresh and hardened properties of fly ash high strength concrete,” *Applied Mechanics and Materials*, vol. 567, pp. 381–386, 2014.

[93] T. Ayub, N. Shafiq, and M. F. Nuruddin, “Mechanical Properties of High-Performance Concrete Reinforced with Basalt Fibers,” in *Procedia Engineering, Fourth International Symposium on Infrastructure Engineering in Developing Countries, IEDC 2013*, 2014, vol. 77, pp. 131–139.

[94] A. B. Kizilkanat, N. Kabay, V. Akyüncü, S. Chowdhury, and A. H. Akça, "Mechanical properties and fracture behavior of basalt and glass fiber reinforced concrete: An experimental study," *Construction and Building Materials*, vol. 100, pp. 218–224, 2015.

[95] T. Ayub, N. Shafiq, and S. U. Khan, "Compressive Stress-Strain Behavior of HSFRC Reinforced with Basalt Fibers," *Journal of Materials in Civil Engineering*, vol. 28, no. 4, pp. 1–11, 2016.

[96] M. E. Arslan, "Effect of basalt fibers on fracture energy and mechanical properties of HSC," *Computers and Concrete*, vol. 17, no. 4, pp. 553–566, 2016.

[97] S. Jalasutram, H. Khas, D. R. Sahoo, H. Khas, and V. Matsagar, "Experimental investigation on mechanical properties of basalt fibre-reinforced concrete," *Structural Concrete*, pp. 1–22, 2016.

[98] H. Zhang, B. Wang, A. Xie, and Y. Qi, "Experimental study on dynamic mechanical properties and constitutive model of basalt fiber reinforced concrete," *Construction and Building Materials*, vol. 152, pp. 154–167, 2017.

[99] Y. R. Zhao, L. Wang, Z. K. Lei, X. F. Han, and Y. M. Xing, "Experimental study on dynamic mechanical properties of the basalt fiber reinforced concrete after the freeze-thaw based on the digital image correlation method," *Construction and Building Materials*, vol. 147, pp. 194–202, 2017.

[100] Z. Algin and M. Ozen, "The properties of chopped basalt fibre reinforced self-compacting concrete," *Construction and Building Materials*, vol. 186, pp. 678–685, 2018.

[101] J. Zhang, Y. Zhao, and H. Li, "Effect of basalt fibers on mechanical properties of high-performance concrete containing supplementary cementitious materials," *RILEM Bookseries*, vol. 15, pp. 181–187, 2018.

[102] D. Wang, Y. Ju, H. Shen, and L. Xu, "Mechanical properties of high performance concrete reinforced with basalt fiber and polypropylene fiber," *Construction and Building Materials*, vol. 197, pp. 464–473, 2019.

[103] X. Sun, Z. Gao, P. Cao, and C. Zhou, "Mechanical properties tests and multiscale numerical simulations for basalt fiber reinforced concrete," *Construction and Building Materials*, vol. 202, pp. 58–72, 2019.

[104] M. Li, F. Gong, and Z. Wu, “Study on mechanical properties of alkali-resistant basalt fiber reinforced concrete,” *Construction and Building Materials*, vol. 245, p. 118424, 2020.

[105] H. Zhou, B. Jia, H. Huang, and Y. Mou, “Experimental study on basic mechanical properties of basalt fiber reinforced concrete,” *Materials*, vol. 13, no. 6, p. 20, 2020.

[106] B. Ramesh and S. Eswari, “Mechanical behaviour of basalt fibre reinforced concrete: An experimental study,” *Materials Today: Proceedings*, vol. 43, pp. 2317–2322, 2020.

[107] Y. Wang, S. Hu, and Z. He, “Mechanical and fracture properties of geopolymer concrete with basalt fiber using digital image correlation,” *Theoretical and Applied Fracture Mechanics*, vol. 112, no. September 2020, p. 102909, 2021.

[108] J. H. Haido, B. A. Tayeh, S. S. Majeed, and M. Karpuzcu, “Effect of high temperature on the mechanical properties of basalt fibre self-compacting concrete as an overlay material,” *Construction and Building Materials*, vol. 268, p. 121725, 2021.

[109] A. Gültekin, A. Beycioğlu, M. E. Arslan, A. H. Serdar, M. Dobiszewska, and K. Ramyar, “Fresh Properties and Fracture Energy of Basalt and Glass Fiber–Reinforced Self-Compacting Concrete,” *Journal of Materials in Civil Engineering*, vol. 34, no. 1, pp. 1–9, 2022.

[110] M. S. Pawar and A. C. Saoji, “Performance Of Self Compacting Concrete By Using Alccofine,” *International Journal of Engineering Research and Applications*, vol. 3, no. 4, pp. 190–192, 2013.

[111] S. Kavitha and T. Felix Kala, “Evaluation of strength behavior of self-compacting concrete using alccofine and GGBS as partial replacement of cement,” *Indian Journal of Science and Technology*, vol. 9, no. 22, pp. 1–5, 2016.

[112] B. V. Kavyateja, J. Guru Jawahar, and C. Sashidhar, “Effectiveness of alccofine and fly ash on mechanical properties of ternary blended self compacting concrete,” in *Materials Today: Proceedings*, 2020, vol. 33, pp. 73–79.

[113] K. A. A., S. G. S., and M. A. M., “Alccofine and steel in self-compacting concrete,” *Int. International Journal of Advance Engineering and Research Development*, vol. 5, no. 04, pp. 504–508, 2018.

[114] L. J. Sanjeev Kumar, P. Bhuvaneshwari, M. Eswar, and K. Aditya Subramanian,

"Strength characteristics of alccofine based light weight concrete," *International Journal of Advanced Research in Engineering and Technology (IJARET)*, vol. 10, no. 1, pp. 268–275, 2019.

[115] R. Balamuralikrishnan and J. Saravanan, "Effect of addition of alccofine on the compressive strength of cement mortar cubes," *Emerging Science Journal*, vol. 5, no. 2, pp. 155–170, 2021.

[116] S. Suthar, B. K Shah, and P. J Patel, "Study on effect of Alccofine & Fly ash addition on the Mechanical properties of High performance Concrete," *International Journal for Scientific Research & Development*, vol. 1, no. 3, pp. 464–467, 2013.

[117] G. G. K. Reddy and P. Ramadoss, "Performance evaluation of ultra-high performance concrete designed with alccofine," *Innovative Infrastructure Solutions*, vol. 6, no. 1, pp. 1–11, 2020.

[118] S. P. Upadhyay and M. A. Jamnu, "Effect on compressive strength of high performance concrete incorporating alcofine and fly ash," *International Journal of Innovative Research & Development*, vol. 2, no. 2, pp. 125–130, 2014.

[119] S. C. Boobalan, V. A. Srivatsav, A. M. T. Nisath, A. P. Babu, and V. Gayathri, "A comprehensive review on strength properties for making Alccofine based high performance concrete," *Materials Today: Proceedings*, vol. 45, pp. 4810–4812, 2021.

[120] M. M. Magdum and V. V Karjinni, "Influence of Mineral Admixture (Alccofine-1203) On the Properties of Hybrid Fiber Reinforced Concrete," *American Journal of Engineering Research*, vol. 5, no. 10, pp. 72–75, 2016.

[121] K. Srinivas, L. P. Sankar, and C. K. Swamy, "Experimental investigation on rapid strength gain by adding alccofine in high strength concrete," in *Materials Today: Proceedings*, 2021, vol. 46, pp. 925–929.

[122] D. Sharma, S. Sharma, and A. Goyal, "Utilization of Waste Foundry Slag and Alccofine for Developing High Strength Concrete," *International Journal of Electrochemical Science*, vol. 7, no. March, pp. 1–10, 2016.

[123] Saurav and A. K. Gupta, "Experimental study of strength relationship of concrete cube and concrete cylinder using ultrafine slag Alccofine," *International Journal of Scientific & Engineering Research*, vol. 5, no. 5, pp. 102–107, 2014.

[124] K. S. Rajesh, A. K. Samanta, and D. K. Singha Roy, “An experimental study on the mechanical properties of alccofine based high grade concrete,” *International Journal of Multidisciplinary Research and Development*, vol. 2, no. 10, pp. 218–224, 2015.

[125] A. N. Reddy and T. Meena, “An experimental investigation on mechanical behaviour of eco-friendly concrete,” in *14th International Conference on Science, Engineering the Technology, IOP Conference Series: Materials Science and Engineering*, 2017, vol. 263, no. 3.

[126] A. N. Reddy and T. Meena, “Study on Compressive Strength of Concrete Incorporating Alccofine and Ground Granulated Blast Furnace Slag (GGBS),” in *International Conference on Materials, Manufacturing and Modelling*, 2017, no. March, pp. 1–11.

[127] B. B. Jindal, D. Singhal, S. K. Sharma, D. K. Ashish, and P. Parveen, “Improving compressive strength of low calcium fly ash geopolymer concrete with alccofine,” *Advances in concrete construction*, vol. 5, no. 1, pp. 17–29, 2017.

[128] K. Srinivasreddy and S. Balamurugan, “Effect of alccofine 1203 on setting times and strength of ternary blended geopolymer mixes with msand cured at ambient temperature,” *Revista Romana de Materiale/ Romanian Journal of Materials*, vol. 49, no. 4, pp. 527–534, 2019.

[129] Parveen, D. Singhal, M. T. Junaid, B. B. Jindal, and A. Mehta, “Mechanical and microstructural properties of fly ash based geopolymer concrete incorporating alccofine at ambient curing,” *Construction and Building Materials*, vol. 180, pp. 298–307, 2018.

[130] ACI-318-2019(22), *Building Code Requirements for Structural Concrete and Commentary*. Farmington Hills, USA: American Concrete Institute, 2018.

[131] IS 12269-2013, “Ordinary Portland Cement, 53 Grade — Specification,” Bureau of Indian Standards, New Delhi, India, 2013.

[132] IS 3812 (Part 1) - 2013, “Pulverized Fuel Ash - Specification: Part 1 For Use as Pozzolana in Cement, Cement Mortar and Concrete,” Bureau of Indian Standards, New Delhi, India, 2013.

[133] IS 456-2000, “Plain and Reinforced Concrete -Code of Practice,” Bureau of Indian Standards, New Delhi, India, 2000.

[134] IS 12089-1987, “Specification for granulated slag for the manufacture of Portland slag

cement," Bureau of Indian Standards, New Delhi, India, 1987.

[135] IS:383-2016, "Coarse and Fine Aggregate for Concrete-Specification," Bureau of Indian Standards, New Delhi, India, 2016.

[136] IS 9103-1999, "Concrete Admixture-Specifications," Bureau of Indian Standards, New Delhi, India, 1999.

[137] IS 10262-2019, "Concrete Mix Proportioning - Guidlines," Bureau of Indian Standards, New Delhi, India, 2019.

[138] IS 4031 (Pat 4) - 1988, "Methods Of Physical Tests for Hydraulic Cement - Part 4 Determination Of Consistency Of Standard Cement Paste," Bureau of Indian Standards, New Delhi, India, 1988.

[139] IS 5513-1996, "Vicat apparatus-specifications," Bureau of Indian Standards, New Delhi, India, 1996.

[140] IS 4031 (Part 5) - 1988, "Methods Of Physical Tests for Hydraulic Cement - Part 5 Determination of Initial and Final Setting Times," Bureau of Indian Standards, New Delhi, India, 2005.

[141] IS 1199 (Part 2)-2018, "Fresh Concrete - Method of smapling, Testing and Analysis," Bureau of Indian Standards, New Delhi, India, 2018.

[142] IS 516-1959, "Method of Tests for Strength of Concrete," Bureau of Indian Standards, New Delhi, India, 2004.

[143] IS 5816-1999, "Splitting tensile strength of concrete- Mrethod of test," Bureau of Indian Standards, New Delhi, India, 2004.

[144] ASTM C469, "Standard Test Method for Static Modulus of Elasticity and Poisson's Ratio of Concrete in Compression," Annual Book of ASTM Standard, USA, 2010.

[145] Michael Thomas, *Optimizing the use of fly ash in concrete*. Skokie, USA: Portland Cement Association, 2007.

[146] M. Ahmaruzzaman, "A review on the utilization of fly ash," *Progress in Energy and Combustion Science*, vol. 36, no. 3, pp. 327–363, 2010.

[147] F. Moghaddam, V. Sirivivatnanon, and K. Vessalas, "The effect of fly ash fineness on heat of hydration, microstructure, flow and compressive strength of blended cement

pastes," *Case Studies in Construction Materials*, vol. 10, no. 2018, 2019.

[148] S. B. Suthar and B. K. Shah, "Study on Strength Development of High Strength Concrete Containing Alccofine and Fly-Ash," *Indian Journal of Research*, vol. 2, no. 3, pp. 102–104, 2013.

[149] K. M. Ng, C. M. Tam, and V. W. Y. Tam, "Studying the production process and mechanical properties of reactive powder concrete: A Hong Kong study," *Magazine of Concrete Research*, vol. 62, no. 9, pp. 647–654, 2010.

[150] K. O. Kjellsen, O. H. Wallevik, and L. Fjällberg, "Microstructure and microchemistry of the paste-aggregate interfacial transition zone of high-performance concrete," *Advances in Cement Research*, vol. 10, no. 1, pp. 33–40, 1998.

[151] S. Fallah and M. Nematzadeh, "Mechanical properties and durability of high-strength concrete containing macro-polymeric and polypropylene fibers with nano-silica and silica fume," *Construction and Building Materials*, vol. 132, pp. 170–187, 2017.

[152] V.M. Malhotra, "High-performance high-volume fly ash concrete," *Concrete International*, vol. 24, no. 7, pp. 30-34, 2002.

[153] L. Senff, J. A. Labrincha, V. M. Ferreira, D. Hotza, and W. L. Repette, "Effect of nano-silica on rheology and fresh properties of cement pastes and mortars," *Construction and Building Materials*, vol. 23, no. 7, pp. 2487–2491, 2009.

[154] H. Zanni, M. Cheyrezy, V. Maret, S. Philippot, and P. Nieto, "Investigation of hydration and pozzolanic reaction in reactive powder concrete (RPC) using 29Si NMR," *Cement and Concrete Research*, vol. 26, no. 1, pp. 93–100, 1996.

[155] M. K. Yew, I. Othman, M. C. Yew, S. H. Yeo, and H. B. Mahmud, "Strength properties of hybrid nylon-steel and polypropylene-steel fibre-reinforced high strength concrete at low volume fraction," *International Journal of Physical Sciences*, vol. 6, no. 33, pp. 7584–7588, 2011.

[156] Y. Ling, P. Zhang, J. Wang, and Y. Chen, "Effect of PVA fiber on mechanical properties of cementitious composite with and without nano-SiO2," *Construction and Building Materials*, vol. 229, p. 117068, 2019.

[157] A. Noushini, K. Vessalas, G. Arabian, and B. Samali, "Drying Shrinkage Behaviour of Fibre Reinforced Concrete Incorporating Polyvinyl Alcohol Fibres and Fly Ash,"

Advances in Civil Engineering, vol. 2014, p. 836173, 2014.

[158] V. C. Li, "A simplified micromechanical model of compressive strength of fiber-reinforced cementitious composites," *Cement and Concrete Composites*, vol. 14, no. 2, pp. 131–141, 1992.

[159] H. N. Atahan, B. Y. Pekmezci, and E. Y. Tuncel, "Behavior of PVA Fiber-Reinforced Cementitious Composites under Static and Impact Flexural Effects," *Journal of Materials in Civil Engineering*, vol. 25, no. October, pp. 1438–1445, 2013.

[160] D. V Soulioti, N. M. Barkoula, A. Paipetis, and T. E. Matikas, "Effects of fibre geometry and volume fraction on the flexural behaviour of steel-fibre reinforced concrete," *Strain*, vol. 47, pp. e535–e541, 2011.

[161] A. O. Mydin and S. Soleimanzadeh, "Effect of polypropylene fiber content on flexural strength of lightweight foamed concrete at ambient and elevated temperatures," *Advances in Applied Science Research*, vol. 3, no. 5, pp. 2837–2846, 2012.

[162] A. Noushini, K. Vessalas, and B. Samali, "Flexural and tensile characteristics of polyvinyl alcohol fibre reinforced concrete (PVA-FRC),"In *Proceedings of the Thirteenth East Asia-Pacific Conference on Structural Engineering and Construction (EASEC-13)*, p. B-5, 2013.

[163] L. Sun, Q. Hao, J. Zhao, D. Wu, and F. Yang, "Stress strain behavior of hybrid steel-PVA fiber reinforced cementitious composites under uniaxial compression," *Construction and Building Materials*, vol. 188, pp. 349–360, 2018.

[164] P. Soroushian and Z. Bayasi, "Fiber type effects on the performance of steel fiber reinforced concrete," *Materials Journal*, vol. 88, no. 2, pp. 129–134, 1991.

[165] ACI 5443R-08, "Guide for specifying, proportioning, mixing, placing, and finishing steel fiber reinforced concrete," American Concrete Institute, Farmington Hills, 2008.

[166] I. Padron and R. F. Zollo, "Effect of synthetic fibers on volume stability and cracking of Portland cement concrete and mortar," *Materials Journal*, vol. 87, no. 4, pp. 327–332, 1990.

[167] D. J. Hannant, "Fibre-reinforced concrete," *Advanced concrete technology*, pp. 1–17, 2003.

[168] A Bentur and S. Mindess, *Fiber Reinforced Cementitious Composites*, Second edi. London: Taylor & Francis, 2007.

[169] V. Afroughsabet, G. Geng, A. Lin, L. Biolzi, C. P. Ostertag, and P. J. M. Monteiro, "The influence of expansive cement on the mechanical, physical, and microstructural properties of hybrid-fiber-reinforced concrete," *Cement and Concrete Composites*, vol. 96, no. October 2018, pp. 21–32, 2019.

[170] M. Cao, C. Xie, and J. Guan, "Fracture behavior of cement mortar reinforced by hybrid composite fiber consisting of CaCO 3 whiskers and PVA-steel hybrid fibers," *Composites Part A: Applied Science and Manufacturing*, vol. 120, no. March, pp. 172–187, 2019.

[171] M. Khan, M. Cao, and M. Ali, "Cracking behaviour and constitutive modelling of hybrid fibre reinforced concrete," *Journal of Building Engineering*, vol. 30, no. October 2019, p. 101272, 2020.

[172] J. S. Lawler, T. Wilhelm, D. Zampini, and S. P. Shah, "Fracture processes of hybrid fiber-reinforced mortar," *Materials and Structures*, vol. 36, no. 257, pp. 197–208, 2003.

[173] F. J. Silva and C. Thaumaturgo, "Fibre reinforcement and fracture response in geopolymeric mortars," *Fatigue Fract. Eng. Materials and Structures*, vol. 26, no. 2, pp. 167–172, 2003.

[174] M. F. Arain, M. Wang, J. Chen, and H. Zhang, "Experimental and numerical study on tensile behavior of surface modified PVA fiber reinforced strain-hardening cementitious composites (PVA-SHCC)," *Construction and Building Materials*, vol. 217, pp. 403–415, 2019.

[175] M. Cao, C. Xie, L. Li, and M. Khan, "The relationship between reinforcing index and flexural parameters of new hybrid fiber reinforced slab," *Computers and Concrete*, vol. 22, no. 5, pp. 481–492, 2018.

[176] Ş. Özkan and F. Demir, "The hybrid effects of PVA fiber and basalt fiber on mechanical performance of cost effective hybrid cementitious composites," *Construction and Building Materials*, vol. 263, p. 120564, 2020.

[177] M. Maalej, V. C. Li, and Toshiyuki Hashida, "Effect of Fiber Rupture on Tensile Properties of Short fiber composites," *Journal of Engineering Mechanics*, vol. 121, no.

August, pp. 903–913, 1995.

[178] F. Aslani and S. Nejadi, “Self-compacting concrete incorporating steel and polypropylene fibers: Compressive and tensile strengths, moduli of elasticity and rupture, compressive stress-strain curve, and energy dissipated under compression,” *Composites Part B: Engineering*, vol. 53, pp. 121–133, 2013.

[179] A. Noushini, F. Aslani, A. Castel, R. I. Gilbert, B. Uy, and S. Foster, “Compressive stress-strain model for low-calcium fly ash-based geopolymer and heat-cured Portland cement concrete,” *Cement and Concrete Composites*, vol. 73, pp. 136–146, 2016.

[180] D. J. Carreira and K.-H. Chu, “Stress-Strain Relation for Plain Concrete in Compression,” *ACI Structural Journal*, vol. 82, no. 6, pp. 797–804, 1985.

[181] S. A. Ezeldin and P. N. Balaguru, “Normal- And High-Strength Fiber- Reinforced Concrete under Compression,” *Journal of Materials in Civil Engineering*, vol. 4, no. 170, pp. 415–429, 1992.

[182] M. A. Mansur, M. S. Chin, and T. H. T. H. Wee, “Stress-Strain Relationship of High-Strength Fiber Concrete in Compression,” *Journal of Materials in Civil Engineering*, vol. 11, no. 1, pp. 21–29, 1999.

[183] Y. C. Ou, M. Sen Tsai, K. Y. Liu, and K. C. Chang, “Compressive Behavior of Steel-Fiber-Reinforced Concrete with a High Reinforcing Index,” *Journal of Materials in Civil Engineering*, vol. 24, no. 2, pp. 207–215, 2012.

[184] S. C. Lee, J. H. Oh, and J. Y. Cho, “Compressive behavior of fiber-reinforced concrete with end-hooked steel fibers,” *Materials*, vol. 8, no. 4, pp. 1442–1458, 2015.

[185] M. C. Nataraja, N. Dhang, and A. P. Gupta, “Stress-strain curves for steel fiber-reinforced concrete under compression,” *Cement and Concrete Composites*, vol. 21, no. 5–6, pp. 383–390, 1999.

[186] P. Bhargava, U. K. Sharma, and S. K. Kaushik, “Compressive stress-strain behavior of small scale steel fibre reinforced high strength concrete cylinders,” *Journal of Advanced Concrete Technology*, vol. 4, no. 1, pp. 109–121, 2006.

[187] T. Ayub, S. U. Khan, and A. Ayub, “Analytical model for the compressive stress–strain behavior of PVA-FRC,” *Construction and Building Materials*, vol. 214, pp. 581–593, 2019.

[188] T. Almusallam, S. M. Ibrahim, Y. Al-Salloum, A. Abadel, and H. Abbas, "Analytical and experimental investigations on the fracture behavior of hybrid fiber reinforced concrete," *Cement and Concrete Composites*, vol. 74, pp. 201–217, 2016.

[189] M. Cao and L. Li, "New models for predicting workability and toughness of hybrid fiber reinforced cement-based composites," *Construction and Building Materials*, vol. 176, no. 2, pp. 618–628, 2018.

[190] C. Tang, M. Wu, Y. Wu, and H. Liu, "Effects of fiber surface chemistry and size on the structure and properties of poly(vinyl alcohol) composite films reinforced with electrospun fibers," *Composites Part A: Applied Science and Manufacturing*, vol. 42, no. 9, pp. 1100–1109, 2011.

[191] M. F. Arain, M. Wang, J. Chen, and H. Zhang, "Study on PVA fiber surface modification for strain-hardening cementitious composites (PVA-SHCC)," *Construction and Building Materials*, vol. 197, pp. 107–116, 2019.

[192] M. A. Tasdemir, C. Tasdemir, S. Akyüz, A. D. Jefferson, F. D. Lydon, and B. I. G. Barr, "Evaluation of strains at peak stresses in concrete: A three-phase composite model approach," *Cement and Concrete Composites*, vol. 20, no. 4, pp. 301–318, 1998.

[193] S. F. U. Ahmed and H. Mihashi, "Strain hardening behavior of lightweight hybrid polyvinyl alcohol (PVA) fiber reinforced cement composites," *Materials and Structures*, vol. 44, no. 6, pp. 1179–1191, 2011.

[194] S. U. Khan and T. Ayub, "Modelling of the pre and post-cracking response of the PVA fibre reinforced concrete subjected to direct tension," *Construction and Building Materials*, vol. 120, pp. 540–557, 2016.

[195] S. U. Khan, T. Ayub, and S. F. A. Rafeeqi, "Prediction of Compressive Strength of Plain Concrete Confined with Ferrocement using Artificial Neural Network (ANN) and Comparison with Existing Mathematical Models," *American Journal of Civil Engineering and Architecture*, vol. 1, no. 1, pp. 7–14, 2013.

[196] W. Abbass, M. I. Khan, and S. Mourad, "Evaluation of mechanical properties of steel fiber reinforced concrete with different strengths of concrete," *Construction and Building Materials*, vol. 168, pp. 556–569, 2018.

[197] S. V Biradar, M. S. Dileep, and T. V. Gowri, "Studies of Concrete Mechanical Properties

with Basalt Fibers," in *IOP Conference Series: Materials Science and Engineering*, 2020, p. 012031.

[198] C. Jiang, K. Fan, F. Wu, and D. Chen, "Experimental study on the mechanical properties and microstructure of chopped basalt fibre reinforced concrete," *Materials and Design*, vol. 58, pp. 187–193, 2014.

[199] J. Wang and Y. Zhang, "Experimental research on mechanical and working properties of non-dipping chopped basalt fiber reinforced concrete," in *Proceedings - 3rd International Conference on Information Management, Innovation Management and Industrial Engineering, ICIII 2010*, 2010, vol. 4, pp. 635–637.

[200] Youjiang Wang, H. C. Wu, and V. C. Li, "Concrete reinforcement with recycled fibers," *Journal of Materials in Civil Engineering*, vol. 12, no. November, pp. 314–319, 2000.

[201] Q. Zhao, J. Dong, H. Pan, and S. Hao, "Impact behavior of basalt fiber reinforced concrete," *Fuhe Cailiao Xuebao/Acta Materiae Compositae Sinica*, vol. 27, pp. 120–125, Dec. 2010.

[202] W. Li and J. Xu, "Mechanical properties of basalt fiber reinforced geopolymeric concrete under impact loading," *Materials Science and Engineering A*, vol. 505, no. 1–2, pp. 178–186, 2009.

[203] J. Qin *et al.*, "Mechanical properties of basalt fiber reinforced magnesium phosphate cement composites," *Construction and Building Materials*, vol. 188, pp. 946–955, 2018.

[204] A. Sadrmomtazi, B. Tahmouresi, and A. Saradar, "Effects of silica fume on mechanical strength and microstructure of basalt fiber reinforced cementitious composites (BFRCC)," *Construction and Building Materials*, vol. 162, pp. 321–333, 2018.

[205] V. Manikandan, J. T. Winowlin Jappes, S. M. Suresh Kumar, and P. Amuthakkannan, "Investigation of the effect of surface modifications on the mechanical properties of basalt fibre reinforced polymer composites," *Composites Part B: Engineering*, vol. 43, no. 2, pp. 812–818, 2012.

[206] J. Il Choi and B. Y. Lee, "Bonding properties of basalt fiber and strength reduction according to fiber orientation," *Materials*, vol. 8, no. 10, pp. 6719–6727, 2015.

[207] IS 280-2006, "Mild Steel Wire for General Engineering Purposes," Bureau of Indian Standards, New Delhi, India, 2006.

[208] ASTM D7205/D7205M-06, “Standard Test Method for Tensile Properties of Fiber Reinforced Polymer Matrix Composite Bars,” ASTM International, West Conshohocken, PSA, USA, 2016.

[209] IS 1608 (Part 1) : 2018, “Metallic materials - Tensile testing at ambient temperature, Part 1 Method of test at room temperature,” Bureau of Indian Standards, New Delhi, India, 2018.

[210] Z. Li, H. Zhu, X. Zhen, C. Wen, and G. Chen, “Effects of steel fiber on the flexural behavior and ductility of concrete beams reinforced with BFRP rebars under repeated loading,” *Composite Structures*, vol. 270, no. May, p. 114072, 2021.

[211] S. M. Jeong and A. E. Naaman, “Ductility of concrete beams prestressed with FRP tendons,” in *Structures Congress - Proceedings*, vol. 2, L. Taerwe, Ed. London: CRC Press, 1995, pp. 1466–1469.

[212] and M. A. Jaeger, GL., Tadros, G., “The concept of the overall performance factor in 739 rectangular-section reinforced concrete beams,” in *In: Proc of 3rd int symp on non-metallic (FRP) 740 reinforcement for concrete structures*, 1997, vol. 2, p. Sapporo, Japan; 1997. p. 551–8..

[213] M. A. Adam, M. Said, A. A. Mahmoud, and A. S. Shanour, “Analytical and experimental flexural behavior of concrete beams reinforced with glass fiber reinforced polymers bars,” *Construction and Building Materials*, vol. 84, pp. 354–366, 2015.

[214] M. E. M. Mahroug, A. F. Ashour, and D. Lam, “Experimental response and code modelling of continuous concrete slabs reinforced with BFRP bars,” *Composite Structures*, vol. 107, pp. 664–674, 2014.

[215] G. B. Jumaa and A. R. Yousif, “Numerical modeling of size effect in shear strength of FRP-reinforced concrete beams,” *Structures*, vol. 20, no. March, pp. 237–254, 2019.

[216] Michael Smith, *ABAQUS/Standard User’s Manual, Version 6.9.* Providence, RI, U.S.A: Dassault Systèmes Simulia Corp, 2009.

[217] J. G. Stoner, “Finite Element Modelling of GFRP Reinforced,” University of Waterloo, Waterloo, Ontario, Canada, 2015.

[218] J. Lubliner, J. Oliver, S. Oller, and E. Oñate, “A plastic-damage model for concrete,” *International Journal of Solids and Structures*, vol. 25, no. 3, pp. 299–326, 1989.

[219] J. Lee and G. L. Fenves, “Plastic-Damage Model for Cyclic Loading of Concrete Structures,” *Journal of Engineering Mechanics*, vol. 124, no. 8, pp. 892–900, 1998.

[220] Dassault Systèmes, *Analysis User’s Guide: Volume III: Materials*, vol. III. 2014.

[221] S. Tamai, H. Shima, J. Izumo, and H. Okamura, “Average stress-strain relationship in post yield range of steel bar in concrete,” *Concrete Library of Jsce*, vol. 6. pp. 117–129, 1987.

[222] D. L. Trotsek, “Flexural Behavior of Concrete Using Basalt FRP Rebar,” Florida Atlantic University, 2017.

[223] ASTM A653/A653M-23, “Standard Specification for Steel Sheet, Zinc-Coated (Galvanized) or Zinc-Iron Alloy-Coated (Galvannealed) by the Hot-Dip Process,” ASTM International, USA, 2023.

[224] G. M. Chen, J. G. Teng, and J. F. Chen, “Finite-Element Modeling of Intermediate Crack Debonding in FRP-Plated RC Beams,” *Journal of Composites for Construction*, vol. 15, no. 3, pp. 339–353, 2011.

List of Scientific Publications by the Authors on the Topic of the Dissertation

Following are the international journals published from the research work presented.

1. Sagar, B. and Sivakumar, M.V.N., 2020. "An experimental and analytical study on alccofine based high strength concrete", in ***International Journal of Engineering***, 33(4), pp.530-538. https://doi.org/10.5829/ije.2020.33.04a.03 **(Scopus)**

2. Sagar, B. and Sivakumar, M.V.N., 2022. "Mechanical and microstructure characterization of Alccofine based high strength concrete", in ***Silicon***, 14(3), pp.795-813. https://doi.org/10.1007/s12633-020-00863-x **(SCIE)**

3. Sagar, B. and Sivakumar, M.V.N., 2021. "Compressive properties and analytical modelling for stress-strain curves of polyvinyl alcohol fiber reinforced concrete", in ***Construction and Building Materials***, 291, p.123192. https://doi.org/10.1016/j.conbuildmat.2021.123192 **(SCIE)**

4. Sagar, B. and Sivakumar, M.V.N., 2022. "Study on Basalt Fiber Reinforced Concrete: Mechanical and Microstructural Properties and Analytical Modelling of Compressive Stress-Strain Curves", in ***European Journal of Environmental and Civil Engineering***, pp.1-28. https://doi.org/10.1080/19648189.2022.2110161 **(SCIE)**

5. Sagar, B. and Sivakumar, M.V.N., 2021. "Use of alccofine-1203 in concrete: review on mechanical and durability properties", in ***International Journal of Sustainable Engineering***, 14(6), pp.2060-2073. https://doi.org/10.1080/19397038.2021.1970275 **(Scopus and ESCI)**

6. Sagar, B. and Sivakumar, M.V.N., 2021. "Performance evaluation of basalt fiber-reinforced polymer rebars in structural concrete members–a review", in ***Innovative Infrastructure Solutions***, 6(75), pp.1-18. https://doi.org/10.1007/s41062-020-00452-2 **(Scopus and ESCI)**